



NRL/MR/7320--18-9786

## Forecasting and Hindcasting Waves In and Near the Marginal Ice Zone: Wave Modeling and the ONR “Sea State” Field Experiment

W. ERICK ROGERS

*Ocean Dynamics and Prediction Branch  
Oceanography Division*

PAMELA POSEY

*Vencore, Inc.  
Reston, VA*

LI LI

*Remote Sensing Physics Branch  
Remote Sensing Division*

RICHARD ALLARD

*Ocean Dynamics and Prediction Branch  
Oceanography Division*

April 12, 2018

# REPORT DOCUMENTATION PAGE

Form Approved  
OMB No. 0704-0188

Public reporting burden for this collection of information is estimated to average 1 hour per response, including the time for reviewing instructions, searching existing data sources, gathering and maintaining the data needed, and completing and reviewing this collection of information. Send comments regarding this burden estimate or any other aspect of this collection of information, including suggestions for reducing this burden to Department of Defense, Washington Headquarters Services, Directorate for Information Operations and Reports (0704-0188), 1215 Jefferson Davis Highway, Suite 1204, Arlington, VA 22202-4302. Respondents should be aware that notwithstanding any other provision of law, no person shall be subject to any penalty for failing to comply with a collection of information if it does not display a currently valid OMB control number. **PLEASE DO NOT RETURN YOUR FORM TO THE ABOVE ADDRESS.**

1. REPORT DATE (DD-MM-YYYY) 12-04-2018			2. REPORT TYPE Memorandum Report		3. DATES COVERED (From - To)	
4. TITLE AND SUBTITLE  Forecasting and Hindcasting Waves In and Near the Marginal Ice Zone: Wave Modeling and the ONR "Sea State" Field Experiment					5a. CONTRACT NUMBER	
					5b. GRANT NUMBER	
					5c. PROGRAM ELEMENT NUMBER 0602435N	
6. AUTHOR(S)  W. Erick Rogers, Pamela Posey,* Li Li and Richard Allard					5d. PROJECT NUMBER	
					5e. TASK NUMBER	
					5f. WORK UNIT NUMBER 73-6A50-07-5	
7. PERFORMING ORGANIZATION NAME(S) AND ADDRESS(ES)  Naval Research Laboratory Oceanography Division Stennis Space Center, MS 39529-5004					8. PERFORMING ORGANIZATION REPORT NUMBER  NRL/MR/7320--18-9786	
9. SPONSORING / MONITORING AGENCY NAME(S) AND ADDRESS(ES)  Office of Naval Research One Liberty Center 875 North Randolph Street, Suite 1425 Arlington, VA 22203-1995					10. SPONSOR / MONITOR'S ACRONYM(S)  ONR	
					11. SPONSOR / MONITOR'S REPORT NUMBER(S)	
12. DISTRIBUTION / AVAILABILITY STATEMENT  DISTRIBUTION STATEMENT A: Approved for public release. Distribution is unlimited.						
13. SUPPLEMENTARY NOTES  * Vencore, Inc., Stafford, VA						
14. ABSTRACT  This report describes the development, application, and evaluation of wave models for the ONR "Sea State" Departmental Research Initiative. The Sea State field experiment is described, with particular attention to wave measurements and the wave conditions during the field experiment. Wave forecasting in support of the cruise is described. Implementation of the effects of sea ice on waves in the numerical wave model WAVEWATCH III® is described. The role of the ice forcing in the wave model performance is evaluated by contrasting different ice products and applying them in hindcasts. The relative strengths and weaknesses of the products are discussed. The relative skill of hindcasts with different physical parameterizations is also quantified for the various wave experiments conducted during the cruise. A model-data inversion is conducted to estimate the frequency distribution of the dissipation of wave energy by ice, separated by buoy type and wave experiment. A subset of the inversion results is used to create a new empirical physical parameterization, and this parameterization is compared with distributions given in the literature, and other model parameterizations.						
15. SUBJECT TERMS  WAVEWATCH III; wave model; sea ice; wave-ice interaction; Beaufort Sea						
16. SECURITY CLASSIFICATION OF:			17. LIMITATION OF ABSTRACT SAR	18. NUMBER OF PAGES 180	19a. NAME OF RESPONSIBLE PERSON W. Erick Rogers	
a. REPORT Unclassified Unlimited	b. ABSTRACT Unclassified Unlimited	c. THIS PAGE Unclassified Unlimited			19b. TELEPHONE NUMBER (include area code) (228) 688-4727	

This page intentionally left blank.

<b>LISTING OF TABLES AND FIGURES .....</b>	<b>V</b>
<b>EXECUTIVE SUMMARY .....</b>	<b>E-1</b>
<b>1. INTRODUCTION .....</b>	<b>1</b>
<b>2. OVERVIEW OF CRUISE.....</b>	<b>1</b>
2.1. OBSERVATIONS.....	4
2.1.1. MOORED BUOYS .....	4
2.1.2. DRIFTING BUOYS .....	5
2.1.3. SHIP-BORNE LIDAR AND RADAR.....	7
2.1.4. OTHER DATA .....	7
2.2. DESCRIPTION OF WAVE EXPERIMENTS .....	7
2.2.1. WA1: BUOY CALIBRATION IN OPEN WATER .....	9
2.2.2. WA2: WEAK, OBLIQUELY OFF-ICE WINDS.....	10
2.2.3. IS1: ICE STATION BEN .....	11
2.2.4. WA3: LARGE WAVES IN ICE .....	13
2.2.5. WA4-5: SMALL WAVES (ON-ICE AND OFF-ICE).....	16
2.2.6. WA6: OBLIQUELY OFF-ICE WAVES.....	19
2.2.7. RACETRACK (RT): WEAK OFF-ICE WINDS.....	21
2.2.8. WA7: ON-ICE SWELLS .....	23
2.3. WAVE FORECASTING .....	28
2.3.1. WAVE FORECASTING FOR WA3 AND WA4-5 .....	31
<b>3. OVERVIEW OF ICE TREATMENT IN WAVEWATCH III<sup>®</sup> .....</b>	<b>40</b>
3.1. ICE EFFECTS IN WW3.....	41
3.1.1. SWITCH "ICO" .....	43
3.1.2. SWITCH "IC1" .....	44
3.1.3. SWITCH "IC2" .....	45
3.1.4. SWITCH "IC3" .....	46
3.1.5. SWITCH "IC4" .....	47
3.1.6. SWITCH "IC5" .....	48
3.1.7. SWITCH "IS1" .....	48
3.1.8. SWITCH "IS2" .....	48
3.1.9. DISCUSSION .....	49
3.2. THE ROLE OF NUMERICAL ERROR.....	50
3.2.1. REMOVAL OF $S_{ice}$ FROM DYNAMIC TIME STEPPING.....	50
3.2.2. ERROR FROM SPATIAL DISCRETIZATION (RESOLUTION EFFECTS) .....	51
<b>4. EVALUATION OF ICE FORCING .....</b>	<b>54</b>
4.1. ICE CONCENTRATION FORCING.....	54
4.1.1. DESCRIPTION: NAVY CICE IMPLEMENTATIONS.....	55
4.1.2. DESCRIPTION: AMSR2 GRIDDED PRODUCTS.....	56
4.2. ICE THICKNESS FORCING .....	58
4.3. CASE STUDIES .....	59
4.3.1. SEPTEMBER 9 (PRIOR TO CRUISE) .....	59
4.3.2. OCTOBER 10-15: WAVE ARRAY #3.....	62
4.3.3. OCTOBER 20-25: GAP CLOSURE.....	67
4.3.4. OCTOBER 20-24: FETCH-LIMITED SCENARIO (OFF-ICE WINDS) .....	74

<b>5. EVALUATION OF WIND FORCING .....</b>	<b>77</b>
5.1. SKILL OF WIND SPEED ANALYSES (ENTIRE CRUISE).....	78
5.2. SKILL OF WIND SPEED FORECASTS (WA3 ONLY).....	80
<b>6. WW3 HINDCASTING .....</b>	<b>82</b>
6.1. MODEL IMPLEMENTATION .....	82
6.1.1. GRID DESIGN .....	82
6.1.2. SETTINGS AND INITIALIZATION.....	83
6.2. WW3 INVERSION .....	84
6.2.1. METHODS .....	84
6.2.2. RESULTS (ALL WAVE ARRAYS) .....	88
6.2.3. PARAMETRIC STEP FUNCTIONS FOR USE IN WW3: OLD AND NEW (BASED ON WA3) .....	94
6.2.4. COMPARISONS TO LITERATURE AND OTHER MODELS.....	96
6.2.5. SLOPE OF THE DEPENDENCE ON FREQUENCY (OR PERIOD).....	106
6.2.6. PARAMETRIC BINOMIAL FUNCTIONS: OLD AND NEW (BASED ON WA3).....	109
6.2.7. DIMENSIONS OF POLYNOMIAL FIT .....	110
6.3. WW3 FORWARD MODEL.....	111
6.3.1. SETTINGS.....	111
6.3.2. WAVE PARAMETERS.....	112
6.3.3. VALIDATION, BY WAVE EXPERIMENTS COLLECTIVELY .....	112
6.3.4. VALIDATION, BY WAVE EXPERIMENTS INDIVIDUALLY .....	127
6.3.5. SENSITIVITY ANALYSIS: THERMAL STABILITY EFFECTS (WA3).....	140
6.3.6. DISCUSSION: INCONSISTENCY BETWEEN DATA FROM DIFFERENT BUOY TYPES IN WA3.....	144
<b>7. ICE PHOTOS FROM SWIFT BUOYS (WA3) .....</b>	<b>146</b>
7.1. NEW ICE CODES AND APPLICATION TO $K_1$ PROFILES .....	146
7.2. ICE OBSERVATIONS VS. TKE DISSIPATION AND SALINITY.....	147
7.3. COMPARISON TO SAR.....	149
7.3.1. OCTOBER 11, PM .....	149
7.3.2. OCTOBER 12, AM.....	151
7.3.3. OCTOBER 12, PM .....	152
7.3.4. OCTOBER 13, AM.....	154
<b>8. SUMMARY OF CONCLUSIONS .....</b>	<b>155</b>
<b>ACKNOWLEDGMENTS .....</b>	<b>160</b>
<b>REFERENCES .....</b>	<b>160</b>

## Listing of tables and figures

Table 1. Amplitude attenuation rate, and the implied distance over which the waveheight is decreased to 50% of its original value. This table provides a convenient reference for the physical meaning of $k_i$ values used in this report.....	44
Table 2. Statistics for significant wave height, $H_{m0}$ . For dimensional quantities, units are in meters.....	134
Table 3. Statistics for mean period, $T_{m,-1,0}$ . For dimensional quantities, units are in seconds. ....	135
Table 4. Statistics for fourth moment of spectrum, $m_4$ . For dimensional quantities, units are in $m^2 s^4$ .....	136
Figure 1. Cruise track, reproduced from Thomson (2015), with some minor annotations added. Locations of wave arrays and ice stations are indicated. ....	
Figure 2. Example of ice coverage during the Sea State cruise, taken from the 10 km AMSR2 product described in Section 4.1. Date/time is indicated in title. Thick magenta and white line indicates track of R/V <i>Sikuliaq</i> (prior and future ship positions respectively). Black/white circle indicates present position of ship. The three diamonds mark AWAC moorings (Section 2.1.1). Color scale indicates ice concentration; contours are also included which mark 25%, 50%, and 75% ice concentration.....	4
Figure 3. Top panel: Nortek AWAC buoy, photo provided by UW/APL. Lower panel: photo during retrieval of the Sea State AWAC buoy. UW/APL engineers Joe Talbert and Alex deKlerk are at the left and right, respectively.....	5
Figure 4. Left: Diagram of SWIFT buoy, courtesy of APL/UW. Right: SWIFT buoys ready for deployment in the “Baltic room” of the R/V <i>Sikuliaq</i> .....	6
Figure 5. Time series of wave experiments. Green vertical line indicates the start of a wave experiment and red vertical line indicates the end. Panels, top to bottom are zero-moment waveheight, peak period, and mean wave direction. Dots indicate measurements from drifting buoys deployed from the R/V <i>Sikuliaq</i> . “WA”, “IS”, and “RT” indicate Wave Array, Ice Station, and Race Track, respectively.....	8
Figure 6. WW3 hindcast during WA1 (10 km resolution outer WW3 grid used for hindcasts; see Section 6.1.1). Date/time is indicated in title. Thick magenta and white line indicates track of R/V <i>Sikuliaq</i> (prior and future ship positions respectively). Black/white circle indicates present position of ship. Color scale indicates model $H_s$ and white arrows indicate model mean wave direction. Text “nb:2” indicates that two buoys were deployed at this time. Black rectangle indicates the boundary of the 5 km resolution inner WW3 grid used for hindcasts; see Section 6.1.1. Observations near ship: $H_s$ was 90 to 120 cm; $T_p$ 4.5 to 5.5 s; mean wave direction 45 to 80° (local windsea from northeast quadrant). ....	9
Figure 7. WW3 hindcast (5 km resolution inner WW3 grid; see Section 6.1.1). Date/time is indicated in title. Thick magenta and white line indicates track of R/V <i>Sikuliaq</i> (prior and future ship positions respectively). Black/white circle indicates present position of ship. Color scale indicates model $H_s$ and white arrows indicate model mean wave direction. Contours indicate ice concentration (25%, 50%, 75%). Text “nb:2” indicates that two buoys were deployed at this time. Observations near the ship were: $H_s$ up to 60 cm; $T_p$ 3 to 3.5 s; mean wave direction 300 to 325° (weak local windsea from northwest). All WW3 hindcast results from the “inner WW3 grid” used in this section (Section 2.2) employ the parametric	

Sice “IC4M6H2” introduced in Section 6.2.3 and the 10 km AMSR2 ice concentration forcing introduced in Section 4.1.2. The hindcasts are explained in Section 6.3. ....	10
Figure 8. Photo taken by Prof. Hayley Shen, October 4, 2015, 10:02LT. Multi-year ice and brash ice are visible. Floes with smoother top surfaces may be first-year or second-year ice. ....	11
Figure 9. WW3 hindcast. See caption of Figure 7 for explanation of annotation. Wave observations near ship: negligible energy. ....	12
Figure 10. Photo taken by Prof. Hayley Shen, October 6, 2015, 09:29LT. The ship is moored to a large multi-year floe (Ice Station Ben, or IS1). ....	12
Figure 11. UAS mosaic of IS1, reproduced from Thomson (2015). UAS courtesy of Guy Williams. The ship is visible to the left of the floe. ....	13
Figure 12. WW3 hindcast. See caption of Figure 7 for explanation of annotation. Drifting buoy observations: $H_s$ up to 4.8 m; $T_p$ 8 to 11 s; mean wave direction: 140° on the 11th to 120° on the 13th (from southeast). ....	15
Figure 13. Still image from a video by the author, ER, October 11 2015, 1200LT. Pancakes in heavy frazil ice. ....	16
Figure 14. WW3 hindcast. See caption of Figure 7 for explanation of annotation. Observations near ship: $H_s$ up to 35 cm; $T_p$ 4 to 7 s; mean wave direction 170° to 270° (Thus, primarily weak swell from south and southwest, though the primary system in basin is a windsea from east.) ....	17
Figure 15. Photo taken by Prof. Hayley Shen, October 17, 2015, 1512LT. Multi-year floe is visible, denoted in ice observations as the “AK and MD floe”; it is likely Ice Station 5, “Peter’s floe”. Pancake ice and floes from young ice are also visible. ....	18
Figure 16. WW3 hindcast. See caption of Figure 7 for explanation of annotation. Observations near ship: $H_s$ up to 35 cm; $T_p$ 4 to 7 s; mean wave direction 150° to 250°. (Thus, primarily weak swell from south and southwest, though the primary system in basin is a windsea from east.) ....	18
Figure 17. Photo taken by Prof. Hayley Shen, October 18, 2015, 1454LT. Pancakes near open water. Some have cemented together. Note that there is no visible evidence of frazil ice which is typically present when pancakes are forming: the water between pancakes is very dark, and where there are no pancakes, gravity-capillary waves are visible. ....	19
Figure 18. WW3 hindcast. See caption of Figure 7 for explanation of annotation. Observations near ship: $H_s$ up to 1.3 m; $T_p$ 3.5 to 8.7 s; mean wave direction 110° to 170° (fetch-limited windsea from southeast). ....	20
Figure 19. Wind and wave direction at the ship position during WA6. The former is from measurements on the ship’s mast and the latter is from marine radar. These data were provided by Ola Persson (NOAA); the marine radar operation and data processing was performed by Bjoern Lund (U. Miami). See also wave directions from drifting buoys in Figure 5 and other marine radar measurements in Figure 119. ....	20
Figure 20. Photo taken by Prof. Hayley Shen, October 23, 2015, 1235LT. Pancake and pancake brash. ....	21
Figure 21. WW3 hindcast. See caption of Figure 7 for explanation of annotation. Observations near ship: $H_s$ up to 36 cm; $T_p$ 2 to 5.5 s; mean wave direction 270° to 360° (waves from northwest, associated with local winds). ....	22
Figure 22. Photo taken by Prof. Hayley Shen, October 26, 2015, 1537LT. Open water and ice with snow cover. Ice with smooth snow surface is first year ice of uncertain origin (i.e. may	

have started as either nilas or pancakes). The ice with rougher upper surface is sheet ice formed from cemented pancakes.....	22
Figure 23. Still images from the time-lapse video made by Joe Talbert and Jim Thomson (U. Washington). Annotation added by author ER. This corresponds to dawn to dusk on October 26 2015. Given this date, and a latitude of 72.5°, the length of the day is estimated to be 6 to 6.5 hours.....	23
Figure 24. WW3 hindcast. See caption of Figure 7 for explanation of annotation. Observations near ship: $H_s$ up to 1.4 m; $T_p$ 3.8 to 8 s; mean wave direction 200° to 270° (swells from southwest).....	25
Figure 25. Photo taken by Prof. Hayley Shen, October 31, 2015, 1246LT. The floes with heavier snow cover are from broken first-year ice, likely formed from cemented pancakes, as evidenced by the texture. The floes with partial snow cover are from broken nilas or grey ice. The former are thicker and rigid (tending to fracture under wave motion), while the latter are thinner and flex with the low-amplitude wave motion (but still fracturing on occasion).....	25
Figure 26. WW3 hindcast. See caption of Figure 7 for explanation of annotation. Observations near ship: $H_s$ up to 1.4 m; $T_p$ 3.8 to 8 s; mean wave direction 200° to 270° (swells from southwest).....	26
Figure 27. Photo taken by Prof. Hayley Shen, October 31, 2015, 1538LT. Floes from first year ice and brash. The isolated patches of blue coloration are associated with ice that lies just under the water surface.....	26
Figure 28. Photo taken by Prof. Hayley Shen, October 31, 2015, 1657LT. Floes or cake ice from first year ice (likely was cemented pancakes).....	27
Figure 29. WW3 hindcast. See caption of Figure 7 for explanation of annotation. Observations near ship: $H_s$ up to 1.4 m; $T_p$ 3.8 to 8 s; mean wave direction 200° to 270° (swells from southwest).....	27
Figure 30. Photo taken by Prof. Hayley Shen, November 1, 2015, 1155LT. Open water, brash ice, and some floes from first year ice.....	28
Figure 31. Photo taken by Prof. Hayley Shen, November 1, 2015, 1401LT. Floes or cake ice from first-year ice; also pancakes and brash.....	28
Figure 32. Two forecasts of directional spectrum for the western component of an overlapping double swell event (from west and southwest) which may have contributed significantly to the retreat of the ice near the Racetrack Oct. 30 to Nov. 1. Left panel: Briefed at Oct 25 POD meeting, for AWAC position, 159.0W 72.6N. Right panel: Briefed at Oct 30 POD meeting, for 162.0W 72.0N.....	30
Figure 33. Example forecast graphic briefed at evening POD meetings. This was from the 1200 UTC 23 October run cycle of the on-ship WW3 system, briefed at the 23 October meeting. The original graphic included six time series: the two shown here, plus wind speed, wind direction, peak period, and mean period. There are six lines in each plot, each corresponding to a different location. These locations were indicated in separate graphics not included here.....	31
Figure 34. The second (and final) version of the 10-km inner WW3 nest used for on-ship forecasting. Active grid points are shown in cyan. The ship track is shown in magenta. This is also the inner grid used for hindcasting by Rogers et al. (2016). Note: it is <i>not</i> the inner grid used by Collins and Rogers (2017) and in the hindcasting in the present report. These two reports use a 5-km inner grid (Section 6.1.1).....	33

Figure 35. WW3 forecast of WA3, from the 0Z cycle forecast on Oct. 6. This is the inner grid, using the IC3 module ( $v = 1.0 \text{ m}^2\text{s}^{-1}$ ) and CICE. This is the last forecast for that run cycle, being the 6-day forecast. This is an actual graphic used in POD briefing, so it includes some cryptic notation, marking points to orient the viewer. Asterisks correspond to ECMWF forecast points which were also briefed in the POD. Alphanumeric strings mark the ship's position, e.g. 1006T20A for Oct. 6. "NG" is the position of the recovery of the NAVOCEANO glider. "BF" is Ben's floe, which was later denoted as Ice Station Ben or Ice Station 1 (IS1). "HE" marks the nominal position of a "hard ice edge" and the meaning of "SL" is not recalled. The red line marks the EEZ (economic exclusion zone) of Russia (something to be aware of when planning cruise routes). Note that the color scale is only up to 2 meters, so the forecasted waves are small relative to subsequent figures (and relative to observed waveheights). Since this is the initial 10 km inner nest, it does not extend all the way to the Alaska coast.....33

Figure 36. WW3 forecast of WA3, from the 0Z cycle forecast on Oct. 8. This is the outer grid, using the IC0 module and SSM/I. Since IC0 is used, regions with ice concentration larger than 75% are blank (white). This graphic was produced using the actual forecast fields (the on-ship model), but is not a graphic used in the POD briefing: rather, the graphic was re-created post-cruise, so most of the clutter seen in Figure 35 is removed here. The blue lines indicate the northern and southern transects of WA3. This is the forecast for 4 days and 21 hours in the future. By this time, WW3 was exhibiting good skill for prediction of the incident waves, unlike the forecast run on Oct. 6 (Figure 35).....34

Figure 37. WW3 forecast of WA3, from the 12Z cycle forecast on Oct. 8. This is the inner grid, using the IC3 module ( $v = 1.0 \text{ m}^2\text{s}^{-1}$ ) and CICE. This is the forecast for 4 days and 9 hours in the future. Again, WW3 was exhibiting good skill for prediction of the incident waves. This is an actual graphic used in POD briefing, so it includes some cryptic notation, like in Figure 35, marking points to orient the viewer. Since this is the initial 10 km inner nest, it does not extend all the way to the Alaska coast.....35

Figure 38. WW3 forecast of WA3, from the 00Z cycle forecast on Oct. 9. This is the outer grid, using the IC0 module and SSM/I. Since IC0 is used, regions with ice concentration larger than 75% are blank (white). This is the forecast for 3 days and 21 hours in the future. This is an actual graphic used in POD briefing, so it includes some cryptic notation, like in Figure 35, marking points to orient the viewer.....35

Figure 39. WW3 forecast of WA3, from the 12Z cycle forecast on Oct. 9. This is the inner grid, using the IC3 module ( $v = 1.0 \text{ m}^2\text{s}^{-1}$ ) and CICE. This is the forecast for 2 days and 18 hours in the future. This graphic was produced using the actual forecast fields (the on-ship model), but is not a graphic used in the POD briefing: rather, the graphic was re-created post-cruise, so most of the clutter seen in Figure 35 is removed here. The blue line indicates the southern transect of WA3. This is the revised 10 km inner nest, so it does extend all the way to the Alaska coast.....36

Figure 40. WW3 forecast of WA3, from the 0Z cycle forecast on Oct. 10. This is the inner grid, using the IC3 module ( $v = 1.0 \text{ m}^2\text{s}^{-1}$ ) and CICE. This is the forecast for 2 days and 6 hours in the future. This is an actual graphic used in POD briefing, so it includes the cryptic notation. This is the revised 10 km inner nest, so it does extend all the way to the Alaska coast.....37

Figure 41. WW3 forecast of WA3, from the 0Z cycle forecast on Oct. 10. This field is identical to that shown in Figure 40, but this graphic was re-created post-cruise, so most of the clutter

seen in that figure is removed here; axes and color scaling are also different. The blue line indicates the southern transect of WA3.....	37
Figure 42. This graphic is identical to Figure 41, but the effective viscosity of IC3 is reduced by a factor of 10: $\nu = 0.1 \text{ m}^2\text{s}^{-1}$ . This was run on Oct. 15 (post facto). In other words, it is a re-run of a prior forecast, using a different viscosity. .....	38
Figure 43. WW3 forecast of WA4-5, from the 12Z cycle forecast on Oct. 16. This is the inner grid, using the IC3 module ( $\nu = 0.1 \text{ m}^2\text{s}^{-1}$ ) and CICE. The 2100 UTC 18 October forecast is shown, so 2 days and 9 hours in the future. This is an actual graphic made for the POD briefing, so it includes the cryptic notation. This is the revised 10 km inner nest. The “IB1” marker is near the WA4-5 locations. This was a failed forecast: the Sunday Oct. 18 swell event was not evident at the ship location: see text. .....	38
Figure 44. WW3 hindcast of WA4-5, identical to Figure 14 and Figure 16, but showing the time period used in Figure 43, 2100 UTC 18 October. See caption of Figure 7 for explanation of annotation. This is the inner hindcast grid, which is 5 km resolution, in contrast to the 10 km resolution inner grid of the forecast model. It uses the IC4M6H2 routine and 10 km AMSR2 forcing (Section 6.3). The ship position—and approximate position of WA4-5—are shown with the black and white circle. This correctly shows that easterly and southeasterly swells did not reach the ship location: see text.....	39
Figure 45. Same as Figure 43, but showing time series plots: WW3 forecast of WA4-5, from the 12Z cycle forecast on Oct. 16; inner grid, using the IC3 module ( $\nu = 0.1 \text{ m}^2\text{s}^{-1}$ ); actual graphic made for the POD briefing. The “Ice Band 1” time series is a point near the WA4-5 locations. This was a failed forecast: the Sunday Oct. 18 swell event was not evident at the ship location: see text. .....	40
Figure 46. Waveheight (normalized by incident waveheight) vs. distance along axis for 1-D test case. The four groupings, top to bottom are $k_i=6\text{e-}6, 1\text{e-}5, 5\text{e-}5$ , and $5\text{e-}4 \text{ m}^{-1}$ respectively. Green: $\Delta x = 1 \text{ km}$ ; Blue: $\Delta x = 5 \text{ km}$ ; Black: analytical (true) solution. .....	52
Figure 47. Waveheight vs. distance for 1-D test cases with $\Delta x = 5 \text{ km}$ . The dissipation rates are indicated in the legend. Dots are the analytical (true) solution and crosses are WW3 results. .....	53
Figure 48. Waveheight vs. distance for 1-D test case with $k_i=1\text{e-}4 \text{ m}^{-1}$ . Blue: $\Delta x = 1 \text{ km}$ and $\Delta tg = 180 \text{ s}$ ; Red: $\Delta x = 1 \text{ km}$ and $\Delta tg = 45 \text{ s}$ ; Black: $\Delta x = 5 \text{ km}$ and $\Delta tg = 900 \text{ s}$ . (Here, $\Delta tg$ refers to the largest model time step, a.k.a the “global” time step.) The dissipation rates are indicated in the legend. Solid line is the analytical (true) solution and symbols are WW3 results. .....	53
Figure 49. Waveheight vs. distance for 1-D test case with $k_i=1\text{e-}4 \text{ m}^{-1}$ and $\Delta x = 5 \text{ km}$ . Time steps in seconds are indicated in the legend as three numbers: 1) global $\Delta t$ , 2) $\Delta t$ for geographic propagation, and 3) minimum $\Delta t$ for source terms. Solid black line is the analytical (true) solution.....	54
Figure 50. RADARSAT-2 “browse image” for 0339 UTC 9 Sept. 2015, courtesy of Bedford Institute of Oceanography. The four black square markers are added to compare with Figure 51 and Figure 52. RADARSAT-2 Data and Products © MacDONALD, DETTWILER AND ASSOCIATES LTD. (2015) – All Rights Reserved. RADARSAT is an official mark of the Canadian Space Agency. .....	60
Figure 51. Ice concentration for 0600 UTC 9 Sep. 2015, 3.125 km AMSR2 product, remapped to the 5 km WW3 grid. The four black square markers are added to facilitate comparison with Figure 50.....	61

Figure 52. Ice concentration for 0600 UTC 9 Sep. 2015, GOFS 3.1, remapped to the 5 km WW3 grid. The four black square markers are added to facilitate comparison with Figure 50.....	61
Figure 53. Comparison of ice concentration fields from AMSR2 products (3 of 4 panels) and GOFS (lower left panel). Upper left panel: AMSR2, processed using “Bootstrap” algorithm, plotted on native 10 km grid. Upper right panel: like prior, but processed using “NASA Team 2” algorithm. Lower left: GOFS, remapped to 5 km inner WW3 grid, similar to Figure 52. Lower right panel: AMSR2 using ASI algorithm, provided at 3.125 km resolution but plotted here remapped to the 5 km inner WW3 grid. Dates are indicated above each panel.....	62
Figure 54. Comparison of ice products and in situ observations during WA3. All data shown are contemporaneous, during the period of ice retreat. Magenta line is the cruise track, and the black circle is the ship location at the time of the image (0300 UTC 12 October 2015). Black diamonds indicate the terminal points of the southern transect of WA3, shown as a black line. Colored circles and colorbar indicate the buoy ice observations as described in Section 7 (0=open water and 12=heavy frazil and pancake ice). Gold lines are the IMS ice edge. Orange, green and blue lines are the 50% ice concentration contours from three gridded ice products: GOFS 3.1 reanalysis, 3.125 km AMSR2 (24-hourly), and 10 km AMSR2.....	65
Figure 55. Same as Figure 54, but showing the 10% ice concentration contours for GOFS 3.1 and AMSR2 fields.....	65
Figure 56. Comparison of ice products. Magenta and grey line is the cruise track, and the black circle is the ship location at the time of the image (0000 UTC 15 October 2015). Black diamonds indicate AWAC mooring locations. Black line is the boundary of the inner WW3 nest. Red, orange, green and blue lines are the 50% ice concentration contours from four gridded ice products (see text above plot).....	66
Figure 57. Like Figure 56, except showing 1200 UTC 16 October 2015.....	66
Figure 58. Like Figure 53, but comparing times near 2100 UTC 11 October. Upper left: Bootstrap. Upper right: NASA Team 2. Lower left: GOFS 3.1. Lower right: ASI.....	67
Figure 59. Top panel: SAR image of the ice from the <i>Sikuliaq</i> map server. The instrument, date, and time of the image is indicated in the text box embedded in the image: 0343 UTC 20 October 2015, RADARSAT-2 from BIO. RADARSAT-2: © MDA 2015. The cruise track is shown in red. Lower panel: Blue line is IMS. Red dots are the NIC ice edge. Dates are indicated in the title in year-day format; 294 is October 21. The date of data is one day earlier than the date of the filename, so this corresponds to satellite observations on the 20 <sup>th</sup> . .....	69
Figure 60. Same as Figure 59, but showing a different image, and looking at October 21. “RS2_NIC” indicates that this is a RADARSAT-2 image from the NIC. RADARSAT-2: © MDA 2015.....	70
Figure 61. Same as Figure 59, but showing a different image, and looking at October 24. This image is from ALOS (JAXA).....	71
Figure 62. Same as Figure 59, but showing a different image, and looking at October 25. RADARSAT-2: © MDA 2015.....	72
Figure 63. Same as top panel of Figure 59, but showing different images, October 27 and 30. RADARSAT-2: © MDA 2015.....	73
Figure 64. Like Figure 56, except showing 0000 UTC 22 October 2015. The Sea State AWAC mooring is indicated with a black diamond.....	75

Figure 65. Like Figure 64, except showing 0600 UTC 23 October 2015.....	75
Figure 66. SAR image from screenshot of the <i>Sikuliaq</i> Mapserver created by Steven Roberts (U. Alaska). NIC RadarSAT-2 for 0356 UTC 23 October 2015. RADARSAT-2: © MDA	76
2015. The red line is the cruise track near the Racetrack and AWAC mooring.....	76
Figure 67. Like Figure 64, except showing 1200 UTC 23 October 2015.....	76
Figure 68. Time series of significant waveheight $H_{m0}$ at the location of the Sea State AWAC mooring. Black dots are AWAC observations and the five colored lines are output from WW3 hindcasts, as indicated in the legend. The “ $k_i=0$ ” (purple) line is the case of zero dissipation by ice (with 10 km AMSR2 forcing), but wind input is still reduced by ice cover. The other four lines are hindcasts which are identical except for the source of ice forcing, indicated in the legend. (“Old DA” refers to nowcast and “New DA” refers to the reanalysis.).....	77
Figure 69. Like Figure 68, except showing the dominant wave period $T_m, 01, E4$ , which is defined in Section 6.3.2 .....	77
Figure 70. Evaluation of 10-meter winds from ECMWF. Ground truth is derived from winds measured with an anemometer on the ship. For both quantities, the 10-meter wind speeds have been converted to wind stress using an empirical model (see text). In the case of the anemometer, the wind speed is converted to 10 meters using a simple power law formula. Statistics are shown on the plot.....	79
Figure 71. Like Figure 70, except evaluating the 10-meter wind speeds from NAVGEM. ....	79
Figure 72. Like Figure 70, except evaluating the 10-meter wind speeds from COAMPS. ....	80
Figure 73. NAVGEM wind field 0000 UTC 12 October 2015. Color scaling is 10-meter wind speed. Magenta and grey lines are the ship track and circles are the ship location. Black diamonds indicate the polygon used to evaluate forecast skill in Figure 74. ....	81
Figure 74. Forecast skill for NAVGEM and COAMPS, combining forecasts from several run cycles. All points correspond to the forecast or nowcast for 0000 UTC 12 October 2015. Vertical axis is the mean wind speed within the polygon of Figure 73. Horizontal axis is the run cycle used, so the rightmost value (101200) is the nowcast run cycle and all values to the left are forecast run cycles. The leftmost blue value (100412) is the forecast produced by NAVGEM on 1200 UTC 4 October, and is therefore a 7.5-day forecast. The leftmost red value (100800) is the COAMPS forecast on 0000 UTC 8 October, so it is 4-day forecast. ....	82
Figure 75. WW3 grids. Color indicates mask of outer (10 km) WW3 grid. Cyan indicates active grid points, while red and blue indicate inactive grid points. White is outside the grid. The black rectangle is the outline of the 5 km inner WW3 grid.....	83
Figure 76. Inversion procedure: example of successful inversion. Shown is the inversion for the spectrum measured by SWIFT14 on 0215 UTC 12 Oct. 2015, which is inversion number 593 out of 2590. Position and AMSR2 ice concentration (“aice”) are indicated in title text. Top panel shows model-data mismatch vs. $k_i$ . A zero on vertical axis corresponds to “optimal value” of $k_i$ (circles), determined by linear interpolation from model vs. observation comparisons (dots). Each discrete value on the horizontal axis corresponds to a separate simulation. Each curve corresponds to a frequency interval of the spectrum (see legend). Lower panel: $k_i$ solution vs. frequency. See text for further explanation. ....	85
Figure 77. Inversion procedure: example of failed inversion. The lower panel is intentionally blank. Shown is the inversion for the spectrum measured by SWIFT14 on 2315 UTC 12 Oct. 2015, which is inversion number 916 out of 2590. Position and AMSR2 ice	

concentration (“aice” are indicated in title text. Top panel shows model-data mismatch vs. $k_i$ . Lower panel: $k_i$ solution vs. frequency. See text for full explanation.....	87
Figure 78. Inversion procedure: example inversion for case of very low wave conditions (Ice Station 1). Shown is the inversion for the spectrum measured by SWIFT09 on 0115 UTC 7 Oct. 2015, which is inversion number 79 out of 2590. Position and AMSR2 ice concentration (“aice” are indicated in title text. Top panel shows model-data mismatch vs. $k_i$ . Lower panel: $k_i$ solution vs. frequency. See text for explanation.....	88
Figure 79. Inversion solutions ( $k_i$ profiles) for Ice Station 1 (IS1), with SWIFT buoys. This includes 129 inversions. Purple dashed line: step function IC4M6H2. Black dashed line: step function IC4M6H. The step functions are introduced in Section 6.2.3. Color indicates ice fraction determined from AMSR2 data. ....	89
Figure 80. Similar to Figure 79, but for SWIFT buoys in Wave Array #3 (WA3). The number of inversions plotted is indicated in the title above the plot. ....	90
Figure 81. Similar to Figure 80, but for UK buoys in Wave Array #3 (WA3). ....	90
Figure 82. Similar to Figure 80, but for NIWA buoy in Wave Array #3 (WA3).....	91
Figure 83. Similar to Figure 80, but for SWIFT buoys in Wave Arrays 4 and 5 (WA4-5).....	91
Figure 84. Similar to Figure 80, but for UK buoys in Wave Arrays 4 and 5 (WA4-5).....	92
Figure 85. Similar to Figure 80, but for SWIFT buoys in Wave Array #6 (WA6).....	92
Figure 86. Similar to Figure 80, but for UK buoys in Wave Array #6 (WA6). ....	93
Figure 87. Similar to Figure 80, but for SWIFT buoys in the Racetrack (RT) wave experiment.	93
Figure 88. Similar to Figure 80, but for SWIFT buoys in Wave Array #7 (WA7). ....	94
Figure 89. Similar to Figure 80, but for UK buoys in Wave Array #7 (WA7). ....	94
Figure 90. Dissipation profiles $k_i(f)$ from Rogers et al. (2016). Only the cases with usable ice photos are shown, of which there are 145. The colors indicate “ice codes”, given in the legend, which have been updated since that publication: see Section 7 in this report. The black step function is a fitting to the “P/FR-H” cases in Figure 9 of Rogers et al. (2016), which roughly correspond to the “PF11” and “PF12” ice codes here (heavy frazil and pancake ice, 26 profiles).....	95
Figure 91. Like Figure 90, except that the new inversion using AMSR2 ice forcing (this report) is shown rather than the inversion of Rogers et al. (2016) which used ice forcing from CICE. The black step function is identical to that in Figure 90. The purple step function is a fit to $k_i(f)$ profiles shown here (all ice codes; not just PF12). Only the cases with usable ice photos and ice concentration (estimated from AMSR2) greater than 25% are shown, of which there are 48 .....	96
Figure 92. Amplitude attenuation rate $k_i$ vs. frequency. Profiles from parametric models (IC4) are compared with the IC3 viscoelastic model, and the low frequency $k_i$ estimates from Ardhuin et al. (2016). The parametric models IC4M6H and IC4M6H2, introduced in Section 6.2.3, are shown as step functions (as they are applied in WW3) corresponding to the eight coarse frequency bins used in the inversion. See text for further explanation. ....	97
Figure 93. Amplitude attenuation rate $k_i$ vs. frequency. The two parametric models IC4M6H and IC4M6H2 are compared with the “basal friction” boundary layer model of IC2. The parametric models are shown as step functions.....	98
Figure 94. Amplitude attenuation rate $k_i$ vs. frequency. Identical to Figure 93, except that the parametric models are shown as continuous functions rather than as step functions. ....	98
Figure 95. Amplitude attenuation rate $k_i$ vs. frequency. The two parametric models IC4M6H and IC4M6H2 are compared with profiles determined by Cheng et al. (2017) for WA3. The	

parametric models are shown as continuous functions. The red and green coloring pertains to the fitting of VE parameters to the profiles (see text).....	99
Figure 96. Amplitude attenuation rate $k_i$ vs. frequency. The two parametric models IC4M6H and IC4M6H2 are compared with the Doble et al. (2015) formula, for two difference ice thickness values, 1 and 5 cm. The parametric models are shown as continuous functions.	100
Figure 97. Amplitude attenuation rate $k_i$ vs. frequency. The two parametric models IC4M6H and IC4M6H2 are compared with the IC2 model based on the eddy viscosity concept. The parametric models are shown as continuous functions. ....	101
Figure 98. Amplitude attenuation rate $k_i$ vs. frequency. The two parametric models IC4M6H and IC4M6H2 are compared with low frequency $k_i$ estimates of Ardhuin et al. (2016). The parametric models are shown as continuous functions. ....	102
Figure 99. Amplitude attenuation rate $k_i$ vs. frequency. The two parametric models IC4M6H and IC4M6H2 are compared with the profile suggested by Meylan et al. (2014), based on measurements near Antarctica. The parametric models are shown as continuous functions. ....	103
Figure 100. Amplitude attenuation rate $k_i$ vs. frequency. The two parametric models IC4M6H and IC4M6H2 are compared with the viscoelastic model of Wang and Shen (2010). The parametric models are shown as continuous functions. ....	104
Figure 101. Like Figure 100, but using settings for ice thickness and viscosity taken from Newyear and Martin (1999), for grease ice. ....	104
Figure 102. Amplitude attenuation rate $k_i$ vs. frequency. The two parametric models IC4M6H and IC4M6H2 are compared with the measurements tabulated by Wadhams et al. (1988). The parametric models are shown as continuous functions. ....	105
Figure 103. Amplitude attenuation rate $k_i$ vs. frequency. The two parametric models IC4M6H and IC4M6H2 are compared with results tabulated in the Zhao and Shen (2015) lab experiment. The parametric models are shown as continuous functions. ....	106
Figure 104. Black: inversion dissipation profiles shown in Figure 80, except that only six profiles, those with ice codes PF11 and PF12, are plotted. Red: Meylan et al. (2014) (also shown in Figure 99). ....	107
Figure 105. Like Figure 104, but plotting on a linear scale. ....	107
Figure 106. Like Figure 105, but the $k_i(f)$ profiles are multiplied by $cTn$ , to evaluate slopes of profiles. Here we look at lower frequencies and $n=2, 2.5$ , and 3 as indicated in legend. See text for further explanation. ....	108
Figure 107. Like Figure 106, except here we look at higher frequencies and $n=4, 4.5$ , and 5 as indicated in legend. ....	108
Figure 108. Binomial fits (lines) to the steps functions (symbols) IC4M6H and IC4M6H2. The step functions were shown previously in Figure 79 to Figure 103 using the same color convention (black and purple). ....	110
Figure 109. Time series, scatter plots, and statistics for $H_{m0}$ : drifting buoys vs. hindcasts with three variants of $S_{ice}$ . All use 10 km AMSR2 ice forcing. Model type is indicated on the left. The “ $k_i=[fixed\ value]$ ” models indicate that IC1 is used for $S_{ice}$ . ....	115
Figure 110. Like Figure 109, but comparing $T_{m,-1,0}$ .....	116
Figure 111. Like Figure 109, but comparing $m_4$ .....	117
Figure 112. Like Figure 109, but comparing three other variants of $S_{ice}$ .....	118
Figure 113. Like Figure 112, but comparing $T_{m,-1,0}$ .....	119
Figure 114. Like Figure 112, but comparing $m_4$ .....	120

Figure 115. Time series, scatter plots, and statistics for $H_{m0}$ : drifting buoys vs. hindcasts with four different methods of providing ice concentration. All use the IC4M6H method of $S_{ice}$ . Ice forcing type is indicated on the left.	122
Figure 116. Like Figure 115, but comparing $T_{m,-1,0}$ .	123
Figure 117. Like Figure 115, but comparing $m_4$ .	124
Figure 118. Time series comparisons along track of <i>Sikuliaq</i> , with five different model hindcasts. Top panel: $H_{m0}$ comparison, with observations from ship lidar. Lower panel: $m_4$ comparison (observations not available: see text). Ship observations were provided by Ola Persson (NOAA) and the lidar was operated by Persson and Byron Blomquist (NOAA). The “ $k_i$ =[fixed value]” models indicate that IC1 is used for $S_{ice}$ .	126
Figure 119. Time series comparisons along track of <i>Sikuliaq</i> , with the five model hindcasts shown in Figure 118. Observations (black points) are from ship radar. Top panel: $T_p$ comparison. Lower panel: peak direction comparison. Ship observations were provided by Ola Persson (NOAA); the marine radar operation and data processing was performed by Bjoern Lund (U. Miami).	127
Figure 120. Example scatter plots and statistics for the IC4M6H hindcast. Top panels: $H_{m0}$ . Lower panels: $m_4$ . Left panels: WA3 SWIFT buoys. Right panels: WA3 NIWA buoy.	129
Figure 121. Same as Figure 120, except comparing SWIFTS against the UK buoys.	130
Figure 122. Same as Figure 120, except showing the IC4M6H2 hindcast.	131
Figure 123. Wave height time-series comparison of models vs. SWIFT buoys along the southern transect of WA3. Models use IC4M6 source functions and IC0 of Tolman (2003).	137
Figure 124. Like Figure 123, but comparing against data from the two SWIFT buoys deployed on the northern transect of WA3. These buoys were not recovered and data is from telemetry, so processing was different from data in Figure 123.	138
Figure 125. Like Figure 123, but comparing against data from the NIWA buoy deployed on the northern transect of WA3.	138
Figure 126. Comparison of four models, progressing from outside the ice to further into the ice: SWIFT 11, SWIFT 14, NIWA2, and AWACBGA.	140
Figure 127. Air-sea temperature differences used in WW3 “STAB3” simulation, 0000 UTC 12 October 2015. Air-sea temperature differences less than $-3^{\circ}$ C are shown as white.	142
Figure 128. Time series of significant waveheight for four buoys that were predominately in open water. Green is the baseline model. Blue is the model without dissipation by sea ice. Red uses ECMWF winds instead of NAVGEM. Cyan includes air-sea stability effects.	143
Figure 129. Like Figure 128, but for buoys that are predominately in sea ice, either for a portion of the time series (buoy S09) or most of the time series (the other five buoys).	144
Figure 130. Vertical profiles of TKE dissipation rate measured by SWIFT buoys. Gold and orange corresponds to OW1 and OW3 respectively. Cyan corresponds to PF6. Blue corresponds to PF7 and PF8. Green and red correspond to PF9 and PF12 respectively.	148
Figure 131. Time series of TKE dissipation: buoy (SWIFT 14) vs. parametric model. Black line is buoy total energy in $m^2$ . Blue line is integrated buoy TKE dissipation in $W/m^2$ . Red is the IC4M6H model applied to the buoy spectrum (WW3 is not used here). Green is like IC4M6H, but matching the dissipation of lighter pancake and frazil from Rogers et al. (2016). Grey regions of the plot indicate night-time, when ice observations from the buoy camera are unavailable.	148
Figure 132. Salinity measured by SWIFT buoys, compared against corresponding ice observations.	149

Figure 133. SAR image from screenshot of <i>Sikuliaq</i> Mapserver. BIO RadarSAT-2 for 1640 UTC 11 October 2015. The red line is the cruise track near WA3, and the thick black line indicates the southern transect during WA3. RADARSAT-2: © MDA 2015.....	150
Figure 134. Like Figure 133, but showing the CSTARS TerraSAR-X image for 1823 UTC 11 October 2015.....	150
Figure 135. Ice observations from SWIFT cameras from 1615 to 2345 UTC 11 October 2015. Color scaling is according to the new 0-to-12 ice codes. The black line and diamonds indicate the southern transect of WA3 (same as black line in SAR images shown in this section). .....	151
Figure 136. Like Figure 135, but for 0015 to 0315 UTC 12 October 2015.....	151
Figure 137. Like Figure 133, but showing the Sentinel-1 image for 1650 UTC 12 October 2015.....	152
Figure 138. Like Figure 133, but showing the CSTARS TerraSAR-X image for 1806 UTC 12 October 2015.....	152
Figure 139. Like Figure 135, but for 1615 to 2345 UTC 12 October 2015.....	153
Figure 140. Mosaic of photos from SWIFT-14, 1800 to 1830 UTC 12 October 2015. Ice category on the new 0-to-12 scale is 12. $H_s=2.90$ m.....	153
Figure 141. Like Figure 133, but showing the CSTARS TerraSAR-X image for 0153 UTC 13 October 2015.....	154
Figure 142. Like Figure 135, but for 0015 to 0315 UTC 13 October 2015.....	154

This page intentionally left blank.

## Executive Summary

This report describes the development, application, and evaluation of wave models for the ONR “Sea State” Departmental Research Initiative. The Sea State field experiment is described, with particular attention to wave measurements and the wave conditions during the field experiment. Wave forecasting in support of the cruise is described. Implementation of the effects of sea ice on waves in the numerical wave model WAVEWATCH III® is described. The role of the ice forcing in the wave model performance is evaluated by contrasting different ice products and applying them in hindcasts. The relative strengths and weaknesses of the products are discussed. The relative skill of hindcasts with different physical parameterizations is also quantified for the various wave experiments conducted during the cruise. A model-data inversion is conducted to estimate the frequency distribution of the dissipation of wave energy by ice, separated by buoy type and wave experiment. A subset of the inversion results is used to create a new empirical physical parameterization, and this parameterization is compared with distributions given in the literature, and other model parameterizations.

This page intentionally left blank.

## 1. Introduction

It is well known that there is a trend for reduced ice cover in the Arctic Ocean. Stammerjohn et al. (2012) showed that in the region north of Alaska (Beaufort and Chukchi Seas and neighboring Arctic Ocean) during 1975-2015, there was a loss of over one day per year from *either end* of the ice season. The Office of Naval Research (ONR) funded a Departmental Research Initiative (DRI) “Sea State and Boundary Layer Physics of the Emerging Arctic Ocean” (Thomson et al., 2013) which would study the implications of the reduced ice cover for oceanographic and meteorological processes, such as heat and momentum exchanges. It was also intended to consider practical objectives, such as the evaluation and improvement of the modeling used to create forecasts and other predictions of the Arctic Ocean. The DRI started in December 2012 and ended in September 2017. This report focuses primarily on evaluation and improvement of wave modeling technology during the DRI, but a significant portion of the report deals with ice and winds, since these are critical inputs to the wave model.

In Section 2, we present an overview of the cruise, with brief descriptions of relevant measurements, followed by descriptions of wave experiments, and then an overview of wave forecasting for the cruise. In Section 3, we describe the effects of sea ice on waves, and the implementation in the numerical wave model, WAVEWATCH III®. The role of numerical error in this implementation is evaluated in this section. In Section 4, we describe and evaluate the ice fields which are used as forcing in the wave model. Section 5 is a relatively brief section describing and evaluating the wind forcing used in this report.

In Section 6, the wave hindcasts are described and evaluated in comparison to observational data. This section includes a model-data inversion process used to estimate the frequency distribution of the dissipation of wave energy by interaction with the sea ice during the field experiment. Results from a subset of this inversion are compared with other frequency distributions found in the literature, and the slope of the distribution is evaluated. Parameterizations of the dissipation are applied in a forward model; one of these parameterizations is based on the same subset from the model-data inversion. The forward model hindcasts are evaluated using observational data. The relative skill of hindcasts with different physics parameterizations is evaluated, and the same is done for hindcasts with different ice input. The potential role of thermal stability effects is evaluated for one of the wave experiments (“WA3”). Data quality and the relevance to interpretation of hindcasts results are discussed.

In Section 7, we present a characterization of the ice cover using photos from buoys during WA3. This is compared to other observed variables, and to imagery from Synthetic Aperture Radar. Conclusions are summarized in Section 8.

## 2. Overview of cruise

The center-piece of the DRI was a six-week field campaign in the Beaufort and Chukchi Seas and neighboring Arctic Ocean aboard the UNOLS vessel R/V *Sikuliaq*. To set the field campaign apart from prior oceanographic cruises in that region<sup>1</sup>, it was decided early on that the cruise

---

<sup>1</sup> Figure 3 in Lee and Thomson (2017) gives an excellent summary of ice observations, by month, indicating a tendency for measurements to be associated with spring ice camps and summer cruises (figure by Ben Holt, JPL).

would occur during the autumn ice advance season of 2015: specifically, October and early November.

The cruise is summarized by Thomson et al. (2015), Wadhams and Thomson (2015), and Thomson et al. (2017). The cruise track is shown in Figure 1, which indicates the placement of the ice stations and wave experiments performed during the cruise. The locations of a sub-surface AWAC buoy (Section 2.1.1) and the retrieval of a Naval Oceanographic Office glider are also indicated. Numerous short-term atmospheric “flux stations” were also performed but are not marked on the figure. Figure 2 shows an example of the ice coverage during the field experiment.

A relatively unique feature of the cruise was the use of a “rolling Plan of the Day (POD)”. Instead of scheduling experiments prior to the cruise, the timetable was left flexible such that it could respond to the weather and ice conditions. Each evening, the Chief Scientist, Dr. Jim Thomson, would update the Science Team (including the marine technicians), and set the experiment schedule and watch duties for the following three days. At these “Plan of the Day meetings”, a meteorological forecast and wave forecast would be presented by two members of the Science Team who were assigned to these duties for the duration of the cruise. The Chief Scientist would typically present SAR images showing current ice conditions, displayed on the ship’s “map server”<sup>2</sup>. On days for which interesting marine weather or swell was predicted, the POD would be adapted to include appropriate measurements, e.g. by deploying wave buoys in a specific configuration. On days that were calmer, it was more likely that plans would be made to go north into the ice, establish an ice station, and perform measurements of the ice.

---

<sup>2</sup> This website was updated during the cruise by marine technician Steve Roberts, who has since made it available for use after the cruise. At time of writing, the website is still accessible: <http://realtime.sikuliaq.alaska.edu/SKQ201512S/map/skq.html>.

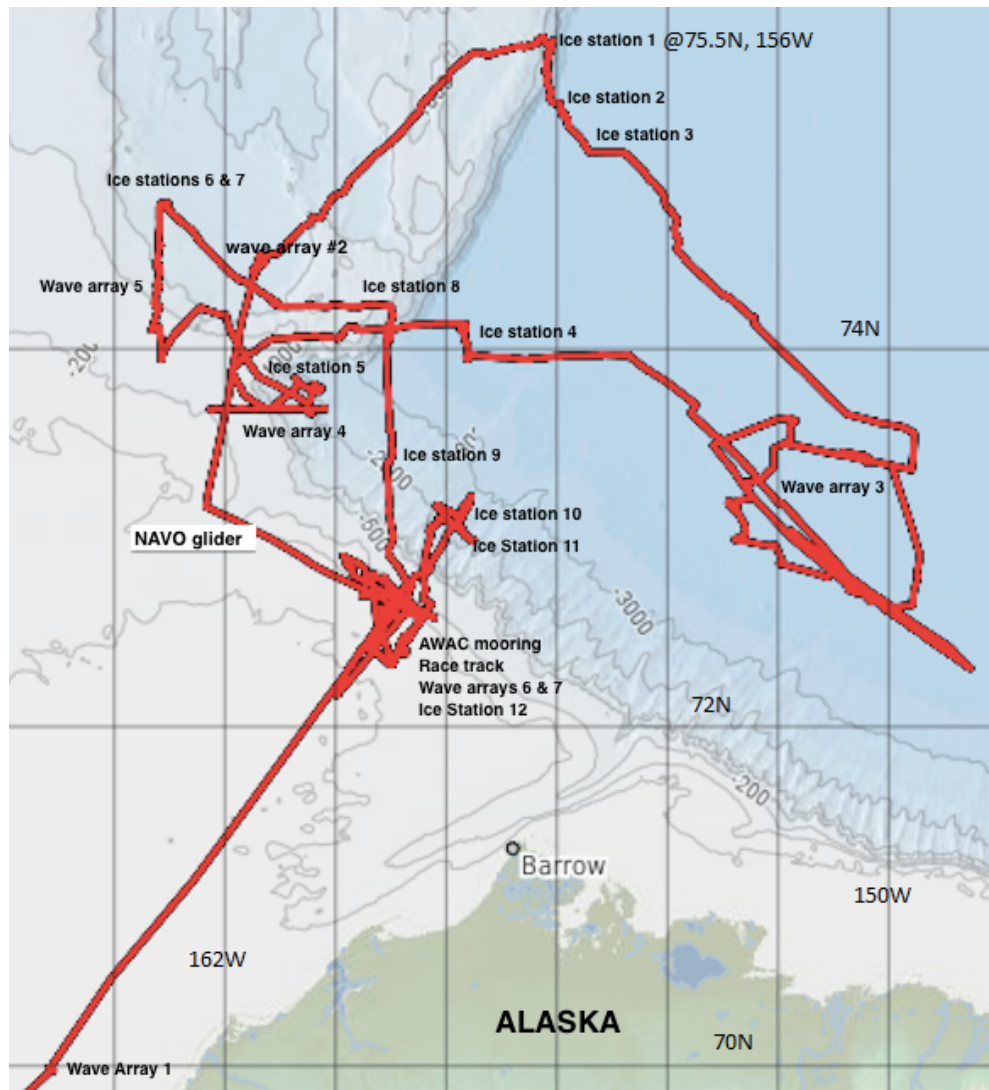


Figure 1. Cruise track, reproduced from Thomson (2015), with some minor annotations added. Locations of wave arrays and ice stations are indicated.

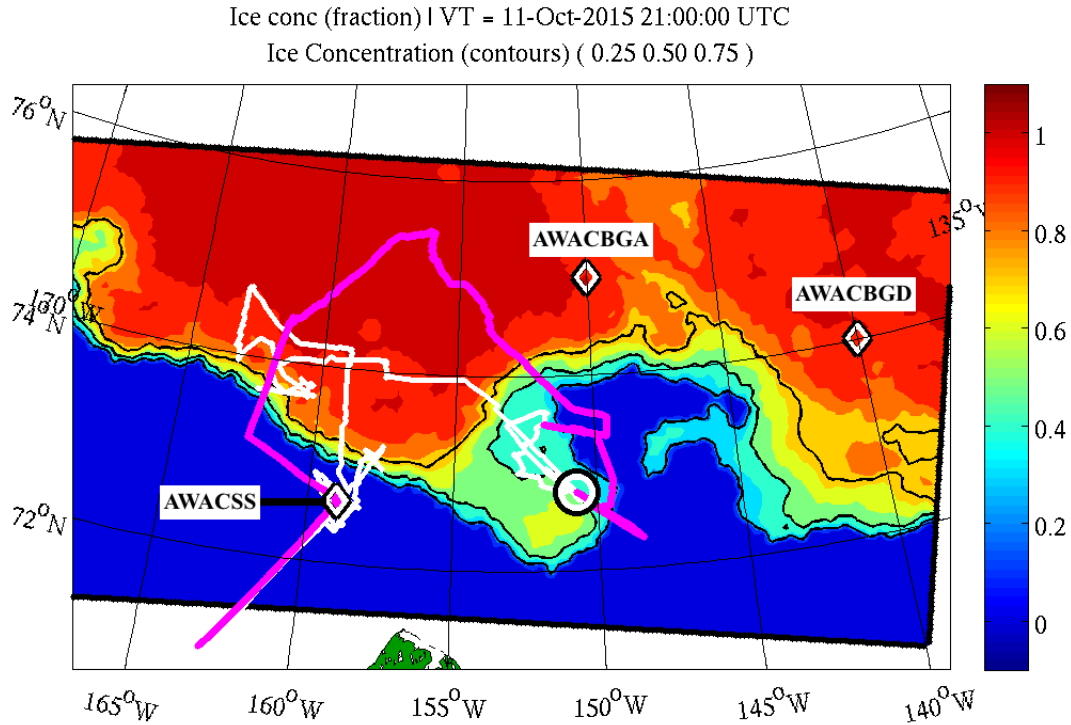


Figure 2. Example of ice coverage during the Sea State cruise, taken from the 10 km AMSR2 product described in Section 4.1. Date/time is indicated in title. Thick magenta and white line indicates track of R/V *Sikuliaq* (prior and future ship positions respectively). Black/white circle indicates present position of ship. The three diamonds mark AWAC moorings (Section 2.1.1). Color scale indicates ice concentration; contours are also included which mark 25%, 50%, and 75% ice concentration.

## 2.1. Observations

### 2.1.1. Moored buoys

There were three moored subsurface Nortek “AWAC” (Acoustic Wave And Current) buoys collecting data in the region during the Sea State cruise, marked with diamonds in Figure 2. The southwest location was at a “one-off” mooring site (159.01W, 72.64N), and the AWAC was deployed and recovered by the *Sikuliaq* during the cruise (Thomson 2015). This is denoted as “AWACSS” or “Sea State AWAC” here. Data from this buoy are used in Figure 68 and Figure 69. The northern-most mooring was at a recurring site (150W, 75N), “Beaufort Gyre A”, denoted as “AWACBGA” here. Both AWACs are owned and operated by the Applied Physics Laboratory, U. Washington (APL/UW). AWACBGA was deployed by the Canadian Coast Guard icebreaker Louis S. St.-Laurent contemporary with the Sea State cruise (October 7 2015). This site is one of three Beaufort Gyre moorings maintained by the Woods Hole Oceanographic Institution. Data from this buoy are used in Figure 126. The eastern-most buoy, “Beaufort Gyre D” or “AWACBGD” (140W, 74N) has wave measurements until 11 October 2015 but that data are not used in the present report, since the mooring is well outside our study area. The buoys measure 1-d (i.e. non-directional) wave spectra, but we consider the energy at high frequencies to be unreliable, so we only use significant waveheight  $H_s$  and dominant wave period  $T_{m01E4}$  here (see Section 6.3 for definitions).



Figure 3. Top panel: Nortek AWAC buoy, photo provided by UW/APL. Lower panel: photo during retrieval of the Sea State AWAC buoy. UW/APL engineers Joe Talbert and Alex deKlerk are at the left and right, respectively.

### 2.1.2. Drifting buoys

Three types of drifting wave buoys were deployed during the R/V *Sikuliaq* cruise:

1. “SWIFT” buoys, engineered and operated by Dr. Jim Thomson and the APL/UW engineering team (see e.g. Thomson 2012). The data were processed by Ms. Madison Smith (APL/UW). This is a spar-shaped buoy (see Figure 4).
2. “British” or “UK” buoys, designed and operated by Dr. Martin Doble (Polar Scientific) as part of a project led by Prof. Peter Wadhams (Cambridge University) with U.S. Office of Naval Research (ONR) funding. Instrumentation is contained in a watertight case placed within a flotation collar, rectangular toroid in shape.
3. “NIWA” buoy, designed and operated by Dr. Alison Kohout of New Zealand’s National Institute of Water and Atmospheric Research. It is an adaptation of the buoy of Kohout et al. (2015).

All of the scientists mentioned above—Thomson, Smith, Doble, Wadhams, and Kohout—participated in the cruise and planned the wave experiments.

In case of (1) and (2), data are available from several wave experiments (denoted as “wave arrays”) during the cruise, and include directional wave spectra. At each frequency, the buoy reports energy density and four Fourier coefficients describing the directional distribution. In case of the NIWA buoy (3), all data used here are from Wave Array #3 (WA3) October 10-14 2015 in the form of 1-d (non-directional) wave spectra. More information on the wave arrays and buoy deployments can be found in Thomson (2015) and Wadhams and Thomson (2015). Additional information about WA3 data can be found in the WAVEWATCH III (WW3) modeling study Rogers et al. (2016), where data from (1) and (2) were utilized. In the present study, newer, reprocessed spectra are used, compared to that used in Rogers et al. (2016). Now, each represents a 30-minute interval. SWIFT buoys are centered at 15 and 45 minutes after the hour, while British buoys are centered at 0 and 30 minutes after the hour.

In addition to directional spectra, SWIFT buoys report wind speed and direction at 1-meter elevation, air temperature, air pressure, water temperature, and salinity. Each is equipped with digital camera (see Section 7) and an ADCP (Acoustic Doppler Current Profiler) which is either up-looking or down-looking. An up-looking ADCP provides estimates of TKE (turbulent kinetic energy) dissipation rate in the water layer above the ADCP. A down-looking ADCP provides estimates of velocity profiles.

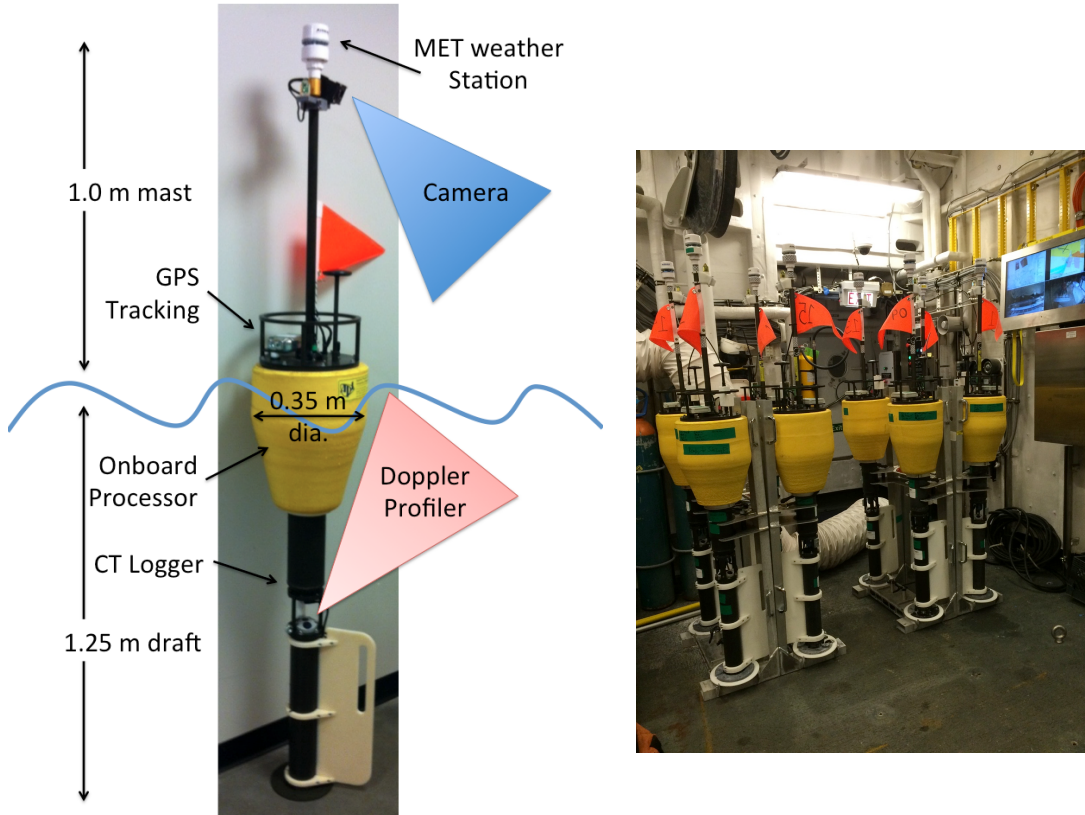


Figure 4. Left: Diagram of SWIFT buoy, courtesy of APL/UW. Right: SWIFT buoys ready for deployment in the “Baltic room” of the R/V *Sikuliaq*.

### 2.1.3. Ship-borne lidar and radar

Ship-borne lidar operated by Ola Persson and Byron Blomquist (NOAA) provided 1-d wave spectra at the ship position. This dataset is described in detail by Collins et al. (2017), where the problem of Doppler shifting from ship movement is addressed. Significant waveheight data from these measurements are used in Figure 118.

Marine radar operated by B. Lund (U. Miami) provided estimates of wave direction and peak period, thus nicely complementing the lidar dataset. Some of these measurements are used in Figure 119. The radar also provided information about ice near the ship and even aided in locating wave buoys when electronic tracking failed.

### 2.1.4. Other data

Visual ice observations were recorded during the entire period that the ship was in or near the ice (hourly for 32 days), using ASSIST (Arctic Shipborne Sea Ice Standardization Tool) protocols<sup>3,4</sup>. This dataset is used in Section 2.2 of this report. Other data were collected during the cruise which are less relevant to wave model evaluation, but are briefly listed here: Autonomous Underwater Vehicle missions, ice mass balance buoy deployments, Unmanned Aerial Vehicle photography mosaics, surveys of ice by on-ice lidar, stereo video of waves in ice, ice photos, physical ice samples, magnetometer ice measurements, weather balloon launches, ship-borne meteorological measurements (e.g. radiative heat fluxes), and underway CTDs (Conductivity, Temperature Depth). In the case of the latter, a remarkable 4292 casts were made. For more detail, see Thomson (2015). There were also data collections which were not based from the ship: six airplane missions for lidar and SAR (Synthetic Aperture Radar) and many satellite SAR images; e.g. there were over 60 RadarSAT-2 SAR images, sent from the National Ice Center (NIC) and Bedford Institute of Oceanography (BIO).

## 2.2. Description of wave experiments

Icing of the buoys and the cost (in ship time) of following and recovering buoys that drifted long distances made it necessary to use short term (one to four day) buoy deployments. These are referred to as “wave experiments” or “wave arrays” here, interchangeably. The wave experiments are described in this section. Figure 5 summarizes these experiments in a timeline. The bulk wave parameters measured by the drifting buoys deployed during the experiments are shown: significant waveheight, peak period, and mean wave direction. Sub-sections below describe wave and ice conditions during each experiment.

Except where noted as “local time”, “LT”, “ship time” or “SQ time” (*Sikuliaq* time), all times given herein are in UTC. Where noted as “local time”, “SQ time”, etc., this all refers to the same time: the time of clocks on the ship, which were set to the time of Nome, Alaska, eight hours behind UTC, and were not changed until the ship reached Dutch Harbor on November 9, several days after the last science experiment ended. Thus, “local time” as used here does not refer to the *actual* local time in the seas north of Alaska.

---

<sup>3</sup> [http://www.arcticobservingsummit.org/sites/arcticobservingsummit.org/files/Hutchings-REVISEDRC--IceWatchWhitePaper\\_review\\_neat.pdf](http://www.arcticobservingsummit.org/sites/arcticobservingsummit.org/files/Hutchings-REVISEDRC--IceWatchWhitePaper_review_neat.pdf)

<sup>4</sup> <http://icewatch.gina.alaska.edu/pages/about>

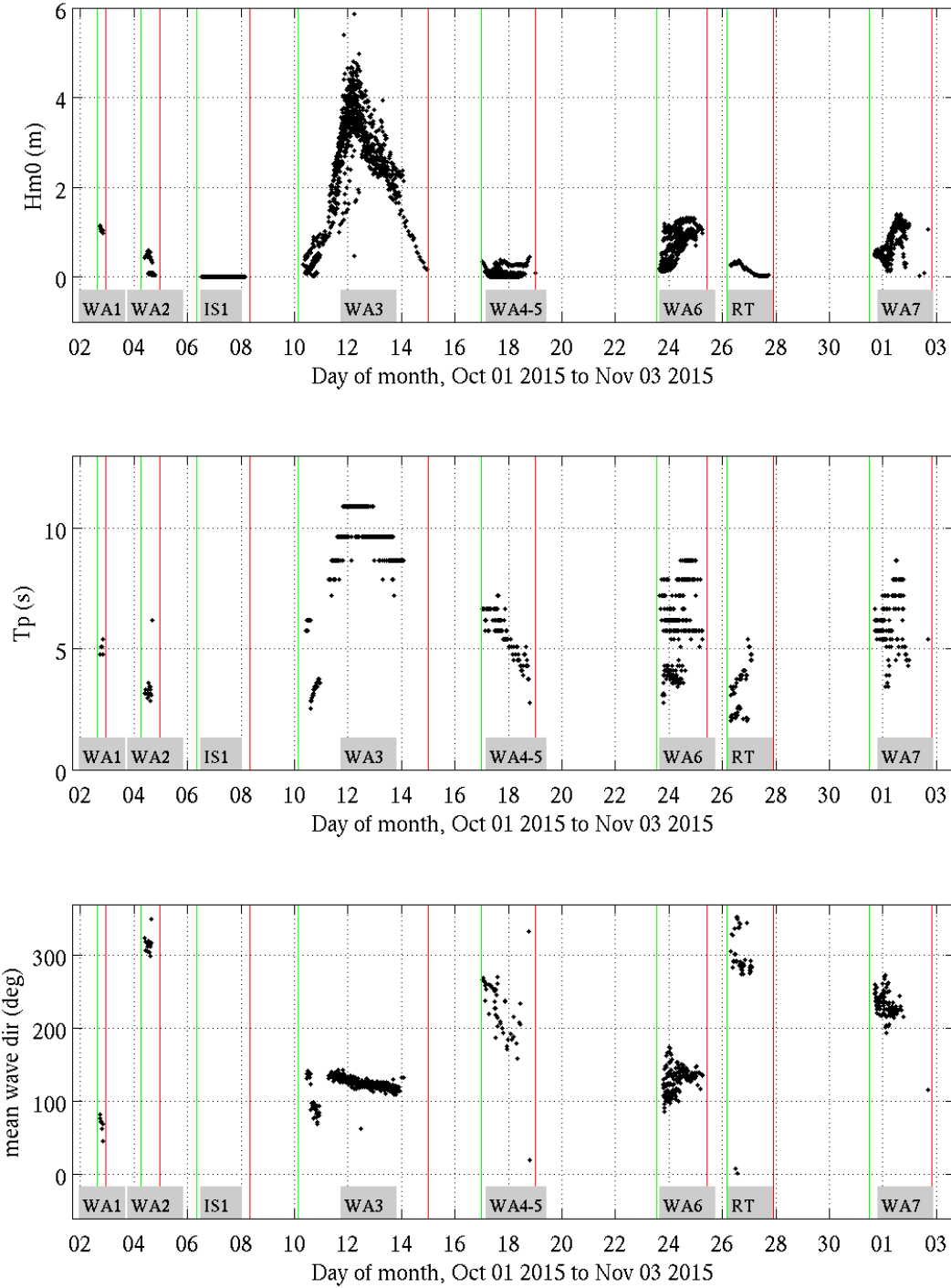


Figure 5. Time series of wave experiments. Green vertical line indicates the start of a wave experiment and red vertical line indicates the end. Panels, top to bottom are zero-moment waveheight, peak period, and mean wave direction. Dots indicate measurements from drifting buoys deployed from the R/V *Sikuliaq*. “WA”, “IS”, and “RT” indicate Wave Array, Ice Station, and Race Track, respectively.

### 2.2.1. WA1: buoy calibration in open water

Wave Array #1, 1700 to 2100 UTC on Oct. 2 2015, was a calibration and buoy inter-comparison exercise performed while en route to the field experiment. Thomson (2015): “*We paused during transit on the afternoon of 2 October to briefly deploy wave measurement buoys for inter-calibration (wave array #1). Wave conditions were approximately 1.2 m waves at 5 s from the east-northeast.*” This deployment was *not* for the study of wave-ice interaction, being far from the MIZ. This is also the only wave array which is geographically outside the inner WW3 grid used for hindcasts in this report (Section 6.1.1).

Significant Wave Height (m) and mean wv. dir. | VT = 02-Oct-2015 18:00:00 UTC  
SQ time = 02-Oct-2015 10:00:00

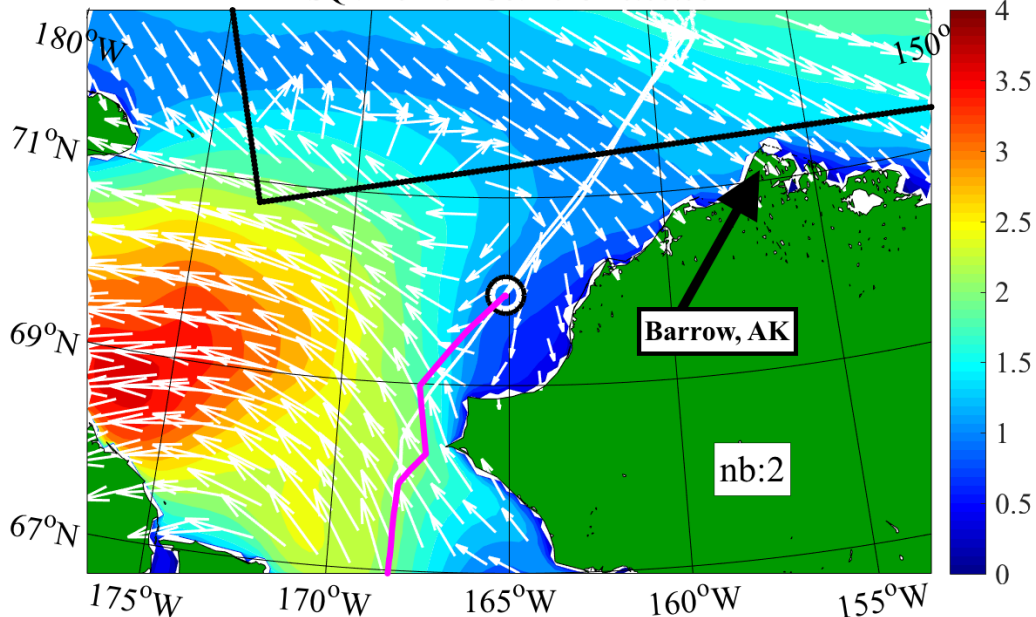


Figure 6. WW3 hindcast during WA1 (10 km resolution outer WW3 grid used for hindcasts; see Section 6.1.1). Date/time is indicated in title. Thick magenta and white line indicates track of R/V *Sikuliaq* (prior and future ship positions respectively). Black/white circle indicates present position of ship. Color scale indicates model  $H_s$  and white arrows indicate model mean wave direction. Text “nb:2” indicates that two buoys were deployed at this time. Black rectangle indicates the boundary of the 5 km resolution inner WW3 grid used for hindcasts; see Section 6.1.1. Observations near ship:  $H_s$  was 90 to 120 cm;  $T_p$  4.5 to 5.5 s; mean wave direction 45 to 80° (local windsea from northeast quadrant).

### 2.2.2. WA2: weak, obliquely off-ice winds

Wave Array #2 was conducted October 4 2015, 0900 to 1900 UTC. Thomson (2015): *We arrived at the ice edge for the first time early in the morning on 4 Oct 2015, where we had entered the deeper waters (> 1000 m) of the Northwind Ridge area. The edge was clearly visible in the Rutter radar. We deployed wave array #2, consisting of three SWIFT buoys crossing from open water into partial ice cover beyond a band of old ice, plus one [UK] wave buoy in the ice bands. .... Winds were obliquely off-ice from the northwest to north and generated 0.5 m waves at 3 s from the same direction. A second wave train at 4 s from the west was also detected, but was small. Waves were detected inside the ice band at 10 cm wave height and 7 s period from the southwest.*

Ice conditions were variable. The following ice observations were recorded in the ASSIST protocols:

- 1360 UTC: 100% ice concentration: 50% second-year ; 50% brash
- 1730 UTC: 70% ice concentration: 20% brash and 50% grease
- 1924 UTC: 90% ice concentration: 20% multi-year ; 30% pancakes ; 40% frazil

Percentages by ice type above are “percent coverage of the total ocean”, not “percent coverage of the ice-covered ocean”.

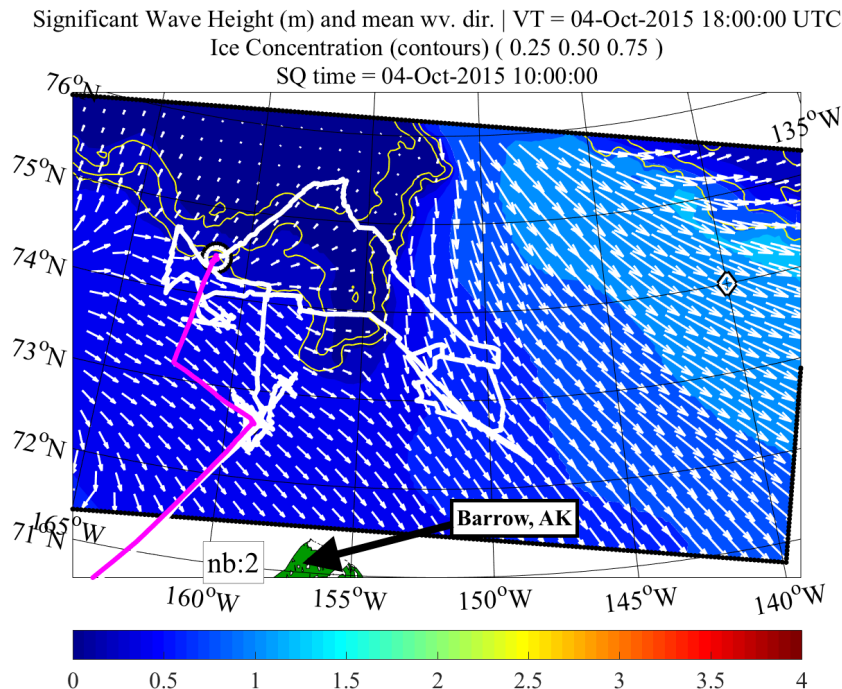


Figure 7. WW3 hindcast (5 km resolution inner WW3 grid; see Section 6.1.1). Date/time is indicated in title. Thick magenta and white line indicates track of R/V *Sikuliaq* (prior and future ship positions respectively). Black/white circle indicates present position of ship. Color scale indicates model  $H_s$  and white arrows indicate model mean wave direction. Contours indicate ice concentration (25%, 50%, 75%). Text “nb:2” indicates that two buoys were deployed at this time. Observations near the ship were:  $H_s$  up to 60 cm;  $T_p$  3 to 3.5 s; mean wave direction 300 to 325° (weak local windsea from northwest). All WW3 hindcast results from the “inner WW3 grid” used in this section (Section 2.2) employ the parametric  $S_{ice}$  “IC4M6H2” introduced in Section 6.2.3 and the 10 km AMSR2 ice concentration forcing introduced in Section 4.1.2. The hindcasts are explained in Section 6.3.



Figure 8. Photo taken by Prof. Hayley Shen, October 4, 2015, 10:02LT. Multi-year ice and brash ice are visible. Floes with smoother top surfaces may be first-year or second-year ice.

### 2.2.3. IS1: Ice Station Ben

During Ice Station 1 (IS1), buoys were deployed from October 6 1200 UTC to October 8 0400 UTC. Wave energy was negligible, but this dataset is nevertheless useful for wave model validation, since a skillful model will also have negligible energy. Thomson (2015): *We transited northward, conducting hourly [underway CTDs], while passing through nilas ice sheets surrounding small thick older floes on 5 Oct, then found a large multi-year floe for Ice Station #1 (“Ben’s floe”, ...) early in the morning on 6 Oct 2015. We spent 6 and 7 Oct 2015 conducting a large ice station on this floe.... The floe was next to a wide lead, in which two SWIFTS were deployed that immediately froze in place... The floe was at least 100 nm from any ice edge, and there was no sign of wave activity [at] this station.*

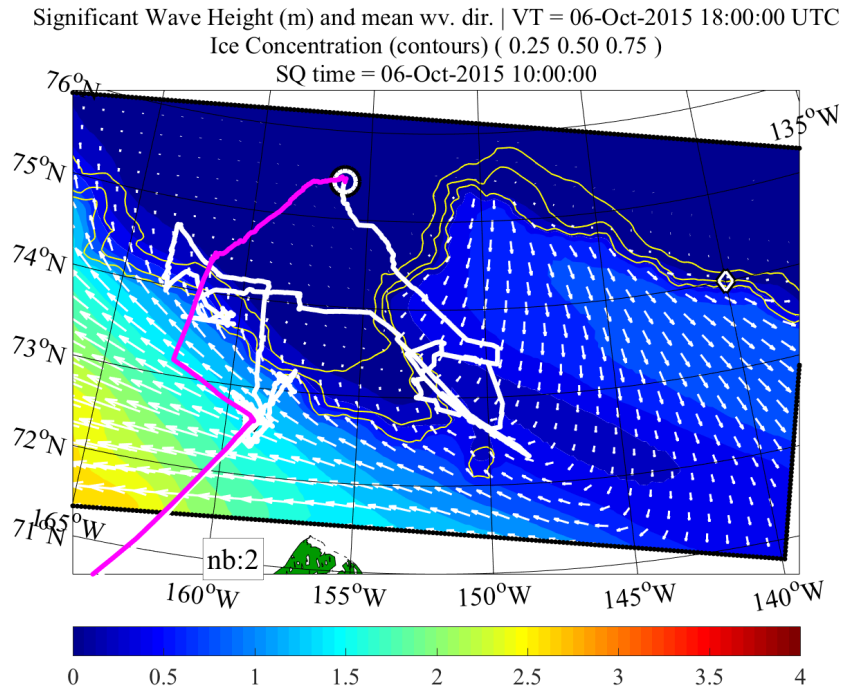


Figure 9. WW3 hindcast. See caption of Figure 7 for explanation of annotation. Wave observations near ship: negligible energy.



Figure 10. Photo taken by Prof. Hayley Shen, October 6, 2015, 09:29LT. The ship is moored to a large multi-year floe (Ice Station Ben, or IS1).

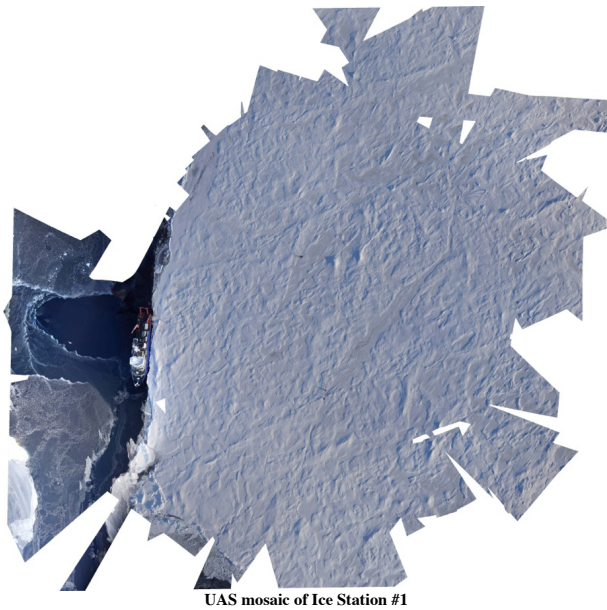


Figure 11. UAS mosaic of IS1, reproduced from Thomson (2015). UAS courtesy of Guy Williams. The ship is visible to the left of the floe.

#### 2.2.4. WA3: large waves in ice

Wave Array #3, October 10 0700 UTC to October 14 2330 UTC, was the “flagship” wave experiment of the cruise, featuring many buoy deployments, and wave heights up to 4.8 m.<sup>5</sup> The observed conditions were part of an easterly wind event, with a high pressure system rotating clockwise to the north, and a low pressure system rotating counter-clockwise to the south; the low was in the Gulf of Alaska, see Rogers et al. (2016). The winds at the wave array were up to 16 m/s at 10-meter elevation but were stronger in the generation region southeast of WA3 (again, see Rogers et al. 2016). Quoting Thomson (2015) (footnotes are added here): *Upon reaching the ice edge on the Beaufort side on 10 Oct, we began deploying SWIFTs, wave buoys, and one NIWA buoy to drift in an array aligned with the forecasted wave directions<sup>6</sup>... Pancake ice was forming rapidly and waves were approximately 1 m from the southeast. A few hours into the deployment, we received new RadarSat2 image and AMSR2 product, and we realized that the fetch for these waves was rapidly decreasing as an embayment of ice filled in. We decided to recover most of the buoys and shift the array to the south, where the full fetch of the Beaufort Sea would be available for this E-SE wind event and where waves were forecast to reach 4 m*

<sup>5</sup> Digressing into an unscientific, but perhaps still interesting, topic: WA3 actually may have broken two records, though by small margins. First, it would be the largest waves measured in situ in that sector of the western Arctic (Beaufort Sea, Chukchi Sea, and nearby Arctic Ocean) at the time, being slightly larger than the 4.7 m waves reported for a September 2012 wave event by Thomson and Rogers (2014). Second, it would be the largest waves measured in ice in the northern hemisphere, being larger than the 4.1 meter waves reported in Collins et al. (2015) (see Figure 1 of that paper). The reader is referred to the supplementary material of Collins et al. (2015) for further information about historical measurements. Takuji Waseda (U. Tokyo) has reported measurements of significant waveheight as high as 4.9 m in the western Arctic in open water in 2016.

<sup>6</sup> This refers to directions indicated in graphical forecast products provided by ECMWF, accidentally offset by 22.5° relative to the actual output from the numerical model.

*significant wave height<sup>7</sup>. We left two SWIFTS and one NIWA buoy in place on the original line, to measure any waves propagating that far into the ice. The second line of buoys spanned 60 nm, from open water to deep within a field of rapidly growing pancakes.<sup>8</sup> This event was part of prevailing easterly winds, with E-SE winds of up to 16 m/s<sup>9</sup>... Early in the storm, waves up 3 m were propagating all the way through the array (i.e., very little attenuation). The expectation was for the pancake ice to eventually freeze in place as the storm progressed<sup>10</sup>. However, the pancakes largely disappeared overnight from 11 Oct to 12 Oct in the immediate vicinity of the buoy array, while the waves reached a maximum 5 m in the middle of the array. Further to the west, the ice concentration increased from this event. The working hypothesis is that near-surface heat flux convergence melted the existing pancake ice cover because of the observed decrease in the magnitude of the heat loss to the atmosphere and an increase in upward mixing of ocean heat stored in the “near surface temperature maximum” observed with the uCTD casts. ... The buoys were recovered on 13 Oct, in alternating bands of open water and pancake ice over a span of 100 nm. Heavy icing on the buoys caused many buoys to miss Iridium reports of position. The NIWA buoy, which was the farthest from the open water, recorded waves reaching 3.3 m during the peak of the storm, and was recovered in compacted pancake ice with little evidence of melting. The two SWIFTS left behind along the initial line were not recovered...*

Ice conditions observed from the ship and buoy cameras during this wave experiment were exclusively some combination of pancake ice, frazil ice, and open water. Frazil ice, when in a thin layer, is known as grease ice. Thin layers of frazil ice can quickly form into sheet ice (e.g. nilas) when the ocean surface is still, but in the presence of waves, the sheet ice cannot form, and so the frazil ice layer thickens as water freezes. Under weak wave action, pancakes often form within this frazil, and this ice cover (frazil and small pancakes) may be sufficient—depending on wind and wave conditions, and the distance to the open water—to fully dissipate wave energy, allowing sheet ice to form. However, under vigorous wave action, and with freezing temperatures, the frazil ice can only accumulate, continuing to become thicker and thicker, and meanwhile the pancakes grow in size, in all dimensions, either by accreting ice at the bowl-shaped underside (basal growth), or at the flat top side where frazil is deposited, with the latter being suggested as dominant by Doble (2007). This leads to the heavy pancake and frazil slurry as shown in Figure 13, where wave heights are 3 to 4 m. From October 12 (UTC) and onwards, some pancakes were observed in a battered and pulverized condition, near bits and pieces of associated ice debris, and this type of ice was categorized as either pancake or brash, depending on the observer (the author feels that both are acceptable). Shuga (small, lumpy ice accumulations, like snowballs) and slush (ice from snow fallen into the water) were both reported during WA3, but the author is not confident of these categorizations, particularly the former.

Estimates of ice thickness during WA3 vary widely (e.g. Figure S6 of Cheng et al. (2017) Supporting Information). Most values are clustered at less than 10 cm, and 5 cm thickness may

<sup>7</sup> A consideration here: the preference to have measurements at an “ice edge” perpendicular to the wave direction, with a large expanse of open water in the upwave direction

<sup>8</sup> This time, the transect was aligned with Navy forecasted wave directions.

<sup>9</sup> This refers to wind speeds at the ship location. Wind speeds in the primary generation area to the southeast were likely stronger, with model  $U_{10}$  up to 23 m/s (Rogers et al. 2016).

<sup>10</sup> Meaning: when the wind event died down, and the water surface stilled, sheet ice could form. This (inevitably) did in fact happen, but several days later, after the remarkable ice melt/retreat.

be taken as a reasonable representative value. The dipnet pancake thickness values (Prof. Wadhams) are an average of 6 cm during the period of October 10 0000 UTC to October 14 0000 UTC. These samples may have been biased by the size of the net: retrieved pancakes tended to be 25 to 50 cm in diameter, while contemporary photographs of the pancakes in the water indicate the pancakes were at times as large as 100 to 180 cm. Assuming an aspect ratio of 1:10 (e.g. Doble 2009), the latter would imply pancake thickness of 10 to 18 cm and a 1:5 ratio would imply twice that. Of course, the pancake thickness is not necessarily a good measure of the equivalent ice thickness of the ice cover as a whole. Thermodynamic estimates (Ola Persson, paper submitted to JGR) average 1.8 cm during the same 4-day period, though this includes periods of low ice concentration.

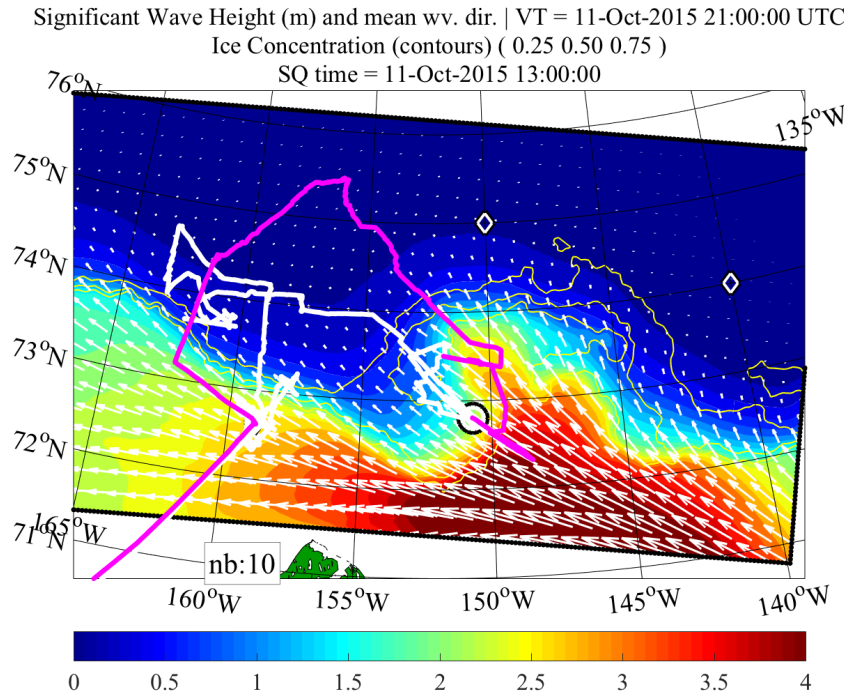


Figure 12. WW3 hindcast. See caption of Figure 7 for explanation of annotation. Drifting buoy observations:  $H_s$  up to 4.8 m;  $T_p$  8 to 11 s; mean wave direction: 140° on the 11th to 120° on the 13th (from southeast).



Figure 13. Still image from a video by the author, ER, October 11 2015, 1200LT. Pancakes in heavy frazil ice.

### 2.2.5. WA4-5: small waves (on-ice and off-ice)

Wave Arrays 4 and 5 occurred in close succession, and the latter one was very brief, so they are treated as a single wave experiment here, “WA4-5”. They were from October 17 000 UTC to October 19 0000 UTC. Quoting Thomson (2015) regarding Wave Array 4: *Upon reaching the ice edge on the Chukchi side, we found a diffuse ice edge with small pancakes. The incident waves were 0.3 m at 6 s from the southwest, and we deployed a line of buoys perpendicular to the ice edge ... The ice was advancing rapidly, and the buoy farthest out was in grease ice. NRL airborne remote sensing flight #2 was conducted, finishing the L-band SAR line from the day before and collecting LiDAR over the small pancakes near the ship... While deploying the line of buoys, we encountered a medium sized piece of multi-year ice that was heaving gently amongst the pancakes. We deployed wave buoys on and around this on 16 Oct, and surveyed the floe as Ice Station #5 (“Peter’s floe”) the following day... [S]ome of the buoys became frozen in when the waves decreased, while others drifted northwest towards more open water.*

And regarding Wave Array 5: *After recovering the buoys from the third pancake line early in the morning on 18 Oct, we stopped northwards on hourly flux stations (ship head-to-wind) through an embayment of open water that was experiencing off-ice winds and rapid cooling... At the second flux station, a narrow sharply-defined band of pancakes was encountered, which under the action of very short waves were causing reflection and scattering at the band edges. To investigate this effect, one SWIFT and two wave buoys were deployed to each side of, and inside, the band (wave array #5). There were very small (<10 cm) local wind waves from the northwest and a hint of the remnant swell at 6 s from the southwest. The array was in place for just over two hours, then recovered. A distinct ice-edge cold front was encountered near the southern end of the flux line. Winds were off-ice from the north at 7-10 m s-1, with low-level, cold-air outflow from the ice interior causing significant heat loss to the atmosphere. This entire embayment was later observed, via satellite, to freeze up within a day of our measurements.*

Here are some examples from the hourly ice observations, reported in ASSIST protocols:

- October 17, 0600 UTC: 100% concentration, 100% pancake
- October 17, 0900 UTC: 100% concentration, 80% pancake, 20% frazil
- October 17, 1200 UTC: 100% concentration, 100% frazil
- October 17, 1500 UTC: 100% concentration, 10% young grey, 70% pancake, 20% frazil
- October 17, 1800 UTC: 100% concentration, 90% pancake ice, 10% frazil
- October 17, 2000 UTC: 90% concentration, 10% second year, 20% first year, 60% pancake
- October 18, 0300 UTC: 100% concentration, 100% young grey ice
- October 18, 0615 UTC: 100% concentration, 70% pancake, 30% nilas
- October 18, 0900 UTC: 100% concentration, 10% young grey ice, 80% pancake, 10% nilas

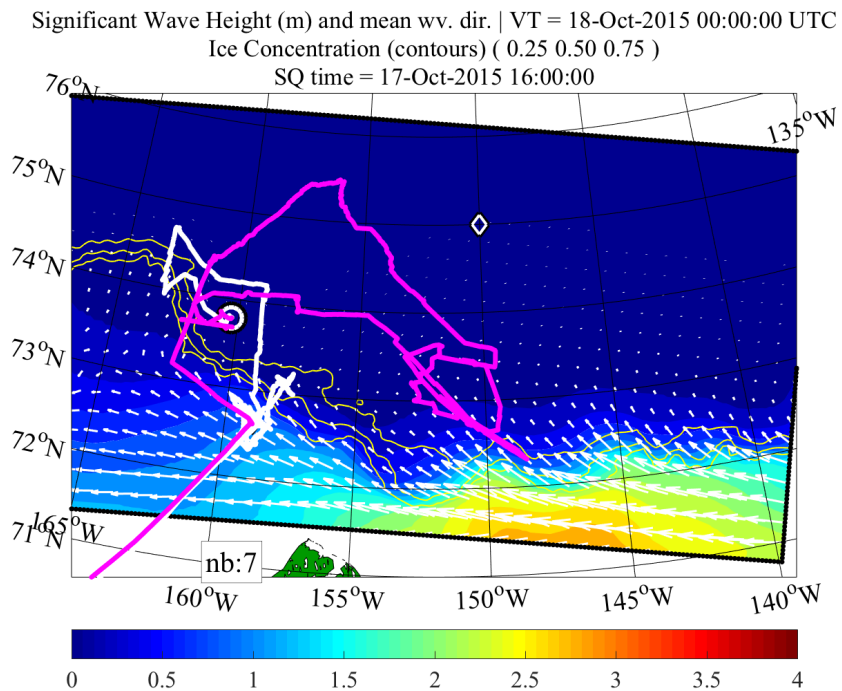


Figure 14. WW3 hindcast. See caption of Figure 7 for explanation of annotation. Observations near ship:  $H_s$  up to 35 cm;  $T_p$  4 to 7 s; mean wave direction  $170^\circ$  to  $270^\circ$  (Thus, primarily weak swell from south and southwest, though the primary system in basin is a windsea from east.)



Figure 15. Photo taken by Prof. Hayley Shen, October 17, 2015, 1512LT. Multi-year floe is visible, denoted in ice observations as the “AK and MD floe”; it is likely Ice Station 5, “Peter’s floe”. Pancake ice and floes from young ice are also visible.

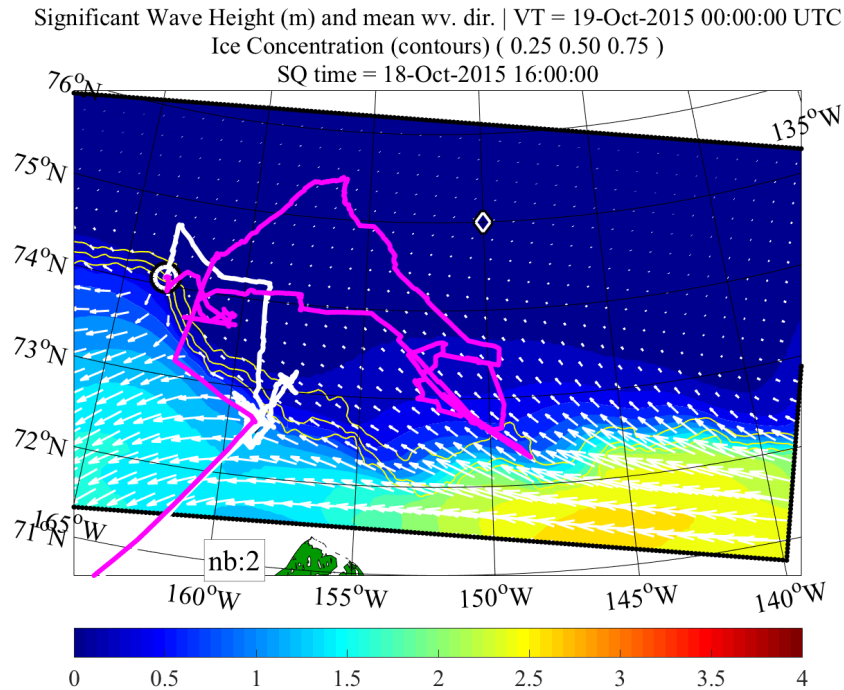


Figure 16. WW3 hindcast. See caption of Figure 7 for explanation of annotation. Observations near ship:  $H_s$  up to 35 cm;  $T_p$  4 to 7 s; mean wave direction 150° to 250°. (Thus, primarily weak swell from south and southwest, though the primary system in basin is a windsea from east.)



Figure 17. Photo taken by Prof. Hayley Shen, October 18, 2015, 1454LT. Pancakes near open water. Some have cemented together. Note that there is no visible evidence of frazil ice which is typically present when pancakes are forming: the water between pancakes is very dark, and where there are no pancakes, gravity-capillary waves are visible.

#### 2.2.6. WA6: obliquely off-ice waves

Wave Array #6 occurred from October 23 1300 UTC to October 25 1000 UTC. Thomson (2015): “*During the southward transit, we conducted hourly uCTD casts and then arrived at the southern ice edge, near the AWAC mooring site, on the morning of 23 Oct. We deployed wave array #6 as a line of buoys extending from 20 km penetration out to open water... Bands of pancakes were forming. Waves were 0.5 m at 7 s from the southeast and 0.5 m at 4 s from the east-southeast. Drift patterns suggested strong eddies at the shelf-break, and the buoys were alternately drifting in and out of bands of ice... Buoys were recovered on 24 Oct. NRL airborne remote sensing flight #4 was conducted on 23 Oct, with LiDAR and SAR lines crossing the ice edge. NRL airborne remote sensing flight #5 was conducted on 25 Oct, with select repeated lines at the ice edge, and a repeated SAR line up 159° W. Several flux stations were obtained in 9-12 m s-1 winds blowing obliquely off ice from the ESE.*”

Though winds were primarily from an easterly direction (Figure 19), the waves tended to be from the southeast (Figure 18 and Figure 19), running parallel to the ice edge. This is a result of the larger fetch available to waves from the southeast. This is known as a “slanting fetch” or “oblique fetch” condition in coastal oceanography, but here the fetch is defined by the ice edge to the east, rather than by a coastline. The wave model (Figure 18) indicates that the height of the waves was strongly dependent on the distance from the ice edge.

Here are some examples from the hourly ice observations, recorded in ASSIST protocols:

- October 23, 1800 UTC: open water
- October 23, 2040 UTC: 90% concentration, 50% pancake, 40% brash
- October 24, 0000 UTC: 50% concentration, 30% pancake, 20% nilas

- October 24, 0325 UTC: 10% concentration, 10% pancake
- October 24, 0800 UTC: open water
- October 24, 1920 UTC: 20% ice concentration, 20% pancake

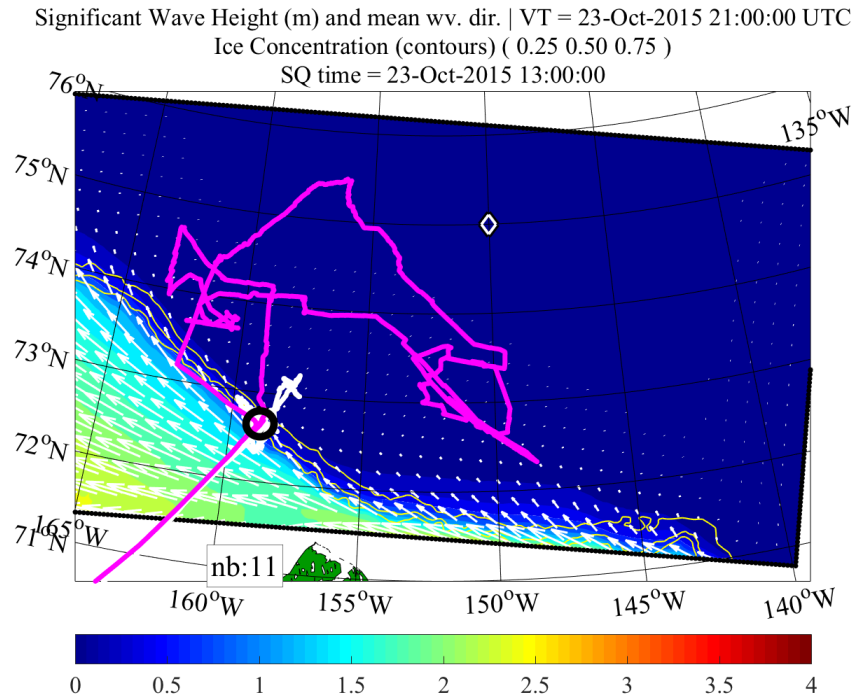


Figure 18. WW3 hindcast. See caption of Figure 7 for explanation of annotation. Observations near ship:  $H_s$  up to 1.3 m;  $T_p$  3.5 to 8.7 s; mean wave direction 110° to 170° (fetch-limited windsea from southeast).

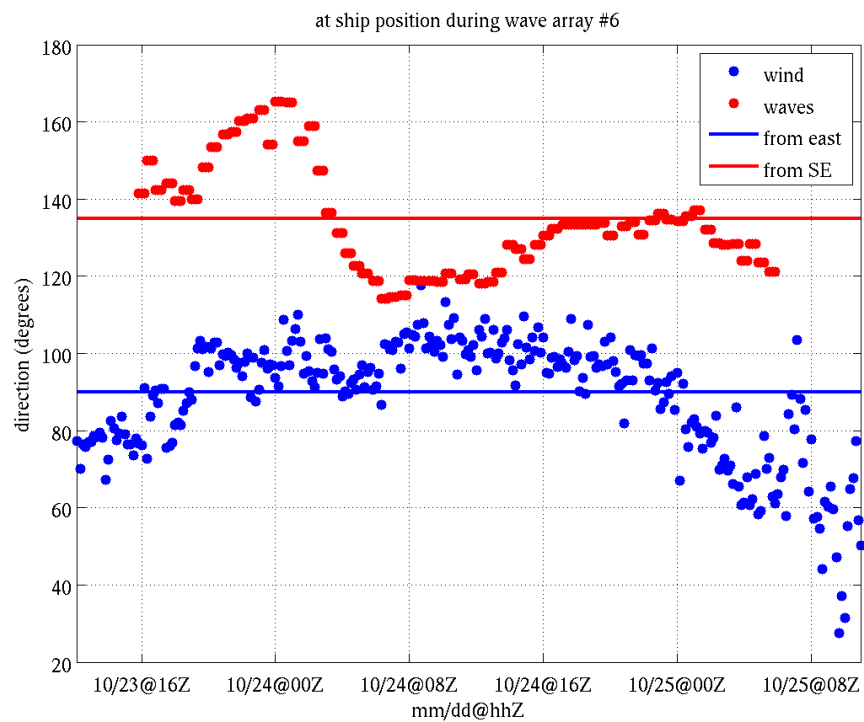


Figure 19. Wind and wave direction at the ship position during WA6. The former is from measurements on the ship's mast and the latter is from marine radar. These data were provided by Ola Persson (NOAA); the marine radar

operation and data processing was performed by Bjoern Lund (U. Miami). See also wave directions from drifting buoys in Figure 5 and other marine radar measurements in Figure 119.



Figure 20. Photo taken by Prof. Hayley Shen, October 23, 2015, 1235LT. Pancake and pancake brash.

#### 2.2.7. Racetrack (RT): weak off-ice winds

The Racetrack (RT) circuits, conducted from October 25 to 27 and November 2 to 3, were primarily focused on CTDs and atmospheric flux stations, but two SWIFT buoys were deployed from October 26 07:00 UTC to October 27 18:00 UTC. Thomson (2015): *The AWAC mooring was recovered on the morning of 25 Oct, and then a race track pattern was established to measure the fluxes and ocean structure of the advancing ice edge during a forecasted cooling event with weak off-ice winds from NW through NE... Two SWIFTS were redeployed in open water and eventually froze in place as pancakes formed around them and joined together.* During an evening planning meeting, most likely on the 27<sup>th</sup>, the Chief Scientist (Thomson) showed a time-lapse video of photos taken by one of the two SWIFT buoys. This remarkable video records the formation of pancake ice from the lagrangian perspective of the drifting buoy. Other applications of the SWIFT photos are described in Section 7.

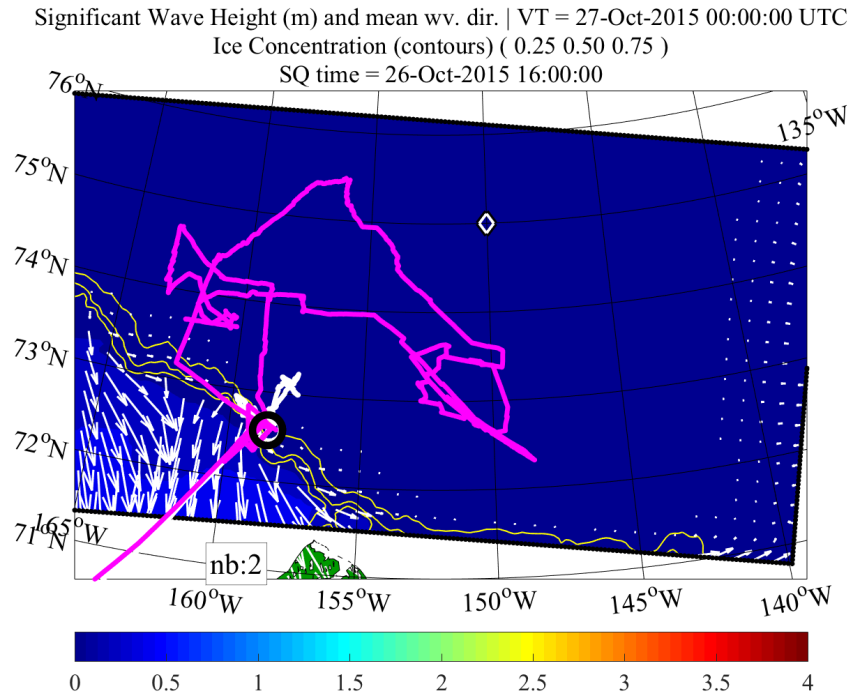


Figure 21. WW3 hindcast. See caption of Figure 7 for explanation of annotation. Observations near ship:  $H_s$  up to 36 cm;  $T_p$  2 to 5.5 s; mean wave direction 270° to 360° (waves from northwest, associated with local winds).



Figure 22. Photo taken by Prof. Hayley Shen, October 26, 2015, 1537LT. Open water and ice with snow cover. Ice with smooth snow surface is first year ice of uncertain origin (i.e. may have started as either nilas or pancakes). The ice with rougher upper surface is sheet ice formed from cemented pancakes.

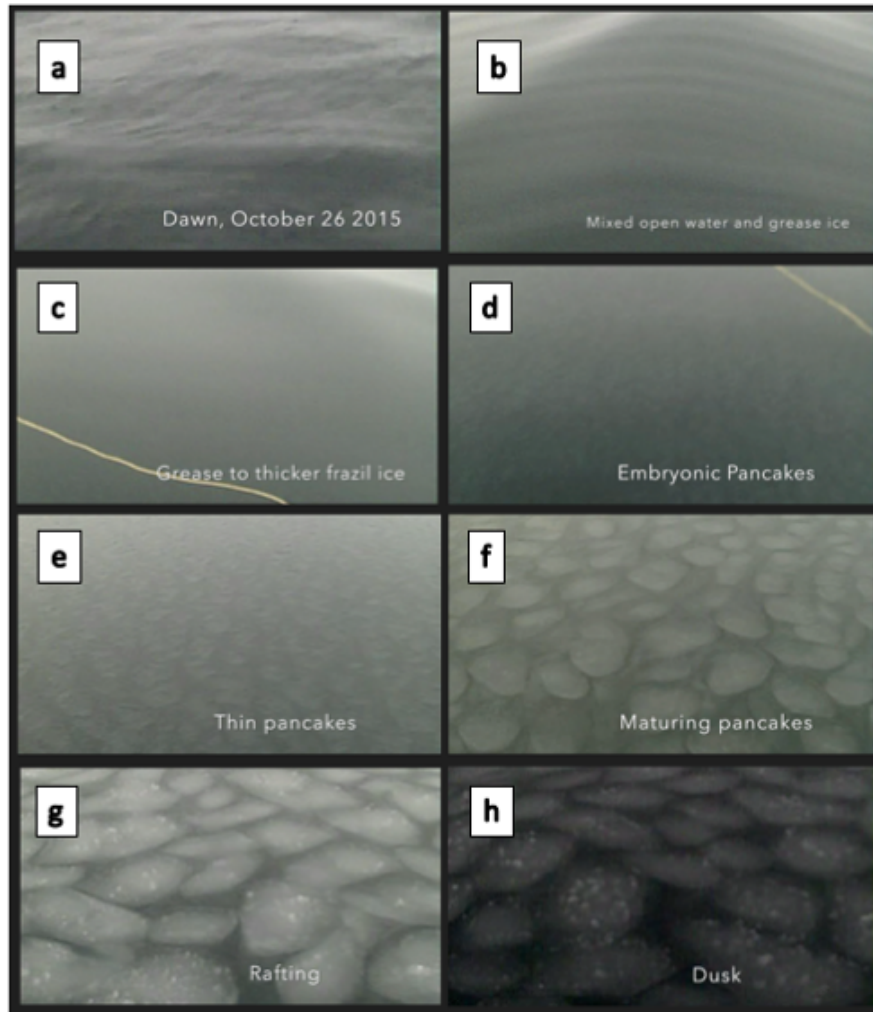


Figure 23. Still images from the time-lapse video made by Joe Talbert and Jim Thomson (U. Washington). Annotation added by author ER. This corresponds to dawn to dusk on October 26 2015. Given this date, and a latitude of 72.5°, the length of the day is estimated to be 6 to 6.5 hours.

Here are some examples from the hourly ice observations, recorded in ASSIST protocols:

- October 26, 10:05 UTC: 40% concentration, 30% young grey ice, 10% brash
- October 26, 13:35 UTC: open water
- October 26, 23:00 UTC: 80% concentration, 70% pancakes, 10% young grey ice
- October 27, 00:32 UTC: 70% concentration, 60% pancakes, 10% young grey ice
- October 27, 03:52 UTC: 50% concentration, 30% pancakes, 10% young grey ice, 10% nilas
- October 27, 08:05 UTC: 100% concentration, 30% pancakes, 70% nilas
- October 27, 16:00 UTC: 100% concentration, 80% pancakes, 20% nilas

#### 2.2.8. WA7: on-ice swells

Wave Array #7 (WA7) started October 31 16:00 UTC. Most buoys were retrieved before November 1 21:00 UTC, and the experiment was completed November 2 17:00 UTC. Thomson (2015): *We ran the western side of the race track ... during the night, arriving at the end of the*

*line in the morning. This line had been mostly sheet ice during the previous race track laps just a few days prior, but was now broken by waves into small cakes and brash ice. Presumably, this was caused by the western swell arriving at the ice edge (0.6 m at 7 s from W and another system from SW). We intended to deploy buoys to measure these waves at the edge around point #3, based on recent SAR images, but the ice retreated almost 10 miles overnight and we deployed at the new ice edge...instead. We deployed a tight array of 5 wave buoys, 4 SWIFTS, and 1 NIWA buoy for the morning inside the pancakes, at an internal boundary which marked a transition from pancakes to larger cemented floe-sized ice elements of 20 m and more in diameter... The tight array was designed to measure scattering, reflection and spectral broadening at a transition to large cakes whose diameters were a substantial fraction of a wavelength, with the hypothesis of scattering as the dominant mechanism of local wave-ice interaction. In the afternoon, we moved two SWIFT buoys out to open water for a larger-scale attenuation measurement. In the evening, we moved one wave buoy further inside the ice. We then resumed the ...upper leg ... of the racetrack. The Rutter radar was collecting data throughout the experiment. It detected waves in a variety of conditions ranging from new sheet ice, pancake ice, and brash ice, to open water. The ice retreated farther during the early morning of 1 Nov... Active breaking of sheets was observed while transecting out ... and back .... The westerly swell died and the southwesterly swell built to 1.7 m at 4.5 s (from the buoys on the edge). In the morning, we left [the Racetrack] to recover buoys that had drifted to the northwest. A few of the buoys were recovered from open water, the rest were in loose-cake ice. Moderate SSE winds transitioned into weak and variable as a shallow low-pressure system moved over the array, bringing substantial warm-air advection.*

The author (ER) recorded that at approximately November 1 07:00 UTC (or October 31 23:00 SQ time), a member of the crew observed sheet ice broken by swells from the southwest.

Here are some examples from the hourly ice observations, recorded in ASSIST protocols:

- October 31, 18:09 UTC: 80% concentration, 40% pancake, 20% brash, 20% frazil
- October 31, 21:00 UTC: 90% concentration, 80% brash, 10% grease
- November 1, 00:00 UTC: 100% concentration, 90% brash, 10% slush
- November 1, 03:10 UTC: 90% concentration, 40% first year ice, 40% nilas, 10% pancake
- November 1, 07:00 UTC: 50% concentration, 40% pancake, 10% frazil
- November 1, 08:00 UTC: open water
- November 1, 15:25 UTC: 90% concentration, 30% young grey ice, 60% brash
- November 1, 18:02 UTC: 100% concentration, 50% first year ice, 50% pancake

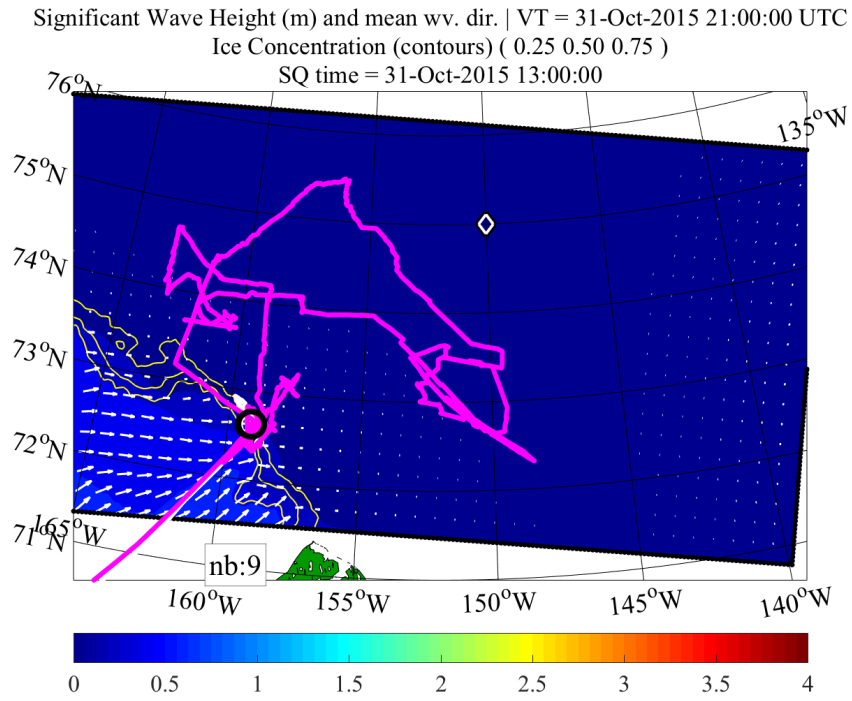


Figure 24. WW3 hindcast. See caption of Figure 7 for explanation of annotation. Observations near ship:  $H_s$  up to 1.4 m;  $T_p$  3.8 to 8 s; mean wave direction 200° to 270° (swells from southwest).



Figure 25. Photo taken by Prof. Hayley Shen, October 31, 2015, 1246LT. The floes with heavier snow cover are from broken first-year ice, likely formed from cemented pancakes, as evidenced by the texture. The floes with partial snow cover are from broken nilas or grey ice. The former are thicker and rigid (tending to fracture under wave motion), while the latter are thinner and flex with the low-amplitude wave motion (but still fracturing on occasion).

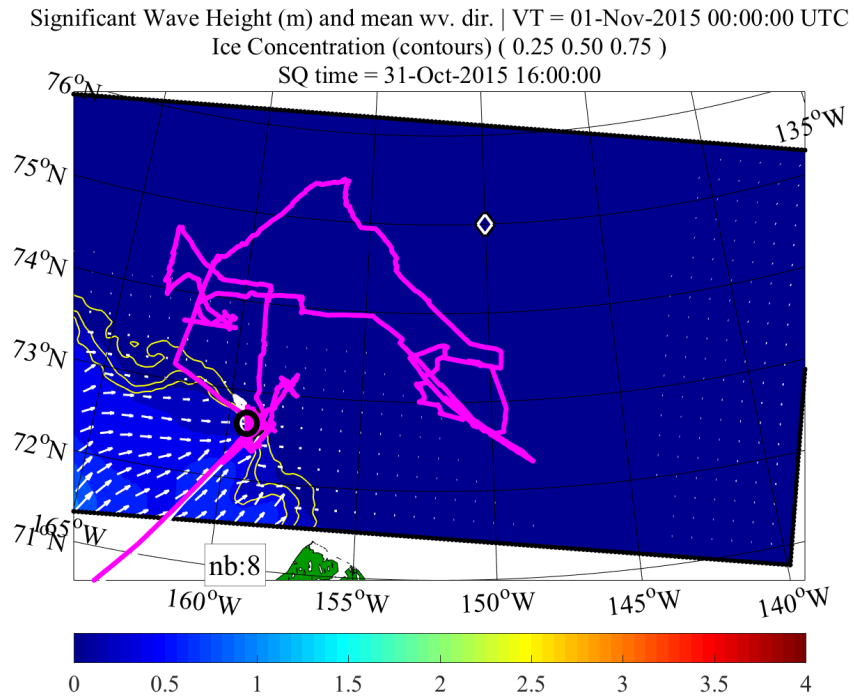


Figure 26. WW3 hindcast. See caption of Figure 7 for explanation of annotation. Observations near ship:  $H_s$  up to 1.4 m;  $T_p$  3.8 to 8 s; mean wave direction 200° to 270° (swells from southwest).

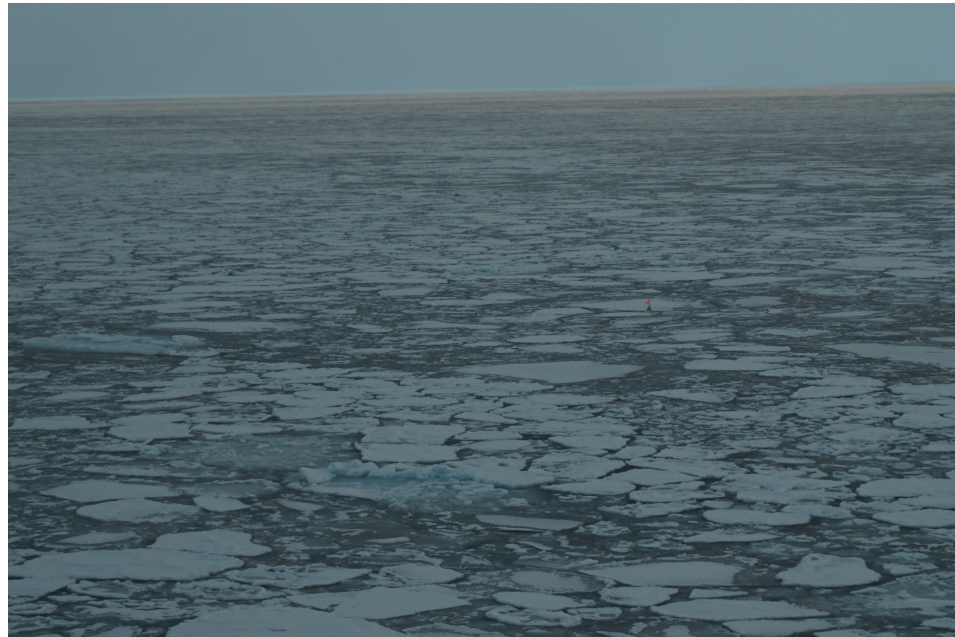


Figure 27. Photo taken by Prof. Hayley Shen, October 31, 2015, 1538LT. Floes from first year ice and brash. The isolated patches of blue coloration are associated with ice that lies just under the water surface.



Figure 28. Photo taken by Prof. Hayley Shen, October 31, 2015, 1657LT. Floes or cake ice from first year ice (likely was cemented pancakes).

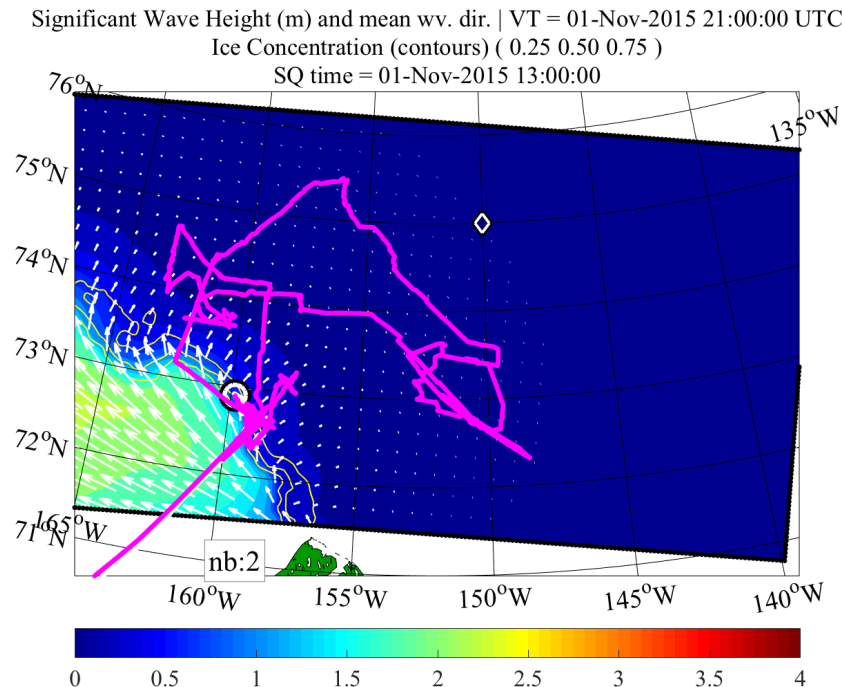


Figure 29. WW3 hindcast. See caption of Figure 7 for explanation of annotation. Observations near ship:  $H_s$  up to 1.4 m;  $T_p$  3.8 to 8 s; mean wave direction  $200^\circ$  to  $270^\circ$  (swells from southwest).



Figure 30. Photo taken by Prof. Hayley Shen, November 1, 2015, 1155LT. Open water, brash ice, and some floes from first year ice.



Figure 31. Photo taken by Prof. Hayley Shen, November 1, 2015, 1401LT. Floes or cake ice from first-year ice; also pancakes and brash.

### 2.3. Wave forecasting

The short duration of the wave experiments, coupled with episodic nature of waves, implies significant benefit from utilization of wave forecasts during planning of the wave experiments, and decisions regarding whether to spend cruise time on wave experiments or other priorities, such as ice stations, which were mostly well north of the MIZ. With a few exceptions, the wave forecasts were briefed at the Plan of the Day (POD) meetings held each evening on the ship. These forecasts were based on wave model simulations from three sources. The first was a

nested modeling system run from the ship, a development version of the open-source community model, WAVEWATCH III® (Tolman and the WAVEWATCH III Development Group 2014). Both nests were designed to run in approximately 45 minutes (each) on a Linux/MacOS laptop, with forecast out to six days. The outer domain incorporated half of the Arctic Ocean and the northern Bering Sea, with a 15 km resolution polar stereographic grid, including all areas likely to generate swells that may propagate into the experimental area of the Beaufort and Chukchi Seas. This model was forced with winds from the Navy's global atmospheric model NAVGEM, (Hogan et al. 2014, 0.5° resolution) and associated ice concentration analyses from the SSMI passive microwave radiometer. Both of these fields (winds and ice concentration analyses) were available twice per day (0Z and 12Z "run cycles")<sup>11</sup>. A pre-DRI representation of ice effects on waves (IC0, introduced in Section 3.1.1) was used for this grid. The inner grid was a 10 km resolution polar stereographic grid for the Beaufort and eastern Chukchi Sea, added to the forecasting on October 6, with modifications on October 9. This nest used the same wind forcing as the outer grid, but used ice concentration and thickness from a 2 km implementation of the ice model CICE (Community Ice Code, the Los Alamos Sea Ice model of Hunke et al. 2015), run by David Hebert and Pamela Posey at NRL-Stennis. This CICE model was run once per day, for 0Z (0000 UTC). For this inner WW3 grid, an experimental form of physics for ice effects on waves, developed under the DRI, was employed (IC3, introduced in Section 3.1.4). These ship-based model runs were used to generate spatial plots of bulk parameters (e.g. significant waveheight, peak direction), time series of wind and wave bulk parameters for up to seven locations of interest (which changed during the cruise), and directional spectra, also at locations of interest, for presentation at the POD meetings<sup>12</sup>. Figure 32 and Figure 33 provide example graphics from this modeling system. The 6-day forecast was performed zero to two times daily, depending on planning requirements. The outer grid was run 34 times and the inner grid was run 24 times during the cruise.

The second wave modeling system used was provided by ECMWF (European Centre for Medium-Range Weather Forecasts), which was another ONR-funded participant in the DRI. This model was based on the ECMWF version of WAM ("WAve Model", WAMDIG 1988; Komen et al. 1994). Outputs included spatial plots of bulk parameters for a short-range forecast high-resolution deterministic model, and long-range (10 day) time series forecasts for wind and wave bulk parameters at specific points in the Beaufort Sea, the so-called "EPS Meteogram" based on a high-resolution deterministic model, and lower resolution ensemble probabilistic model. These meteograms were especially useful, given the long-range of the forecast, and also it was not uncommon for the ECMWF atmospheric model to pick up important wind features further in the future (1 to 1.5 days, typically) relative the Navy atmospheric model, though they showed comparable skill for short-term forecasts (see Section 5).

The third wave modeling system was another system using the WAVEWATCH III code, run by James Dykes at NRL-Stennis, with non-DRI ONR funding, using a system that was established for support of the Healy cruises in the summer of 2015. The shore-side computational resources meant that the model could be run at higher resolution than the on-ship model: it used a 5 km polar stereographic grid, run within a global grid (two-way nesting). It used IC0 for

<sup>11</sup> "0Z" is sometimes written as "00Z" or "00z" and is read as "zero Z", meaning "zero Zulu" and "00:00 UTC".

<sup>12</sup> This was useful feature of the on-ship forecasting: the model and graphical products could be adapted in realtime according to requirements. The 'in-person' aspect of the forecasting enhanced awareness of these requirements.

representation of ice effects on waves, and was forced by ice and atmospheric models that were also established for Healy support (the former being the same forcing as used in the inner grid of the first wave modeling system above, and the latter being a high resolution COAMPS grid operated by NRL-Monterey). Unfortunately, this wave modeling system suffered a failure just prior to WA3: the winds were apparently not updating and the wave model was producing spurious results.

Well prior to the cruise, automated systems were created to deliver the outputs from the second and third modeling systems, and the ice and wind inputs necessary to run to the first (ship-based) modeling system, to the ftp site administered by the University of Victoria. This proved to be a highly reliable method for aggregation and transfer of data. In the author's experience, this site was available 100% of the time during the entire cruise. In the case of the twice-daily NAVGEM wind forecast and SSMI ice analysis, the fields were typically available eight hours after the valid time of the analysis; for example, the 12Z forcing was available around noon local time. In the case of the once-daily CICE output, it was somewhat later, since it was a regional implementation: the file with 0Z forcing was available around 0300 local time.

The three modeling systems were not redundant and in fact the multiple sources provided a mechanism for establishing confidence (or uncertainty) in a forecast. For example, in cases where the on-ship WW3 was different from the ECMWF forecast, this implied less confidence, and when the forecasts were similar, they could be briefed at the POD meetings as something to definitely expect. The shore-based WW3 system was useful especially during the first 10 days of the cruise, since during that period, though the outer on-ship WW3 grid was up and running, the details of the inner on-ship WW3 grid were still being worked out, as noted above (how far south it would extend, etc.).

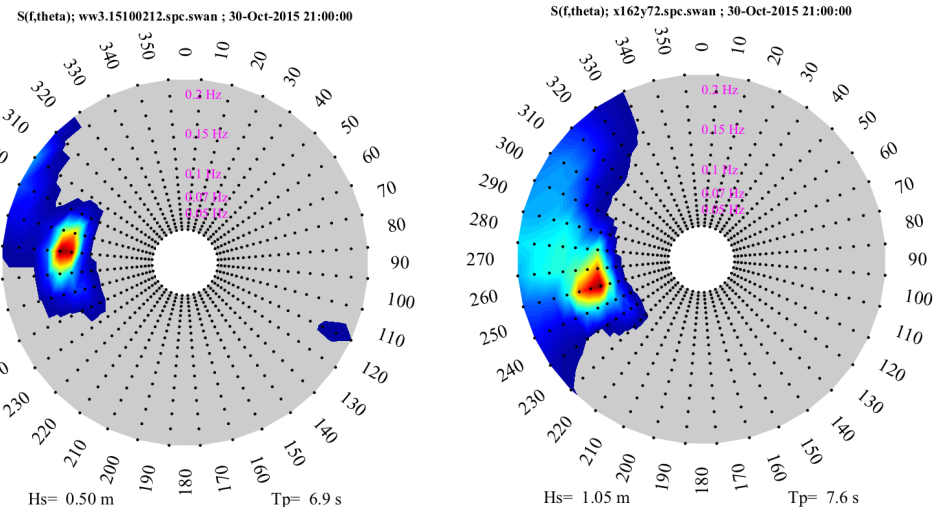


Figure 32. Two forecasts of directional spectrum for the western component of an overlapping double swell event (from west and southwest) which may have contributed significantly to the retreat of the ice near the Racetrack Oct. 30 to Nov. 1. Left panel: Briefed at Oct 25 POD meeting, for AWAC position, 159.0W 72.6N. Right panel: Briefed at Oct 30 POD meeting, for 162.0W 72.0N.

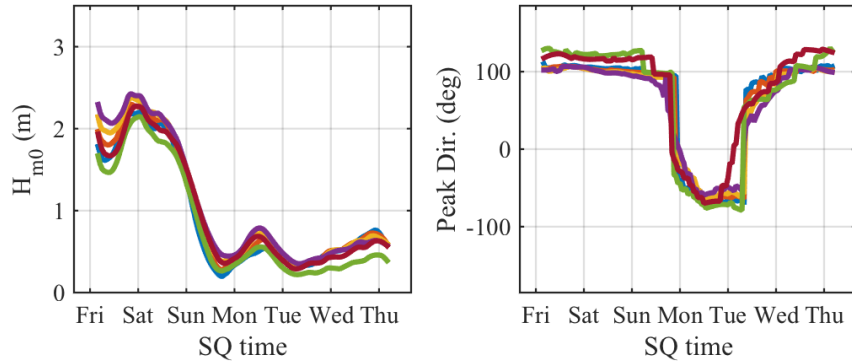


Figure 33. Example forecast graphic briefed at evening POD meetings. This was from the 1200 UTC 23 October run cycle of the on-ship WW3 system, briefed at the 23 October meeting. The original graphic included six time series: the two shown here, plus wind speed, wind direction, peak period, and mean period. There are six lines in each plot, each corresponding to a different location. These locations were indicated in separate graphics not included here.

### 2.3.1. Wave forecasting for WA3 and WA4-5

Wave array #3 (WA3) is of particular interest, being the only wave experiment of the cruise for which large waves ( $H_s > 3$  m) were measured in ice. Here, we briefly review the forecasting for this wave event. Below is a list of WW3 forecasts performed by author ER prior to WA3:

- Sep. 20-25: no forecast
- Sep. 26: 15 km grid, 12Z cycle
- Sep. 27: 15 km grid, 0Z cycle
- Sep. 28: 15 km grid, 12Z cycle
- Sep. 29: no forecast (ER en route to Nome, AK)
- Sep. 30: 15 km grid: 0Z cycle (ER boarded ship)
- Oct. 1: 15 km grid: 12Z cycle
- Oct. 2: 15 km grid: 12Z cycle
- Oct. 3: 15 km grid: 0Z cycle
- Oct. 4-5: no forecast (see below)
- Oct. 6: [15 km grid, 0Z cycle], [10 km grid 0Z cycle]
- Oct. 7: no forecast (ice drilling at IS1)
- Oct. 8: [15 km grid: 0Z cycle and 12Z cycle], [10 km grid, 12Z cycle]
- Oct. 9: [15 km grid: 0Z cycle and 12Z cycle], [10 km grid: 0Z cycle and 12Z cycle]
- Oct. 10: [15 km grid: 0Z cycle and 12Z cycle], [10 km grid: 0Z cycle and 12Z cycle]

No on-ship wave model runs were presented at the POD meetings for Oct. 4, 5, and 6. Ice Station Ben (IS1) started Oct. 6. A model was run for Oct. 6 0Z cycle, but this was presented at Oct 7 POD meeting. On Oct. 4 and 5, ER was creating the initial 10 km nest, which was modified on the 9<sup>th</sup>: at that time, it was necessary to move it further south, all the way to Alaskan coast, since the MIZ was advancing south (Figure 34).

#### *Forecast skill*

Example forecasts are shown in Figure 35 to Figure 42. The figures indicate that the wind/wave event was inadequately captured in the 144 hour (6-day) forecast, but was adequately captured in the 117 hour (4 days and 21 hours) forecast. The atmospheric forcing is, of course, the primary controlling factor in this forecast skill. Direct evaluation of the skill of the atmospheric forcing is

briefly addressed in Section 5.2. The 144 hour and 117 hour forecasts correspond to the “100600” and “100800” run cycles in the NAVGEM forecast (blue line) in Figure 74. This suggests that the run cycle shown in Figure 36 is the first run cycle for which the wind/wave event is adequately captured by NAVGEM.

#### *Viscosity setting in IC3*

As noted in Section 2.3, the IC3 module (introduced in Section 3.1.4) was used for the inner nest of the on-ship WW3 forecasting system, and ice concentration and ice thickness were taken from the NRL 2 km CICE implementation. The IC3 is a viscoelastic model, so it also requires user input for effective viscosity and effective elasticity. The latter was set to zero throughout the cruise. The viscosity was set at  $\nu = 1.0 \text{ m}^2\text{s}^{-1}$  during the first half of the cruise. This value was chosen on a fairly arbitrary basis: in comparison to IC0 by Rogers and Zieger (2014), it provided rough parity in mean wave height, though the spatial distribution differs strongly (see Figure 1h of that paper). It is a fairly high setting, appropriate for rigid ice. By contrast, Newyear and Martin (1999) found a value of 0.02 to 0.03  $\text{m}^2\text{s}^{-1}$  for grease ice (i.e. thin frazil) in laboratory experiments<sup>13</sup>. After WA3, author ER judged that this setting was too high for the ice conditions encountered in WA3 (pancake and frazil, see Rogers et al. (2016) or Section 7 of this report), and changed the setting to 0.1  $\text{m}^2\text{s}^{-1}$  on October 14. At that time, the WA3 forecast was re-run with the new setting to evaluate sensitivity (see Figure 41 and Figure 42 which use the old and new setting, respectively). The new  $\nu = 0.1 \text{ m}^2\text{s}^{-1}$  setting was used for the remainder of the cruise.

On October 18, it was found that the original setting may have been more appropriate. It was exactly one week after the WA3 event and the forecast called for what could be considered the “little brother” to the WA3 event since it was also an easterly event, but was weaker. Also, the ship had moved northwest, where it was more sheltered by ice from easterly and southeasterly waves: those waves needed to pass through relatively rigid sheet ice in order to arrive at the ship’s position which was west of 160W, near WA4-5 and IS5. IC3 with  $\nu = 0.1 \text{ m}^2\text{s}^{-1}$  permitted this wave energy to reach the ship (Figure 43), but the waves were not observed at the ship. This was the most memorable failure of the on-ship wave forecasting during the entire cruise. The IC4M6H2 hindcast model (Section 6.3) does not have this problem: it adequately predicts the complete damping of these easterly and southeasterly swells (Figure 44). We did not repeat the WA4-5 hindcast using the IC3  $\nu = 1.0 \text{ m}^2\text{s}^{-1}$  model. However, Figure 100 implies that this model would have damped these swells as much as the IC4 models, provided that the peak frequency of these swells was not less than 0.1 Hz. Figure 45 indicates that the spurious swell had peak frequency of 0.11 Hz.

Of course, this discussion highlights a rather obvious assertion: the effective viscosity should not be uniform in time and space, but rather should vary according to ice type. Similarly, if a parametric model like IC4 is used, it should vary according to ice type. Unfortunately, gridded fields of ice type are not available even now, two years after the cruise, and are far from being feasible in an operational context. That remains a major objective of ongoing research.

---

<sup>13</sup> Wadhams et al. (2004) also cite Newyear and Martin (1999), but they reference a slightly higher viscosity:  $0.03 \pm 0.0025 \text{ m}^2\text{s}^{-1}$ .

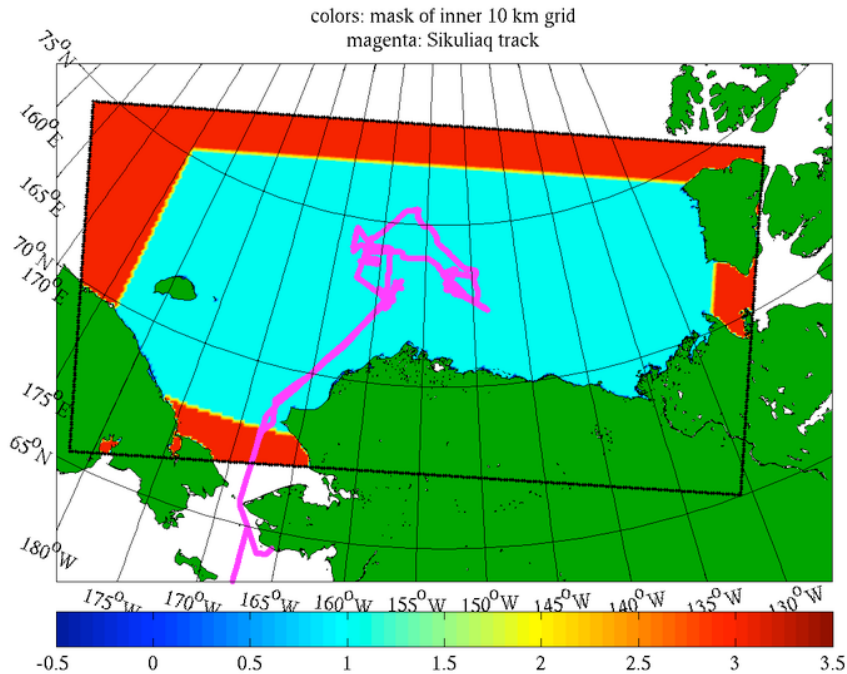


Figure 34. The second (and final) version of the 10-km inner WW3 nest used for on-ship forecasting. Active grid points are shown in cyan. The ship track is shown in magenta. This is also the inner grid used for hindcasting by Rogers et al. (2016). Note: it is *not* the inner grid used by Collins and Rogers (2017) and in the hindcasting in the present report. These two reports use a 5-km inner grid (Section 6.1.1).

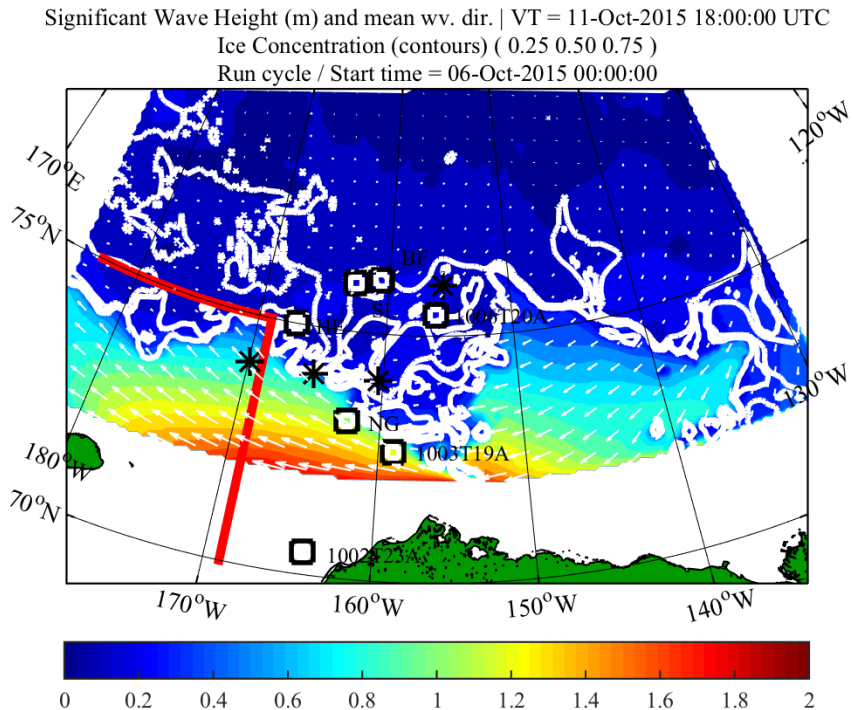


Figure 35. WW3 forecast of WA3, from the 0Z cycle forecast on Oct. 6. This is the inner grid, using the IC3 module ( $\nu = 1.0 \text{ m}^2\text{s}^{-1}$ ) and CICE. This is the last forecast for that run cycle, being the 6-day forecast. This is an actual graphic used in POD briefing, so it includes some cryptic notation, marking points to orient the viewer. Asterisks correspond to ECMWF forecast points which were also briefed in the POD. Alphanumeric strings mark the ship's position, e.g. 1006T20A for Oct. 6. "NG" is the position of the recovery of the NAVOCEANO glider. "BF" is Ben's floe, which was later denoted as Ice Station Ben or Ice Station 1 (IS1). "HE" marks the nominal position of a "hard

ice edge" and the meaning of "SL" is not recalled. The red line marks the EEZ (economic exclusion zone) of Russia (something to be aware of when planning cruise routes). Note that the color scale is only up to 2 meters, so the forecasted waves are small relative to subsequent figures (and relative to observed waveheights). Since this is the initial 10 km inner nest, it does not extend all the way to the Alaska coast.

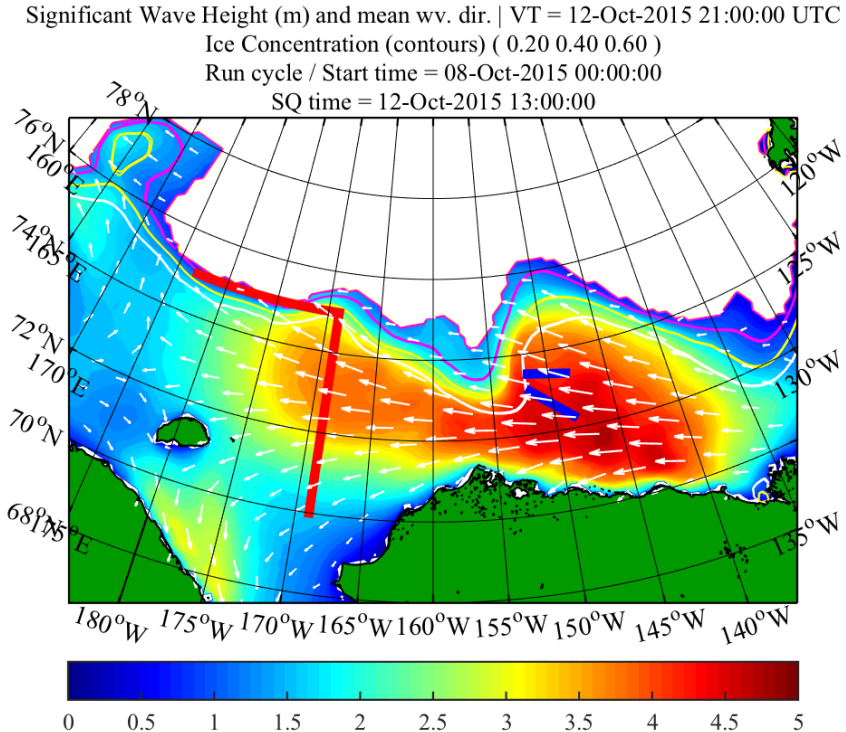


Figure 36. WW3 forecast of WA3, from the 0Z cycle forecast on Oct. 8. This is the outer grid, using the IC0 module and SSM/I. Since IC0 is used, regions with ice concentration larger than 75% are blank (white). This graphic was produced using the actual forecast fields (the on-ship model), but is not a graphic used in the POD briefing: rather, the graphic was re-created post-cruise, so most of the clutter seen in Figure 35 is removed here. The blue lines indicate the northern and southern transects of WA3. This is the forecast for 4 days and 21 hours in the future. By this time, WW3 was exhibiting good skill for prediction of the incident waves, unlike the forecast run on Oct. 6 (Figure 35).

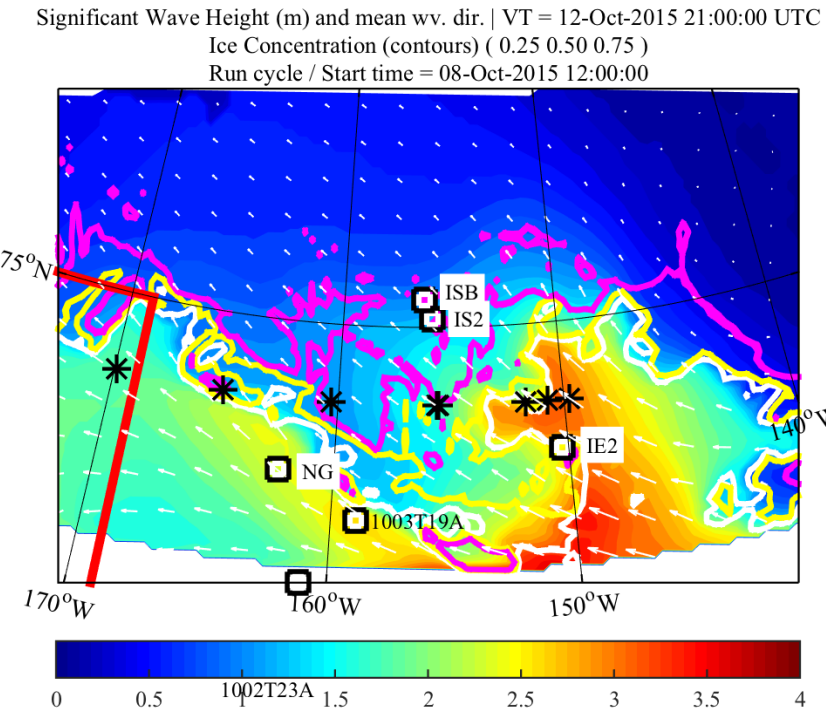


Figure 37. WW3 forecast of WA3, from the 12Z cycle forecast on Oct. 8. This is the inner grid, using the IC3 module ( $v = 1.0 \text{ m}^2\text{s}^{-1}$ ) and CICE. This is the forecast for 4 days and 9 hours in the future. Again, WW3 was exhibiting good skill for prediction of the incident waves. This is an actual graphic used in POD briefing, so it includes some cryptic notation, like in Figure 35, marking points to orient the viewer. Since this is the initial 10 km inner nest, it does not extend all the way to the Alaska coast.

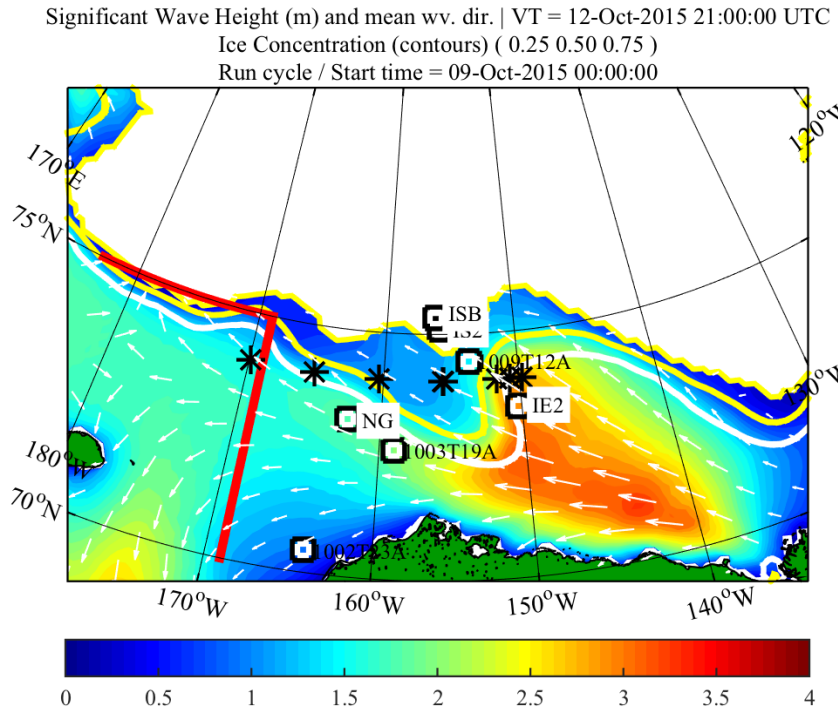


Figure 38. WW3 forecast of WA3, from the 00Z cycle forecast on Oct. 9. This is the outer grid, using the IC0 module and SSM/I. Since IC0 is used, regions with ice concentration larger than 75% are blank (white). This is the forecast for 3 days and 21 hours in the future. This is an actual graphic used in POD briefing, so it includes some cryptic notation, like in Figure 35, marking points to orient the viewer.

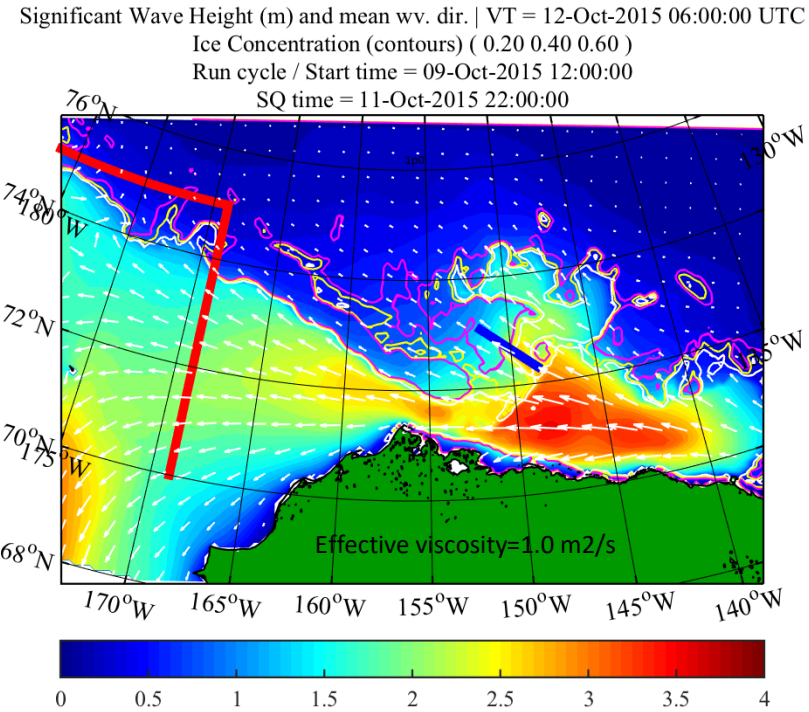


Figure 39. WW3 forecast of WA3, from the 12Z cycle forecast on Oct. 9. This is the inner grid, using the IC3 module ( $v = 1.0 \text{ m}^2\text{s}^{-1}$ ) and CICE. This is the forecast for 2 days and 18 hours in the future. This graphic was produced using the actual forecast fields (the on-ship model), but is not a graphic used in the POD briefing: rather, the graphic was re-created post-cruise, so most of the clutter seen in Figure 35 is removed here. The blue line indicates the southern transect of WA3. This is the revised 10 km inner nest, so it does extend all the way to the Alaska coast.

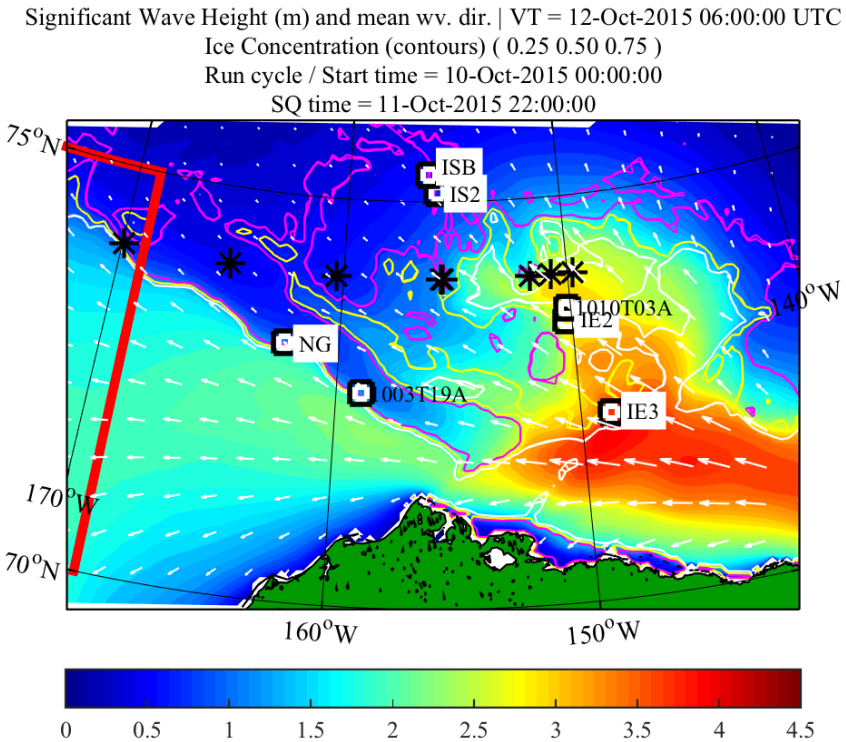


Figure 40. WW3 forecast of WA3, from the 0Z cycle forecast on Oct. 10. This is the inner grid, using the IC3 module ( $v = 1.0 \text{ m}^2\text{s}^{-1}$ ) and CICE. This is the forecast for 2 days and 6 hours in the future. This is an actual graphic used in POD briefing, so it includes the cryptic notation. This is the revised 10 km inner nest, so it does extend all the way to the Alaska coast.

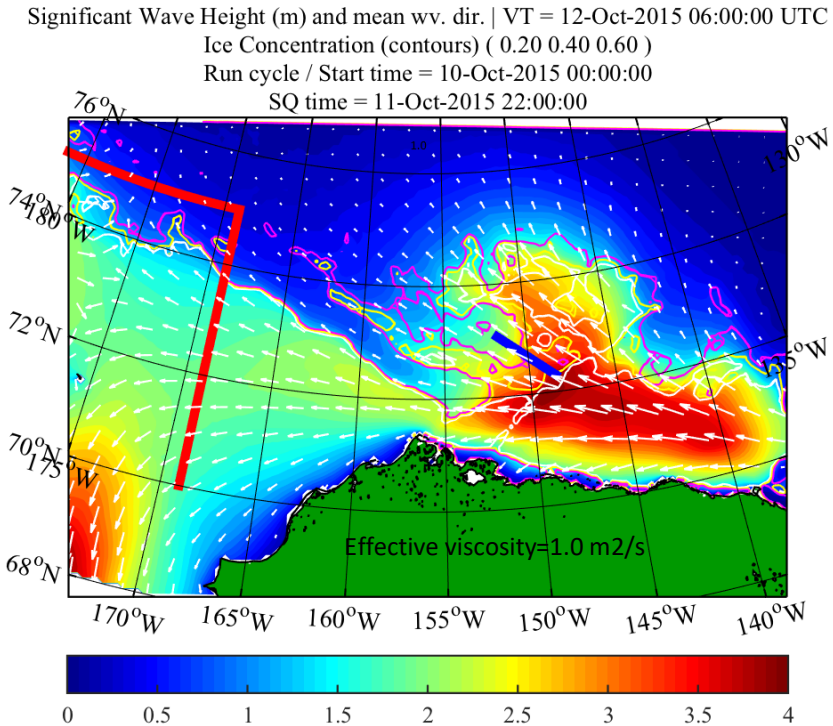


Figure 41. WW3 forecast of WA3, from the 0Z cycle forecast on Oct. 10. This field is identical to that shown in Figure 40, but this graphic was re-created post-cruise, so most of the clutter seen in that figure is removed here; axes and color scaling are also different. The blue line indicates the southern transect of WA3.

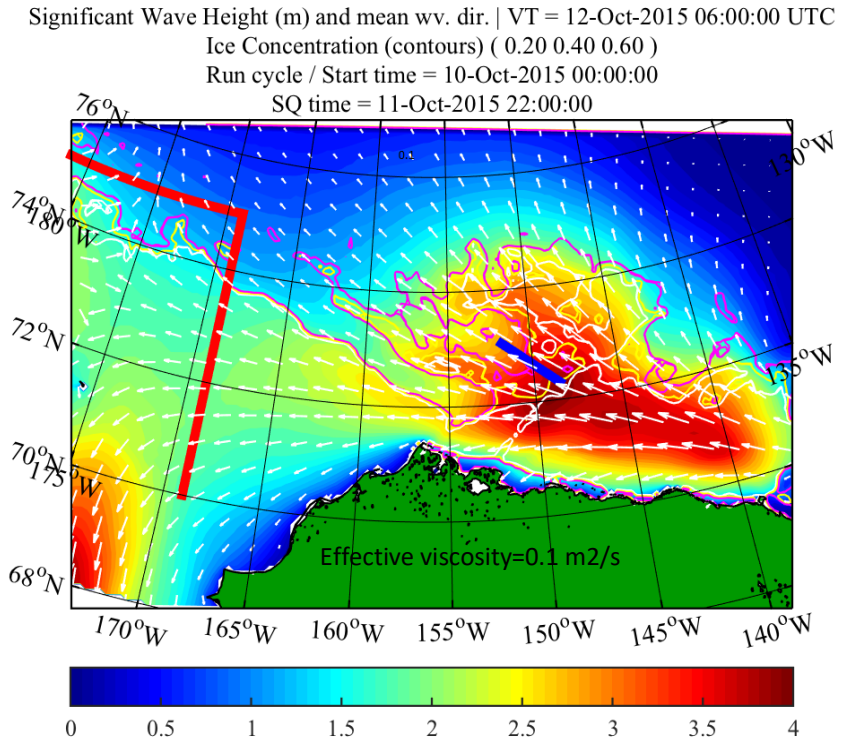


Figure 42. This graphic is identical to Figure 41, but the effective viscosity of IC3 is reduced by a factor of 10:  $\nu = 0.1 \text{ m}^2 \text{s}^{-1}$ . This was run on Oct. 15 (post facto). In other words, it is a re-run of a prior forecast, using a different viscosity.

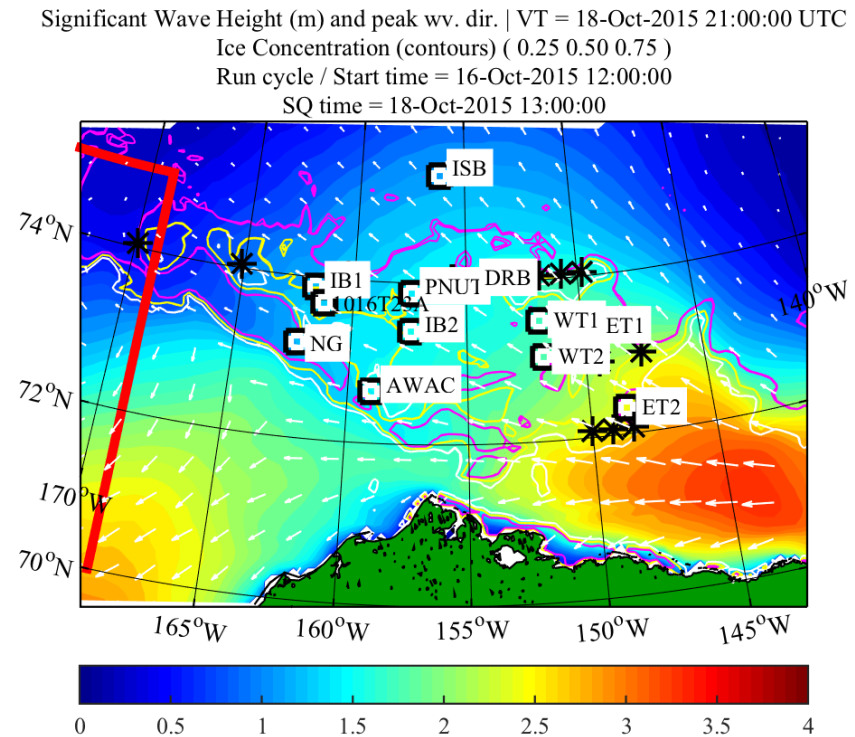


Figure 43. WW3 forecast of WA4-5, from the 12Z cycle forecast on Oct. 16. This is the inner grid, using the IC3 module ( $\nu = 0.1 \text{ m}^2 \text{s}^{-1}$ ) and CICE. The 2100 UTC 18 October forecast is shown, so 2 days and 9 hours in the future.

This is an actual graphic made for the POD briefing, so it includes the cryptic notation. This is the revised 10 km inner nest. The “IB1” marker is near the WA4-5 locations. This was a failed forecast: the Sunday Oct. 18 swell event was not evident at the ship location: see text.

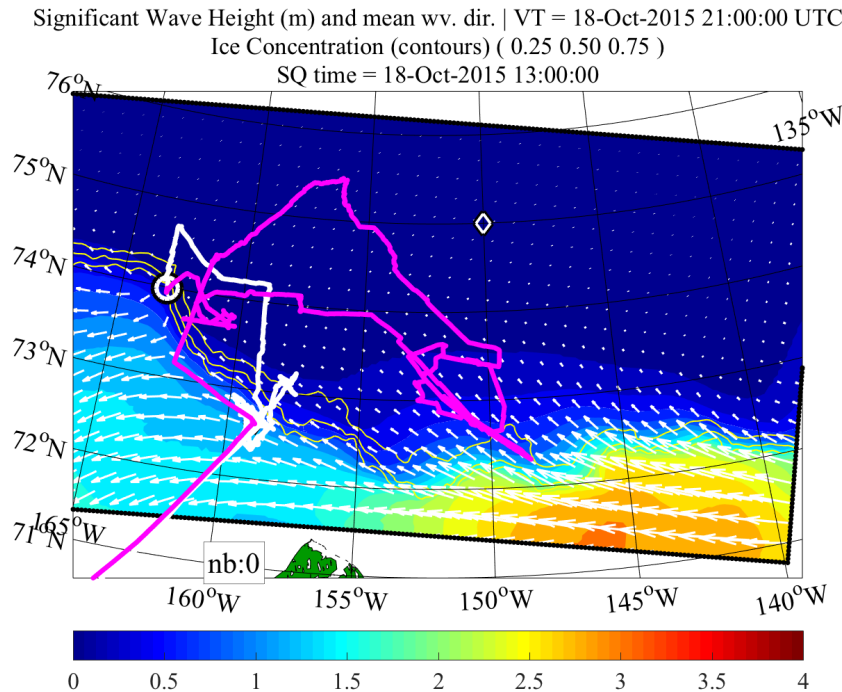


Figure 44. WW3 hindcast of WA4-5, identical to Figure 14 and Figure 16, but showing the time period used in Figure 43, 2100 UTC 18 October. See caption of Figure 7 for explanation of annotation. This is the inner hindcast grid, which is 5 km resolution, in contrast to the 10 km resolution inner grid of the forecast model. It uses the IC4M6H2 routine and 10 km AMSR2 forcing (Section 6.3). The ship position—and approximate position of WA4-5—are shown with the black and white circle. This correctly shows that easterly and southeasterly swells did not reach the ship location: see text.

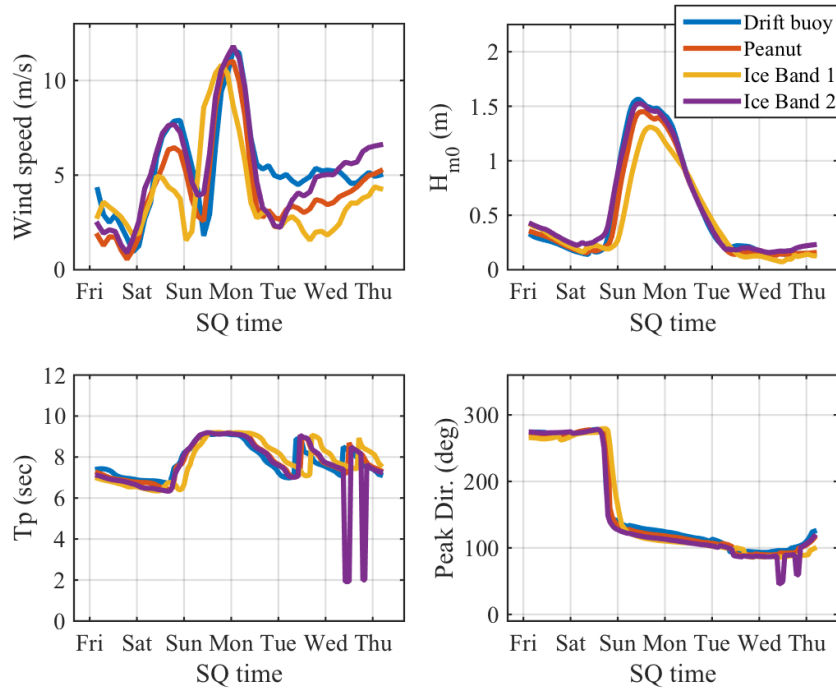


Figure 45. Same as Figure 43, but showing time series plots: WW3 forecast of WA4-5, from the 12Z cycle forecast on Oct. 16; inner grid, using the IC3 module ( $v = 0.1 \text{ m}^2 \text{s}^{-1}$ ); actual graphic made for the POD briefing. The “Ice Band 1” time series is a point near the WA4-5 locations. This was a failed forecast: the Sunday Oct. 18 swell event was not evident at the ship location: see text.

### 3. Overview of ice treatment in WAVEWATCH III®

There are three ways to list the various methods for treating the effects of ice in a wave model. One way is to enumerate the effect that it has on the waves. A second is to separate into physical processes. Third is to list associated routines that have been implemented in WW3. We will start with the first two, and then begin discussion of implementation in WW3 in Section 3.1.

Sea ice can affect waves in the following ways:

- 1) Sea ice can dissipate wave energy. For example, the cyclical bending of a piece of ice can result in internal friction and losses to heat within the ice. Compression of an ice sheet or collision of floes could also lead to internal friction. Also, there can be friction at the ice-water interface which creates turbulence in the water, which is lost as heat in the water. A last example, unique because it is not thermal: collisions of floes produces noise, which also implies loss of energy, though this is likely small.
- 2) Sea ice can change the physical wavelength. Since this implies a change to phase velocity, this can produce refraction in cases where ice is non-uniform along the wave crests, turning the waves. This also implies a change to group velocity, so a process analogous to shoaling or de-shoaling can occur, if ice is non-uniform along the direction of wave propagation. Just as with refraction and shoaling by bathymetry and currents, changes to wave energy can occur. These are kinematic rather than dissipative processes.
- 3) Sea ice can redirect wave energy by scattering and reflection. This does not necessarily imply dissipation of energy, though it can be considered a type of attenuation, since wave energy is decreased along the primary direction of propagation.

Through the following physical properties and mechanisms, sea ice can affect waves:

- 1) Viscous property of the ice layer. This can actually mean one of two things. Either a resolved sheet of ice has a measurable viscosity, or the aggregate behavior of a mix of sea ice and water can behave as a viscous fluid. For example, a slurry of frazil ice, brash ice, and pancakes with patches of open water: here, individual pieces of ice are not resolved by a 100 m or 5 km grid cell, but together have an un-measurable “effective viscosity”. This can also be considered as a way to represent internal friction or hysteresis. The primary impact of viscosity is to cause dissipation of wave energy.
- 2) Elastic property of the ice layer. Again, this may be a measurable or non-measurable “effective” parameter. A purely elastic layer does not produce dissipation. However, it can change the physical wavelength, and in a viscoelastic (VE) model, the elasticity does have an impact on the dissipation rate. In a VE model, elasticity is *not required* to produce changes in the physical wavelength. Also worth noting: energy is “stored” in elasticity as a kind of potential energy, different from the traditional potential energy of waves which is associated with the height of the waves and weight of the water. This implies that waves moving under an elastic ice layer will have lower height than waves with the same energy in open water, so a reduction factor should be applied to model predictions of elevation spectra.
- 3) Mass-loading property of the ice layer. Again, a pure mass-loading model does not produce dissipation, but it can change the physical wavelength.
- 4) Friction at the ice-water interface. Since the ice and the water are not generally moving at the same velocity, there is a shear, and so friction occurs, analogous to waves in non-deep water over a rough seafloor. This can be associated with laminar or turbulent boundary layer.
- 5) Scattering and reflection, already mentioned in the prior list.

One can readily imagine cases where multiple processes co-exist. In fact, this is a theme of the “continuum” model of Wang and Shen (2010), which combines the first three into a single mathematical model. This list is not comprehensive, and the author (ER) does not claim to have expansive knowledge of sea ice mechanics. However, some not listed here are merely subsets. For example, the anelastic or “delayed elastic” model is a special type of visco-elastic model, where the material does not immediately return to its original form when the force is removed.

### 3.1. Ice effects in WW3

The WAVEWATCH III® model (henceforth denoted “WW3”, Tolman 1991, WW3DG 2016) is a phase-averaged model for wind-generated surface gravity waves based on the radiative transfer equation. In this approach, the dependent variable is the wave spectrum (denoted  $E$  for wave energy spectral density or  $N$  for wave action spectral density,  $N=E/\sigma$ ), which is a function of wavenumber or frequency ( $k$  or  $\sigma$ ), direction ( $\theta$ ), space ( $x, y$ ), and time ( $t$ ), with spectral density most commonly defined on frequency and direction. The left hand side of the radiative transfer equation includes terms for time rate of change and propagation in the four dimensions (kinematics), while the right hand side includes source functions (dynamics):

$$\frac{\partial N}{\partial t} + \nabla \cdot \vec{c}N = \frac{S}{\sigma} \quad (1)$$

where  $\vec{c}$  is a four-component vector describing the propagation velocities in  $x$ ,  $y$ ,  $k$ , and  $\theta$ . For example, in absence of currents,  $c_x$  is the  $x$ -component of group velocity  $C_g$ . The sum of all source functions is denoted as  $S$ , and individual source functions are denoted with appropriate

subscript, for example dissipation by whitecapping is  $S_{wc}$ , and dissipation by ice is  $S_{ice}$ . For more detailed description of the model, we refer the reader to WW3DG (2016).

The  $S_{ice}$  source function are scaled by ice concentration. The “open water” source functions in WW3 for input from the wind and dissipation by whitecapping<sup>14</sup> are scaled according the fraction of open water. The source term for four wave nonlinear interactions is not scaled. These treatments represent a major source of uncertainty in the modeling of waves in ice, as discussed at length by Rogers et al. (2016), and this topic—the treatment of the wind input in particular—would benefit from dedicated studies in the field or laboratory.

Source terms in WW3 are activated using “switches” selected at compile time. There is not a one-to-one correspondence between physical processes and these switches. In fact, one of the ice-related switches (IC0) is not actually a source function, some of the switches (IC0, IC1, and IC4) are not physical at all, and there are two switches which represent visco-elastic models (IC3 and IC5). Thus, one should think of these as “code selection” rather than “physics selection”. We start by summarizing the routines in short lists, and follow with more detailed descriptions. Short descriptions are given in the first list:

- IC0 (pre-existing): ice as land or quasi-land, no  $S_{ice}$ .
- IC1: simple  $S_{ice}$  dissipation, no variation with frequency.
- IC2: thin elastic plate, with friction at ice-water interface
- IC3: visco-elastic layer (Wang and Shen)
- IC4: parametric and empirical  $S_{ice}$
- IC5: visco-elastic layer (extended Fox and Squire)
- IS1: simple diffusive scattering
- IS2: scattering based on Meylan and Masson

Next, here is the same list, describing usage of these schemes:

- IC0 (pre-existing): This is used in a) the shore-side WW3 forecasting system during the Sea State cruise, b) the outer grid of the ship-based WW3 forecasting system during the cruise, c) a vast majority of operational WW3 implementations prior to 2016. It is still used by FNMOC (Fleet Numerical Meteorology and Oceanography Center) at time of writing.
- IC1: This is used in a) inversion process by Rogers et al. (2016) and Section 6.2 of this report, and b) for comparative purposes in hindcasts in this report (Section 6.3).
- IC2: The boundary layer dissipation model and Liu et al. (1991) dispersion model in IC2 are used by Ifremer.
- IC3: This was used in a) the inner grid of the ship-based WW3 forecasting system during the cruise, b) hindcasting by Rogers et al. (2016), and c) hindcasting and inversion by Cheng et al. (2017).

---

<sup>14</sup> As far as whitecapping  $S_{ds}$  is concerned, there is a reasonable argument for *not scaling* by open water fraction: instead,  $S_{ds}$  can be left at 100% even with full ice cover, under the presumption that  $S_{ds}$  will likely be zero anyway. The ice cover modifies the spectrum such that it is below the breaking threshold, so  $S_{ds}$  is zero for most (or all) frequencies. This simplification will probably be implemented by the WW3 development team soon.

- IC4: This is used in a) hindcasts in this report (Section 6.3), and b) in ESPC (Earth System Prediction Capability; Metzger et al. 2014) coupled wave modeling:  $1/4^\circ$  and  $1/8^\circ$  global models. The latter is undergoing testing at time of writing.
- IC5: N/A
- IS1: N/A
- IS2: This is used by Ifremer.

Next is the list with notable references. These pertain to uses in WW3, not the source material such as Wang and Shen (2010). Source material for the routines are noted in following sections.

- IC0: Tolman (2003); WW3 version 2 User's Manual (Tolman 2002).
- IC1: Rogers and Orzech (2013); WW3 version 4 User's Manual (Tolman et al. 2014).
- IC2: Liu et al. (1991) dispersion model: Rogers and Orzech (2013) and WW3 version 4 User's Manual (Tolman et al. 2014). Boundary layer dissipation model: Stopa et al. (2016).
- IC3: Rogers and Zieger (2014), WW3 version 4 User's Manual (Tolman et al. 2014), Li et al. (2015), Rogers et al. (2016), Cheng et al. (2017)
- IC4: WW3 version 5 User's Manual (WW3DG 2016), Collins and Rogers (2017)
- IC5: N/A
- IS1: WW3 version 5 User's Manual (WW3DG 2016)
- IS2: WW3 version 5 User's Manual (WW3DG 2016), Ardhuin et al. (2016)

The implementation of IC1 and IC2 in WW3 by Rogers and Orzech (2013) was a first for WW3, but not for wave models in general. A source term was implemented in ECWAM by Doble and Bidlot (2013), published in the same year. The concept was earlier proposed by Masson and LeBlond (1989), Masson (1994), and Perrie and Hu (1996).

### 3.1.1. Switch “IC0”

IC0 is based on Tolman (2003) and it predates the use of  $S_{ice}$  in WAM and WW3. In early versions of WAM and WW3 (e.g. WW3 version 1; Tolman 1997), the model was designed such that ice concentration could be ingested, and if the concentration exceeded some threshold (e.g. 50%), the grid cell was deactivated (treated as land). Below the threshold, the grid cell was treated as open water. In WW3 version 2 (circa 2002), the Tolman (2003) scheme was implemented, which optionally instructs the model to use partial transmission for intermediate ice coverage (e.g. 25% to 75%). This scheme, known as the “continuous treatment” was also used in version 3 (circa 2009). It was not known as “IC0” in those versions. The IC0 designation was added in version 4 (circa 2014), to distinguish it from the other options (IC1, IC2, IC3) which appeared for the first time in version 4.

The “continuous treatment” in versions 2 and 3 of WW3 had unintentional behavior (i.e. a bug): there were situations in which one could double the resolution, and the “partial blocking” *per grid cell* stayed the same, resulting in a strongly resolution-dependent outcome. This bug was corrected in version 4, at the same time that it gained the label “IC0”.

IC0 removes wave energy by partial blocking during the propagation. This makes it different from all other ICx switches, which act on the model via the model source terms. The removal of

wave energy is not frequency-dependent: this is probably the most serious shortcoming of IC0. However, it is noted that IC1, and IC4 sub-method #4 (“IC4M4”) shares this shortcoming.

The supporting argument for the simplistic treatment of ice circa 1997-2012 was to the effect that “to represent ice properly, one must implement something extremely complicated and impractical”. The complicated model in question was that of Masson and LeBlond (1989), which was the reference of choice for dissipation by sea ice in the WAM community for many years (e.g. Komen et al. 1994). This argument had two flaws. First, it was incorrect to imply that this is the only way to represent ice in a WAM-type model. We already had a counter-example: the simplistic treatment of dissipation by bottom friction, which existed despite the acknowledged complexity and heterogeneity of wave-seafloor interaction. Second, we now know that the scattering mechanism treated by Masson and LeBlond (1989) plays only a secondary role in many situations in the real ocean. It can be important, but it is not sufficient on its own.<sup>15</sup>

IC0 does have one notable advantage: the disabling of grid cells associated with high ice concentration implies faster computations than all other ICx switches. However, this comes with the caveat that the parallelization of WW3 does not work optimally with the deactivating and reactivating of grid cells, meaning that there is a scaling penalty, so there is not a 1:1 correspondence between the number of grid cells deactivated and computational speed-up.

### 3.1.2. Switch “IC1”

IC1 was the first  $S_{ice}$  source function in WW3, implemented by Rogers and Orzech (2013). In this source term, the user provides the exponential attenuation rate for wave amplitude with distance,  $k_i$ . In all ICx source functions,  $k_i$  in WW3 is related to the exponential attenuation rate for wave energy with distance,  $\alpha = 2k_i$ , and is related to the temporal decay rate of energy  $D_{ice}$  by  $D_{ice} = -2C_g k_i$ , and to  $S_{ice}$  by  $S_{ice} = D_{ice} E$ , where  $E$  is energy spectral density. To summarize:

$$D_{ice} = \frac{S_{ice}}{E} = -C_g \alpha = -2C_g k_i$$

The above equation is used for calculation of dissipation by sea ice in IC1, IC3, IC4, and IC5. The boundary layer model of IC2 is the exception, since  $k_i$  is not explicitly calculated.

The  $k_i$  values referenced in this report may seem rather abstract, in the context of what is a high dissipation rate vs. a low dissipation rate. Table 1 puts this in a physical context: the distance required to reduce a wave to half of its original height.

Table 1. Amplitude attenuation rate, and the implied distance over which the waveheight is decreased to 50% of its original value. This table provides a convenient reference for the physical meaning of  $k_i$  values used in this report.

$k_i$ (1/m)	$x$ (km)
2.00e-06	347
4.00e-06	173
8.00e-06	86.6

<sup>15</sup> The wave-ice interaction problem has definite attractions for the applied mathematics community, particularly the scattering mechanism, with its opportunities for performing elegant mathematics after simplifying assumptions are made. However, we should be mindful of disconnects between idealized scenarios being modeled and the complexity of sea ice in the real ocean.

1.60e-05	43.3
3.20e-05	21.7
6.40e-05	10.8
1.28e-04	5.42
2.56e-04	2.71
5.12e-04	1.35
1.02e-03	0.68
2.05e-03	0.34
4.10e-03	0.17

In IC1,  $C_g$  is simply from traditional ice-free (open water) linear dispersion. As noted above, IC1 has the severe defect of being independent of frequency.

Within the “intermediate” values of ice coverage in IC0 (e.g. 25% to 75% coverage, if these thresholds are selected by the user), the practical outcome of IC0 after the aforementioned IC0 bug fix is not very different from that of IC1. However, with IC1, low concentrations are not treated as open water, and high concentrations are not treated as land. Note that even with  $k_i = 0$  and ice concentration  $a_{ice} > 0$ , ice will still affect waves in IC1 via the impact on the open water source functions.

### 3.1.3. Switch “IC2”

IC2 was the second of the two new source functions implemented by Rogers and Orzech (2013). This is based on the method of Liu and Mollo-Christensen (1988) and Liu et al. (1991), henceforth “LMC” and “LHV”. In open water, WW3 is modeling gravity waves, meaning that the restoring force is gravity. In the LHV model, and the viscoelastic (VE) model of IC3 and IC5, the restoring force is gravity and the elasticity of the ice, so it is modeling “flexural gravity waves”. LHV offer a new dispersion relation, to provide an ice-modified wavenumber  $k_r$ , where  $k = k_r + ik_i$ . This elastic model accounts for effects of bending forces and inertia, but does not produce dissipation. LMC therefore added a phenomenological “eddy viscosity” to their model so that it would produce dissipation, based on the argument of turbulent eddies generated by roughness at the ice-water interface.

The new dispersion relation was coded by Rogers and Orzech (2013), but was never really exercised by NRL. Originally, the intent was to use it to produce refraction and shoaling by ice, but attention shifted to IC3, and so NRL work on these effects was done in IC3. Thus, for practical purposes, NRL only exercised the dissipation effect of IC2, which is ironic considering that the dissipation was only added as an afterthought by LMC. In truth, this eddy viscosity concept is unsatisfactory because the scales of wave motion are comparable to the scales of turbulent eddies. Further, the degree of variation of input parameter(s) is a concern if our objective is to select suitable value(s) for use in a forecast model. The eddy viscosity  $\nu_e$  example values given by LMC show a wide range of values. Dissipation depends on  $\nu_e^{0.5}$ , and  $\nu_e^{0.5}$  variation is up to factor 29 in these examples. Though to be fair, similar concern exists for other methods of predicting  $S_{ice}$ .

With NRL focusing on IC3, the IC2 routine was essentially abandoned until it was picked up again by Dr. Fabrice Ardhuin (Ifremer), who implemented a boundary layer model to replace the unsatisfactory eddy viscosity model. The boundary layer model is analogous to the boundary

layer at the seafloor in finite depth, and accounts for both laminar and turbulent flow regimes. This is described in an appendix of Stopa et al. (2016), and the WW3 manual. Unlike most other  $S_{ice}$  functions in WW3, the IC2 boundary layer model yields nonlinear dissipation, i.e. it depends on wave amplitude. The boundary layer model has a large number of free parameters associated with it, but it is this author's impression they will be treated as fixed parameters by most users, much like the free parameters of the whitecapping source function. The boundary layer model, unlike the IC2 based on Liu et al., is non-dispersive: it does not predict modification of the wavelength or group velocity due to ice.

In 2016, Ifremer also extended WW3 to incorporate the refraction and shoaling effects using the IC2 dispersion relation originally coded by NRL. We do not have first-hand experience with this feature: the reader is referred to the “ww3\_tic2.3” regression test provided with the WW3 code distribution. Primary inputs are ice concentration and thickness.

### 3.1.4. Switch “IC3”

IC3 is based on the model of Wang and Shen (2010). It is a viscoelastic (VE) model, combining the effects of elasticity, viscosity, and mass loading. It is calculated by solving a dispersion relation, yielding a wavenumber which is a complex number. The real part of the wavenumber provides information to produce refraction and shoaling by ice. The imaginary part of the complex wavenumber provides the dissipation rate  $k_i$ . The group velocity in ice is calculated using the same relation that holds true in open water:

$$C_g \equiv \frac{\partial \omega}{\partial k}$$

In WW3, only the real part of the wavenumber is used in this calculation, so the group velocity is also a real number. However, in dissipative mediums,  $C_g$  is complex, and the imaginary part is associated with the drift in  $C_g$  for a wave packet which is experiencing frequency-dependent dissipation, see Dixon et al. (1998).

The user decides whether to enable the effects of ice on group velocity, to produce the shoaling effect. In usual applications, this is not enabled, since WW3 has conditionally stable propagation and so a large increase to group velocity can result in instability. The refraction effect is activated using the code switch “REFRX”. No code has been implemented yet to scale by ice concentration the impact of ice on the real part of the wavenumber or the group velocity. Admittedly, it is intuitive that refraction and shoaling by ice should be different for cases of 1% vs. 99% concentration.

In the real ocean, the impact of sea ice on the real part of the wavenumber is difficult to detect (e.g. Cheng et al. 2017). Thus, incorporation of these effects in models remains rather academic. Idealized examples are provided with the regression tests that come with the WW3 code distribution. By contrast, the dissipation of wave energy by interaction with sea ice is readily apparent in the real ocean. As such, most efforts to date have focused on the dissipation and attenuation problems, rather than the refraction and shoaling effects.

Inputs to the VE models are ice concentration, thickness, density, viscosity, and elasticity. The concentration is not used when solving the dispersion relation, but is just used to scale the

dissipation. For cases of zero elasticity, the model solution should be the same as that of Keller (1998).

One crucial point must be made about VE models. The two free parameters, associated with viscosity and elasticity, though they might be measured for synthetic sheets used to represent ice in lab experiments are *not measurable in the real ocean*. Instead they are *effective parameters*. They represent the aggregate effect of sea ice which may be highly variable within a model grid cell, which could be as large as 34 km  $\times$  34 km in a coarse global model. This is analogous to using a probability density function (PDF) to represent floe sizes (the floe size distribution, or FSD), or a spectrum to represent waves. Determination of these two parameters is a challenge. Cheng et al. (2017) estimate  $k_i(f)$  using observational data and then look for the best fit of the Wang and Shen model (IC3) to these profiles, thus determining the two free rheological parameters via inversion.

The IC3 dispersion relation calculation results in multiple solutions or “modes” which must be selected using some internal logic (e.g. least dissipative, most dissipative, or wavenumber closest to that of open water). IC3 in WW3 exhibits erratic mode selection, which results in irregular profiles of  $k_i(f)$ , e.g. Mosig et al. (2015), Rogers et al. (2016). This issue is evidently possible to resolve; see the profiles of Cheng et al. (2017).

### 3.1.5. Switch “IC4”

The IC4 option, implemented by Collins and Rogers (2017), allows a user to select from a list of parametric and empirical source functions. The methods are as follows:

- IC4M1, a new regression fit to the data in the seminal work of Wadhams et al. (1988)
- IC4M2, a flexible polynomial in the form of  $\alpha = C_0 + C_1f + C_2f^2 + C_3f^3 + C_4f^4$ , where the coefficients are user-defined. An example is provided with WW3 for the case of the Meylan et al. (2014) polynomial.
- IC4M3, from Horvat and Tziperman (2015), which uses quadratic polynomials that depend on frequency  $f$  and ice thickness  $h_{ice}$ .
- IC4M4, from Kohout et al. (2014), which is nonlinear, depending on wave height, but does not vary with wave frequency.
- IC4M5, a step function with up to 4 steps. The step function can be spatially or temporally varying.
- IC4M6, a step function with up to 10 steps. The step function is stationary and uniform for the simulation.
- IC4M7 (added after Collins and Rogers (2017) was published). This is based on the monomial expression of Doble et al. (2015). Like IC4M3, it depends on frequency  $f$  and ice thickness  $h_{ice}$ .

The idea behind the step function sub-methods IC4M5 and IC4M6 is to allow direct use of  $k_i(f)$  profiles that come from data inversion analyses. In the author’s experience, these analyses are performed for discrete frequency bins which are significantly coarser than that of the model or observed spectra. For example, model spectra typically have 25 to 35 frequency bins. The 4 to 10 coarser frequency bins used in the inversion analyses results in smoother  $k_i(f)$  profiles and appropriately reflect the inexact nature of the inversion. As such, the 10 steps of IC4M6 are

sufficient to represent the coarse spectral bins used in the inversion. Inversion is presented in Section 6.2 and hindcasts with IC4M6 are presented in Section 6.3.

### 3.1.6. Switch “IC5”

IC5 is a second viscoelastic (VE) model, using the “Extended Fox and Squire” (EFS) model described in Mosig et al. (2015). The latter authors argued that the EFS model is superior to IC3 on the grounds that it is mathematically simpler (see discussion of the mode selection problem above). However, they simultaneously—and incongruously—expressed reservations about the use of any VE model. Mosig et al. use unrestricted rheology parameters, saying that since the parameters are *effective* and not *real*, “...no restrictions on the acceptable values of the rheological parameters, except positiveness, can be imposed.” In fact, one concern we have about the EFS model is that, when adjusting the parameters to match observation-based  $k_i(f)$  profiles, it may be necessary to use high elasticity, comparable to that of titanium or steel. Mosig et al. (2015) use modulus of elasticity  $G=4.9e+12$  Pa to match Meylan et al. (2014); that is 4900 GPa. Typical modulus values for titanium and annealed steel are 120 and 190 GPa, respectively.

Notwithstanding these concerns, we implemented the EFS model in WW3 as IC5, based on the feeling that the model’s simplicity would make it easy to implement, and that it would provide an interesting alternative to the more complex IC3. The work was performed by Dr. Qingxiang Liu of the University of Melbourne, with funding from the ONR Sea State DRI. A paper led by Dr. Liu is in preparation.

### 3.1.7. Switch “IS1”

Whereas “ICx” switches are used for dissipation (and/or refraction and shoaling) by ice “ISx” switches are for scattering by ice. Either dissipation or scattering will produce attenuation of wave energy, i.e. a reduction of wave energy along the primary axis of propagation. However, dissipation is non-conservative (energy is lost to heat, etc.) while scattering is conservative: energy is just redistributed within the spectrum, comparable to what happens with four-wave nonlinear interactions.

IS1 (WW3DG 2016) is a simple diffusive scattering model, where the user specifies the diffusion and scattering coefficients. This was implemented by Dr. Stefan Zieger, while he was working as a contractor for NRL, via the University of Southern Mississippi, with funding from the ONR Sea State DRI.

### 3.1.8. Switch “IS2”

IS2 is a much more physics-based form of scattering, based on the theoretical/mathematical work of Meylan and Masson (2006). The IS2 routine was coded entirely by Ifremer, funded (at least partially) by the ONR Sea State DRI. Over time, the routine has expanded to include things which are not scattering, but are just included for reasons of convenience, to permit easier coupling within WW3:

- 1) Floe size distribution estimate and floe-breaking routine was included
- 2) The dispersion model of IC2 was merged into IS2. The reader is referred to the “ww3\_tic2.3” regression test provided with the WW3 code distribution

3) A “creep” dissipation model was added by Arduin et al. (2016). This was to provide a desired behavior: “nonlinear dissipation that yields a fast decrease in wave height near the ice edge, turning into a much slower decay at larger distances, e.g., between 1000 and 1500 km for a wave period  $T = 25$  s”, which was presumably not provided by the IC2 boundary layer dissipation, since that predicts a laminar regime near the ice edge, implying that dissipation is too small: “Average dissipation rates are consistent with creep effects but are 12 times those expected for a laminar boundary layer under a smooth solid ice plate.” Though this model may produce the desired effect, we are concerned about the underlying physics. Creep is associated with slow deformation under constant loading (e.g. flow of glaciers), not the fast, cyclical loading associated with waves. Arduin et al. (2016) cite the work of Cole et al. (1998), who present both creep (constant load) experiments and cyclic loading experiments. In the Cole et al. (1998) model of cyclic loading, they separate strain into elastic, viscous, and anelastic<sup>16</sup> components. Their *viscous strain* term for cyclic loading includes a “creep parameter”, so named because it was measured in the lab using creep experiments (stationary loading). The Cole model is best categorized as viscoelastic or visco/elastic/anelastic.

The reader is referred to WW3DG (2016) for description of IS2 and these three additional effects.

### 3.1.9. Discussion

#### *Switch/parameterization usage herein*

In this report, we use IC2 and IC4M6 in hindcasts. The flawed (uniform in frequency) IC0 and IC1 are also used to provide comparison. Simple comparisons of  $k_i(f)$  to other models (e.g. IC3, IC4M7) are made in Section 6.2.4, but hindcasts are not performed with them. IC3 hindcasts for the Sea State case can be found in Cheng et al. (2017). IC5 hindcasts for WA3 will be presented in another paper, which is in preparation (Liu et al.).

#### *Simultaneous switches*

As discussed above, WW3 is designed so that switches (e.g. IC1) activate particular source term parameterizations. The compile scripts presently require that exactly one ICx switch be activated. The ICx routine can act simultaneously with an ISx routine. However, it is not presently possible to activate a VE model (e.g. IC3) and a boundary layer model (IC2) at the same time. Originally, this design was sensible: it would not have made any sense to use the dispersion model of Liu et al. (the original IC2) together with the dispersion model of IC3, because that would be redundant and would result in ambiguity regarding which wavelength and group velocity to use. However, as things have evolved, IC3 is a dispersive VE model and IC2 can be used as a non-dispersive boundary layer model. Thus, there is no problem, in principle, with using them together.

Physically, this is also plausible: in context of dissipation, one predicts dissipation within the ice (e.g. by hysteresis) and the other predicts dissipation below the ice. In the real ocean, these two things can co-exist, and simultaneous calculation was the intent of the Sea State group from the beginning (see page 36 of the Science Plan, Thomson et al. (2013)). And in fact, this is already done by Ifremer when they combine the IC2 boundary layer model, the IC2 (Liu et al.)

---

<sup>16</sup> Anelastic behavior is like elastic behavior, but has a delayed recovery when the stress is removed. In an elastic material, the recovery is immediate.

dispersion calculation, with IS2 which has been supplemented with viscous dissipation (hysteresis). This should be a priority for future work: testing simultaneous use of IC2 and IC3.

#### *Selection of switches by future users*

Users of WW3 are required to select a switch to activate at compile time, since there are no “default physics”, so inevitably, a question arises: “What ICx, ISx switches should I use?”. It is beyond the scope of this report to compare and contrast in detail, but to illustrate the thought process, we compare IC3 and IC4 here:

- 1) Mathematically, IC3 is complex and IC4 is simple. However, both are fast, so computation time is not a significant concern. The mathematical complexity is invisible to a user and therefore also not necessarily a concern.
- 2) IC3 provides an entire  $k_i(f)$  profile with only two free parameters, viscosity and elasticity. This is convenient for a user. (Ice concentration, thickness, and density are required input variables but are physically measurable and not considered as freely adjustable parameters.)
- 3) Though the IC3 rheology parameters determine  $k_i(f)$ , the shape of  $k_i(f)$  is restricted. Thus, it can be difficult to find a close fit to observed  $k_i(f)$ : see, for example Figure S14b in the Supporting Information of Cheng et al. (2017). IC4 allows any shape of  $k_i(f)$ .
- 4) IC3 predicts the effect of sea ice on wave length and group velocity. IC4 does not: it is non-dispersive. As noted already, the effect on wave length and group velocity is difficult to detect in the real ocean, while the dissipative effects are unambiguously significant. IC4 prioritizes the latter, while IC3 is more complete.
- 5) Deciding on user input can be difficult with either, even in the optimistic scenario where the user has knowledge of the ice type, and how it varies within the model domain. In case of IC3, the two free rheology parameters are not known a priori, though some guidance may be found in the literature for specific examples if the ice type is known (e.g. Newyear and Martin 1999, Cheng et al. 2017, Rabault et al. 2017). In case of IC4, a  $k_i(f)$  function that is appropriate for one ice type is likely not appropriate for another ice type.

### 3.2. The role of numerical error

#### 3.2.1. Removal of $S_{ice}$ from dynamic time stepping

WW3 uses dynamic time stepping, such that the time step for source term integration is reduced to provide more accurate calculations when the source term is large. IC3 often results in very strong dissipation of higher frequencies (e.g. Figure 100), which would normally result in very slow computations in WW3 version 4 when IC3 was used. This was first addressed by applying a user-defined limiter to  $k_i$ . However, in WW3 version 5, Ifremer removed the ice source functions from the dynamic time stepping, which made the limiter unnecessary. This is implemented by replacing the operation within the dynamic integration:

$$S_2 = S_1 + S_{ice} a_{ice}$$

with the operation outside the dynamic integration:

$$E_2 = E_1 \exp (a_{ice} D_{ice} \Delta t_g)$$

where  $S_1$  and  $S_2$  are the source term total before and after adding the ice source term;  $E_1$  and  $E_2$  are the energy level before and after adjusting for the dissipation by sea ice; and  $\Delta t_g$  is the

“global time step”, i.e. the time step outside the dynamic source term integration. The new method is exact if no other source terms are active. The drawback is that the new method will less accurately account for the dynamic coupling between  $S_{ice}$  and other source functions, e.g. four-wave nonlinear interactions. At time of writing, no attempt has been made to quantify this penalty.

### 3.2.2. Error from spatial discretization (resolution effects)

The piece-wise integration used by numerical models like WW3 can introduce numerical error, as it deviates from continuous integration. This was already investigated by Rogers and Orzech (2013) but it is worthwhile to reevaluate the error, since the ice source terms are now outside the dynamic time stepping. In the following, only the ice source function is active, so interplay between simultaneous source terms is not evaluated. The IC1 function is used. The incident wave condition is a narrow 10 second swell of 1 m significant waveheight. It is a 1-d test case (propagation along a single axis).

WW3 uses split time stepping, such that propagation and source terms are integrated separately in an alternating sequence. One of the two integrations is performed until a specific time is reached, at which point the other integration is performed. The hand-off is performed at an interval known as a “global time step”. Thus, in WW3, four time-step sizes are specified:

- 1) The global time step, at which forcing is updated and output is performed
- 2) The geographic propagation time step, solved fractionally until the global time step is reached
- 3) The intra-spectral propagation time step, which is not of interest here.
- 4) The source term time step, solved fractionally until the global time step is reached

This brief description overlooks some features, e.g. the automatic scaling of (2) according to group velocity, and the dynamic sizing of (4), and the possibility for time step (2) to be larger than (1). A detailed description can be found in WW3DG (2016).

An analytical solution is used as ground truth, simply:

$$H(x) = H_0 e^{-k_i x}$$

which follows from

$$\eta(x, t) = \text{Re}[a e^{i(kx - \sigma t)}]$$

where  $\text{Re}[\cdot]$  denotes real component,  $H$  is waveheight,  $a$  is half the wave height, and  $\eta(x, t)$  is the free surface.

Figure 46 shows the results from one set of tests. Two grid spacings are shown:

- 1) In green,  $\Delta x = 1$  km spacing, with time steps 1 through 4 of 60/60/60/6 (in seconds)
- 2) In blue,  $\Delta x = 5$  km spacing, with time steps of 900/225/450/25. This matches the resolution and time steps of the hindcast on the inner grid in Section 6.1.

Four  $k_i$  values are tested using IC1. From top to bottom (least to most dissipative), they are 6e-6, 1e-5, 5e-5 and 5e-4  $\text{m}^{-1}$ . These results indicate minimal error associated with the 5 km resolution.

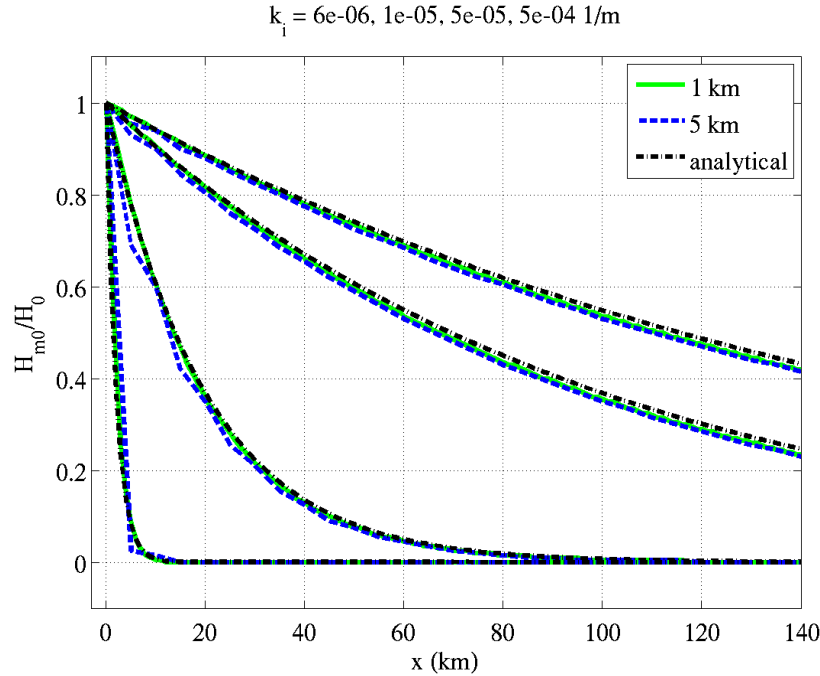


Figure 46. Waveheight (normalized by incident waveheight) vs. distance along axis for 1-D test case. The four groupings, top to bottom are  $k_i=6e-6$ ,  $1e-5$ ,  $5e-5$ , and  $5e-4 \text{ m}^{-1}$  respectively. Green:  $\Delta x = 1 \text{ km}$ ; Blue:  $\Delta x = 5 \text{ km}$ ; Black: analytical (true) solution.

A second set of tests is shown in Figure 47. All tests use the  $\Delta x = 5 \text{ km}$  spacing of the WW3 hindcasts, for which the time step sizes given above still apply. This time, we are looking at a smaller distance (50 km instead of 140 km) and a different set of  $k_i$  values:  $1e-5$ ,  $1e-4$ , and  $1e-3 \text{ m}^{-1}$ . This comparison reveals something interesting: when dissipation is weak, the discretization is sufficient to resolve the changes; when the dissipation is strong, the energy drops to zero quickly, so there is nothing to model, and again, the 5 km resolution is sufficient; but in the intermediate range of dissipation, this is where the discretization error is a problem. As will be shown later, the irregularity of the  $k_i=1e-4 \text{ m}^{-1}$  profile (in green) is associated with the split time stepping.

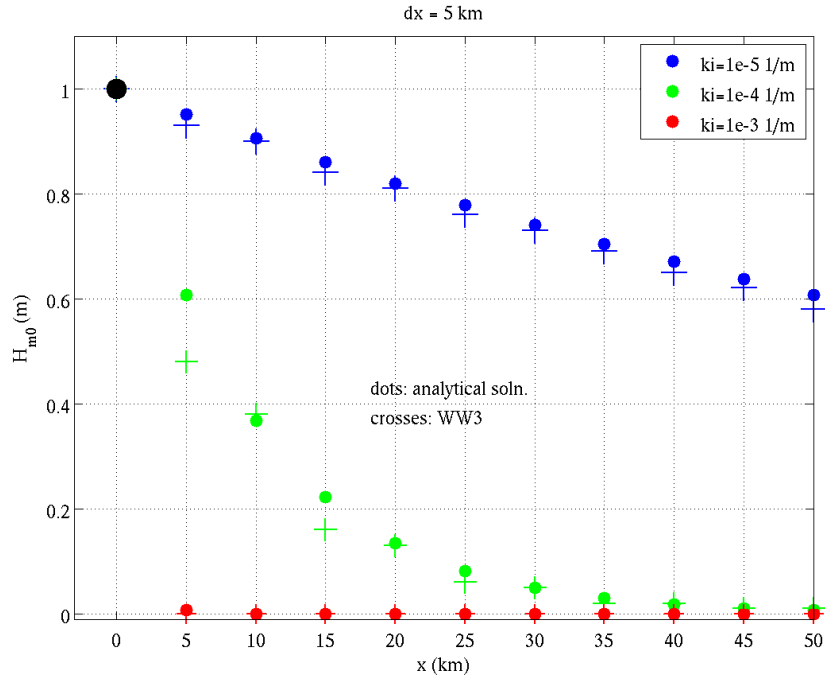


Figure 47. Waveheight vs. distance for 1-D test cases with  $\Delta x = 5$  km. The dissipation rates are indicated in the legend. Dots are the analytical (true) solution and crosses are WW3 results.

The third set of tests is shown in Figure 48. All tests are with the intermediate dissipation rate of  $k_i=1e-4 \text{ m}^{-1}$ . Even with  $\Delta x = 1$  km, the model is biased slightly low, but this can be corrected by changing the time steps from 180/45/90/5 to 45/45/45/45 seconds.

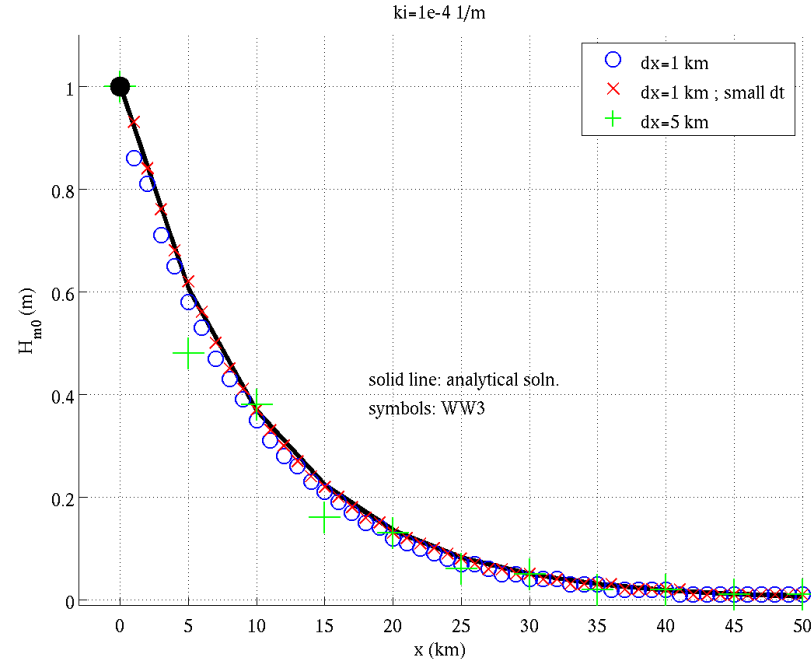


Figure 48. Waveheight vs. distance for 1-D test case with  $k=1e-4 \text{ m}^{-1}$ . Blue:  $\Delta x = 1$  km and  $\Delta t_g = 180$  s; Red:  $\Delta x = 1$  km and  $\Delta t_g = 45$  s; Black:  $\Delta x = 5$  km and  $\Delta t_g = 900$  s. (Here,  $\Delta t_g$  refers to the largest model time step, a.k.a the “global” time step.) The dissipation rates are indicated in the legend. Solid line is the analytical (true) solution and symbols are WW3 results.

A fourth set of tests is given in Figure 49. All tests are with  $k_i = 1e-4 \text{ m}^{-1}$  and  $\Delta x = 5 \text{ km}$ . This figure clarifies the cause of the irregularity seen in the  $k_i = 1e-4 \text{ m}^{-1}$  case (green crosses) of Figure 47. The irregularity can be removed by adopting smaller time step, but a positive bias remains, associated with the geographic discretization error.

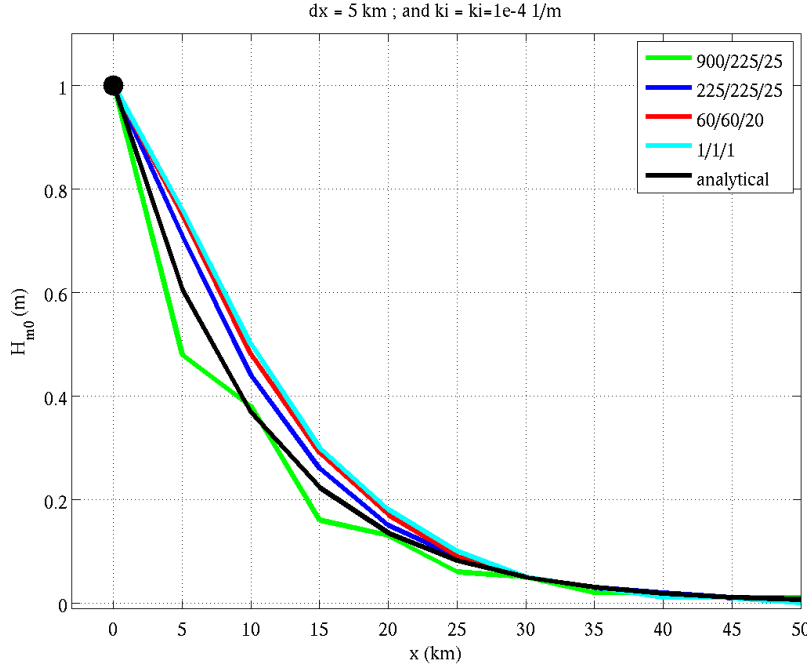


Figure 49. Waveheight vs. distance for 1-D test case with  $k_i=1e-4 \text{ m}^{-1}$  and  $\Delta x = 5 \text{ km}$ . Time steps in seconds are indicated in the legend as three numbers: 1) global  $\Delta t$ , 2)  $\Delta t$  for geographic propagation, and 3) minimum  $\Delta t$  for source terms. Solid black line is the analytical (true) solution.

#### 4. Evaluation of ice forcing

In this section, we discuss the topic of ice forcing for WW3, and what it implies for the accuracy of WW3. One important factor to keep in mind is that WW3 requires *gridded input*. Some ice products are provided as shape files defining ice edge as line segments, for example, but since this is not a gridded product, it is not directly usable by WW3.

##### 4.1. Ice concentration forcing

There are many potential sources for gridded fields of ice concentration,  $a_{ice}$ . We provide a short summary and follow with detailed descriptions of selected products:

- 1) Two types of analyses provided with FNMOC atmospheric model fields. Fields from these sources were provided to the ship for forcing the outer grid of the on-ship WW3 forecasting, via the U. Victoria ftp site. These are based on the satellite passive microwave radiometer product SSM/I (special sensor microwave/imager):
  - a. Analyses provided with the FNMOC NAVGEM (Hogan et al. 2014),  $0.5^\circ$  resolution.
  - b. Analyses provided with FNMOC COAMPS (Hodur 1997), on a 16-km resolution Arctic grid.
- 2) Four implementations of CICE (Hunke et al. 2015) run by the Navy. The data assimilation of these systems ingest fields from the NIC's (National Ice Center's) IMS

(Interactive Multisensor Snow and Ice Mapping System) “ice” vs. “no ice” mask via data assimilation (DA):

- a. A 2-km implementation of CICE, run by David Hebert (NRLSSC) in realtime during the Sea State field experiment. Fields from this were provided to the ship for forcing the inner grid of the on-ship WW3 forecasting, via the U. Victoria ftp site. WW3 simulations with this forcing are not evaluated in this report, since this report focuses on WW3 hindcasts, rather than the realtime WW3 forecasts.
- b. ACNFS (Arctic Cap Nowcast/Forecast System, Posey et al. 2010). This is a realtime 1/12° ice forecast system with products for the Arctic region only, with resolution of approximately 3.5 km in the region of interest. It was replaced as the Navy’s operational system by Global Ocean Forecast System (GOFS 3.1) (Metzger et al. 2017) on 1 October 2017. ACNFS products were used for WW3 hindcasts of 2012-2014. During the 2015 Sea State DRI fieldwork, the ACNFS product was available, but was not used for forecasts or hindcasts of waves, since the 2 km CICE was available.
- c. GOFS 3.1 realtime. This is the Navy’s global ocean/ice system with resolution comparable to that of ACNFS. DA ingests yesterday’s IMS field for today’s analysis, since that is when they are available to the realtime system. WW3 simulations with this forcing are evaluated in this report.
- d. GOFS 3.1 reanalysis. This is like the realtime product, except that the DA ingests today’s IMS field for today’s analysis, since all IMS fields are available in this historical/hindcast run. WW3 simulations with this forcing are also evaluated in this report.

3) Three products based on AMSR2 (Section 4.1.2), which is passive microwave satellite product like SSM/I, but is available at higher resolution than SSM/I.

- a. AMSR2 3.125 km 24-hourly with ASI algorithm (see Section 4.1.2)
- b. AMSR2 3.125 km 12-hourly with ASI algorithm
- c. AMSR2 10 km with NRT algorithm (see Section 4.1.2)

4) Other atmospheric products exist which are publicly available, but were not used here. Examples include CFSR and CFSv2 (NOAA/UCAR Climate Forecast System Reanalysis and Climate Forecast System Version 2) and ERA (analysis and reanalysis by the European Center for Medium-range Weather Forecasts).

#### 4.1.1. Description: Navy CICE implementations

As noted above, for the western Arctic in autumn 2015, there are four Navy implementations of the CICE model available. They all share a common feature, that they ingest information from IMS (Interactive Multisensor Snow and Ice Mapping System, Helffrich et al. (2007)<sup>17</sup>) via DA. IMS is described in the context of assimilation into ACNFS by Hebert et al. (2015), and in the context of assimilation into ACNFS and GOFS 3.1 by Posey et al. (2015).

A key feature of IMS is that it includes ice mask information derived from National Ice Center (NIC) analyses. Typically, meteorological and oceanographic models utilize analysis fields of ice

---

<sup>17</sup> IMS was preceded by a similar product, Multisensor Analyzed Sea Ice Extent (MASIE), produced by the National Snow and Ice Data Center (NSIDC).

concentration from passive microwave radiometer, e.g. SSM/I and AMSR2. The NIC analysis uses this data, but also utilizes visible/infrared imagery (e.g. VIIRS, MODIS) and Synthetic Aperture Radar (SAR, e.g. RADARSAT-2). Thus, by ingesting IMS via their DA, the Navy CICE implementations are indirectly bringing in data from products that are of much higher resolution and higher quality than passive microwave data which are traditionally used. The DA used by Navy CICE implementations for 2015 forced the model to conform closely to IMS; this has been relaxed since. Some important points about these products are:

- IMS is an ice mask. As such, it does not provide quantification of ice concentration, in contrast to passive microwave products, which do.
- IMS relies on a NIC ice analysis. A human analyst uses all available imagery—as well as other data types—to produce information used to create the daily IMS. This implies three negative factors 1) its availability may be delayed, relative to automatically generated products, 2) it is a subjective process: a different analyst may have a different opinion when looking at the same data, and 3) human blunders can affect the product in unpredictable ways. However, it also implies a significant benefit: an expert is able to review the many different data products and decide which is best to rely upon, thus giving a way to exploit strengths and circumvent weaknesses of the various products.
- The visible/infrared imagery and SAR data have obvious advantages over passive microwave because of generally higher resolution.
- Passive microwave data has a particular disadvantage: melt ponds on ice appear as open water. Also, these instruments may misidentify any ice with a wet surface (e.g. frazil ice) as open water (M. Doble, personal communication). These tend to be greater problems in the summer. Thus, we suggest to not use passive microwave to force WW3 in hindcasts of summer months. In the autumn, melt ponds are not a major issue. The “wet ice” problem likely still occurs in the autumn, but it will not be as severe then.
- Visible/infrared imagery cannot see through clouds. This problem can be overcome by combining multiple images: exploiting the gaps between clouds and the fact that ice tends to be more stationary, relative to the clouds.
- Revisit time, swath width (or footprint), and resolution is of course different for different satellite products. Even among specific data types (e.g. SAR), and specific instruments (e.g. TerraSAR-X), there is significant variation.

So, one can readily see that different products have different advantages and disadvantages. However, it is not an exaggeration to say that assimilation of IMS is a game-changer insofar as it brings in information from so many data sources, rather than relying on one product.

As will be shown below, the CICE/IMS gridded products were clearly superior during the later summer period just prior to the Sea State cruise. Thus, at the beginning of the cruise, the fields from CICE were used to force WW3 with much enthusiasm and confidence. Unfortunately, as will also be shown, the quality of IMS turned out to be disappointing during the period of the cruise. This appears to have been associated with analyst error.

#### 4.1.2. Description: AMSR2 gridded products

AMSR2 (Advanced Microwave Scanning Radiometer 2) is on a satellite of the Japanese space agency, JAXA, which provides the calibrated brightness temperature data. As mentioned above, we had access to three types of gridded ice concentration products from AMSR2 for hindcasts of

the Sea State experiment: 1) AMSR2 3.125 km 24-hourly 2) AMSR2 3.125 km 12-hourly, and 3) AMSR2 10 km. We review each here.

#### *AMSR2 3.125 km with ASI algorithm, 24-hourly*

These fields are available from the University of Hamburg (Kaleschke et al. (2001); Spreen et al (2008); Beitsch et al. (2013, 2014)). It uses the 89 GHz channel (W band) of AMSR2 which has a field of view of around  $3 \times 5$  km, which makes the 3.125 km sampling resolution possible. It uses the ASI method for processing the data from L1R brightness temperatures. “ASI” stands for “ARTIST sea ice” and “ARTIST” stands for “Arctic Radiation and Turbulence Interaction Study”. This is a near-realtime product. We downloaded the files June 2016.

The fields correspond to measurements taken at 00:00 to 23:59 UTC each day, so when run inside WW3, a 12:00 UTC time stamp is applied to the files. WW3 interpolates wind fields in the time domain but *does not interpolate ice fields* in the time domain; it uses the temporal “nearest neighbor”.

#### *AMSR2 3.125 km, 12-hourly*

The 12-hourly product comes from Christian Melsheimer of the University of Bremen, shared with the Sea State participants by Dr. Fanny Ardhuin (Ifremer) in July 2017. The fields correspond to morning (00:00-11:59) and afternoon (12:00-23:59). Much of our analysis had already been performed prior to receiving this data, so this dataset is not used in the present report.

#### *AMSR2 10 km with NRT algorithm, high temporal resolution*

These files were created by co-author Li in January 2017. Two alternate datasets were created, using the “NASA Team 2” (NT2) (Markus & Cavalieri, 2000, 2009) and “Bootstrap” methods for estimating ice concentration (Comiso et al. 2003). Only NT2 is used for forcing WW3 in this report: it was developed for the predecessor instrument AMSR-E (Advanced Microwave Scanning Radiometer - Earth Observing System). Though the sampling resolution is coarser than the German fields, the processing method reduces problems caused by atmospheric/weather effects, so there is less risk of false ice detection. These files use the 18, 37, and 89 GHz channels of AMSR2 ([Ku or K], [Ka], and [W] band respectively). NT2 additionally uses the 22 GHz channel; this channel is used to apply a “weather filter” to further reduce the weather effects.

The highest priority of this dataset was *temporal resolution*: we wanted a product which would allow updating of ice conditions for WW3 in situations where the ice fields were rapidly changing in the MIZ, such as WA3. Whereas the 3.125 km datasets are given at regular intervals (24-hourly or 12-hourly) and combine multiple satellite passes into single fields, the 10 km dataset is provided such that temporal information about the passes (or swaths) is retained. Not every swath was used: only those which passed over the cruise area were used. A minimum 90% coverage of the cruise area was set as a threshold, and prior swath data was used to fill regions on the grid not covered by the current swath. This direct use of swath results in  $a_{ice}$  fields which

are irregular in time; WW3 permits this in forcing fields. The processing resulted in 180 fields over 39.4 days 13:13 UTC 1 October to 22:22 UTC 9 November 2015. This is an average of 4.6 fields per day or 5.3 hours per field.

Our scheme for transferring the swath data into forcing files for WW3 requires that the region of interest (around 400 km in our case) be smaller than the swath width (1450 km with AMSR2). In other words, it is appropriate for a model of the portion of the Arctic Ocean north of Alaska, but would not be appropriate for a model of the entire Arctic.

#### 4.2. Ice thickness forcing

Ice thickness  $h_{ice}$  is not used in the present report, but it is a required input for some of the physics parameterizations:

- The VE models IC3 and IC5
- The IC2 routine. Though, this only pertains to the dispersion model used to calculate group velocity and wavenumber. The boundary layer model used to calculate dissipation does not require ice thickness. A user can run IC2 with only the latter activated, so ice thickness is not strictly required.
- The scattering model IS2.
- Two of the seven IC4 parameterizations: IC4M3 and IC4M7.

We discuss two possible sources of ice thickness: CICE and SMOS.

##### CICE

The CICE model has already been introduced (Section 4.1.1). Since it is a physics-based model, naturally ice thickness is computed and available as output. This is, in fact convenient in the context of WW3, since it means that  $a_{ice}$  and  $h_{ice}$  are provided on the same grid (latitude, longitude and time). Thus, a WW3 simulation can be prepared more quickly. Also, the two fields are mutually consistent: something that is not guaranteed when using two different satellite instruments.

##### SMOS

SMOS (Soil Moisture and Ocean Salinity) is a passive microwave instrument operating at 1.4 GHz (L-band), which is a lower frequency than that used by AMSR2 and SSM/I. It is able to estimate ice thickness of thinner ice. The limit is often taken to be 1.0 m. However, it is not recommended for use in cases where ice concentration is less than 100%. In other words, it is meant for sheet ice, outside the MIZ, where there are no waves. It can, in principle, be used in the MIZ anyway (in other words, disregarding the warnings). However, we have a specific concern about how this should be performed in the context of WW3. Does the ice thickness from SMOS then pertain to the mean ice thickness of the entire footprint, or the mean ice thickness of the portion of the footprint that contains ice, or something in between? In other words, should the SMOS thickness be normalized by the ice concentration? Since SMOS is not recommended for cases where ice concentration is less than 100%, there is no guidance for this.

The supplementary material provided by Cheng et al. (2017) has an excellent comparison of ice thickness values during the Sea State cruise, based on CICE, SMOS, and estimates from the ship.

### 4.3. Case studies

One objective of this report is to analyze the accuracy of the ice forcing for the Sea State hindcasts, and estimate the implications for wave model accuracy. However, this would require some sort of ground truth for the ice products. One approach that has been used in the past, e.g. Posey et al. (2015), is to use the NIC ice edge. The ice edge product made by NIC analysts is independent from the ice mask (IMS) which is also produced by NIC analysts for the same location and the same time. The former is used for ground truth and the latter is used in the CICE DA. Unfortunately, as we will see below, we found that the NIC ice edge product and the IMS product suffer from similar problems during WA3, which was the only “large waves in ice” experiment of the Sea State cruise.

Thus, to perform a thorough validation of the ice products during the cruise, we would need to generate our own ice edge products using the SAR imagery, optical/infrared images, passive microwave scans, aircraft observations, and ship-based observations. For example, recall that there were over 60 RADARSAT-2 images alone. This would be beyond the scope of the present study, which is focused on wave modeling. So instead, we present a few specific case studies to examine. Though not comprehensive nor systematic, they serve to make important points about the ice forcing.

#### 4.3.1. September 9 (prior to cruise)

Prior to the cruise, the Sea State group conducted “virtual Plans of the Day” discussions to prepare for the actual cruise. These included mock discussions of imaginary measurement plans given the conditions seen in satellite and modeling products available. One topic of discussion was an “ice tongue” which had developed in the region of the planned cruise, a remnant after the pack ice had melted north and south of its position during the summer<sup>18</sup>. The eastern portion of the ice tongue corresponded neatly with the location of the future WA3. Figure 50 shows a RADARSAT-2 “browse image” during this period. Figure 51 and Figure 52 show the ice concentration forcing provided to WW3 and remapped to the 5 km inner WW3 grid used for hindcasts (Section 6). Figure 51 is the 24-hourly AMSR2 product, and Figure 52 is the GOFS 3.1 reanalysis product. The plot frame of Figure 50 is different from that of Figure 51 and Figure 52, so small black squares have been added to the figures to facilitate comparison: the squares are in the same position in all three figures.

These figures indicate that AMSR2 fails to detect most of the ice in the ice tongue. In contrast, the field from GOFS 3.1 has excellent correspondence with the SAR image. This can be credited to the assimilation of IMS. We can guess that the latter had access to the SAR image shown in Figure 50, among other products, and this would imply that the NIC analyst correctly created the ice mask favoring the SAR imagery over passive microwave products.

Passive microwave radiometers like AMSR2 have well-known difficulties identifying melt ponds as open water. However, the ice in the ice tongue is clearly not the conventional case of

---

<sup>18</sup> A paper by Dr. Sharon Stammerjohn is in preparation, which will describe this ice tongue and its relation to ice conditions observed the following month, during the cruise. A working title is “Episodic Ice-Edge Advances & Reversals in the Chukchi & Beaufort Seas in Relation to Summer Preconditioning, Upper Ocean Variability & Winds”.

pack ice and vast floes with melt ponds. Rather, the image suggests that the ice cover is composed of medium and smaller floes and/or brash which in aggregation has the appearance of a liquid at this scale. These floes or brash ice are likely to have wet upper surfaces in the summer which can cause the ice cover to be misidentified as water by the instrument (M. Doble, personal communication). The latter is a less well-known limitation of the passive microwave radiometer.

During the month of September, prior to the cruise, we were pleased with the accuracy of NRL's 2 km CICE product, which produced results comparable to this, and so as the cruise approached, author ER was fully confident that the NRL CICE product was the easily the best ice forecast available anywhere.

Figure 53 compares three different AMSR2 products: 1) AMSR2, 10 km resolution, processed using "Bootstrap" algorithm, 2) AMSR2, 10 km resolution, processed using "NASA Team 2" (NT2) algorithm, 3) AMSR2, 3.125 km resolution, processed using ASI algorithm. The corresponding GOFS 3.1 concentrations are also shown. The Bootstrap algorithm appears to be most similar to GOFS (and therefore SAR) in terms of spatial coverage of ice. However, it has the lowest maximum concentrations of the four products. The NT2 and ASI fields are surprisingly similar in terms of spatial coverage of ice, though the variance of concentration is clearly higher in the higher resolution ASI field.

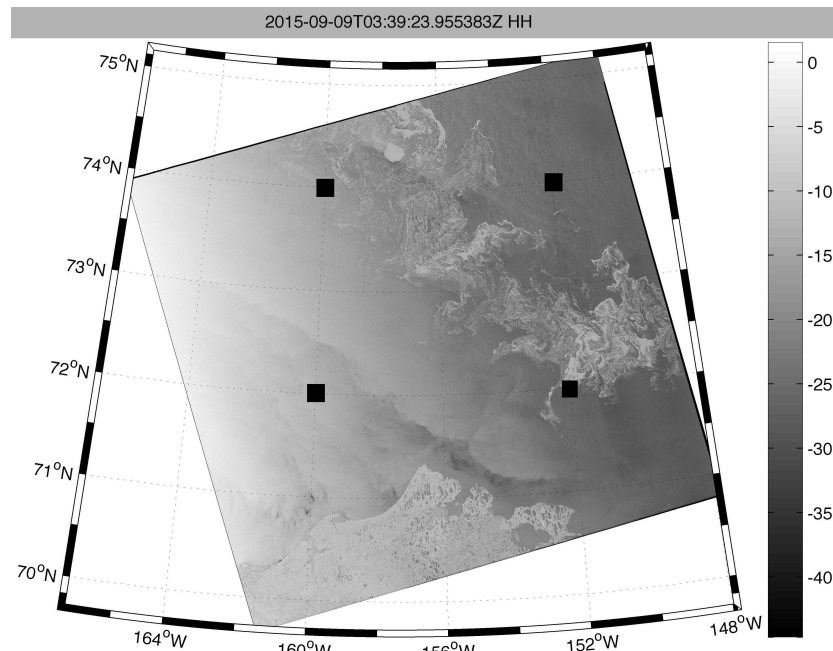


Figure 50. RADARSAT-2 "browse image" for 0339 UTC 9 Sept. 2015, courtesy of Bedford Institute of Oceanography. The four black square markers are added to compare with Figure 51 and Figure 52. RADARSAT-2 Data and Products © MacDONALD, DETTWILER AND ASSOCIATES LTD. (2015) – All Rights Reserved. RADARSAT is an official mark of the Canadian Space Agency.

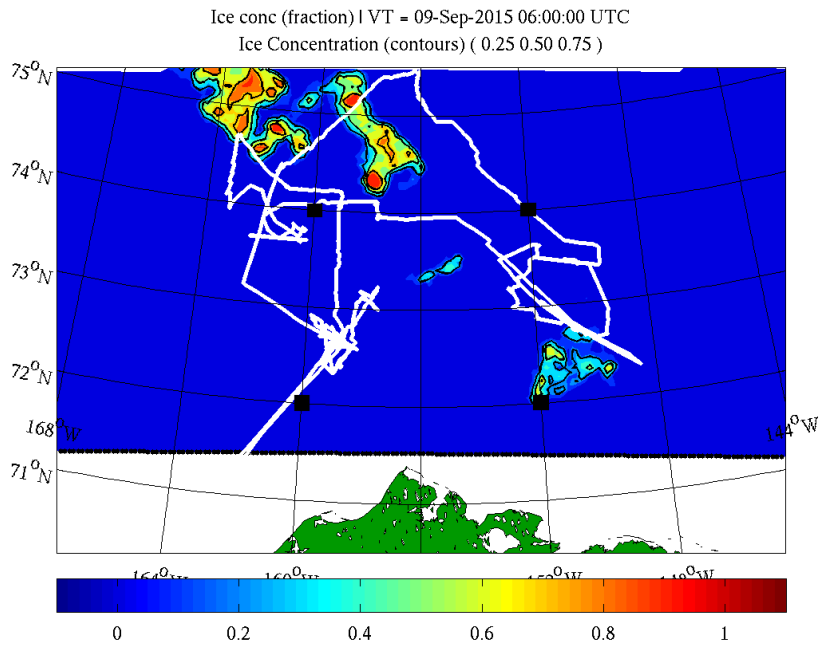


Figure 51. Ice concentration for 0600 UTC 9 Sep. 2015, 3.125 km AMSR2 product, remapped to the 5 km WW3 grid. The four black square markers are added to facilitate comparison with Figure 50.

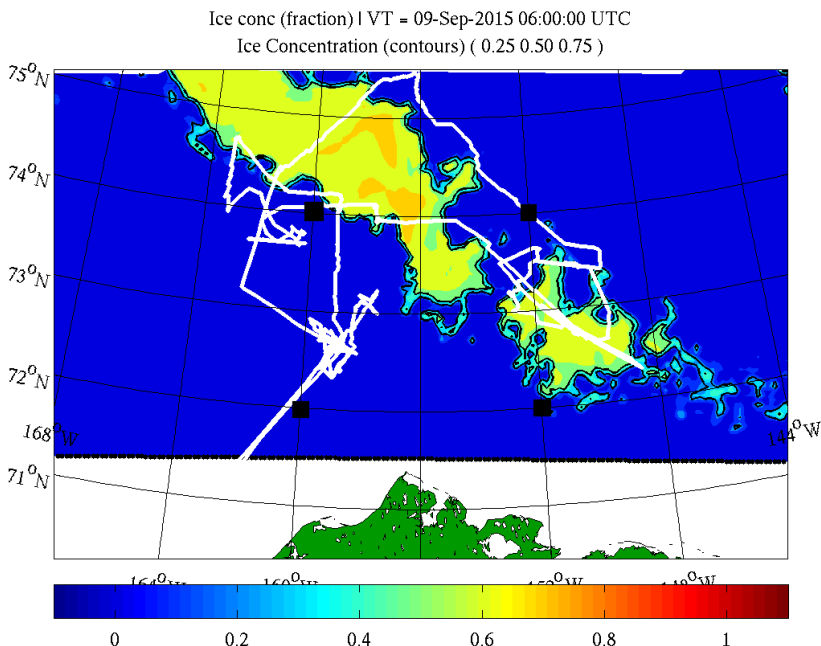


Figure 52. Ice concentration for 0600 UTC 9 Sep. 2015, GOFS 3.1, remapped to the 5 km WW3 grid. The four black square markers are added to facilitate comparison with Figure 50.

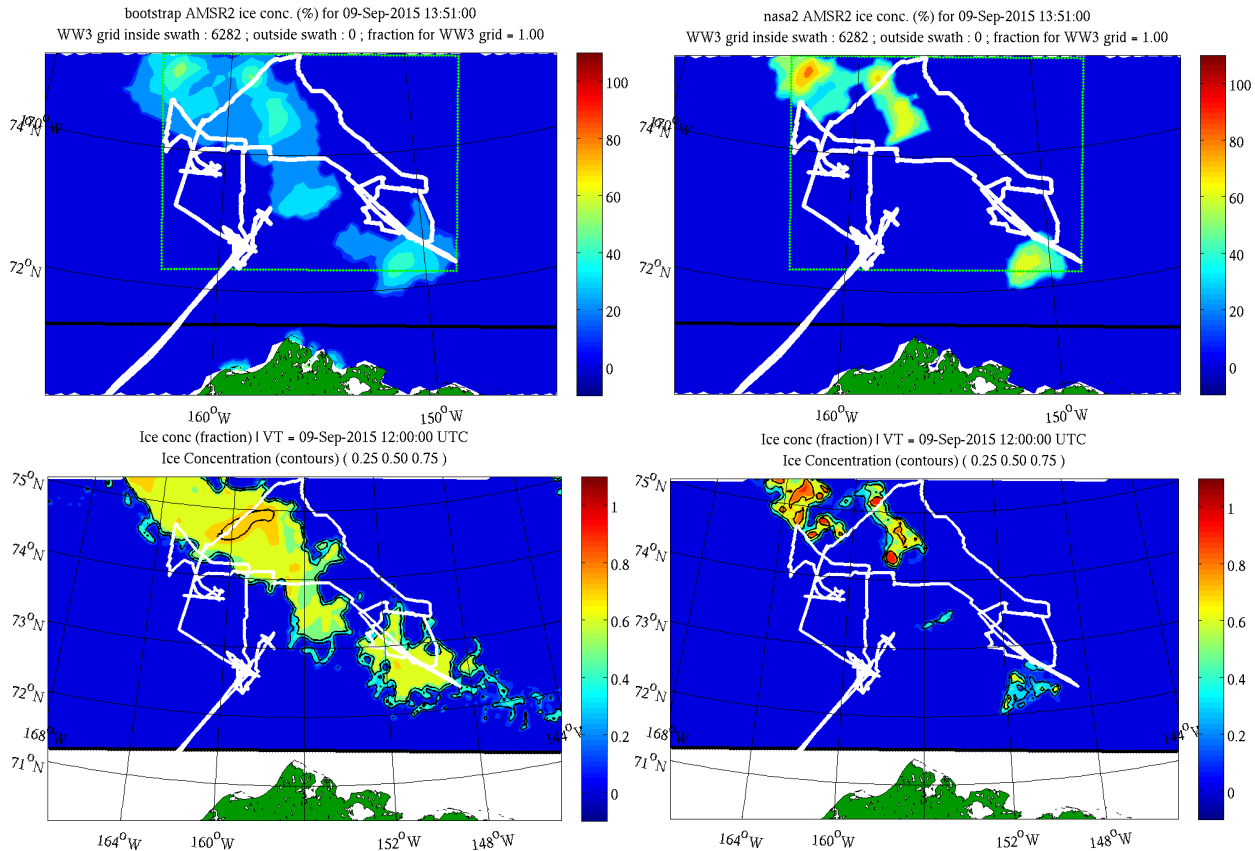


Figure 53. Comparison of ice concentration fields from AMSR2 products (3 of 4 panels) and GOFS (lower left panel). Upper left panel: AMSR2, processed using “Bootstrap” algorithm, plotted on native 10 km grid. Upper right panel: like prior, but processed using “NASA Team 2” algorithm. Lower left: GOFS, remapped to 5 km inner WW3 grid, similar to Figure 52. Lower right panel: AMSR2 using ASI algorithm, provided at 3.125 km resolution but plotted here remapped to the 5 km inner WW3 grid. Dates are indicated above each panel.

#### 4.3.2. October 10-15: Wave array #3

Wave array #3 (WA3) was the flagship wave experiment of the cruise, the much-anticipated “large waves in ice” event. The 2 km NRL CICE model was used to force the inner WW3 grid of the forecasts run on the ship. In this section, we use a comparable product, NRL CICE from GOFS 3.1 reanalysis, since the latter is used in hindcasts in this Section 6.3. At the beginning of WA3, the ice edge of GOFS 3.1 was extremely accurate, relative to the ice edge observed from the ship. Unfortunately, the IMS field was not updated for the region of the cruise for the next several days, so even as the CICE model physics would try to move the ice edge, it would always be reset back to its original position. The latter position was wrong, since the ice edge retreated rapidly toward the northwest during the wave experiment.

Figure 54 shows the ice edge from IMS (intended to correspond with the 40% concentration contour) and the 50% ice concentration contour from three types of WW3 forcing fields: GOFS 3.1 reanalysis, 3.125 km AMSR2 (24-hourly), and 10 km AMSR2. Colored dots indicate the buoy ice observations as described in Section 7. A value of 0 (dark blue) indicates open water, and a value of 12 (garnet or dark red) indicates heavy frazil and pancake ice. The magenta line includes the southern transect of WA3 and the black diamond at the southeast end of that transect corresponds to the ice edge position at 1400 UTC 11 October. The IMS and GOFS 3.1 contours

closely correspond, which reflects the very aggressive DA used in GOFS 3.1 at that time. At the southeast end of the WA3 southern transect, the GOFS 3.1 ice edge is shifted slightly toward the northwest, in the predominant drift direction, so this offset is presumably associated with ice drift in CICE. The figure corresponds to 0300 UTC 12 October, so it is 15 hours after the arrival of the ship at the southeast end of the WA3 southern transect. By 0300 UTC 12 October, the ice edge had already retreated to the northwest, as indicated by the blue circles. GOFS 3.1 does not capture this retreat.

The AMSR2 products do capture the retreat of the ice edge, but may overdo it somewhat, as indicated by the garnet dots: this is SWIFT14, which is in heavy frazil and pancake ice for much of the experiment (Figure 140). During the PM (UTC) of the 12<sup>th</sup>, SAR images indicate that the ice in which the buoy floats is in a narrow band (Section 7.3.3) (something which is entirely non-apparent given the buoy's limited field of view), which may be a problem for the geographic resolution of the AMSR2 products (3.125 and 10 km). Further, the ice is relatively wet, which may also explain its absence from the AMSR2 products. Figure 54 is somewhat ambiguous on this point, however, since the ice is in narrow bands, and the 40% concentration contours are plotted: thus, it does not indicate whether the products *completely* miss these ice bands. Thus, the figure is replotted in Figure 55, this time showing the 10% concentration contours. This reveals that the 10 km AMSR2 *does not* necessarily miss this ice: in fact, an ice concentration between 10% and 40% is credible from the PM SAR image (Figure 138). There are notable differences between the two AMSR2 products (ASI 3.125 km in green and NT2 10 km in blue). These differences are *not* associated with processing method (ASI vs. NT2). In fact, we can see from Figure 58 that ASI and NT2 tend to be similar, at least in terms of spatial coverage. Instead, the difference here is associated with the time coding of the ice fields. In case of NT2 (blue), WW3 is selecting the nearest swath in time, which is 2115 UTC 11 October (about 6 hours prior). In case of the 24-hourly ASI (green), it is using a combination of data collected between 0000 and 2359 UTC 12 October, and is probably relying most on data collected in a satellite pass on 1254 UTC (around 10 hours in the future). Because it is using the later satellite pass, the ASI field is showing larger retreat.

Figure 56 indicates that on 0000 UTC 15 October, the NRL CICE model's ice edge is still in its original position, several days after the start of the wind wave event, even though there had been dramatic movement of the ice edge during this time. This is extremely disappointing, given that the removal of this ice during this period, either by advection or melting, and explanations thereof (e.g. what causes the upward mixing of heat which contributed to the melting?), turned out to be a major focus of study coming out of the Sea State experiment<sup>19</sup>. On 0000 UTC 17 October, the IMS field was finally updated for the region. This permitted CICE to move the ice edge from the 11 October position, which results in a first significant update of the WW3 hindcast forcing 1200 UTC 16 October (Figure 57). (WW3 applies the update 12 hours earlier, since it uses "nearest neighbor in time" for ice forcing.) However, by this time, the ice had largely recovered (advanced back toward the southeast), and the *Sikuliaq* had moved to the

---

<sup>19</sup> For example, the reader is referred to <[http://www.apl.washington.edu/project/project.php?id=arctic\\_sea\\_state](http://www.apl.washington.edu/project/project.php?id=arctic_sea_state)> and <[http://www.apl.washington.edu/project/projects/arctic\\_sea\\_state/pdfs/arctic\\_sea\\_state\\_script\\_01.pdf](http://www.apl.washington.edu/project/projects/arctic_sea_state/pdfs/arctic_sea_state_script_01.pdf)>, retrieved December 6 2017. Also, the upcoming JGR Special Issue centered on the Sea State experiment and related work will have papers on the topic of the change to the ice cover during WA3.

northwest, well outside of the WA3 study area (indicated with the black circle). The four to five day duration retreat was missed.

Discussion with Sean Helfrich at the NIC confirm that the non-update of IMS was most likely caused by human error. Either the analyst was somehow unaware of the available SAR imagery, or simply forgot to update this region for several days. The NIC “ice charts” from this period—specially made by the NIC for use by those on the *Sikuliaq* at that time—do indicate that the NIC was aware of at least one of the relevant SAR images: the 1723 UTC 13 October RADARSAT-2 image, which does indicate the retreat. This relates to another hypothesis, entirely speculative: that the special NIC chart may have been created by the analyst that would otherwise have worked on the IMS updates for that sector; in other words, there may have been a shift in human resources associated with the special NIC chart which had a negative impact on the IMS. This would be ironic and unfortunate, as the NIC charts were largely superfluous during the cruise, since cruise participants had extensive access to rapidly updated imagery on the ship via the “Mapserver” system<sup>20</sup>, while the NIC IMS turned out to be critical to the success or failure of the wave model.

Based on discussion with the NIC, our recommendation is to provide metadata with IMS fields, indicating the “age” of data (or “last observed” date), and thus when and where the fields may have not seen any update for several days. This could be used as a data quality flag by the CICE system to decide whether or not to include that portion of IMS in the CICE DA. In the context of WW3 forcing, our recommendation is to consider using AMSR2 forcing until the proposed IMS flagging is operational. Though, this is not an easy decision, given that the existing CICE/IMS systems are far superior to AMSR2 in at least one documented case (Section 4.3.1), and we have reason to believe that this was not an anomaly.

Figure 58 shows three different AMSR2 products and the corresponding GOFS 3.1, like the comparison made in Figure 53. Again, the Bootstrap algorithm produces the greatest spatial coverage of ice, of the three AMSR2 products, but has the lowest maximum concentrations in the region of WA3. Also like Figure 53, the NT2 and ASI fields are similar in terms of spatial coverage of ice, though the variance of concentration is higher in the higher resolution ASI field.

---

<sup>20</sup> The Mapserver was designed and updated by Marine Tech Steven Roberts. He has generously turned that realtime on-ship server into a static web page for use after the cruise: <<http://realtime.sikuliaq.alaska.edu/SKQ201512S/map/skq.html>> (retrieved December 6 2017)

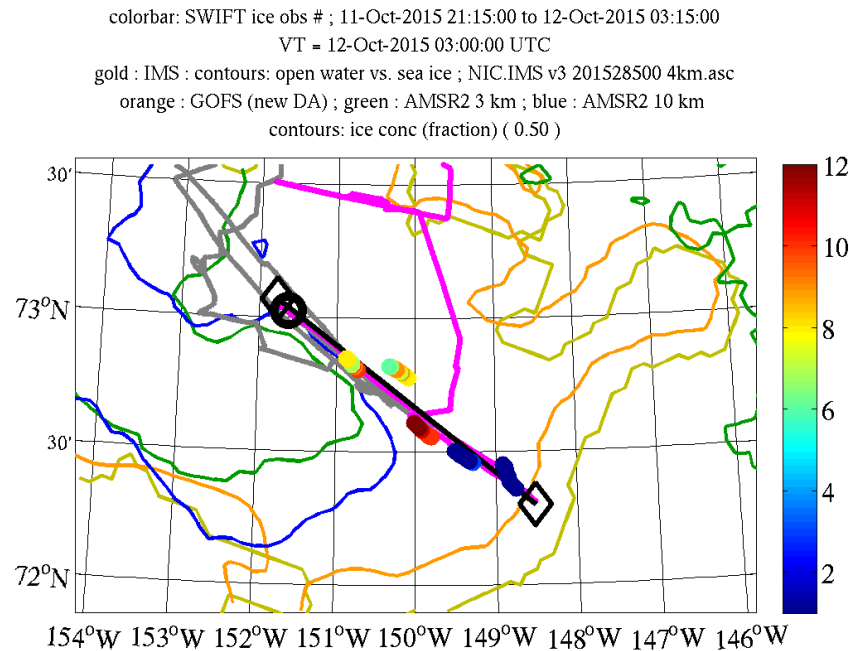


Figure 54. Comparison of ice products and in situ observations during WA3. All data shown are contemporaneous, during the period of ice retreat. Magenta line is the cruise track, and the black circle is the ship location at the time of the image (0300 UTC 12 October 2015). Black diamonds indicate the terminal points of the southern transect of WA3, shown as a black line. Colored circles and colorbar indicate the buoy ice observations as described in Section 7 (0=open water and 12=heavy frazil and pancake ice). Gold lines are the IMS ice edge. Orange, green and blue lines are the 50% ice concentration contours from three gridded ice products: GOFS 3.1 reanalysis, 3.125 km AMSR2 (24-hourly), and 10 km AMSR2.

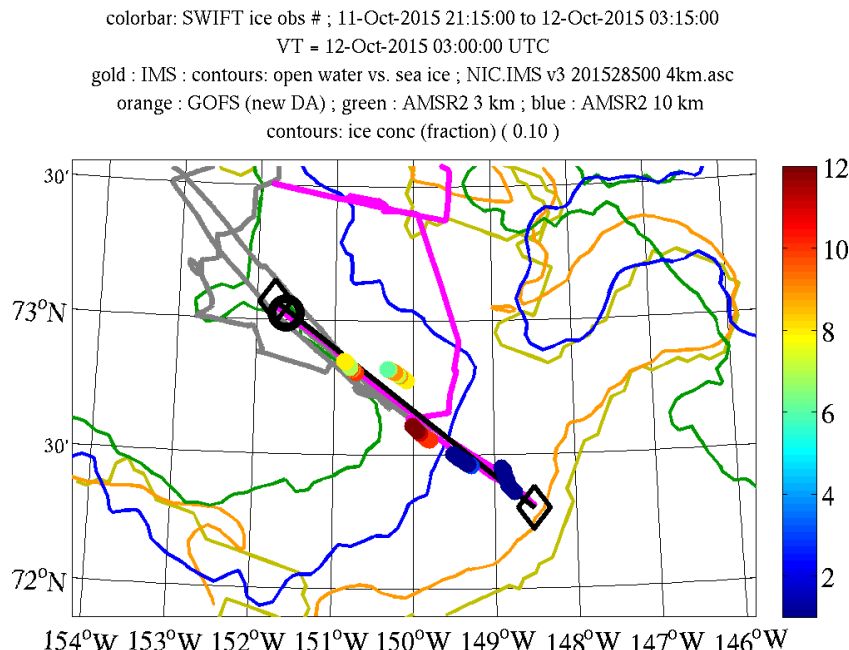


Figure 55. Same as Figure 54, but showing the 10% ice concentration contours for GOFS 3.1 and AMSR2 fields.

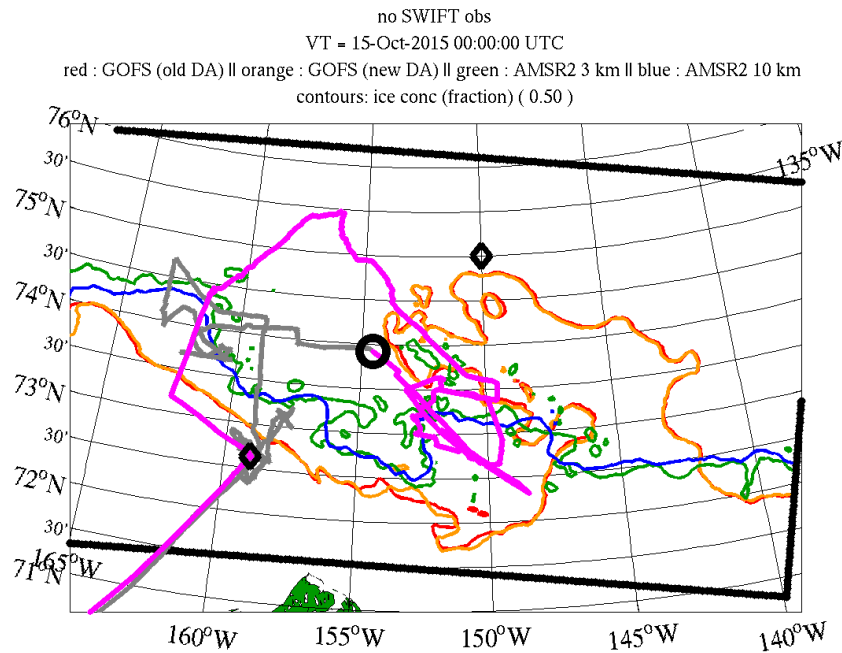


Figure 56. Comparison of ice products. Magenta and grey line is the cruise track, and the black circle is the ship location at the time of the image (0000 UTC 15 October 2015). Black diamonds indicate AWAC mooring locations. Black line is the boundary of the inner WW3 nest. Red, orange, green and blue lines are the 50% ice concentration contours from four gridded ice products (see text above plot).

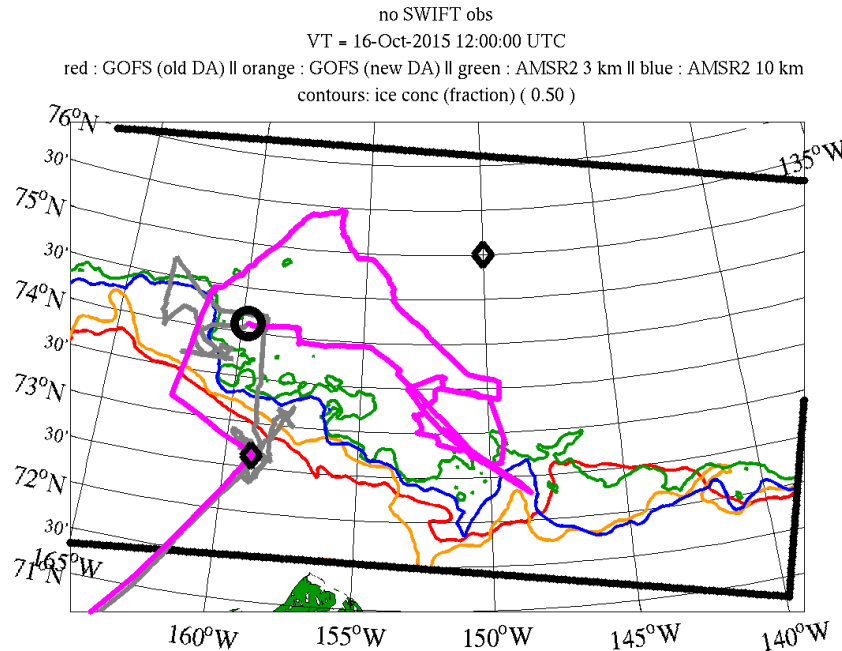


Figure 57. Like Figure 56, except showing 1200 UTC 16 October 2015

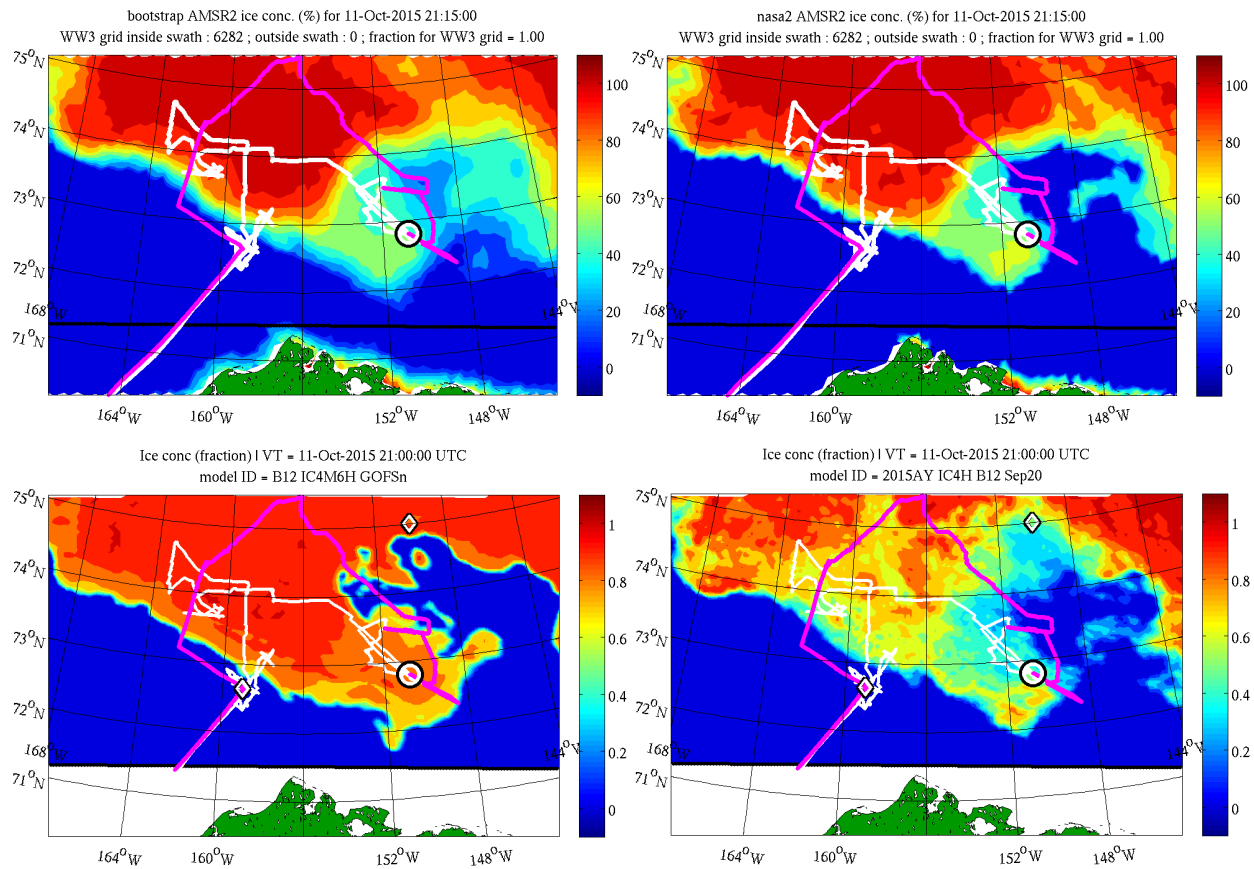


Figure 58. Like Figure 53, but comparing times near 2100 UTC 11 October. Upper left: Bootstrap. Upper right: NASA Team 2. Lower left: GOFS 3.1. Lower right: ASI.

#### 4.3.3. October 20-25: Gap closure

During the cruise, author ER received criticism that the ice fields used to force the inner WW3 grid indicated a premature closure of the gap separating the pack ice (north of the gap) from the ice adjacent to the Alaska coastline (south of the gap). Though the issue did not—as far as we know—significantly impact the wave predictions at the ship and buoy locations, which were at least 100 km away, northwest of the gap, it would obviously affect wave predictions near the gap, and would have affected conditions at the wave experiments if there had been substantial winds from the direction of the gap (southeast) during that period<sup>21</sup>. Also, we can speculate that the timing of the gap closure would be important if the ice product is used for navigational planning.

Those realtime ice fields came from NRL’s 2 km CICE system, but the same general behavior is exhibited by the GOFS 3.1 products. In this section, rather than showing the CICE fields, we present NIC IMS fields which are assimilated into the CICE systems. This removes any ambiguity regarding the source of the problems. We also show the NIC ice edge in this section. This product is *not* used in the CICE DA and has been used previously for independent

<sup>21</sup> Recall that winds during WA6 (October 23 to 25) were from the east, and waves were from the southeast, traveling predominately parallel to the ice edge. If the winds had been from the southeast, the waves at WA6 would have been more substantially affected by the ice near the gap, and would have received energy along a longer fetch.

evaluation of CICE model skill (Posey et al. 2015). The two NIC products have different meaning in context of ice concentration: the ice edge is interpreted to correspond to an ice concentration of 10% and the IMS mask delineation is at an ice concentration of 40%.

Figure 59 and Figure 60 demonstrate that on October 20 and 21 (respectively), the gap is still wide according to SAR, but the NIC products show a narrowing gap. In Figure 61 (October 24), the gap is largely unchanged according to the SAR, but the NIC ice edge (10%) has it closed and the IMS (40%) has it very narrow. On October 25 (Figure 62), both NIC products have the gap completely closed, and the SAR image has the gap still wide east of 153W; one can assume that the gap is still open west of 153W also, but the SAR image does not include that area. Figure 63 shows the gap finally closing in the SAR imagery on the 27<sup>th</sup> and 30<sup>th</sup>, approximately seven days after it occurs in the NIC products.

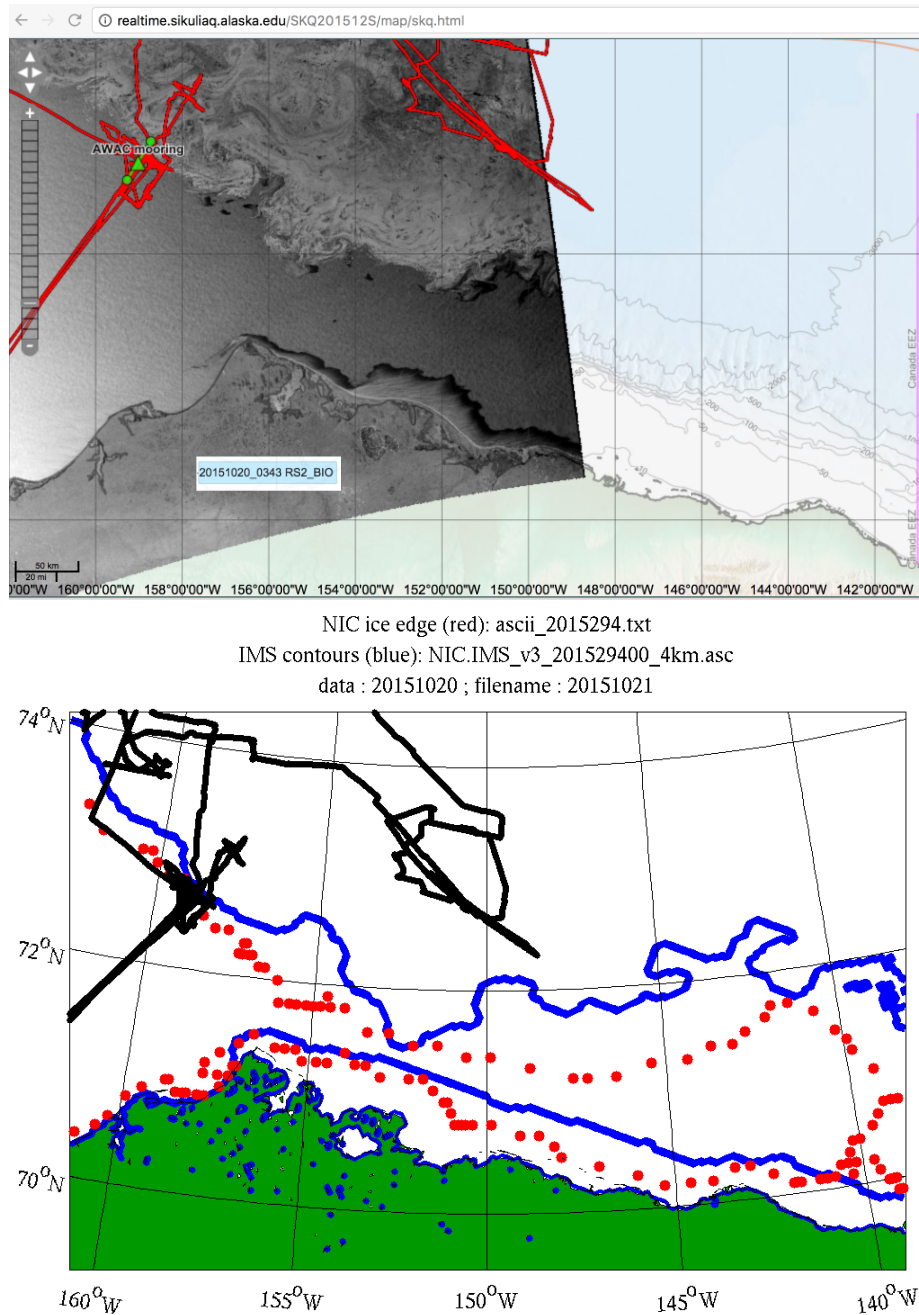


Figure 59. Top panel: SAR image of the ice from the Sikuliaq map server. The instrument, date, and time of the image is indicated in the text box embedded in the image: 0343 UTC 20 October 2015, RADARSAT-2 from BIO. RADARSAT-2: © MDA 2015. The cruise track is shown in red. Lower panel: Blue line is IMS. Red dots are the NIC ice edge. Dates are indicated in the title in year-day format; 294 is October 21. The date of data is one day earlier than the date of the filename, so this corresponds to satellite observations on the 20<sup>th</sup>.

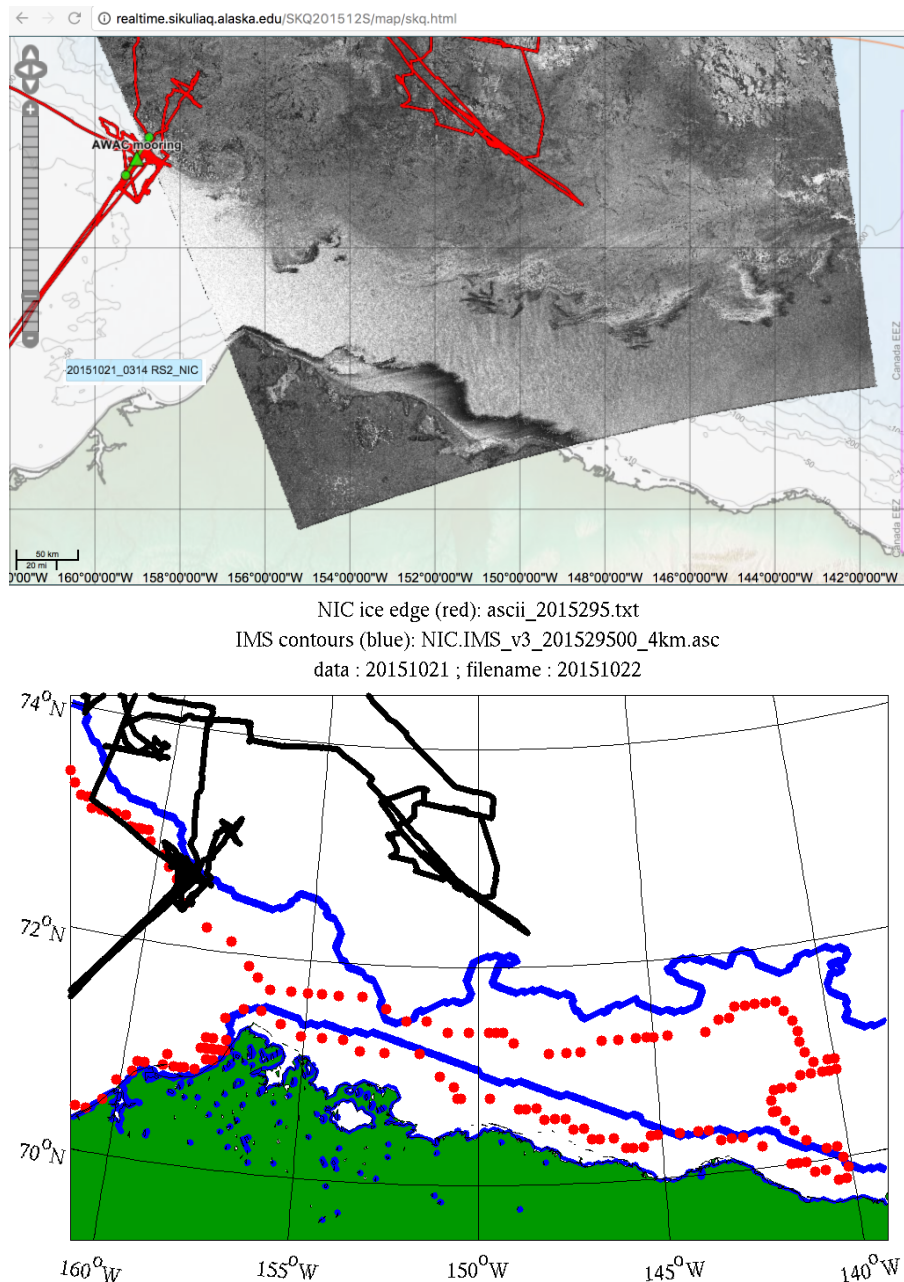


Figure 60. Same as Figure 59, but showing a different image, and looking at October 21. "RS2\_NIC" indicates that this is a RADARSAT-2 image from the NIC. RADARSAT-2: © MDA 2015.

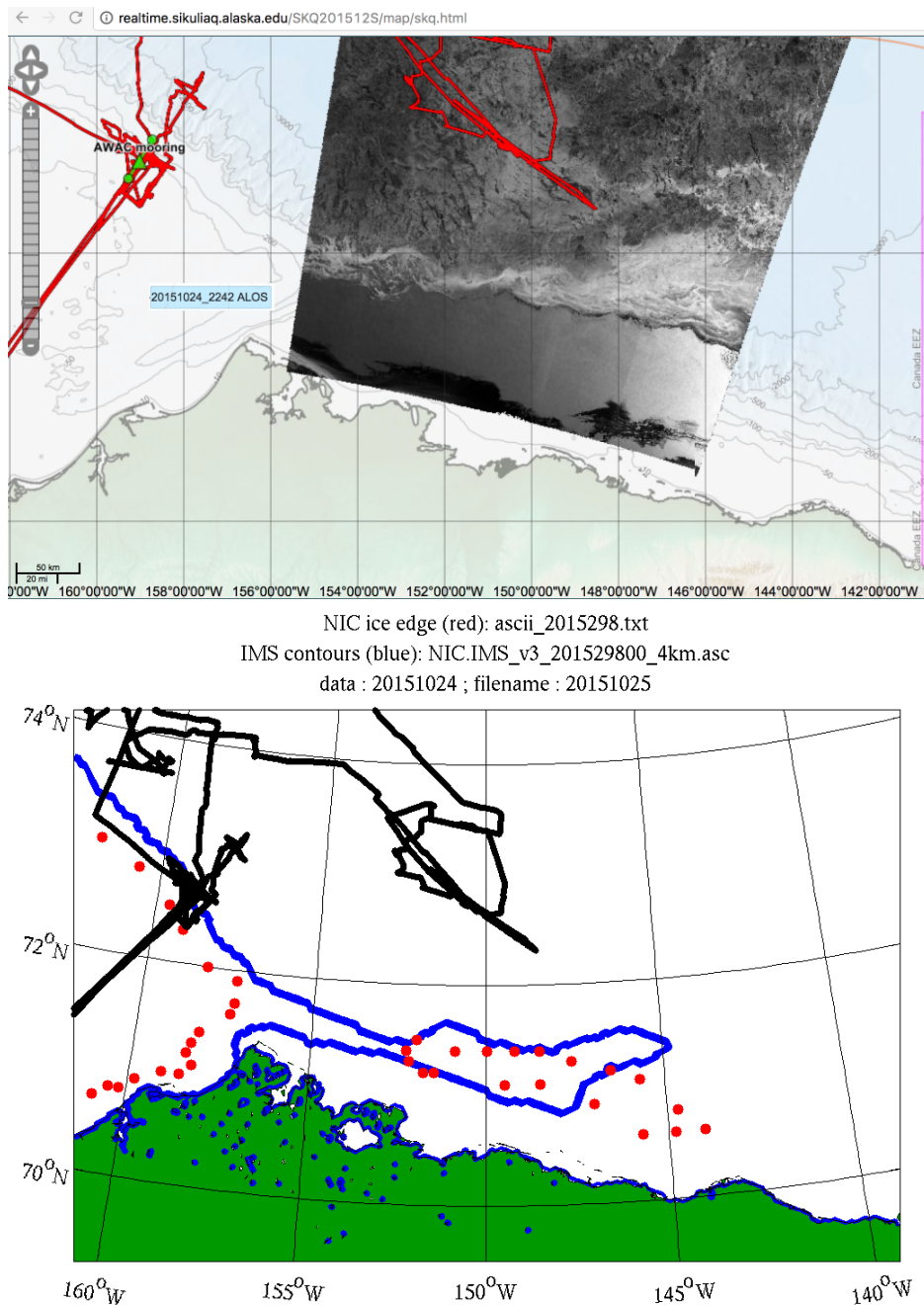


Figure 61. Same as Figure 59, but showing a different image, and looking at October 24. This image is from ALOS (JAXA).

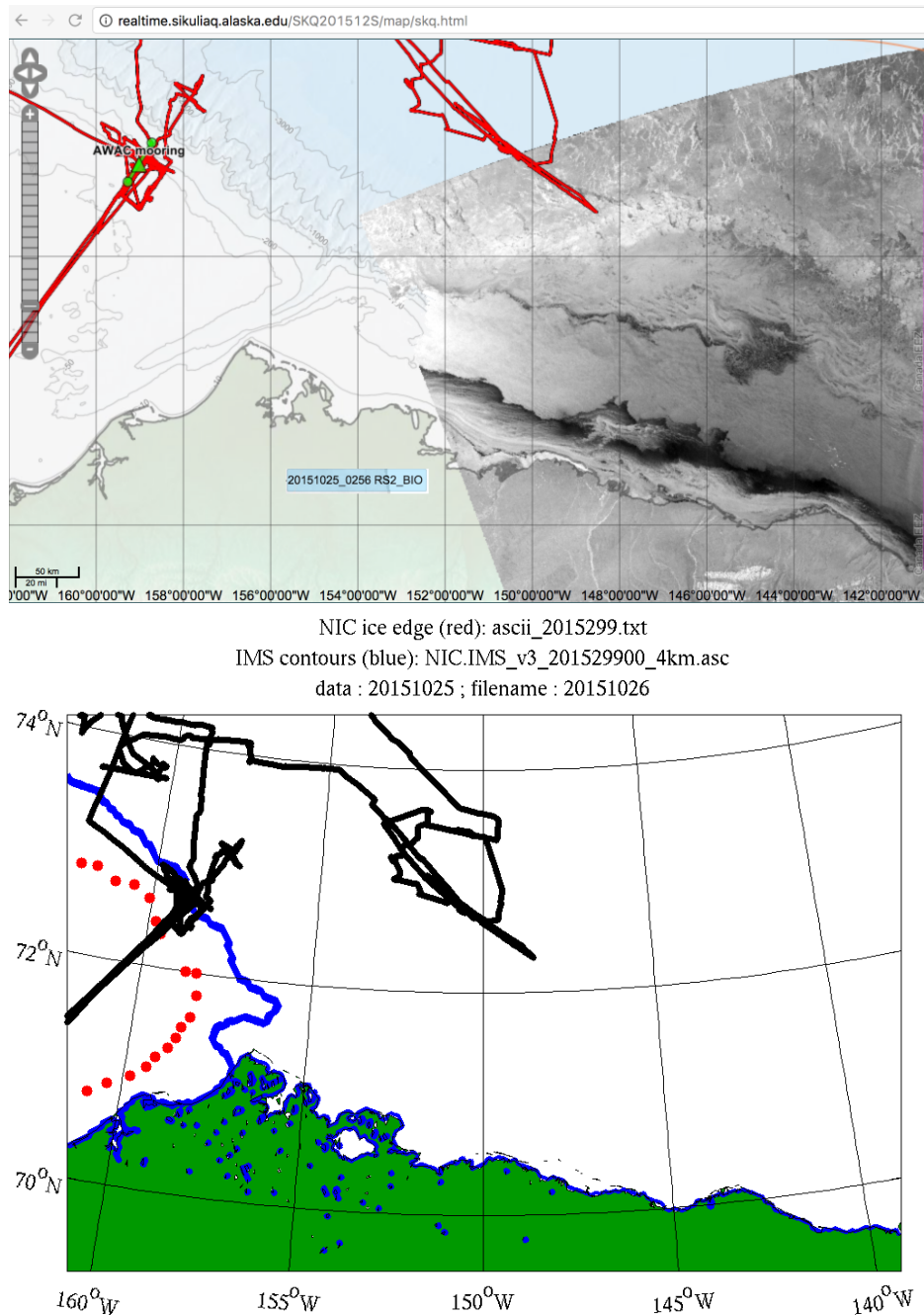


Figure 62. Same as Figure 59, but showing a different image, and looking at October 25. RADARSAT-2: © MDA 2015.

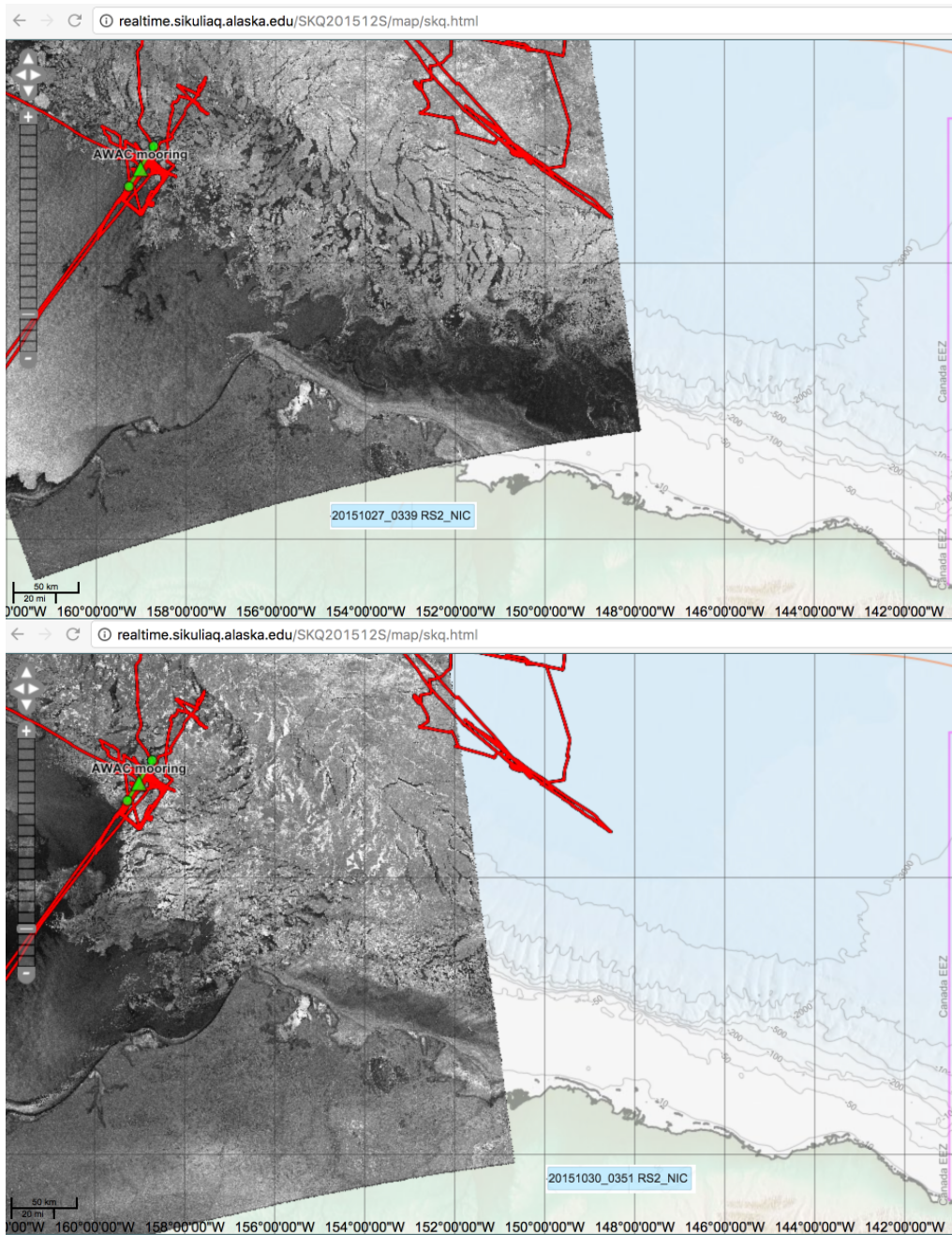


Figure 63. Same as top panel of Figure 59, but showing different images, October 27 and 30. RADARSAT-2: © MDA 2015.

#### 4.3.4. October 20-24: Fetch-limited scenario (off-ice winds)

This section covers October 20-24, nearly the same time period as the previous section, but focuses on the implications for wave predictions at the Sea State AWAC mooring. By this time period, the ice had advanced to a position quite close to the mooring, and all four ice products reflected this (Figure 64). Recall that the wind direction was easterly and the wave direction southeasterly (Figure 19). The distance to the ice edge was 5 to 10 km, which is not much greater than the resolution of the wave model used in Section 6 (5 km). With such proximity, small differences in the ice edge position can make a large difference in wave height. The GOFS 3.1 products and 10 km AMSR2 are in general agreement on the ice position near the buoy in Figure 64. The ice edge of the 3.125 km AMSR2 (in green) is more recessed; the SAR imagery suggests that the former three are correct, and the latter incorrect. Larger differences exist to the southeast. There, the GOFS 3.1 products are more recessed, and the 10 km AMSR2 (blue) most advanced. There is no contemporary SAR imagery in this case, but 30 hours later, at 0600 UTC 23 October, the relative positions are unchanged (Figure 65) and a SAR image for 0356 UTC 23 October (Figure 66) is most similar to the 10 km AMSR2 product. By 1200 UTC 23 October, the GOFS 3.1 hindcast product has advanced this ice edge to a better position (Figure 67), and the advance occurs in the GOFS 3.1 realtime product 24 hours later (1200 UTC 24 October) (not shown).

Though the wave model hindcasts have not been introduced yet (Section 6), we present some results from the hindcasts here. The details of the simulations are not important here, and we are comparing results with different ice forcing, which has been introduced. Time series comparisons of wave height and wave period are given in Figure 68 and Figure 69 respectively. We use the same color coding for the ice products in these figures that we used in Figure 64. The results indicate that the wave field development is dependent on the position of the ice edge to the southeast (the dominant wave direction) more than the position of the ice edge to the east (the dominant wind direction). The order of the most advanced to the least advanced ice edge (blue, green, orange, red, so 10 km AMSR2; 3.125 km AMSR2; GOFS 3.1 reanalysis; and GOFS 3.1 nowcast respectively) is identical to the order from the smallest to largest significant wave height. The hindcast with 10 km AMSR2 forcing is most accurate, with much smaller bias. That is, of course, an encouraging outcome: at this time/location, the hindcast with most accurate forcing yields the most accurate wave prediction. However, even for that hindcast, the correlation with observations is not good during October 21 to 25.

The step-wise advance of ice edge in the GOFS 3.1 hindcast product on 1200 UTC 23 October, and the GOFS 3.1 realtime product on 1200 UTC 24 October corresponds to a visible drop in the waveheight on these dates (orange and red lines respectively in Figure 68).

Interestingly, the dominant period does not follow the order given above, and the most advanced ice edge corresponds to the longest period (10 km AMSR2). Presumably, this is caused by preferential damping of higher frequencies in the model, which would have a very slight effect on the dominant period. In any case, the wave period values are quite similar between the four hindcasts, with the hindcast using forcing from GOFS 3.1 reanalysis yielding the most accurate wave period.

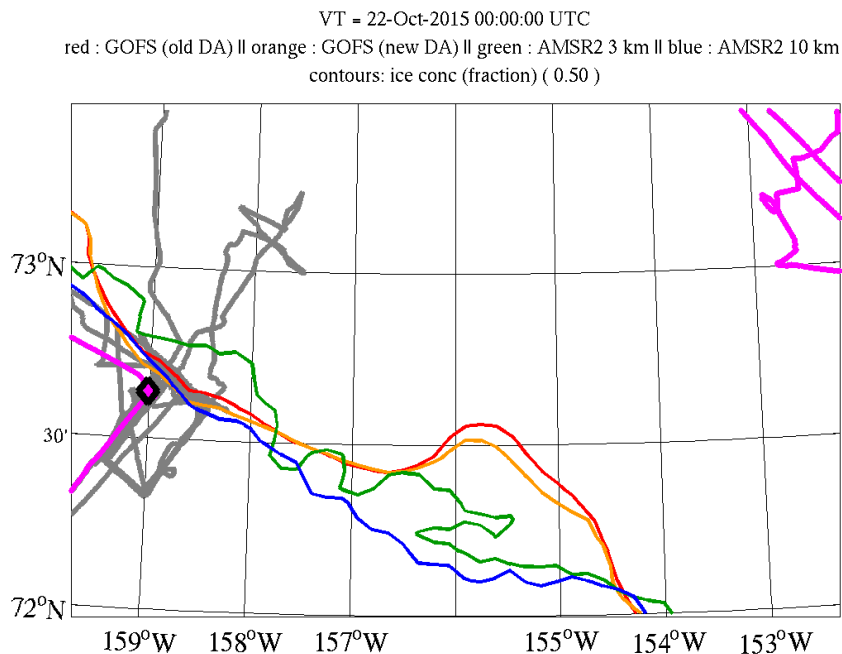


Figure 64. Like Figure 56, except showing 0000 UTC 22 October 2015. The Sea State AWAC mooring is indicated with a black diamond.

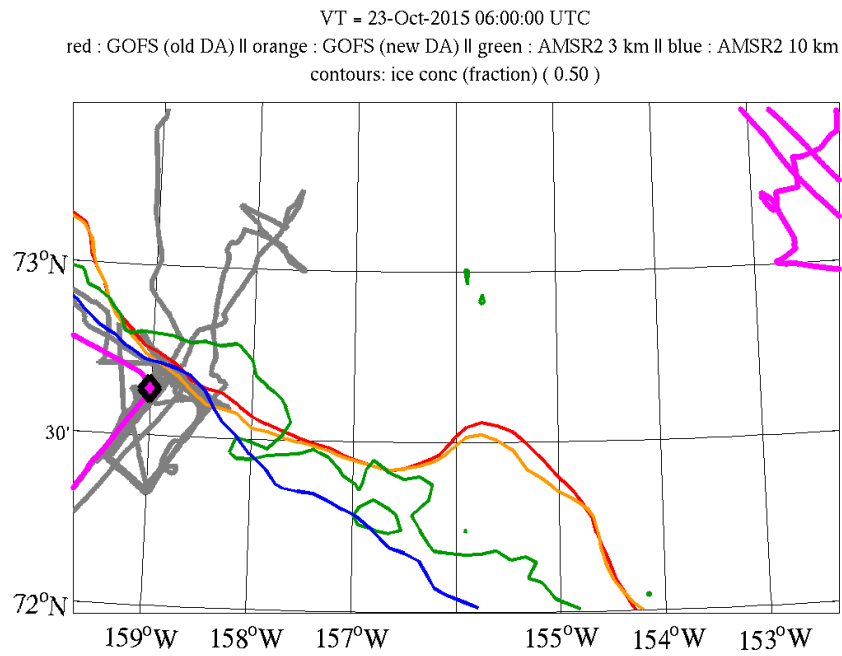


Figure 65. Like Figure 64, except showing 0600 UTC 23 October 2015.



Figure 66. SAR image from screenshot of the *Sikuliaq* Mapserver created by Steven Roberts (U. Alaska). NIC RadarSAT-2 for 0356 UTC 23 October 2015. RADARSAT-2: © MDA 2015. The red line is the cruise track near the Racetrack and AWAC mooring.

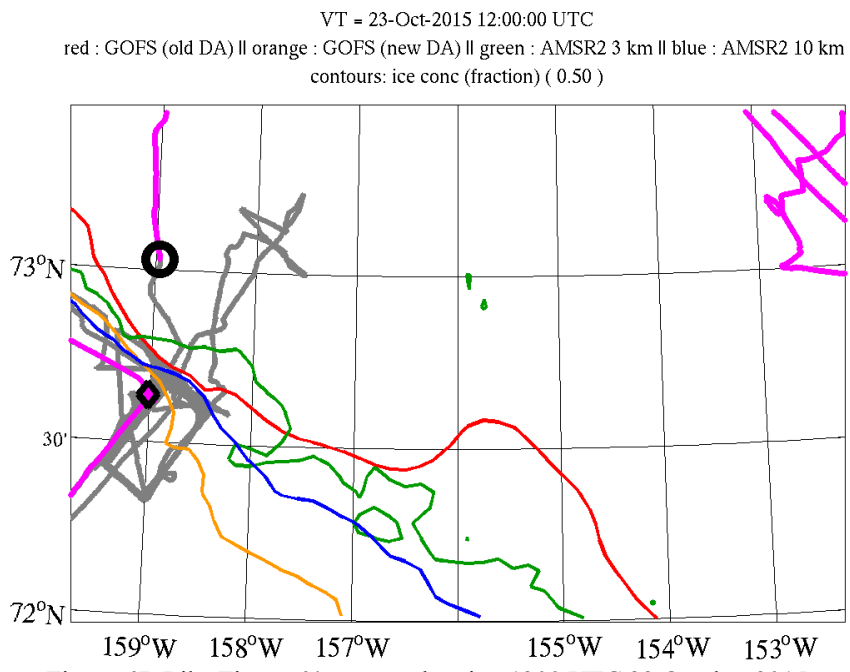


Figure 67. Like Figure 64, except showing 1200 UTC 23 October 2015.

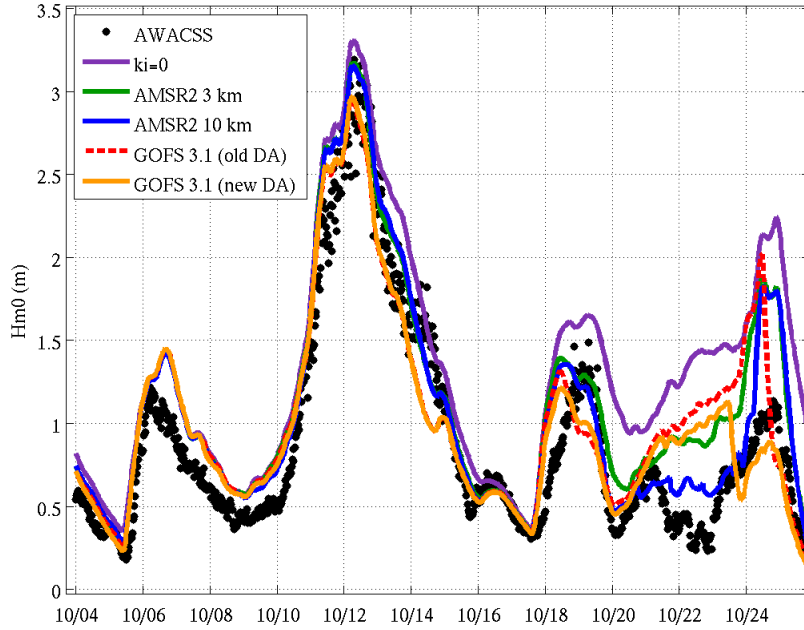


Figure 68. Time series of significant waveheight  $H_{m0}$  at the location of the Sea State AWAC mooring. Black dots are AWAC observations and the five colored lines are output from WW3 hindcasts, as indicated in the legend. The “ $k_i=0$ ” (purple) line is the case of zero dissipation by ice (with 10 km AMSR2 forcing), but wind input is still reduced by ice cover. The other four lines are hindcasts which are identical except for the source of ice forcing, indicated in the legend. (“Old DA” refers to nowcast and “New DA” refers to the reanalysis.)

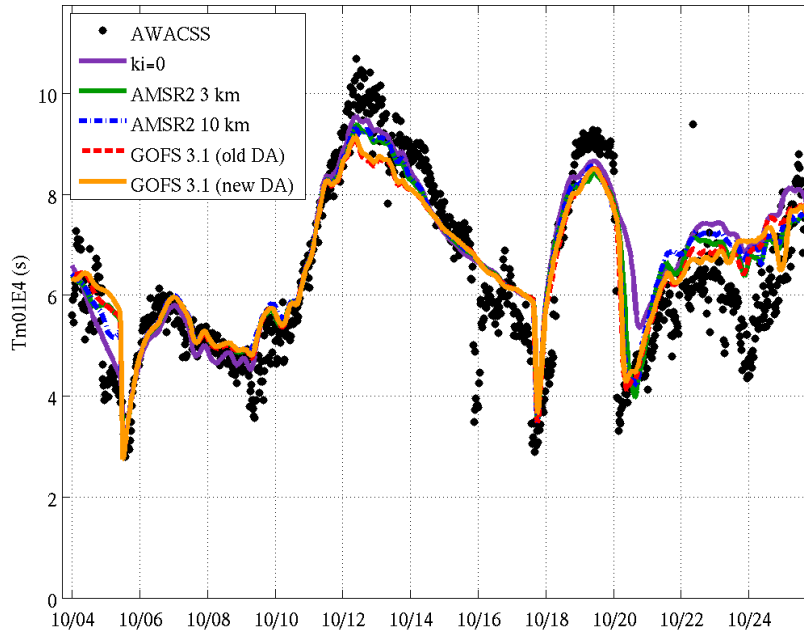


Figure 69. Like Figure 68, except showing the dominant wave period  $T_{m,01,E4}$ , which is defined in Section 6.3.2.

## 5. Evaluation of wind forcing

In this section, we briefly review the quality of wind forcing during the cruise. This is done in two ways: skill of wind speed analyses for the duration of the cruise and skill of forecasts during the WA3 wind event. We look at three products:

1. FNMOC NAVGEM (Hogan et al. 2014),  $0.5^\circ$  resolution<sup>22</sup>.
2. FNMOC COAMPS (Hodur 1997), on a 16-km resolution polar stereographic Arctic grid.
3. ECMWF winds, remapped to a 12.4 km polar stereographic grid, provided by Dr. Justin Stopa (Ifremer).

Items 1 and 2 are essentially the same products that were sent to the *Sikuliaq* for forcing the on-ship wave model during the cruise.

The potential role of thermal stability effects on wave growth during Wave Array 3 (WA3) is evaluated in another section of this report, after the hindcasts are presented: see Section 6.3.5.

### 5.1. Skill of wind speed analyses (entire cruise)

In this case, we are using the analyses from the realtime products. NAVGEM and COAMPS fields are created by using  $\tau = 0$  hours (analysis) to  $\tau = 9$  hours (forecast) fields from consecutive 12 hour run cycles, with spacing of 3 hours between fields. Ifremer fields are used as provided, also at 3 hour intervals.

The wind forcing provided to WW3 is as 10-meter wind vectors. This is compared to wind vectors measured by the anemometer on the ship, adjusted to 10 meters using a simple power law relation. Meteorological data were provided by Drs. Ola Persson, Byron Bloomquist, and Chris Fairall (NOAA). Scatter plots and statistics for these  $U_{10}$  match-ups were created for each of the three wind products. However, these comparisons are not included in this report. Instead, we target a less conventional quantity for comparison: one that is of direct relevance to the wave model: wind stress. This quantity puts higher emphasis (in bias calculations, etc.) on the higher wind speeds, consistent with the fact that a disproportionate fraction of wave energy is produced by higher winds. We do not compare *actual* wind stresses, however. [In the context of the wave model, the *actual* wind stress would be that associated with the  $U_*$  calculated by the model's wind input source function,  $\tau = \rho_a U_*^2$ , where  $\rho_a$  is the density of air<sup>23</sup>. In the context of the observations, the *actual* wind stress would be calculated from one of two methods: eddy covariance or inertial dissipation.] Since our goal is to emphasize higher wind speeds, while still essentially evaluating the 10-meter wind speed forcing, we simply take the  $U_{10}$  from model and observations and pass it through a bulk formula:  $\tau = \rho_a C_d U_{10}^2$ , where  $C_d$  is calculated using the algorithm of Hwang (2011). This is shown in Figure 70, Figure 71, and Figure 72 for ECMWF, NAVGEM, and COAMPS respectively. The results indicate that skill associated with correlation (r) and scatter index (SI) is roughly comparable for all three models, with the ECMWF winds having a slight advantage (SI=0.43 vs. 0.46 for NAVGEM). The ECMWF winds also seem better in terms of bias: -6% compared to +11% with NAVGEM. However, we can see something in the plots not obvious in the skill scores: ECMWF does not capture the highest winds, under-predicting all the points with  $\tau$  of 0.42 to 0.62 Pa. COAMPS has a similar problem, though not as severe. NAVGEM, on the other hand, is relatively well-centered on the best fit line at the higher wind speed range,  $\tau = 0.1$  to 0.62 Pa. These higher wind speeds are associated primarily with

---

<sup>22</sup> A  $0.28^\circ$  NAVGEM product is also available for 2015. In this report, we use that higher resolution product only during our evaluation of thermal stability effects. See Section 6.3.5.

<sup>23</sup> Note that the symbol  $\tau$  is used here for two very different variables: the time of the forecast in hours, and the wind stress. However, it should be clear from context which one is referred to.

WA3, which implies that the Navy models may be a better choice for WA3 hindcasts. Yet, we should also keep in mind that most of the wave energy in WA3 was generated southeast of the array, where the winds were not measured by ship anemometer.

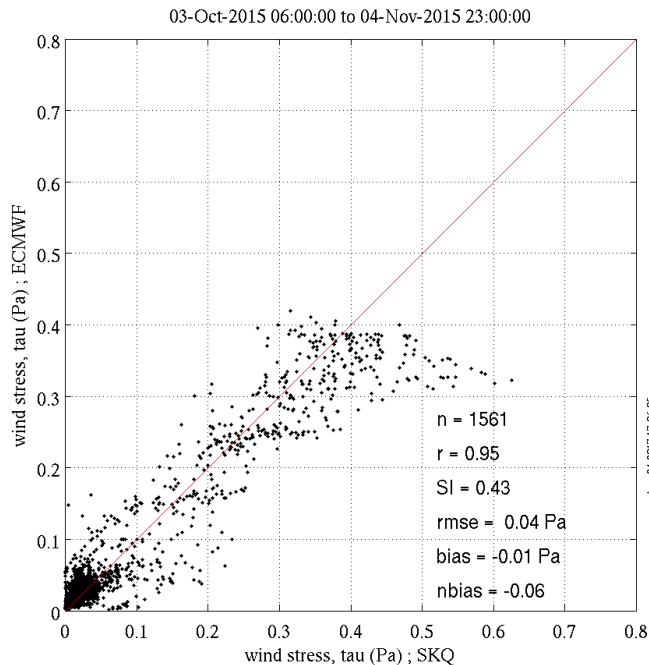


Figure 70. Evaluation of 10-meter winds from ECMWF. Ground truth is derived from winds measured with an anemometer on the ship. For both quantities, the 10-meter wind speeds have been converted to wind stress using an empirical model (see text). In the case of the anemometer, the wind speed is converted to 10 meters using a simple power law formula. Statistics are shown on the plot.

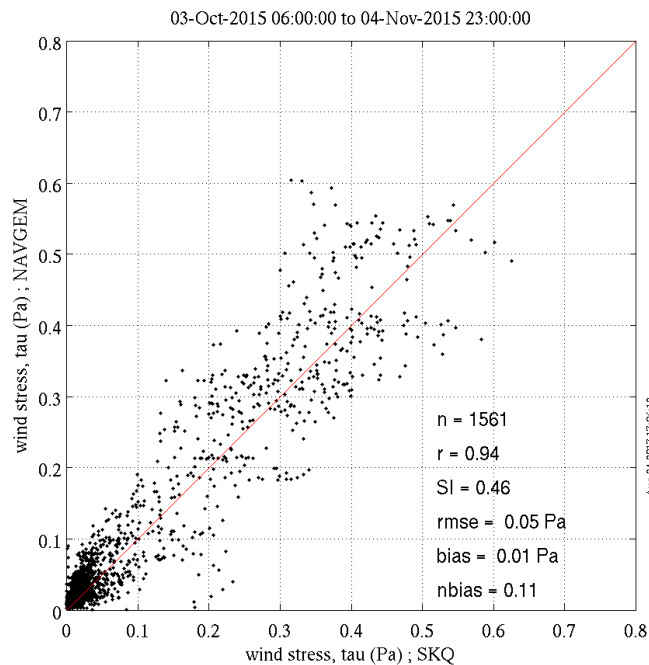


Figure 71. Like Figure 70, except evaluating the 10-meter wind speeds from NAVGEM.

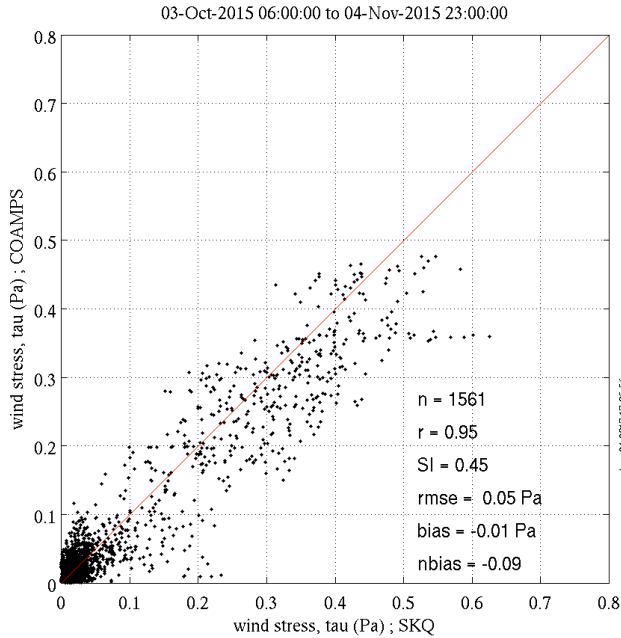


Figure 72. Like Figure 70, except evaluating the 10-meter wind speeds from COAMPS.

## 5.2. Skill of wind speed forecasts (WA3 only)

In this section, we look at the skill in the multi-day forecasts for the WA3 case. Here, we only consider the COAMPS and NAVGEM models, since we do not have access to the ECMWF multi-day forecasts. We are interested in the primary generation region for the waves encountered in WA3, and the underlying question is “Which model best forecast the WA3 wind event several days before it happened?” We define the generation region by drawing a polygon for the higher winds from NAVGEM on 0000 UTC 12 October (Figure 73). Then, the mean wind speed within the polygon is calculated for all forecasts of that date. This is shown in Figure 74. The rightmost points in this figure are the analyses (nowcasts) and may be considered as the “target value”. COAMPS provides forecasts out to 4 days and NAVGEM to 7.5 days.

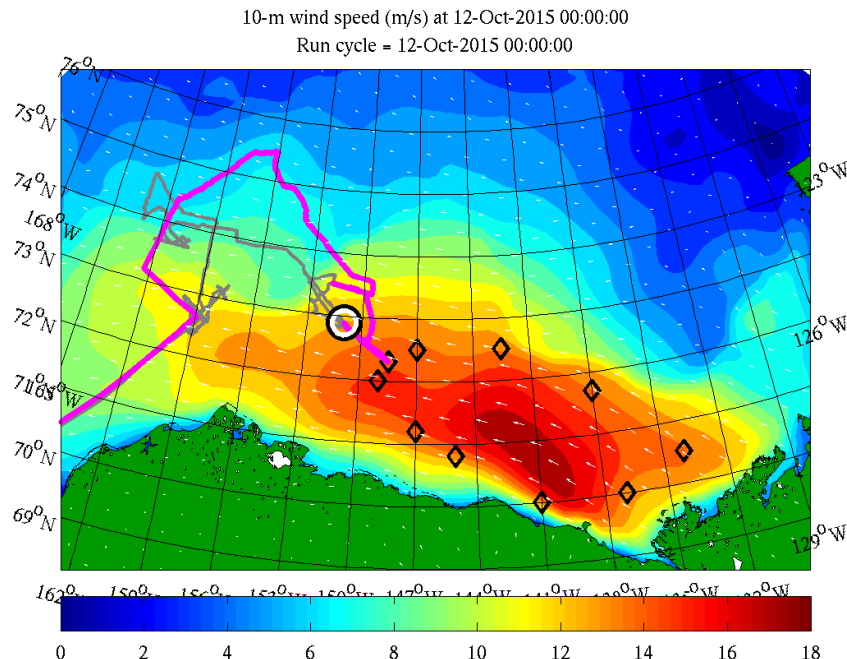
We do not believe that using NAVGEM to draw the polygon gives any advantage over COAMPS in the subsequent comparison, since COAMPS and NAVGEM have the same mean wind speed in the polygon at the analysis time, 0000 UTC 12 October. In other words, both models have identical values in the rightmost points in Figure 74.

The comparison indicates that both models underpredicted the strength of the wind event in their forecasts. However, the NAVGEM prediction was clearly superior. Four days prior, NAVGEM was not far below the target wind speed, and by two days prior, it was fairly close. By contrast, COAMPS lagged far behind, and didn’t predict mean wind speed above 12 m/s until 12 hours prior. We do not know the cause of the problem in COAMPS. It is surprising that this model would be less skillful, since the conventional wisdom is that higher resolution models are better able to handle larger pressure gradients and thus higher wind speeds.

The results are consistent with the impressions of the author (ER) about the skill of the forecasts for WA3 in the week prior to WA3: wave model forecasts using NAVGEM winds tended to be

better than those using COAMPS winds. Further, though we did not look at the ECMWF model in this section, it is the author's impression that the ECMWF atmospheric model (in the graphical products provided by Dr. Jean Bidlot in realtime) predicted the WA3 event better than the Navy models; insofar as the event first appeared in the ECMWF forecasts a day or two sooner, giving more advance notice.

The skill of the NAVGEM forcing in context of WW3 skill for WA3 was also discussed in Section 2.3.1.



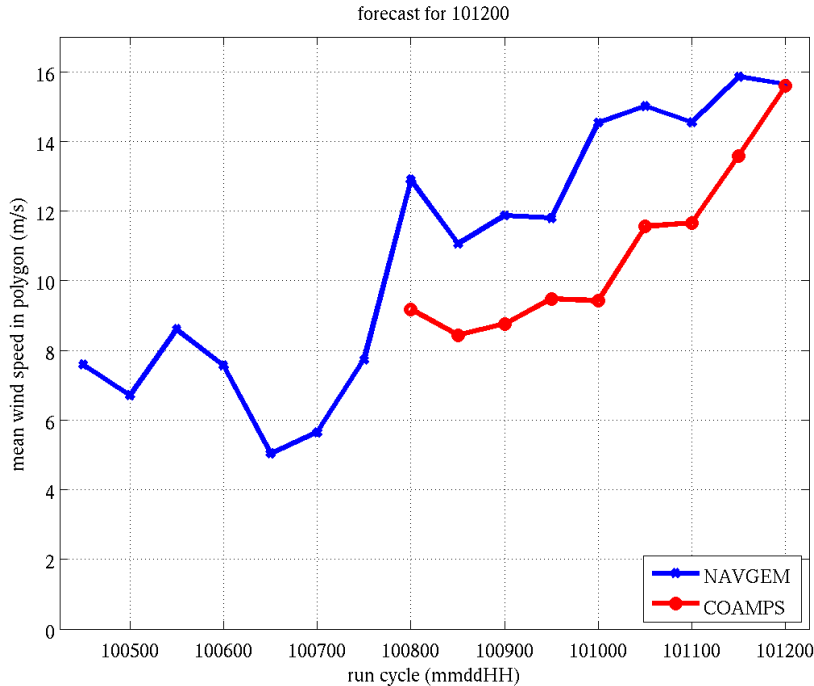


Figure 74. Forecast skill for NAVGEM and COAMPS, combining forecasts from several run cycles. All points correspond to the forecast or nowcast for 0000 UTC 12 October 2015. Vertical axis is the mean wind speed within the polygon of Figure 73. Horizontal axis is the run cycle used, so the rightmost value (101200) is the nowcast run cycle and all values to the left are forecast run cycles. The leftmost blue value (100412) is the forecast produced by NAVGEM on 1200 UTC 4 October, and is therefore a 7.5-day forecast. The leftmost red value (100800) is the COAMPS forecast on 0000 UTC 8 October, so it is 4-day forecast.

## 6. WW3 hindcasting

Here, we describe wave hindcasts performed for the field experiment post facto, using the analysis forcing rather than forecast forcing.

### 6.1. Model Implementation

#### 6.1.1. Grid design

The model is run in a nested fashion, with two irregular grids. The outer grid has 10 km resolution and the inner grid has 5 km resolution. The outer grid is a polar stereographic grid covering half the Arctic, including portions north of eastern Siberia, Alaska, and most of Canada (cyan region in Figure 75). Swell energy from outside this grid is excluded, as it is insignificant within the study area. The inner WW3 grid fully encloses the study area, and is also shown in Figure 75, as a black rectangle. This grid is irregular but not polar stereographic: it has a central meridian at 156.5W (near Barrow, Alaska), and grid lines were constructed by tracing great circles west and east from the central meridian, starting from points at 5 km intervals on the meridian; similarly, spacing along the great circles is 5 km.

These grids were also used in Collins and Rogers (2017), but are different from those used for the on-ship forecasting and the Rogers et. al (2016) hindcasting (Figure 34); for the latter, the inner grid was coarser (10 km) and extended all the way to the Alaska coast.

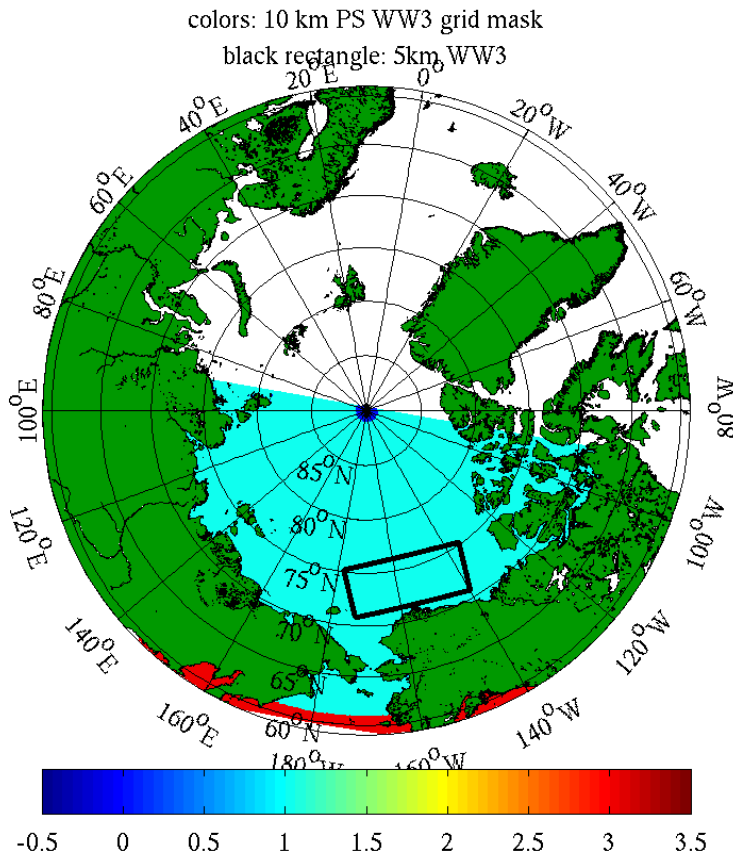


Figure 75. WW3 grids. Color indicates mask of outer (10 km) WW3 grid. Cyan indicates active grid points, while red and blue indicate inactive grid points. White is outside the grid. The black rectangle is the outline of the 5 km inner WW3 grid.

### 6.1.2. Settings and Initialization

Settings used for all grids are as follows:

- 36 directional bins
- 30 frequency bins, from 0.045 to 0.7138 Hz
- overall time step is 900 s
- Ardhuin et al. (2010) physics parameterizations (denoted "ST4").
- ST4 physics has a parameter,  $\beta_{max}$  ("BETAMAX" in the WW3 code), intended to be adjusted to accommodate gross wind bias. Altering this parameter is, in practice, similar to a "blunt tool" adjustment of the wind speeds. In these simulations, we used  $\beta_{max} = 1.2$ .<sup>24</sup> This is a relatively low value, appropriate to the positive bias of the NAVGEM wind forcing. It is selected here to be consistent with the  $\beta_{max}$  used in Navy global models undergoing testing now for ESPC, also with NAVGEM forcing. The value is appropriate judging from comparisons of model waveheight to data measured by WA3 buoys which were primarily in open water, see Figure 128.

Settings for the outer grid are as follows:

<sup>24</sup> Collins and Rogers (2017) used a similar model design, but used  $\beta_{max} = 1.1$ .

- Run time is 1200 UTC 20 September 2015 to 0000 UTC 10 November 2015 (cold start)
  - propagation time step is 450 s
  - $S_{ice}$  is IC4M6H, defined in Section 6.2.3.
  - Ice concentration forcing from the 24-hourly AMSR2 (ASI algorithm)

Settings for the inner grid are as follows:

- Run time is 1500 UTC 1 October 2015 to 0000 UTC 10 November 2015 (hot start, see below)
  - propagation time step is 225 s
  - Several  $S_{ice}$  parameterizations are employed: see descriptions.
  - Ice concentration forcing is from 10 km AMSR2 (NT2 algorithm), except where otherwise noted, e.g. the hindcasts using GOFS 3.1 forcing.

The inner grid is hot-started 1500 UTC 1 October 2015 from a prior simulation with the same grid, using the 24-hourly AMSR2. That simulation is cold-started on 1200 UTC September 20 2015 (same as the outer grid). Here, we use the term “cold start” to indicate that there is a period of spin-up with invalid output, though the model was not actually started from rest. We judge that for this relatively small basin, the 10-day spin-up time is conservative.

## 6.2. WW3 Inversion

In this section, we describe use of the WW3 hindcasts in an inversion process. This is described prior to the forward modeling because results from the inversion are used in the forward modeling.

The inversion process follows that of Rogers et al. (2016), but with some significant differences:

- 1) A higher resolution grid is used (5 km inner grid rather than 10 km inner grid).
- 2) Different ice forcing is used (the 10 km AMSR2 product rather than a Navy CICE product).
- 3) The inversion is performed for all wave experiments (excepting WA1, which falls outside the inner grid), whereas the Rogers et al. (2016) inversion was only for WA3.

### 6.2.1. Methods

#### *Inversion method*

A model inversion determines the model inputs that will produce a desired model output. Here, we determine the optimal dissipation profile  $k_i(f)$  that provides a match to each buoy spectrum. In the first step, the model is run for 17 different fixed  $k_i$  values (IC1 model), from 0 to 0.005 m<sup>-1</sup>. The buoy and model spectra are then organized into eight coarse frequency bins centered at 0.075, 0.120, 0.175, 0.225, 0.275, 0.325, 0.375, and 0.445 Hz. The coarse resolution increases the degrees of freedom of the spectra with the intent of providing more reliable results (e.g. Elgar 1987). As the spectra are now co-located in time, space, and frequency, the inversion is simply a minimization process for  $|\log_{10}(E_{model}(f)/E_{obs}(f))|$ , as illustrated in Figure 76. The end result

is the dissipation profile  $k_i(f)$  for each buoy spectrum<sup>25</sup>. Thus, for each spectrum and for each frequency bin, we have determined the optimal  $k_i$ , where  $E_{obs}(f) = E_{model}(f)$ .

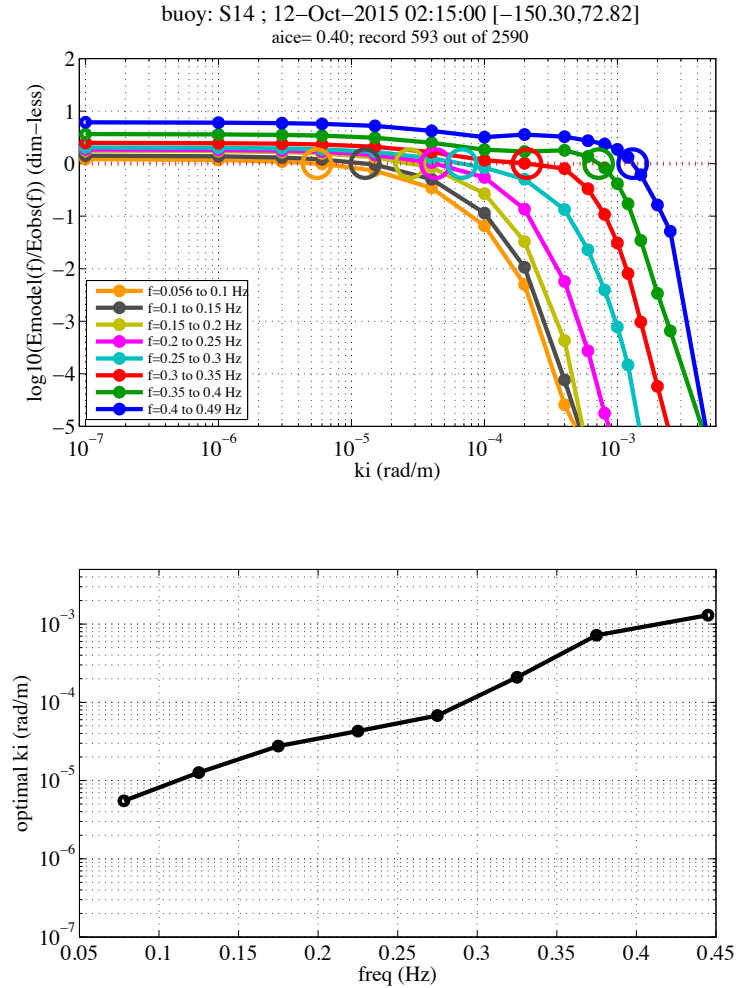


Figure 76. Inversion procedure: example of successful inversion. Shown is the inversion for the spectrum measured by SWIFT14 on 0215 UTC 12 Oct. 2015, which is inversion number 593 out of 2590. Position and AMSR2 ice concentration (“aice”) are indicated in title text. Top panel shows model-data mismatch vs.  $ki$ . A zero on vertical axis corresponds to “optimal value” of  $ki$  (circles), determined by linear interpolation from model vs. observation comparisons (dots). Each discrete value on the horizontal axis corresponds to a separate simulation. Each curve corresponds to a frequency interval of the spectrum (see legend). Lower panel:  $ki$  solution vs. frequency. See text for further explanation.

#### *Limitations and assumptions*

The following is a recapitulation of the discussion in Rogers et al. (2016): This method does have limitations. First, dissipation is not instantaneous, but is rather an integrated effect. This implies that the  $k_i(f)$  includes the effect on the wave spectrum of ice at previous times, and other (up-wave) locations, and it must be recognized that this ice is variable in time and space.

<sup>25</sup>  $E_{model}(f)$  can be zero. To prevent  $\log_{10}(0) = -\infty$ , we apply a minimum limit on  $\log_{10}(E_{model}(f)/E_{obs}(f))$  of -5. In other words, differences larger than five orders of magnitude are just treated as differences of five orders of magnitude.

Second, there is an assumption of linearity, specifically that the solution for optimal  $k_i$  at one frequency is not affected by use of non-optimal  $k_i$  at neighboring frequencies in the same “fixed  $k_i$ ” simulation. The validity of this assumption is discussed further in Rogers et al. (2016). This assumption in particular implies that any parameterization coming from the inversion must be tested in a forward model. Third, the inversion, like the forward model, does depend on the accuracy of the forcing: the outcome depends on the accuracy of the ice concentration fields, since the source functions are scaled with ice concentration (Section 3.1). For example, if the input concentration is biased low, the inversion will compensate by reporting a higher  $k_i$ . Fourth, the inversion, like the forward model, depends on the accuracy of the wave model. As discussed in Rogers et al. (2016), we have particular concerns about the assumption that wind input scales with the fraction of open water.

*Lower ice concentration: implication for inversion*

In Rogers et al. (2016), the Navy CICE ice concentration was used in the inversion, and it was done only for WA3. In WA3, Navy CICE models had unrealistically high ice concentration over the entire array (Section 4.3.2); this being the case, the Rogers et al. (2016) inversion *did not* include cases of where the buoy was—according to the model forcing—in low ice concentration. As noted above, here we are using AMSR2 concentration, and looking at all relevant drifting buoy data. Thus, we have *many cases* where the buoy was—according to the model forcing—in low concentration ice. This has implications for the inversion, since it operates on the sensitivity of the WW3 model to the  $k_i$  in IC1. The  $S_{ice}$  source function is scaled by ice concentration, so in the extreme case of zero ice concentration everywhere in the domain, the sensitivity of WW3 to  $k_i$  is zero, and for the less extreme cases of low ice concentration, the sensitivity may exist, but will be weak. Similarly, if there is ice in the domain, but not near the buoy, the sensitivity may be weak. Figure 77 is an example. Here, the ice concentration is zero near the buoy. The model results do show some sensitivity to the  $k_i$  in IC1 (the frequency lines are not horizontal), which indicates that some wave energy is traveling through a region with ice before arriving at the buoy. However, that sensitivity is weak: the lines are nearly horizontal, and so they do not intersect the line  $|\log_{10}(E_{model}(f)/E_{obs}(f))| = 0$ , so there is a null solution, and the inversion fails for these frequencies/lines (in this case, all of them). In subsequent presentation of  $k_i(f)$  profiles, we only include those corresponding to  $a_{ice} > 0.25$ , and only cases with a valid solution for at least 4 of the 17 frequencies. 1649 of the 2590 buoy spectra met both criteria. None of the  $k_i(f)$  profiles from WA2 pass these criteria.

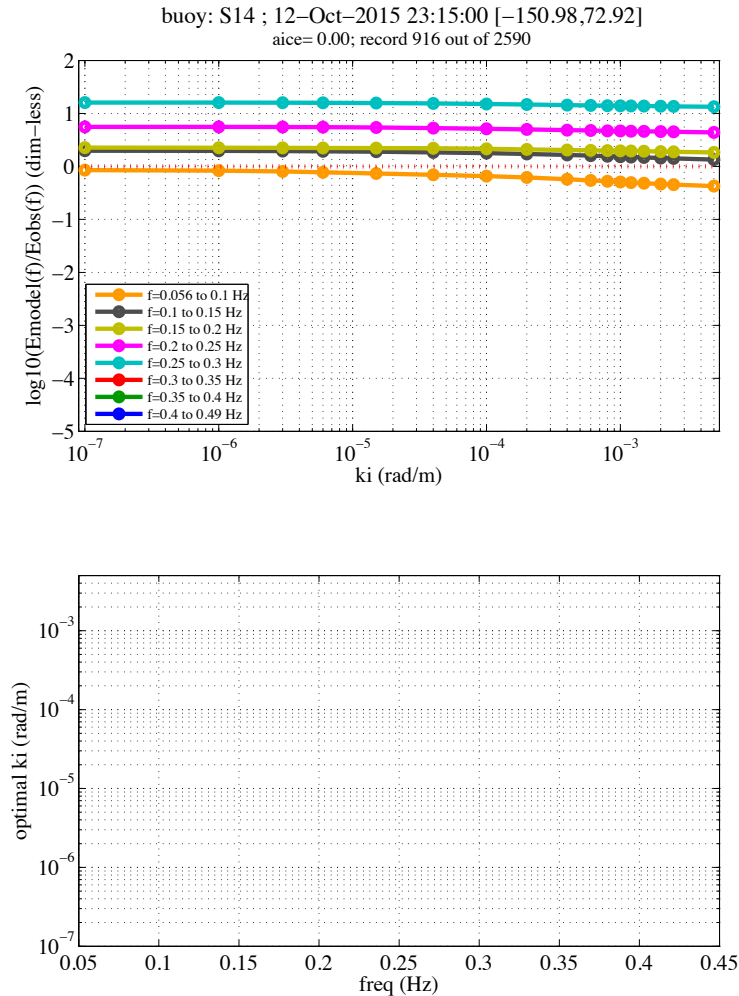


Figure 77. Inversion procedure: example of failed inversion. The lower panel is intentionally blank. Shown is the inversion for the spectrum measured by SWIFT14 on 2315 UTC 12 Oct. 2015, which is inversion number 916 out of 2590. Position and AMSR2 ice concentration (“aice” are indicated in title text. Top panel shows model-data mismatch vs.  $ki$ . Lower panel:  $ki$  solution vs. frequency. See text for full explanation.

#### Low wave energy: implication for inversion

In Rogers et al. (2016), only WA3 was investigated, so there were no buoy spectra with low waveheight. Here, since we include all relevant wave experiments, there are cases with low waveheight. A notable example is IS1, where wave energy was near zero, e.g. Figure 78. These cases exhibit extreme sensitivity to the  $ki$  in IC1 (most lines are nearly vertical), since wave energy must pass through a large amount ( $>100$  km) of rigid ice to reach the buoys. This high sensitivity would tend to imply high confidence in the resulting  $ki(f)$  profiles. However, in this case, the wave energy is so low that the buoy spectra may contain significant noise. Thus, the IS1 profiles must be taken with a grain of salt.

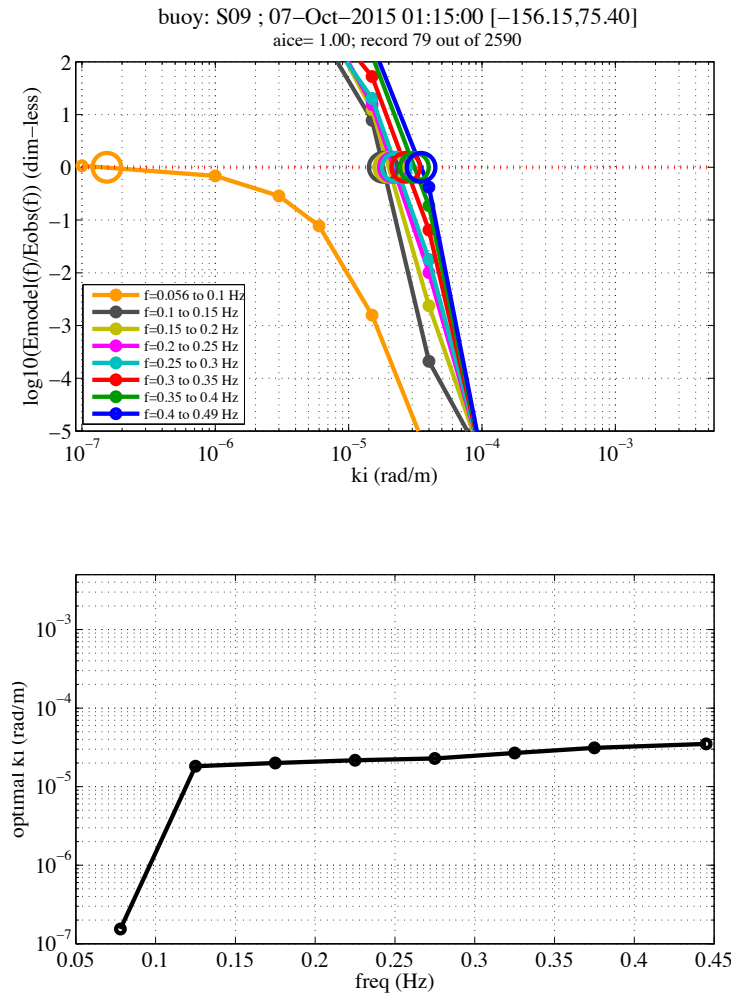


Figure 78. Inversion procedure: example inversion for case of very low wave conditions (Ice Station 1). Shown is the inversion for the spectrum measured by SWIFT09 on 0115 UTC 7 Oct. 2015, which is inversion number 79 out of 2590. Position and AMSR2 ice concentration (“aice” are indicated in title text. Top panel shows model-data mismatch vs.  $k_i$ . Lower panel:  $k_i$  solution vs. frequency. See text for explanation.

### 6.2.2. Results (all wave arrays)

Figure 79 to Figure 89 show the inversion results— $k_i(f)$  profiles—broken out by wave experiment and buoy type. The profiles are color-coded according to the AMSR2 ice concentration; all else being equal, higher concentration values imply more confidence in the inversion. Two step functions are shown. These step functions are fully explained in Section 6.2.3. Briefly: the black step function is for pancake and frazil ice from Rogers et al. (2016) using Navy CICE forcing in the inversion and the purple step function is for similar ice in the present report, using AMSR2 forcing in the inversion. Since the step functions are the same in all the plots, they provide a convenient reference for comparison between plots.

Recall that the inversion is not performed for WA1 since it falls outside the inner grid and was an open water experiment, and also recall that none of the  $k_i(f)$  profiles passed the two quality control criteria. Thus, IS1 is the first experiment for which we show  $k_i(f)$  profiles; this is Figure 79.

With respect to IS1: if we take these profiles as correct (and not just as an artifact of noise in these extremely low-energy spectra), they are telling us that even for higher frequencies, only very weak damping is required to match the buoy observations. This is, in fact, not unreasonable. If damping is highly nonlinear in the real ocean (similar to the IC2 boundary layer model), then these extremely low-amplitude waves would experience weak dissipation while travelling through the 100+ km of rigid ice.

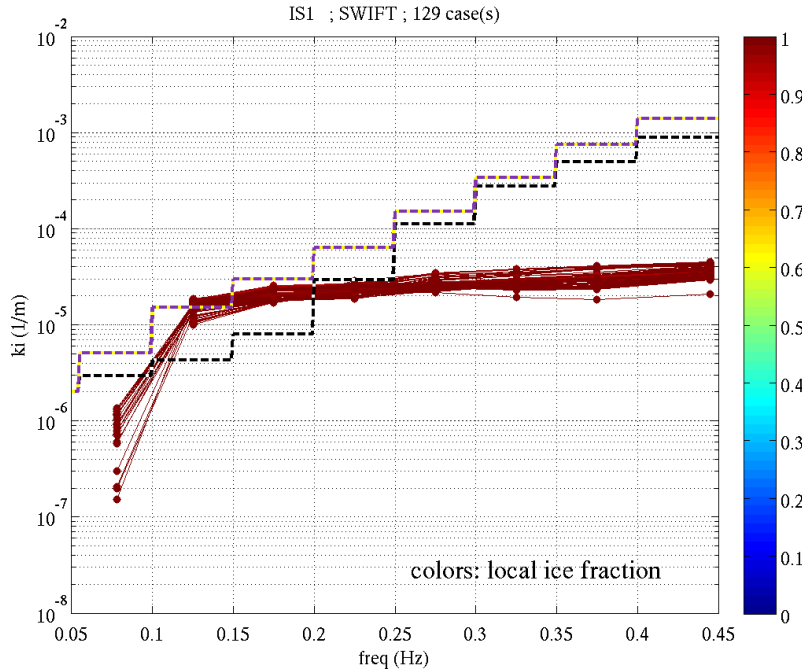


Figure 79. Inversion solutions ( $k_i$  profiles) for Ice Station 1 (IS1), with SWIFT buoys. This includes 129 inversions. Purple dashed line: step function IC4M6H2. Black dashed line: step function IC4M6H. The step functions are introduced in Section 6.2.3. Color indicates ice fraction determined from AMSR2 data.

For the WA3 cases (Figure 80, Figure 81, Figure 82), there is strong qualitative similarity. The  $k_i(f)$  profiles using SWIFT spectra tend to be higher than those using the UK buoys, which is consistent with known dissimilarity between the two buoy types: SWIFT spectra from WA3 tended to be less energetic than those from the UK buoys (Section 6.3.6). More dissipation is required to match the less energetic spectra. The NIWA buoys should not necessarily have similar  $k_i(f)$  profiles, since the NIWA buoys are further into the ice, but they are in fact quite similar to those from the UK buoys.

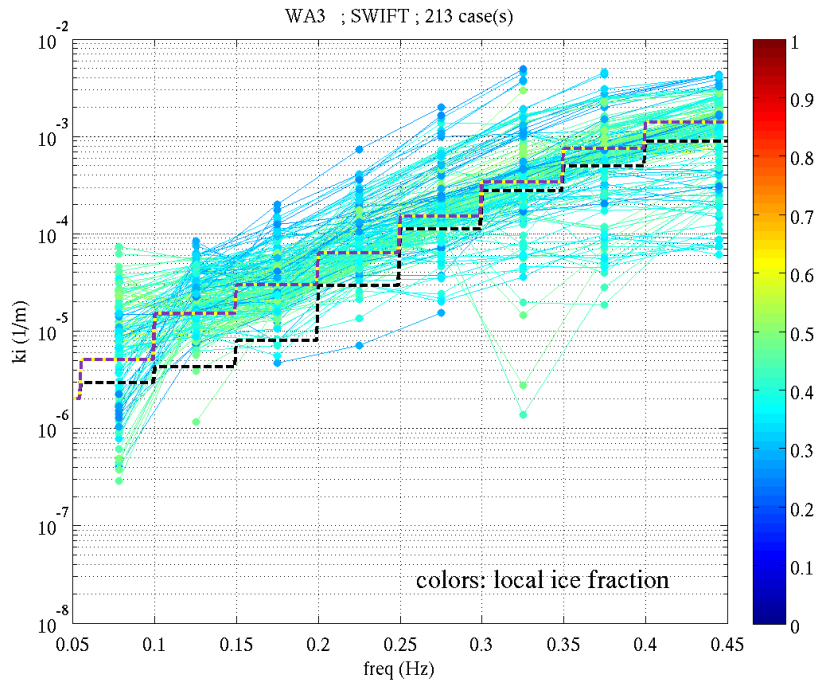


Figure 80. Similar to Figure 79, but for SWIFT buoys in Wave Array #3 (WA3). The number of inversions plotted is indicated in the title above the plot.

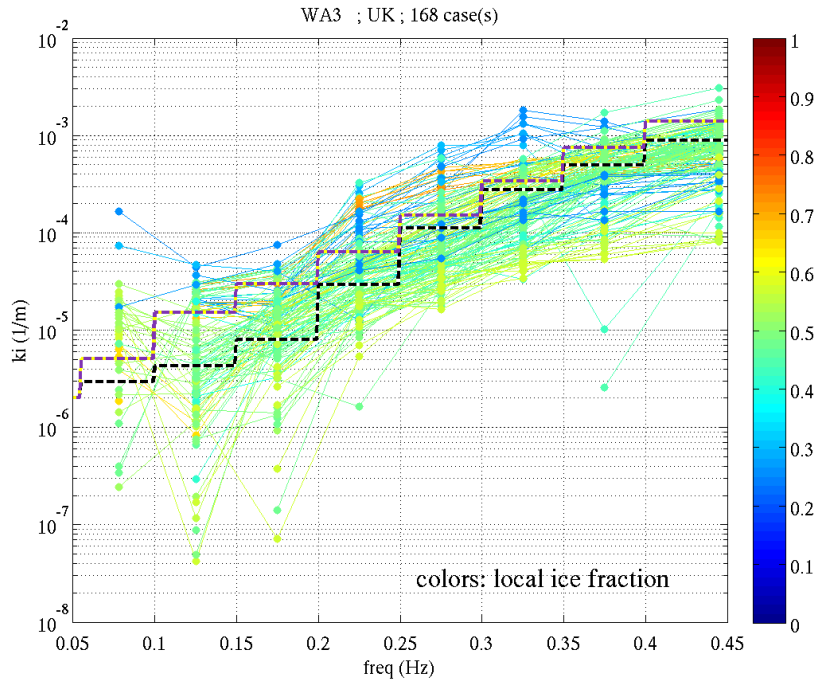


Figure 81. Similar to Figure 80, but for UK buoys in Wave Array #3 (WA3).

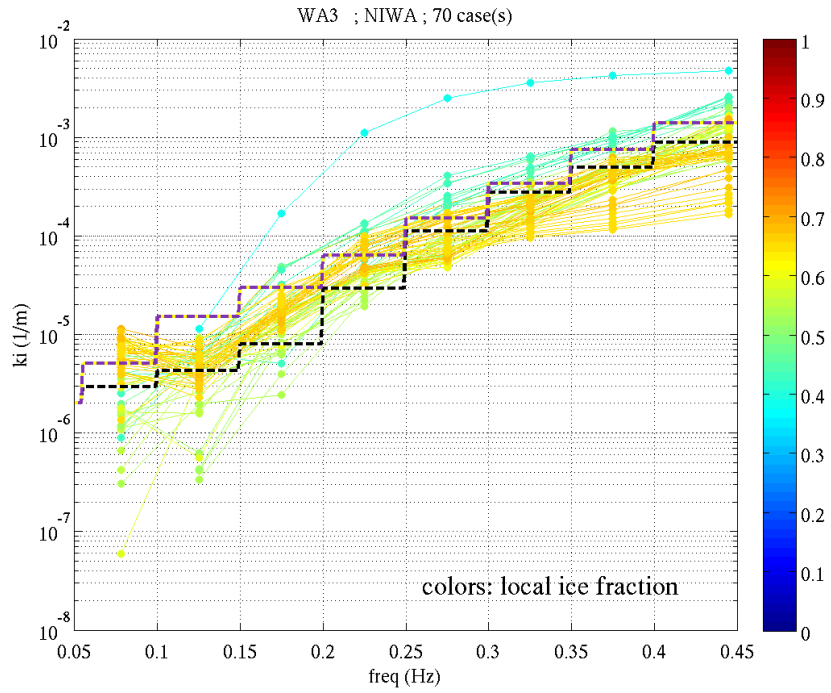


Figure 82. Similar to Figure 80, but for NIWA buoy in Wave Array #3 (WA3).

The profiles for WA4-5 (Figure 83, Figure 84) indicate a leveling off of  $k_i$  at medium to high frequencies, and perhaps even a slight rollover. [“Rollover”, as used in this report, refers to non-monotonic  $k_i(f)$ , and more specifically, the case where  $k_i$  is not maximum at the highest frequencies. ]

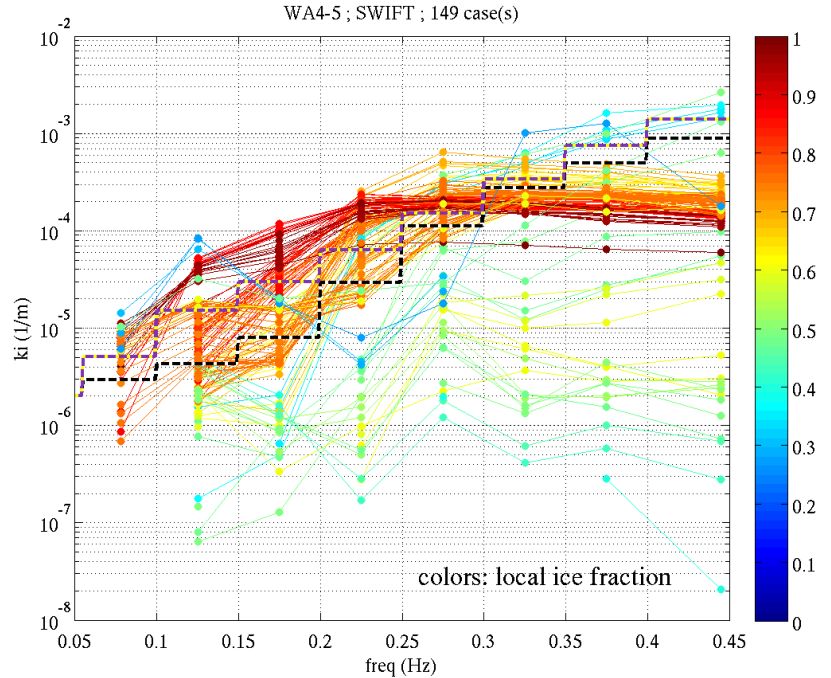


Figure 83. Similar to Figure 80, but for SWIFT buoys in Wave Arrays 4 and 5 (WA4-5).

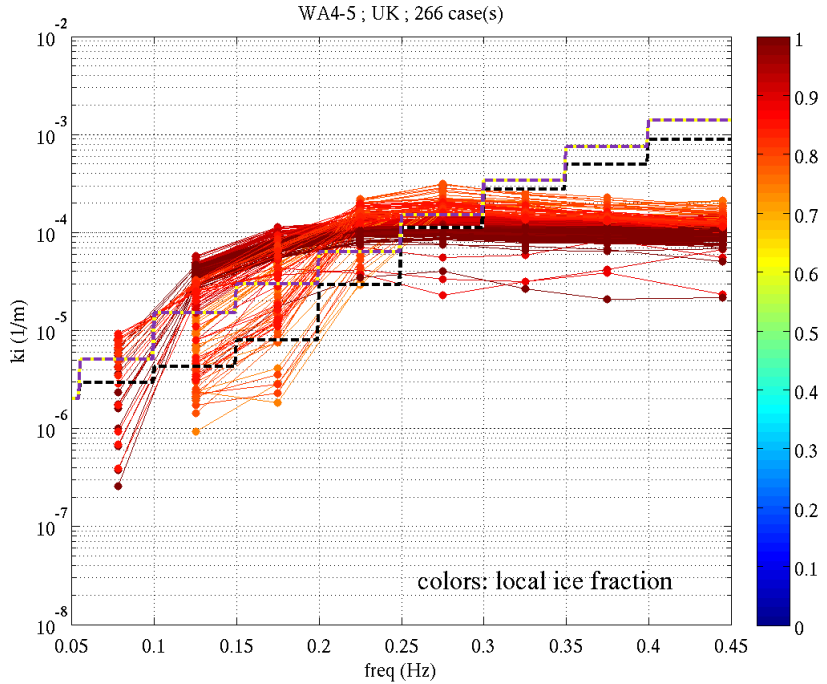


Figure 84. Similar to Figure 80, but for UK buoys in Wave Arrays 4 and 5 (WA4-5).

The WA6  $k_i(f)$  profiles (Figure 85 and Figure 86) are more similar to the WA3 profiles, though the dissipation at the lower frequencies is moderately higher. The RT profiles (Figure 87) show a leveling off similar to those of WA4-5; in this case, there is no inversion estimate for the lowest frequencies. The WA7 profiles (Figure 88 and Figure 89) are similar to those of WA3 again, but there appears to be more spread at the lower frequencies.

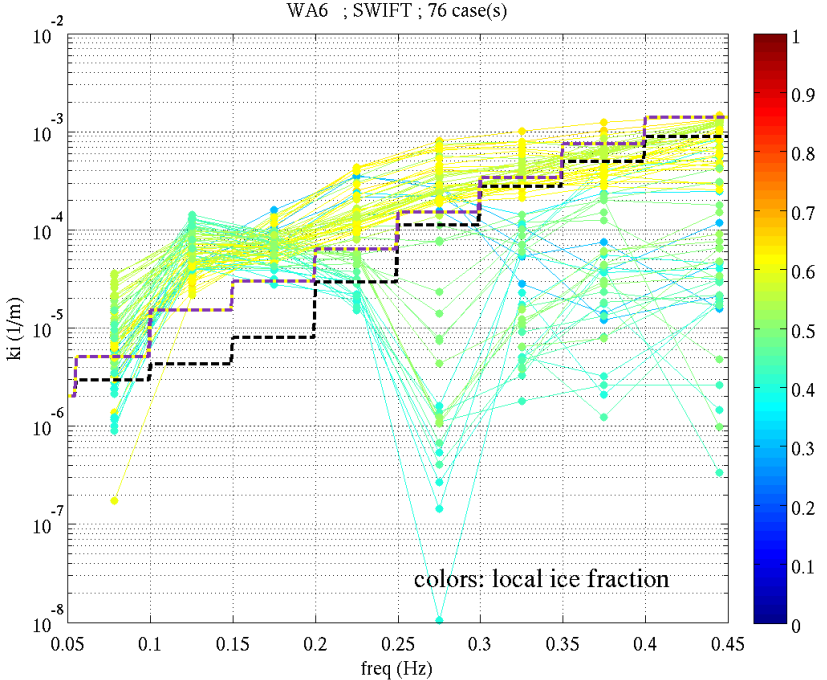


Figure 85. Similar to Figure 80, but for SWIFT buoys in Wave Array #6 (WA6).

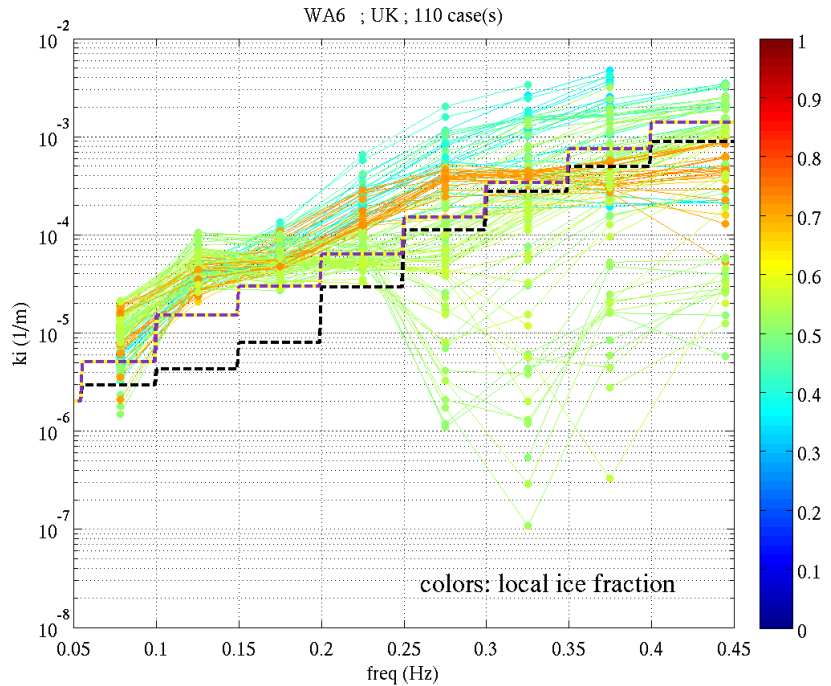


Figure 86. Similar to Figure 80, but for UK buoys in Wave Array #6 (WA6).

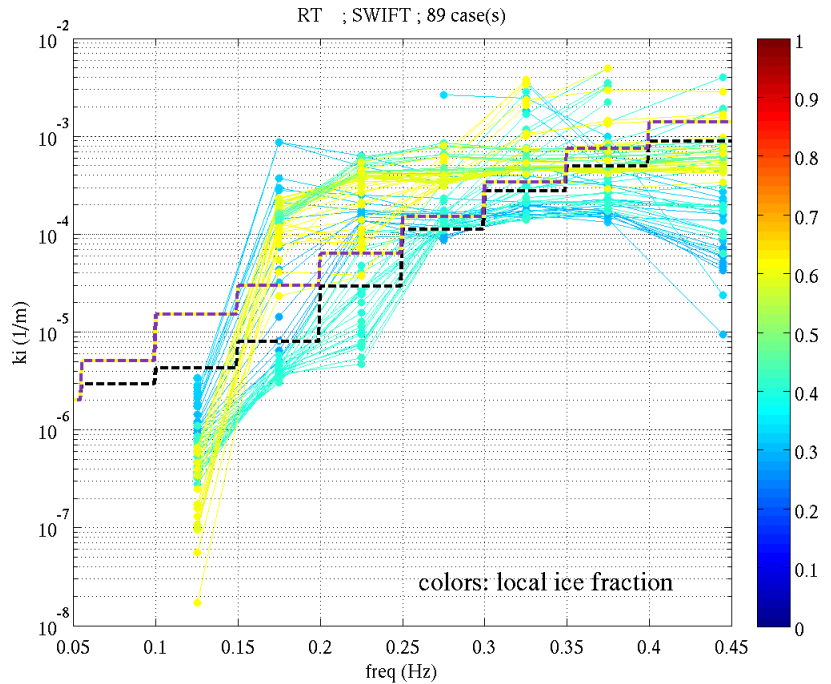


Figure 87. Similar to Figure 80, but for SWIFT buoys in the Racetrack (RT) wave experiment.

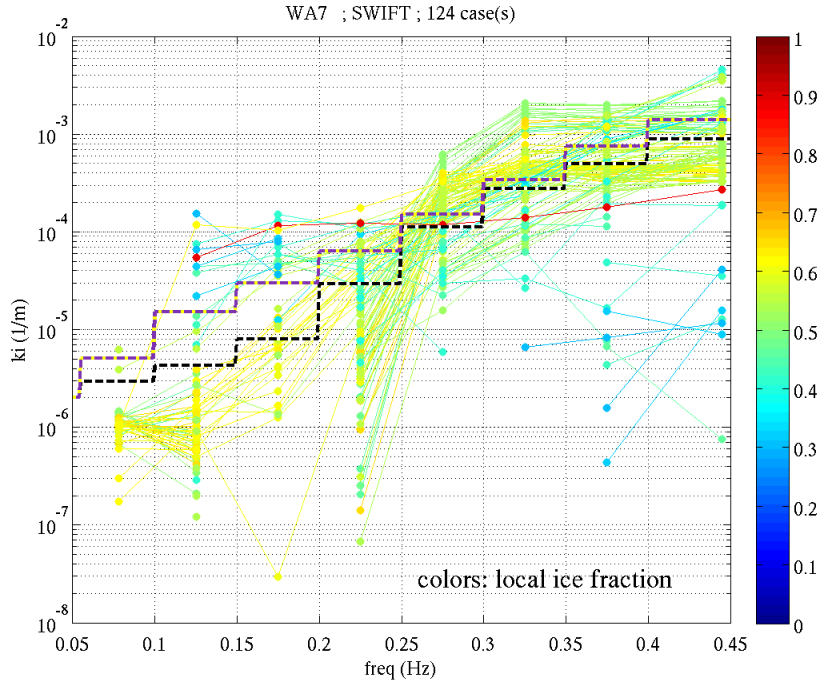


Figure 88. Similar to Figure 80, but for SWIFT buoys in Wave Array #7 (WA7).

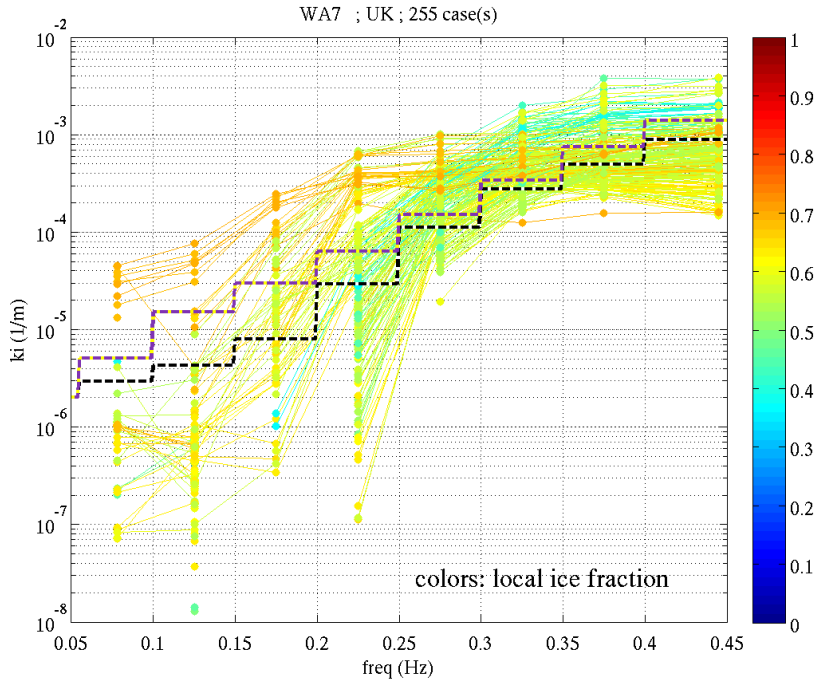


Figure 89. Similar to Figure 80, but for UK buoys in Wave Array #7 (WA7).

### 6.2.3. Parametric step functions for use in WW3: old and new (based on WA3)

The black step function in Figure 79 to Figure 89 is designed to match the “heavy frazil and pancake” cases of Rogers et al. (2016): see the “P/FR-H” (red lines) in Figure 9 of that paper. The figure is reproduced in Figure 90, except that here we use the new ice coding (introduced in Section 7.1) and the black step function is added. This step function was introduced as

“IC4M6H” in Collins and Rogers (2017) and the same name is used herein, when applied using the IC4 routine. However, one change is made: the two steps are added at the lowest frequencies corresponding to the low-frequency dissipation rate estimated by Arduuin et al. (2016). In that paper, they use swells measured by a tiltmeter in the high Arctic; the swell energy had been generated by a massive storm near Svalbard. For users of WW3, the namelist for IC4M6H of Collins and Rogers (2017), with the two low-frequency points added is:

```
&SIC4 IC4METHOD = 6,
  IC4FC = 0.045 , 0.055 , 0.10 , 0.15 , 0.20 ,
          0.25 , 0.30 , 0.35 , 0.40 , 99.0
  IC4KI = 1.0e-6 , 2.0e-6 , 2.94e-06, 4.27e-06, 7.95e-06,
          2.95e-05, 1.12e-04, 2.74e-04, 4.95e-04, 8.94e-04
          /
```

Of course, these two new low-frequency steps do not affect the Sea State hindcasts, due to absence of long waves in the hindcasts.

The purple step function in Figure 79 to Figure 89 is designed to match the cases in Figure 80 and Figure 91 with ice code values from 6 to 12. This implies a larger range of ice code values than IC4M6H, but the  $k_i(f)$  profiles are tightly grouped in Figure 89. This step function is referred to herein as IC4M6H2 when applied within the IC4 module. For users of WW3, the namelist for IC4M6H2 is:

```
&SIC4 IC4METHOD = 6,
  IC4FC = 0.045 , 0.055 , 0.10 , 0.15 , 0.20 ,
          0.25 , 0.30 , 0.35 , 0.40 , 99.0
  IC4KI = 1.0e-6 , 2.0e-6, 5.1e-06 , 1.5e-05 , 3.0e-05,
          6.4e-05 , 1.5e-04, 3.4e-04 , 7.5e-04 , 1.4e-03
          /
```

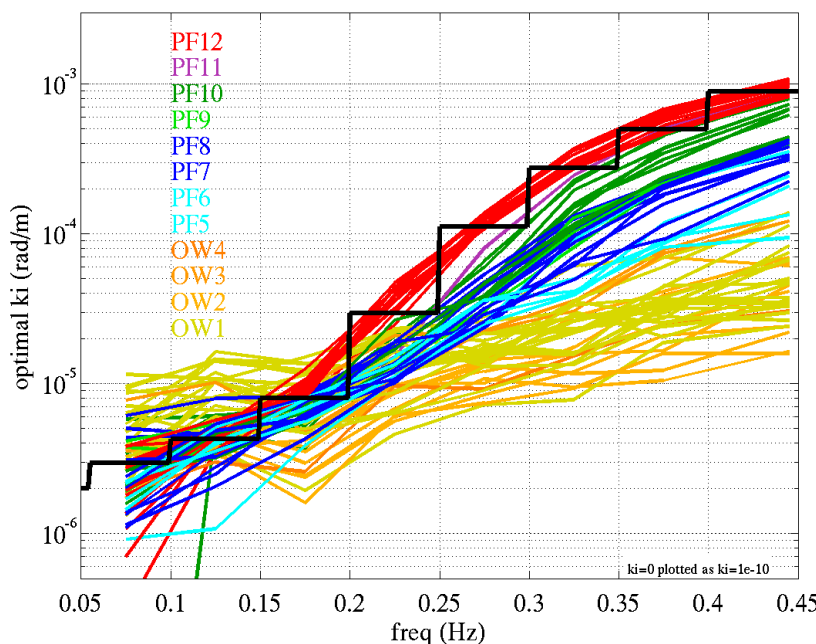


Figure 90. Dissipation profiles  $k_i(f)$  from Rogers et al. (2016). Only the cases with usable ice photos are shown, of which there are 145. The colors indicate “ice codes”, given in the legend, which have been updated since that publication: see Section 7 in this report. The black step function is a fitting to the “P/FR-H” cases in Figure 9 of Rogers et al. (2016), which roughly correspond to the “PF11” and “PF12” ice codes here (heavy frazil and pancake ice, 26 profiles).

We now recapitulate the similarities and differences between the two step functions and the inversions which they are based on:

- The two inversions were performed on different grids (IC4M6H: 10 km and IC4M6H2: 5 km)
- Inversion was performed with different ice concentration input (IC4M6H: Navy CICE and IC4M6H2: AMSR2)
- The step functions are fitted to different range of ice codes
- Both step functions are based on  $k_i(f)$  profiles during WA3 calculated using SWIFT buoys
- Both step functions are fitted to only  $k_i(f)$  profiles which have valid corresponding ice observations (i.e. the entire set of WA3 SWIFT spectra was not used).
- 26  $k_i(f)$  profiles are used in IC4M6H and 48  $k_i(f)$  profiles are used in IC4M6H2.

Also, note that if SWIFT spectra are biased low (see Section 6.3.6), this would cause our step function(s) to be high.

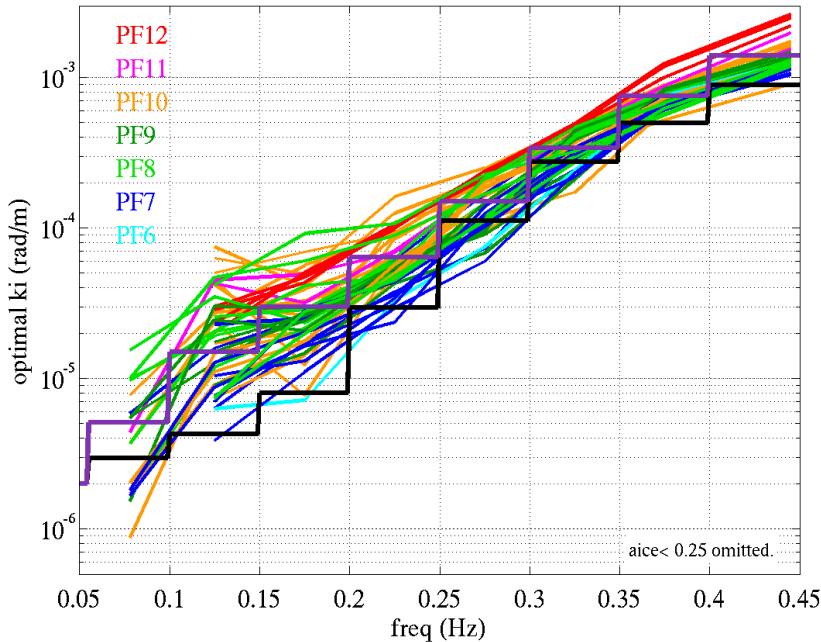


Figure 91. Like Figure 90, except that the new inversion using AMSR2 ice forcing (this report) is shown rather than the inversion of Rogers et al. (2016) which used ice forcing from CICE. The black step function is identical to that in Figure 90. The purple step function is a fit to  $k_i(f)$  profiles shown here (all ice codes; not just PF12). Only the cases with usable ice photos and ice concentration (estimated from AMSR2) greater than 25% are shown, of which there are 48.

#### 6.2.4. Comparisons to literature and other models

In Section 6.2.2, we looked at the variation of the  $k_i(f)$  profiles between the wave experiments. It is also of interest to compare the Sea State  $k_i(f)$  profiles against those from the literature, and from models. Figure 92 compares both step functions against:

- Two variants of the IC3 VE model (Wang and Shen 2010). Both have zero elasticity. Viscosity of each is indicated in the legend.

- The profile proposed by Meylan et al. (2014), which is the example setting for IC4M2 provided with the WW3 distribution (Collins and Rogers 2017).
- The example setting for IC4M1 provided with the WW3 distribution, which is a fitting to the Wadhams et al. (1988) data by Collins and Rogers (2017).
- An unpublished precursor inversion performed by author ER for an AWAC mooring during the advance of the MIZ over the mooring in October 2012.
- The two low-frequency  $k_i$  values from Ardhuin et al. (2016). These are also built into the IC4M6H and IC4M6H2 step functions.

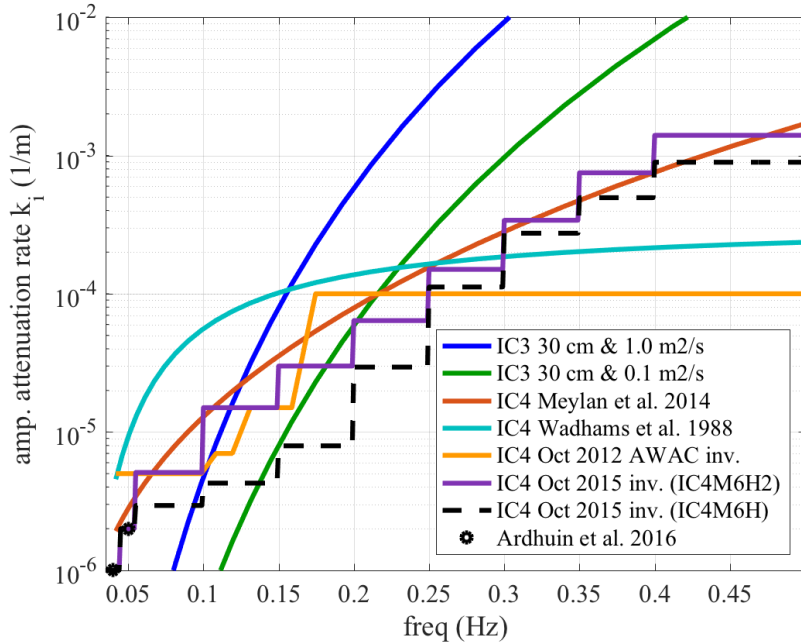


Figure 92. Amplitude attenuation rate  $k_i$  vs. frequency. Profiles from parametric models (IC4) are compared with the IC3 viscoelastic model, and the low frequency  $k_i$  estimates from Ardhuin et al. (2016). The parametric models IC4M6H and IC4M6H2, introduced in Section 6.2.3, are shown as step functions (as they are applied in WW3) corresponding to the eight coarse frequency bins used in the inversion. See text for further explanation.

Figure 93 compares the step functions to the IC2 boundary layer model. This model is nonlinear, where the  $k_i(f)$  profiles depend on the wave conditions, and so here  $k_i(f)$  is computed by running multiple cases. The significant waveheight is indicated in the legend. The peak period is 10 s for all IC2 cases. The IC2 profiles for the two lowest waveheights are nearly identical, since this is below or near the threshold for transition from a laminar to turbulent regime. There is remarkable agreement between the IC2 profiles and the IC4 step functions. However, the IC2 case for  $H_s=4.0$  m, which is closest to the waveheight of WA3, has  $k_i$  values that are higher than those from the inversions in the middle range of frequencies.

By plotting the IC4M6H and IC4M6H2 parametric models as step functions, this is a honest representation insofar as the inversion gives  $k_i$  values for discrete frequency bands, and they are applied in WW3 as step functions. However, this is not a conventional presentation, and one could argue, is not a particularly attractive one. Thus, in Figure 94, we have the same comparison, but presenting the parametric models as continuous functions, using the central frequency of each step.

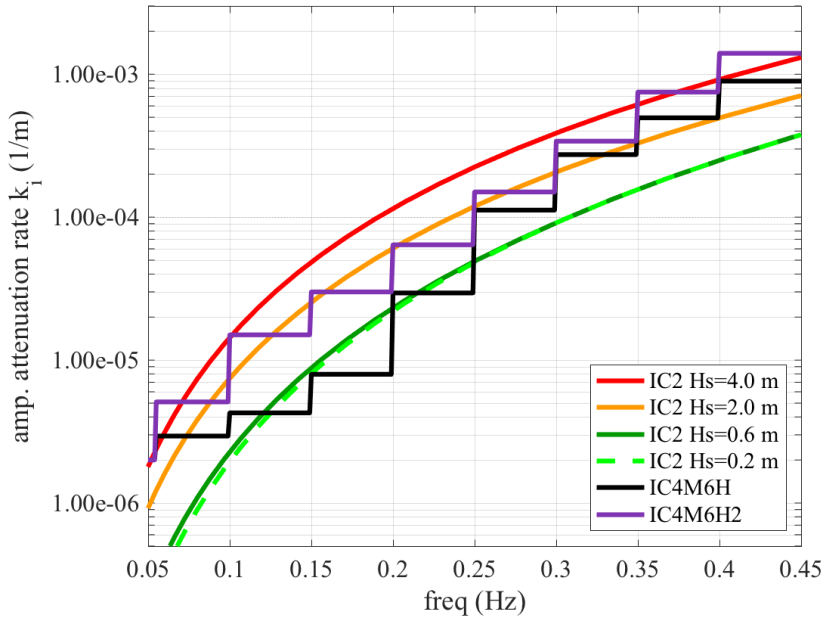


Figure 93. Amplitude attenuation rate  $k_i$  vs. frequency. The two parametric models IC4M6H and IC4M6H2 are compared with the “basal friction” boundary layer model of IC2. The parametric models are shown as step functions.

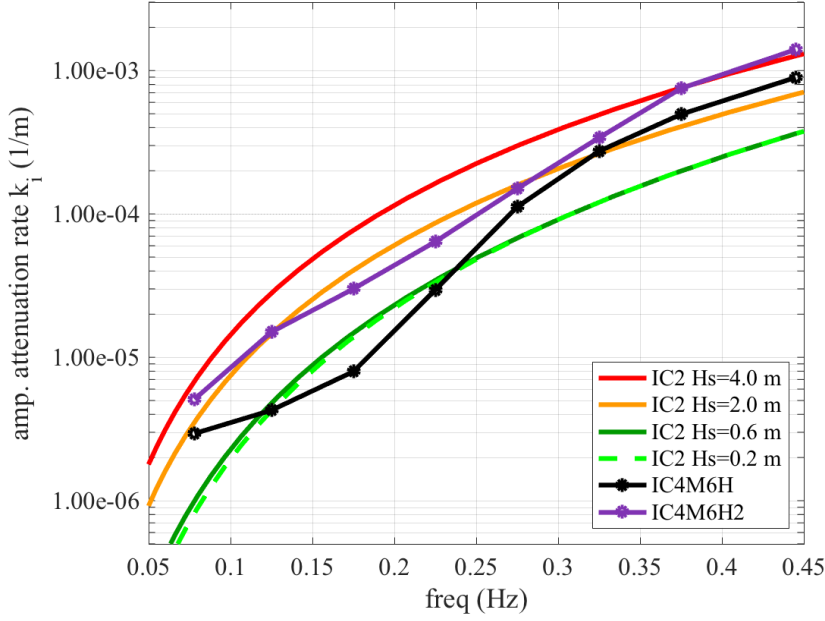


Figure 94. Amplitude attenuation rate  $k_i$  vs. frequency. Identical to Figure 93, except that the parametric models are shown as continuous functions rather than as step functions.

Figure 95 compares the parametric models to the profiles determined by Cheng et al. (2017) for WA3. The latter are not published in complete form in that paper, but an example profile is given in Figure S14b in the Supporting Information for Cheng et al. (2017) (the red circles for “measured”  $k_i$ ). The Cheng et al. (2017) values are higher than the parametric models by a factor

of around 3. Both the Cheng et al. (2017) values and the IC4M6H2 profile are derived using the 10 km AMSR2 forcing. Cheng et al. (2017) point out three possible reasons for the differences versus Rogers et al. (2016) which still apply here:

1. Cheng et al. (2017) use the ST1 source function package while we use ST4 here.
2. In the Cheng et al. (2017) inversion, the  $\partial E / \partial t$  term is assumed negligible relative to the advection term, whereas the  $\partial E / \partial t$  is included in the inversion here.
3. In the Cheng et al. inversion, the inverted dissipation rate is associated with the ice between buoy pairs. In Rogers et al. (2016) and this report, the inverted dissipation rate is associated with the ice between the open water and the buoy location.

We can add a fourth difference:

4. In Rogers et al. (2016) and this report, the inversion relies on an assumption of linearity: that dissipation rate at any frequency is not affected by the non-uniformity of  $k_i$  in frequency space (Section 6.2.1).

Also, though this is not a difference in the inversion, it should be recognized that the two IC4M6 profiles in Figure 95 are from SWIFT buoys; a parametric model based on UK buoys in WA3 would be *lower* than these (compare Figure 80 and Figure 81), implying an even larger disagreement with the Cheng et al. profiles.

The red and green coloring in Figure 95 pertains to the fitting of VE parameters to the profiles and is not important to the present discussion. Red indicates the “cluster” of profiles with low G (modulus of elasticity) and green is the “cluster” of profiles with high G; see Cheng et al. (2017) for more explanation.

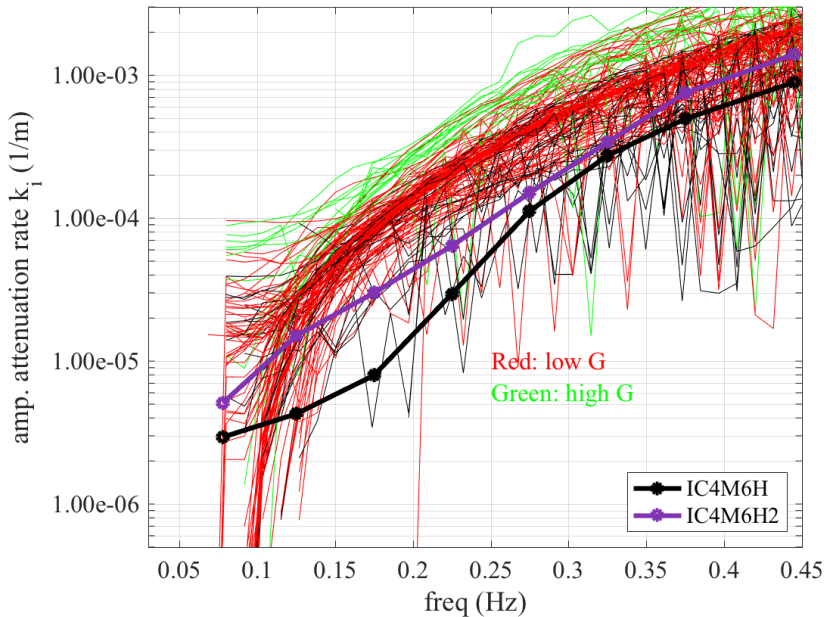


Figure 95. Amplitude attenuation rate  $k_i$  vs. frequency. The two parametric models IC4M6H and IC4M6H2 are compared with profiles determined by Cheng et al. (2017) for WA3. The parametric models are shown as continuous functions. The red and green coloring pertains to the fitting of VE parameters to the profiles (see text).

Doble et al. (2015) propose a parametric dissipation model that depends on frequency  $f$  and ice thickness  $h_{ice}$ , based on buoy measurements of waves in pancake ice in the Weddell Sea (Southern Ocean):  $k_i \propto f^{2.13} h_{ice}$ . See also IC4M7 in Section 3.1.5. The “equivalent ice thickness” values in that experiment were 5 to 50 cm. Estimates of ice thickness during WA3

vary widely; see discussion in Section 2.2.4. Most values are clustered at less than 10 cm, and 5 cm thickness may be taken as a reasonable representative value. Figure 96 compares the IC4M6 profiles to the Doble et al. (2015) using pancake thickness of 1 and 5 cm. The slope of these curves (frequency to power 2.13) is a bit less than the IC4M6 curves, especially at the higher frequencies. The 1-cm curve shows a trend that is consistent with the inset figure of Doble et al. (2015) when they compare the  $k_i \propto f^{2.13}$  curve to *their own measured data*: there is a good match at low frequencies (or high period in their plot), but the  $f^{2.13}$  curve is too low for high frequencies (shorter period). This is further explored via analysis of our  $\partial k_i(f)/\partial f$  slope in Section 6.2.5, which indicates that  $f^2$  is a good fit for lower frequencies but a stronger dependence (higher power) is needed at higher frequencies. In other words, the slope of the Doble et al. (2015) curve at high frequencies is inconsistent with both our measurements and—albeit to a lesser extent—the measurements used by Doble et al. (2015) to create their curve. We also point out that their dissipation estimates may be artificially low for shorter waves if regrowth of wave energy occurred in their observational dataset<sup>26</sup>. A better fit to their short-period data (especially if a correction is made for possible regrowth) would have steeper slope than  $f^{2.13}$ .

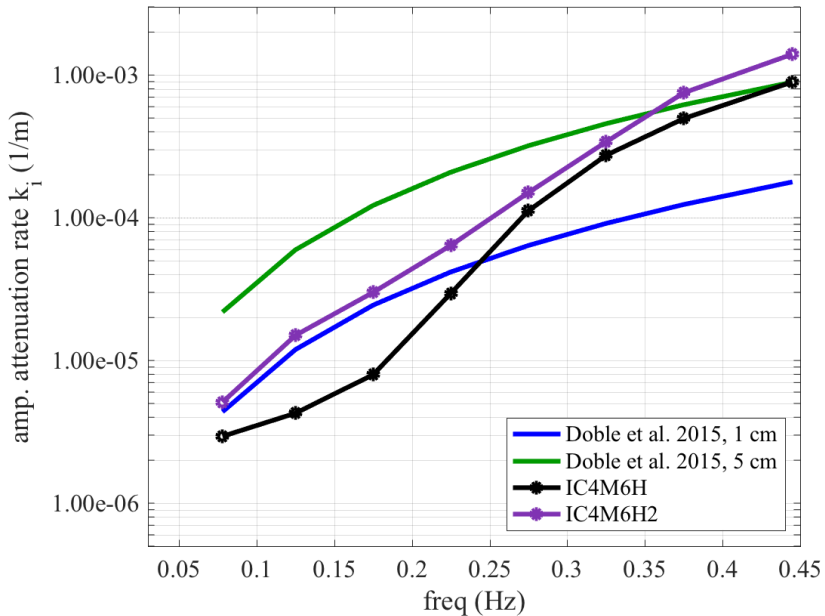


Figure 96. Amplitude attenuation rate  $k_i$  vs. frequency. The two parametric models IC4M6H and IC4M6H2 are compared with the Doble et al. (2015) formula, for two difference ice thickness values, 1 and 5 cm. The parametric models are shown as continuous functions.

Figure 97 compares the IC4M6 profiles to the eddy viscosity parameterization used by Liu and Mollo-Christensen (1988) (LMC). This model requires ice thickness and eddy viscosity: the example here uses 15 cm and  $1.0e-4$  m<sup>2</sup>/s respectively. The leveling off and weak rollover in the LMC model is consistent with examples such as Liu et al. (1991) Figure 11. It is in complete contradiction to the IC4M6 WA3 curves, but is actually similar to the inversion results for WA4-5 (Figure 83 and Figure 84). In any case, we do not favor the eddy viscosity model on physical grounds; see discussion in Section 3.1.3.

<sup>26</sup> This regrowth may also lead to a spurious rollover of  $k_i$  at high frequencies in some of the older literature, as discussed by Wadhams (1988), Rogers et al. (2016), and Li et al. (2017).

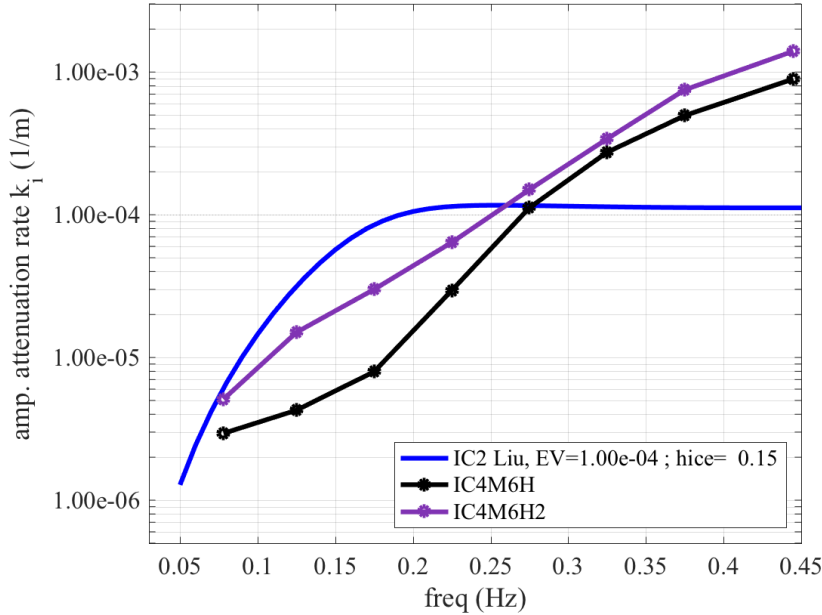


Figure 97. Amplitude attenuation rate  $k_i$  vs. frequency. The two parametric models IC4M6H and IC4M6H2 are compared with the IC2 model based on the eddy viscosity concept. The parametric models are shown as continuous functions.

Ardhuin et al. (2016) studied the wave energy generated by a massive storm near Svalbard, which propagated into the high Arctic where it was measured by a tiltmeter. The study was used to estimate dissipation of low frequency waves by ice. Figure 98 compares the IC4M6 WA3 profiles to these low-frequency estimates. The WA3 profiles do not overlap in frequency space with the latter, but the comparison does give an impression that the Arduin estimates would be a natural extension of these profiles into the lower frequencies. For this reason, the two points are included in the IC4M6 step functions, given as namelists in Section 6.2.3. These two points do not play a role in the Sea State hindcasts (Section 6), because energy at these frequencies is very low. However, they could play an important role in a WW3 simulation that includes sea ice in the Southern Ocean or the Nordic Seas.

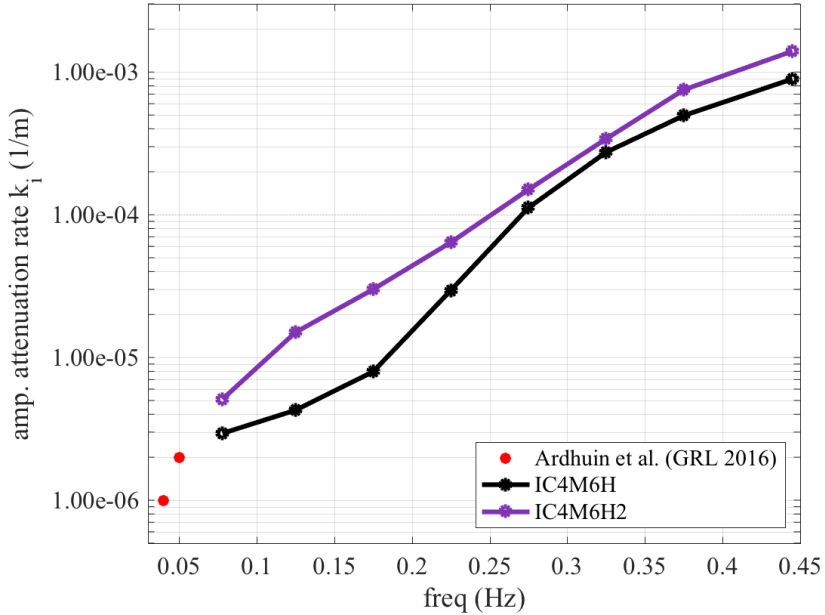


Figure 98. Amplitude attenuation rate  $k_i$  vs. frequency. The two parametric models IC4M6H and IC4M6H2 are compared with low frequency  $k_i$  estimates of Arduin et al. (2016). The parametric models are shown as continuous functions.

Meylan et al. (2014) deployed motion sensors on ice floes in the marginal ice zone near Antarctica. The floes were 10 to 25 m in diameter. Incident waveheights were slightly smaller than in WA3,  $H_s \approx 2$  m, and the dominant wave periods were slightly longer,  $T_p = 11$  to 12 s. The attenuation rates were estimated by comparing energy at different buoys and this was fitted to a binomial:  $2k_i = af^2 + bf^4$ . Figure 99 compares this to the IC4M6 WA3 profiles. The agreement is astounding. Given that the ice conditions and estimation methods are so dissimilar, one has to wonder if the agreement is at least partially accidental.

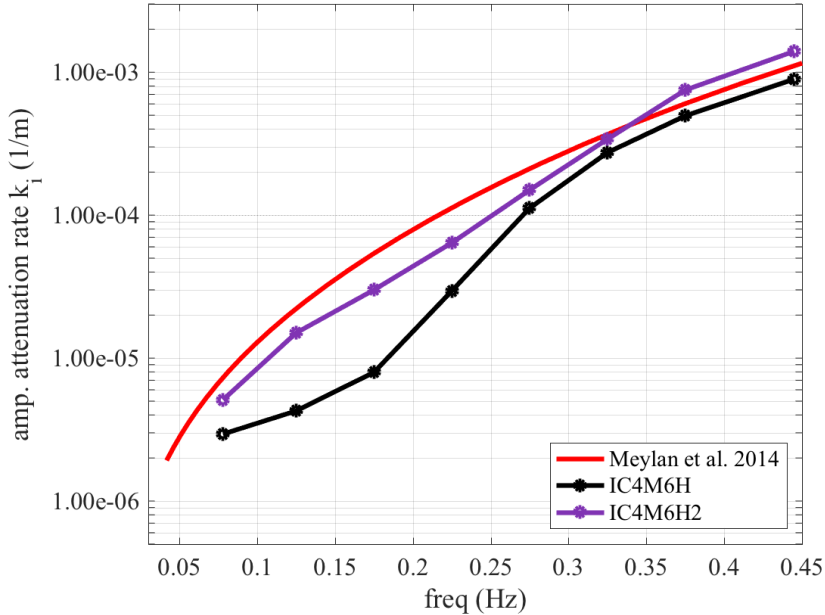


Figure 99. Amplitude attenuation rate  $k_i$  vs. frequency. The two parametric models IC4M6H and IC4M6H2 are compared with the profile suggested by Meylan et al. (2014), based on measurements near Antarctica. The parametric models are shown as continuous functions.

Figure 100 includes the same profiles from IC3 which were shown in Figure 92. Elasticity is zero in both cases, so it is a viscous model, identical to Keller (1998) (see paragraph 19 of Wang and Shen (2010)). The ice thickness is 30 cm in both cases, and the viscosity is set to 1.0 and 0.1 m<sup>2</sup>/s. The elasticity and viscosity settings correspond to settings used for the inner WW3 grid of the realtime on-ship forecasting system during the cruise. Ice thickness for the forecasting system was not a constant/uniform 30 cm, of course: it came from the Navy CICE model, as described in Sections 4.1.1 and 4.2. The higher viscosity setting was prior to and during WA3; the lower setting was used after October 14. The  $k_i(f)$  profiles from the viscous model are much steeper than the IC4M6 WA3 profiles, and by extension, the Cheng et al. (2017) profiles. This feature was also pointed out by Rogers et al. (2016); see their Figure 9 and related text. This has implications for fitting the VE model to a “measured”  $k_i(f)$  profile: since the former tends to be steeper than the latter, the fitting can be weighted to match at lower frequencies, or match at higher frequencies, but not both: see Cheng et al. (2017) Supporting Information, Figure S14b.

Figure 101 is identical to Figure 100, but with smaller settings for ice thickness  $h_{ice}$  and effective viscosity. These settings are taken directly from Newyear and Martin (1999), who report dissipation in grease ice in a laboratory:  $h_{ice}$  is from 12 to 15 cm and viscosity is 0.02 to 0.03 m<sup>2</sup>/s. Those authors use the Keller (1998) model for comparison. Measurements of Newyear and Martin (1999) are restricted to frequencies from 1.0 to 1.6 Hz. Thus, their measurements do not overlap with ours in frequency space. However, their comparative model is essentially the same as the model shown here. Again, we see that the  $k_i(f)$  profile from the viscous model is too steep. Only in the higher frequencies (0.3 to 0.45 Hz) do the model values overlap with the inversion results (IC4M6 WA3 profiles).

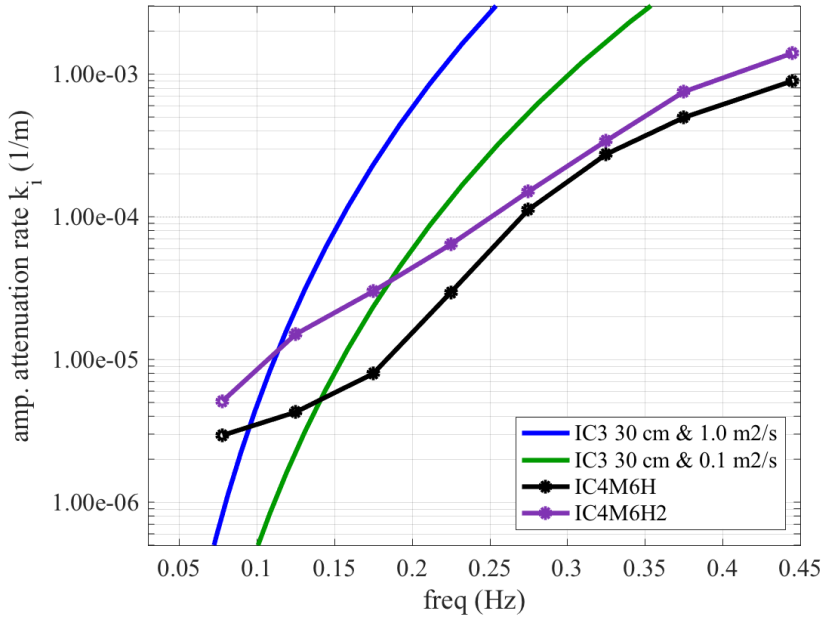


Figure 100. Amplitude attenuation rate  $k_i$  vs. frequency. The two parametric models IC4M6H and IC4M6H2 are compared with the viscoelastic model of Wang and Shen (2010). The parametric models are shown as continuous functions.

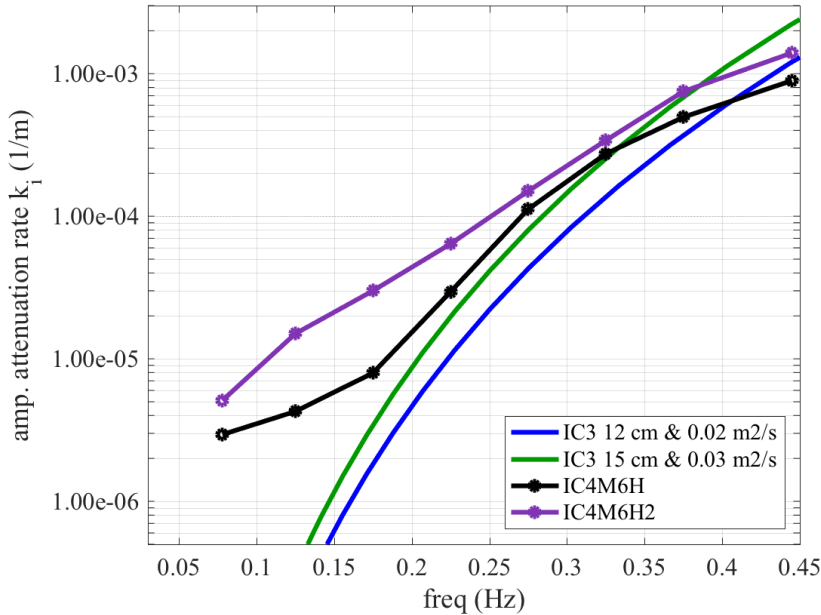


Figure 101. Like Figure 100, but using settings for ice thickness and viscosity taken from Newyear and Martin (1999), for grease ice.

In Collins and Rogers (2017), the seminal aggregated dataset of Wadhams et al. (1988) was fitted to an equation of form  $2k_i = \exp [aT + b]$ , where  $a$  and  $b$  are fitting coefficients, and  $T$  is wave period. Wadhams et al., like Meylan et al. (2014), estimated attenuation by comparing wave energy, measured at different locations using motion sensors on floes of various sizes. They used five different field experiments in the Greenland and Bering Seas from 1978 to 1983. Collins and Rogers implemented the fitted curve in WW3 as IC4M1. In Figure 102, we compare the Wadhams dataset to the IC4M6 WA3 profiles. Almost all the Wadhams et al. data points are

higher than the WA3 profiles. On one hand, this is not surprising, given that waves were measured in and around floes of 20 to 150 m diameter. On the other hand, the Wadhams dissipation rates are also higher than those of Meylan et al. (2014). Perhaps the difference can be attributed to different ice conditions encountered by Wadhams et al. (1988) vs. Meylan et al. (2014), but the differences in these conditions are not apparent to this author (ER). The Wadhams et al. (1988) exhibits considerable scatter. This is partly attributable to the fact that it includes five different field experiments. But according to V. Squire (personal communication), the method of estimating dissipation rate in those experiments was relatively approximate<sup>27</sup>. This would also contribute to the scatter.

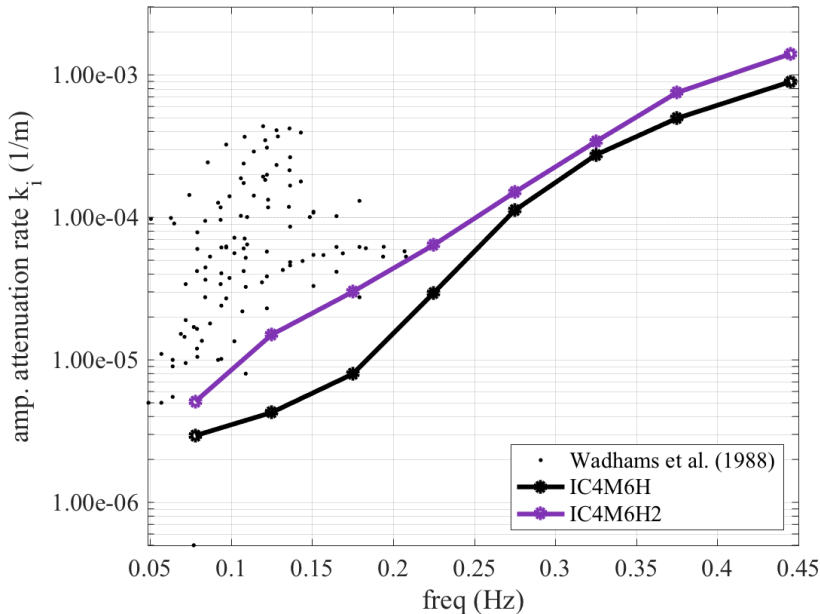


Figure 102. Amplitude attenuation rate  $k_i$  vs. frequency. The two parametric models IC4M6H and IC4M6H2 are compared with the measurements tabulated by Wadhams et al. (1988). The parametric models are shown as continuous functions.

Finally, we compare the IC4M6 WA3 profiles to  $k_i$  values determined from experiments by Zhao and Shen (2015). The experiments were conducted in a refrigerated wave flume in Hamburg, Germany (HSVA) with frazil and pancake ice. As with the Arduuin et al. (2016) data points, there is no overlap in frequency space with WA3, but this time, the dataset is for higher frequency waves, 0.5 to 1.1 Hz, and this time, it is difficult to imagine that the data points are a natural extension of the WA3 profiles: the Zhao and Shen points are about an order of magnitude higher than a hypothetical extension of the WA3 profiles into higher frequencies. In fact, if we do the reverse, and extend the Zhao and Shen point to lower frequencies, we might get a value, of say  $k_i = 0.02 \text{ m}^{-1}$  at 0.4 Hz. Unfortunately, even looking at *all wave experiments and all buoy types* (Figure 79 to Figure 89), we do not find any indication of  $k_i$  values that are this high<sup>28</sup>. This suggests a significant challenge for future research: to reconcile the apparent discrepancy

<sup>27</sup> See also the discussion in the paper led by Dr. Mike Meylan, submitted to the JGR special issue.

<sup>28</sup> In fact, the highest  $k_i$  used in the inversion for these plots was  $0.005 \text{ m}^{-1}$ , since the latter is already difficult to resolve with a 5-km resolution model, since it is an extremely high dissipation: see Table 1. However, we did re-run the inversion with an artificial  $k_i$  row:  $k_i = 0.1 \text{ m}^{-1}$  and  $E(f)=0$  for all frequency bins. These results (not shown here) are not significantly different from Figure 79 to Figure 89, and so they also do not approach the hypothetical extension of Zhao and Shen ( $k_i = 0.02 \text{ m}^{-1}$  at 0.4 Hz).

between high dissipation rates measured in the lab with lower dissipation rates measured in the field. One possible explanation is nonlinearity: for example, if  $k_i(f)$  depends on orbital velocity, the laboratory cases may be quite dissimilar from the field cases.

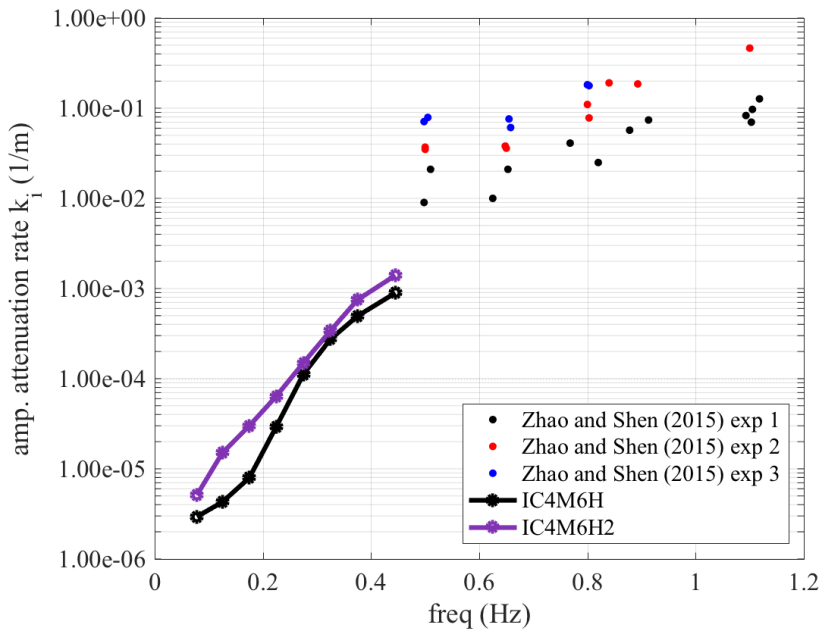


Figure 103. Amplitude attenuation rate  $k_i$  vs. frequency. The two parametric models IC4M6H and IC4M6H2 are compared with results tabulated in the Zhao and Shen (2015) lab experiment. The parametric models are shown as continuous functions.

### 6.2.5. Slope of the dependence on frequency (or period)

While attending a meeting in Cambridge, UK<sup>29</sup>, author ER discussed the  $k_i(f)$  profiles with Prof. Mike Meylan (U. Newcastle), and more specifically, the slopes of these curves and the general trends that might be observable from the observational data, and perhaps even modeling results. In Figure 104 and Figure 105, we plot a small subset of the  $k_i(f)$  profiles from the inversion: the six WA3 SWIFT profiles for which the ice code (Section 7.1) is 11 or 12, indicating the heaviest frazil and pancake cover during WA3 observed by SWIFT photographs. These six profiles are compared with the binomial of Meylan et al. (2014), which is in the form of  $2k_i = c_2f^2 + c_4f^4$ . Figure 105 illustrates how, with the Meylan binomial, the  $f^2$  term is most important in the lower frequencies, while the  $f^4$  term is most important in the higher frequencies. The inversion profiles match the binomial well in the lower frequencies, while the slope of these profiles appears to be a bit higher than the binomial in the higher frequencies, suggesting that a more optimal binomial use  $f^{4.5}$  or  $f^5$  instead of  $f^4$ . We investigate this in the next two figures.

<sup>29</sup> “Mathematics of sea ice phenomena” Programme at the Isaac Newton Institute for Mathematical Sciences, at Cambridge University.

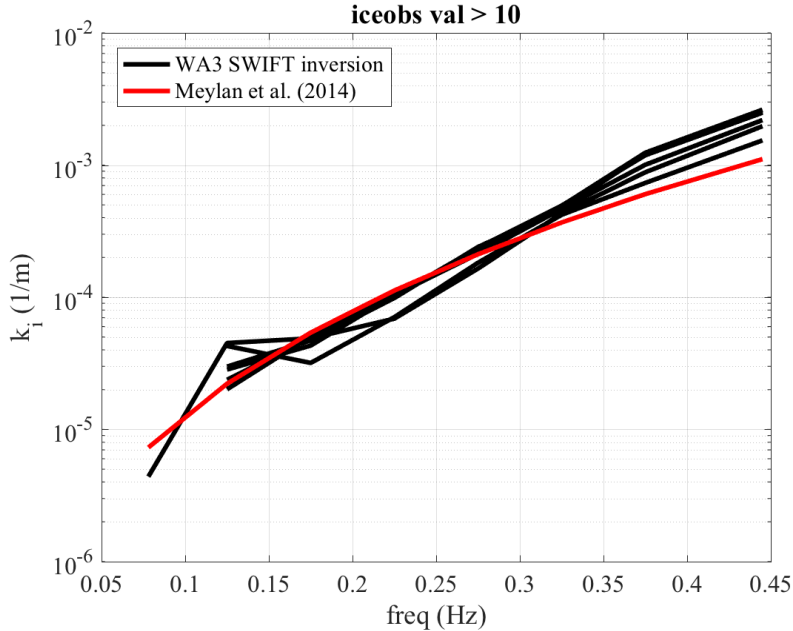


Figure 104. Black: inversion dissipation profiles shown in Figure 80, except that only six profiles, those with ice codes PF11 and PF12, are plotted. Red: Meylan et al. (2014) (also shown in Figure 99)

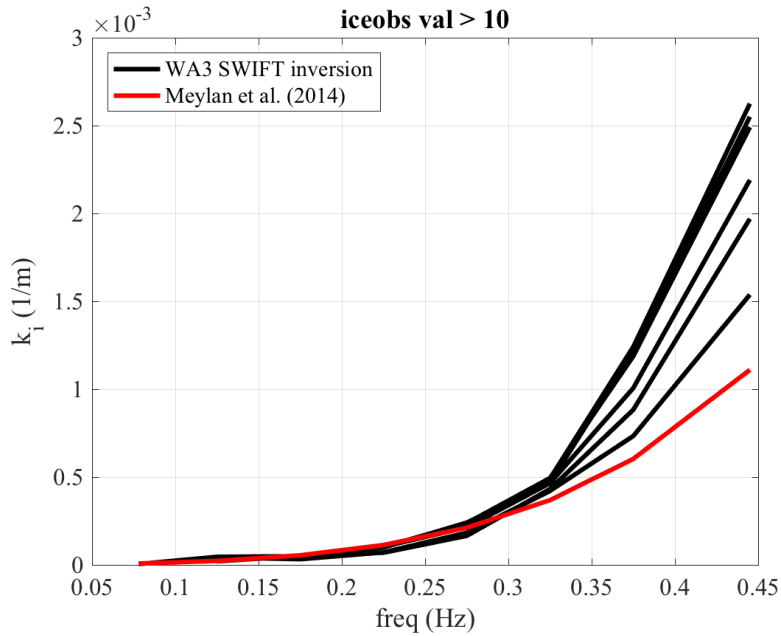


Figure 105. Like Figure 104, but plotting on a linear scale.

In Figure 106 and Figure 107, we look at the slopes of the curves in the lower and higher frequencies, respectively. The plots are in the form of  $ck_i T^n$ , where  $c$  is a coefficient. A flat slope in the plot for any  $n$  value would imply that  $k_i$  is proportional to  $f^n$ . Figure 106 suggests that  $n = 2$  would be credible in the broader frequency range 0.1 to 0.25 Hz and  $n = 3$  would be credible in the narrower frequency range 0.17 to 0.25 Hz. Figure 107 implies that  $n = 4.5$  would be credible in the higher frequency range, 0.22 to 0.45 Hz. A possible binomial would be in the

form  $2k_i = c_2 f^2 + c_{4.5} f^{4.5}$ . This  $k_i(f)$  slope is discussed in the context of Doble et al. (2015) in Section 6.2.4.

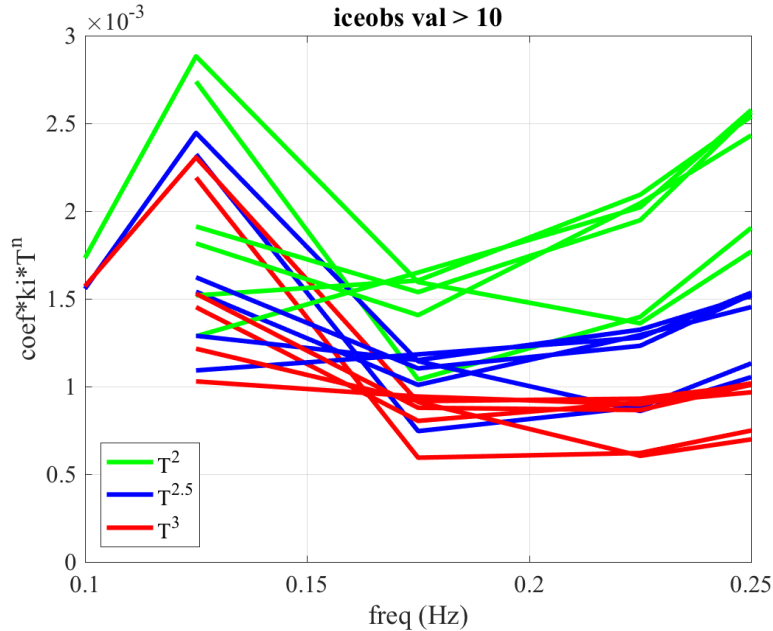


Figure 106. Like Figure 105, but the  $k_i(f)$  profiles are multiplied by  $cT^n$ , to evaluate slopes of profiles. Here we look at lower frequencies and  $n=2, 2.5$ , and  $3$  as indicated in legend. See text for further explanation.

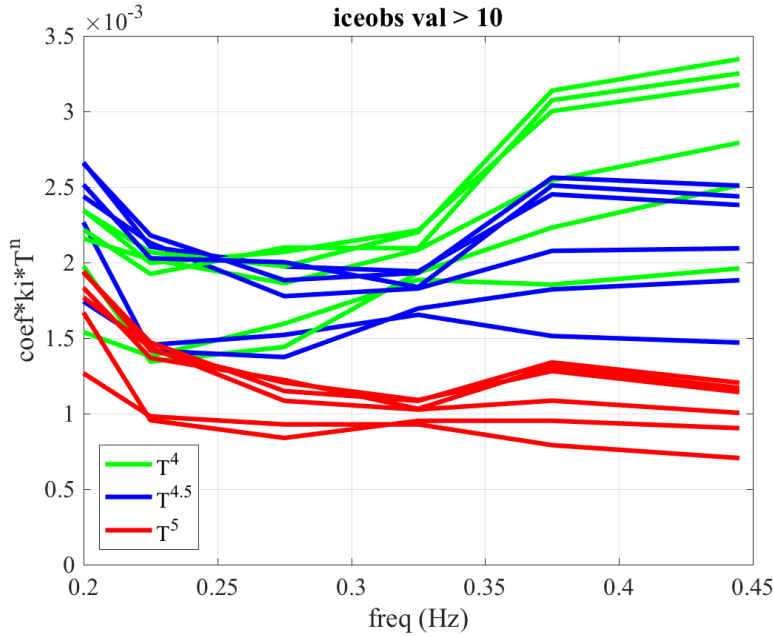


Figure 107. Like Figure 106, except here we look at higher frequencies and  $n=4, 4.5$ , and  $5$  as indicated in legend.

We now take an inventory of the slope dependence  $k_i \propto f^n$  found here, and in the literature:

- Arduuin boundary layer model for friction at ice-water interface, also known as the basal friction model for IC2, from analysis of Figure 94 herein:
  - turbulent regime:  $n = 3$
  - laminar regime:  $n = 3.5$

- Kohout et al. (2011) model for friction at ice-water interface, based on drag formula:  $dE/dt = \tau u_{max} = \rho C_d u_{max}^3$ . This gives  $n = 4$ .
- Keller (1998) viscous layer model (full dispersion relation), from analysis of Figure 101 herein: This gives  $n = 7$ .
- In Lamb (1932), Article 349, which is on “the effect of viscosity on water waves”, there is an estimate for dissipation by viscosity in the entire water column. See also Weber (1987) and Sutherland et al. (2017). This gives  $n = 5$ .
- In Lamb (1932) Article 351, on the “calming effect of oil on waves”. This employs the concept of Stokes boundary layer thickness for the case of an “inextensible surface cover”. See also Weber (1987) and Sutherland et al. (2017). It gives  $n = 3.5$ .
- Meylan et al. (2014). This is an empirical polynomial fit. It suggests two regimes (so binomial):  $n = 2$  and  $n = 4$ .
- This study (empirical, IC4M6H2). Like Meylan et al. (2014), this gives two regimes (see earlier in this section):  $n = 2$  and  $n = 4$  to 5.

This inventory can be expanded by including additional models and empirical studies. The comparison is particularly interesting because it suggests possible physical explanations (via the models) for the observed (empirical) values of  $n$ . For example, the  $n = 4$  portion of the Meylan et al. (2014) and IC4M6H2 binomials may be associated with friction at the ice-water interface.

#### 6.2.6. Parametric binomial functions: old and new (based on WA3)

Recognizing that some readers will find it more convenient to compare to our results using polynomial fit rather than step functions, we performed a fit to our two step functions. This is shown in Figure 108, in the form of  $k_i = c_2 f^2 + c_4 f^4$ . The fit for IC4M6H (Rogers et al. 2016, WA3) is  $c_2 = 1.64\text{e-}4$  and  $c_4 = 1.56\text{e-}2$ . The fit for IC4M6H2 (this study, WA3) is  $c_2 = 5.24\text{e-}4$  and  $c_4 = 2.50\text{e-}2$ . Note that the coefficients are dimensional; this is discussed in the next section.

Fits are based on least squares, using  $\log_{10}(k_i)$  so as to not unduly weight the high values. Figure 108 shows that the binomial provides an excellent fit to the step functions, especially for the newer step function, IC4M6H2.

Our use of the binomial  $c_2 f^2 + c_4 f^4$  follows Meylan et al. (2014). Meylan et al. have:  $\alpha = 2k_i = af^2 + bf^4$  with  $a=2.12\text{e-}3$  and  $b=4.59\text{e-}2$ . Thus, their  $c_2 = 1.06\text{e-}3$  and  $c_4 = 2.30\text{e-}2$  (dividing by two since their equation is for  $\alpha$  and ours is for  $k_i$ ). This means that their  $c_2$  is about twice that of IC4M6H2, while their  $c_4$  is close to that of IC4M6H2. Higher coefficients are expected in the Meylan et al. (2014) case, given the more substantial ice cover.

For WW3 users, this binomial can be activated via IC4M2 (Collins and Rogers 2017). That implementation uses the form  $\alpha = c_2 f^2 + c_4 f^4$ , so coefficients shown in Figure 108 should be multiplied by two.

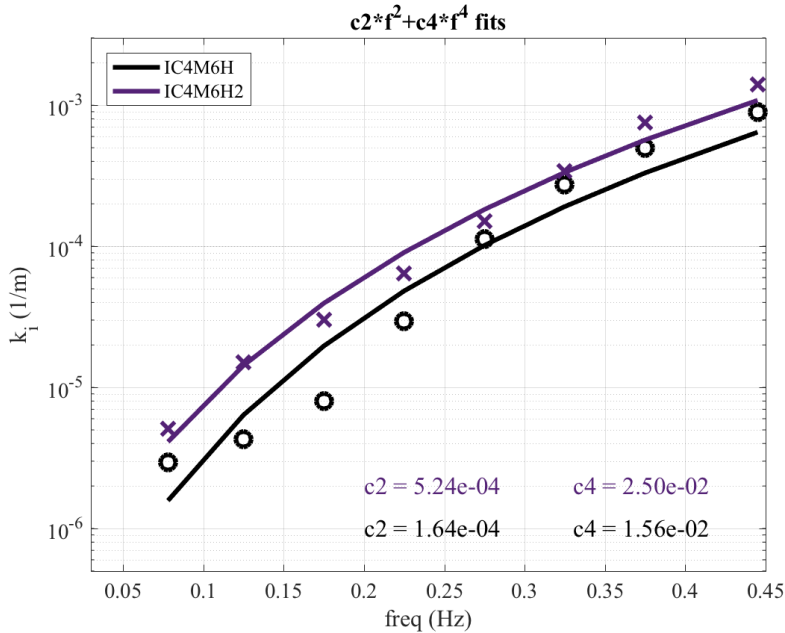


Figure 108. Binomial fits (lines) to the steps functions (symbols) IC4M6H and IC4M6H2. The step functions were shown previously in Figure 79 to Figure 103 using the same color convention (black and purple).

### 6.2.7. Dimensions of polynomial fit

Our discussion of a binomial of the form  $k_i = c_2 f^2 + c_4 f^4$  or  $k_i = c_2 f^2 + c_{4.5} f^{4.5}$  leads to concerns about dimensions. There are three possible approaches here:

1. Rely on coefficients  $c_n$  to make the units consistent. This requires them to have unusual units.
2. Replace  $f$  with a non-dimensional variable and assign units of  $\text{m}^{-1}$  to each  $c_n$ .
3. Replace  $f$  with a non-dimensional variable and also require that each  $c_n$  is dimensionless, which implies that the left-hand side (LHS) must also be non-dimensionalized.

Only the third approach follows the conventions of dimensional analysis, so it is used here. Our first step is to non-dimensionalize the LHS. The simplest approach is to select a variable with units of length. There are a number of relevant variables:

1.  $d_{ice}$ , a representative horizontal scale of the ice floes or cakes
2.  $h_{ice}$ , ice thickness
3.  $L$ , the wavenumber or wave length, or the corresponding wavenumber  $k_r$

If we use the third approach, this has implications for the RHS, since the variable is dependent on frequency. For example,

$$k_i \propto c_2 f^2 + c_{4.5} f^{4.5}$$

would become:

$$k_i/k_r \propto c_0 + c_{2.5} f^{2.5}$$

And, if we do not want to commit to any particular slope of the  $k_i(f)$  profile, we can generalize as:

$$\frac{k_i}{k_r} = \sum c_n f^n$$

Our objective, then is to non-dimensionalize  $f$  on the RHS,

$$\frac{k_i}{k_r} = \sum c_n \tilde{f}^n$$

where  $\tilde{f}$  is the non-dimensional form  $f$ . To do this, we need a variable with units of time. Obvious options are:

1. gravitational acceleration  $g$ . This would tend to direct us toward something like Froude scaling, and is attractive insofar as we are dealing with gravity waves or flexural gravity waves
2. viscosity  $\nu$ . This can be of either the water  $\nu_w$  or the ice  $\nu_{ice}$ .
3. velocity. However, velocities associated with wave motion are proportional to  $f$  (orbital velocity) and  $f^{-1}$  (phase and group velocities), so they are unhelpful to our objective here. If there is physical dependence on these velocities, it is already implicit in our formula via  $f$ .

In the first case, we have  $\tilde{f} = f\sqrt{l/g}$ , where  $l$  is either  $d_{ice}$  or  $h_{ice}$ . In the second case, we have  $\tilde{f} = fl^2/\nu$ . It is of course possible to employ both  $g$  and  $\nu$  in the non-dimensionalization, but this becomes an ill-posed problem with many possible forms. Guidance can be found in the literature. Rabault et al. (2017), Sutherland et al. (2017), Weber (1987) and Lamb (1932) utilize expressions for dissipation by viscosity or eddy viscosity. These expressions come in two varieties (see the list given in the prior section discussing value of  $n$  in  $k_i \propto f^n$ ), but either can be used to create the same non-dimensionalization:  $\tilde{f} = \nu^{1/3} f g^{-2/3}$ . Note that this non-dimensionalization does not use  $h_{ice}$ , which implies that it may not be appropriate if dissipation is occurring in the ice layer.

Since  $\tilde{f}$  is dimensionless, the parameter  $n$  does not need to be an integer. However, integers and simple fractions (e.g. 5/2) have a more plausible argument for physical significance.

### 6.3. WW3 Forward model

#### 6.3.1. Settings

The settings and forcing used in our forward modeling are identical to those used in the IC1 inverse model, except where specifically noted. In cases where ice concentration forcing is not specified, the 10 km AMSR2 (Section 4.1.2) is used. Results are from the 5 km inner WW3 grid, except where otherwise noted. The simulations evaluated here are:

1. IC1 with fixed  $k_i = 0$ . Thus, there is no dissipation by sea ice. However, there is still a reduction of wind input, scaled by ice cover (Section 3.1). This is one of the simulations used in the inversion.
2. IC1 with fixed  $k_i = 4e-5 \text{ m}^{-1}$ . This is another one of the simulations used in the inversion. This  $k_i$  is selected to demonstrate how a model may succeed in predicting waveheight while failing to predict spectral shape, if the frequency distribution of dissipation  $k_i(f)$  is neglected.
3. IC2, the non-dispersive boundary layer model for dissipation by sea ice. Namelist settings are: [&SIC2 IC2DISPER = F, IC2TURB = 1., IC2ROUGH = 0.0001, IC2REYNOLDS = 150000, IC2SMOOTH = 200000., IC2VISC = 1. /]
4. IC4M6H step function, introduced in Section 6.2.3.
5. IC4M6H2 step function, introduced in Section 6.2.3.

6. IC4M6H step function, but using the 3.125 km AMSR2 instead of the 10 km AMSR2
7. IC4M6H step function, but using the realtime GOFS 3.1 output instead of the 10 km AMSR2
8. IC4M6H step function, but using the GOFS 3.1 reanalysis instead of the 10 km AMSR2

### 6.3.2. Wave parameters

We use three wave parameters for evaluation of wave model performance. All use some form of spectral moments:  $m_n = \int_{f_1}^{f_2} E(f) f^n df$ , where  $f$  is frequency and  $E(f)$  is the non-directional (1d) spectrum.

1.  $H_{m0}$ , significant wave height, proportional to the square root of total energy:  

$$H_{m0} = 4\sqrt{m_0}$$
2. "Tmm10", or  $T_{m,-1,0}$ : a parameter for dominant wave period,  $T_{m,-1,0} = m_{-1}/m_0$ .
3.  $m_4$ , the fourth moment of the wave spectrum, proportional to mean square slope. This metric is sensitive to high frequency energy level, and so responds strongly to any damping of high frequencies by ice cover.

Though it is not used in this section, as it is semi-redundant with (2), we provide here a definition for  $T_{m,01,E4}$  which is used in Section 4.3.4 and Figure 69:

4. "Tm01E4", or  $T_{m,01,E4}$ , the mean period  $T_{m,01}$  of  $E(f)^4$ , another parameter for dominant wave period. Where  $T_{m,01}$  is  $\frac{m_0}{m_1}$ ,  $T_{m,01,E4}$  is  $\frac{\int_{f_1}^{f_2} E(f)^4 df}{\int_{f_1}^{f_2} E(f)^4 f df}$ . This has two positive characteristics: it is smoother than  $T_p$  (since it is based on integration rather than discrete bin selection) and it is close to the peak period (by using the fourth power on  $E(f)$ ).

These three parameters taken together provide a nearly complete picture of non-directional spectral shape. However, none of them characterize the width in frequency space (Rogers and van Vledder (2013)).

For ground truth, we use buoy data collected during the field experiment. In all cases, the frequency bounds on the integration,  $f_1$  and  $f_2$ , are set such that they are consistent between model and observations. This is ensured by outputting spectral density  $E(f)$  from WW3 and performing the integration as a post-processing step.

Extracting  $E(f)$  output from WW3 is not simple in the case of drifting buoys. The "track output" feature of WW3 is used. Latitude/longitude/time triplets are provided to WW3, which stores output not at these points, but at the bounding computational grid points. As a post-processing step,  $E(f)$  is integrated into the three wave parameters ( $H_{m0}$ ,  $T_{m,-1,0}$ ,  $m_4$ ) and these parameters are bilinearly interpolated to the buoy locations.

### 6.3.3. Validation, by wave experiments collectively

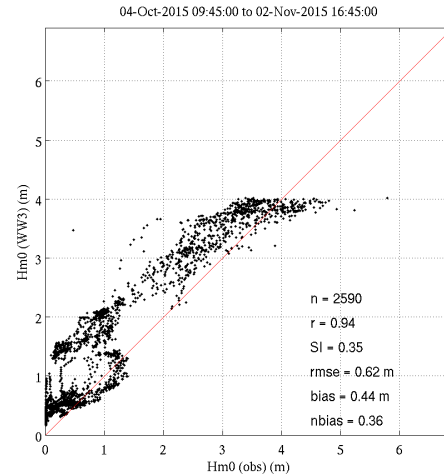
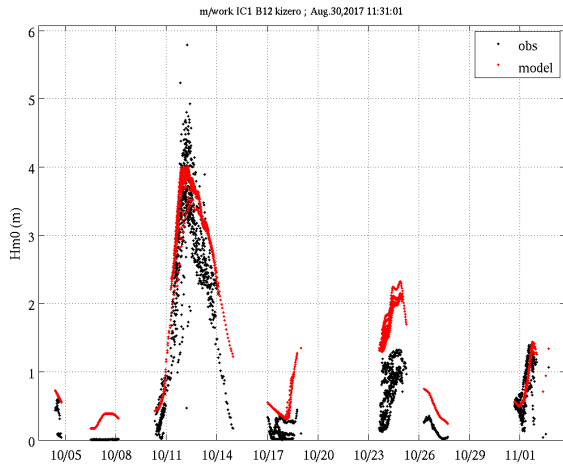
Here, we present comparisons between model output and drifting buoy observations, looking at the *Sea State experiment as a whole*. In the next section (Section 6.3.4), we look at experiments individually. Figure 109 to Figure 114 evaluate the skill of predicting the three wave parameters,

looking at the difference  $S_{ice}$  representations. One model, IC4M6H, is included in all plots in order to provide a common reference. Thus, five simulations are compared (models (1) to (5) in the list in Section 6.3.1). Recognizing that long, unbroken text describing model-observation comparisons can be tedious to read, we put our remarks in a bullet list:

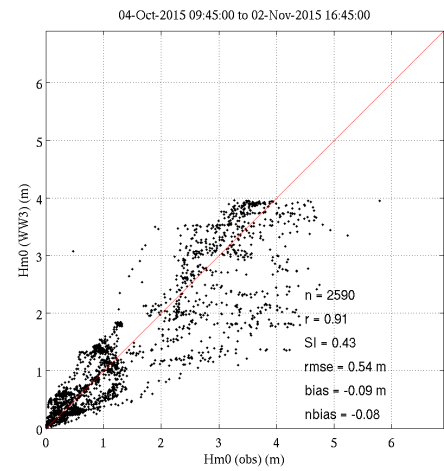
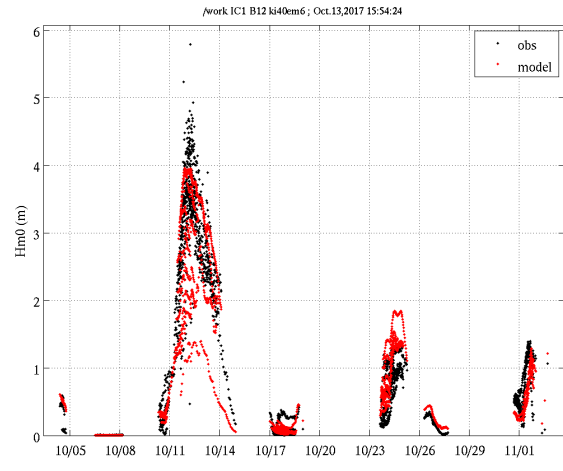
- The model  $H_{m0}$  appears to hit a hard limit at 4 meters, which makes the results look artificial in scatter plots. This behavior is evident even for the  $S_{ice} = 0$  model, so it is not related to dissipation by sea ice. It is related to the wind input, either in the wind forcing fields (e.g., are the NAVGEM fields too smooth?) or in the  $S_{in}$  formulation (e.g. is the  $\beta_{max}$  coefficient too small?). The former seems more probable. Adjustment to  $\beta_{max}$  would presumably not remove the “limit” but just shift it upwards. We also consider the possibility of thermal stability, which is not included in these simulations (see Section 6.3.5). These higher  $H_{m0}$  values are, of course, occurring in WA3. The behavior does not look as artificial when plotted as time series, e.g. Figure 123.
- Unsurprisingly, the  $S_{ice} = 0$  model has a large positive bias in  $H_{m0}$ : 36%
- Even though the fixed  $k_i = 4e-5 \text{ m}^{-1}$  model has small bias in  $H_{m0}$  (-8%), it is very poor in scatter, since the model overpredicts dissipation at some buoys in WA3. This poor performance in  $H_{m0}$  was not expected, but it is encouraging insofar as it supports our argument that it is important to have an  $S_{ice}$  that varies with frequency.
- For  $H_{m0}$  and  $m_4$ , the skill of IC2 is better than IC1. It is similar to, but less than that of IC4. The latter is unsurprising, given that the IC4 step functions are based WA3. However, we should keep in mind that they are created using only a small fraction of the total dataset used here (only WA3, only the SWIFT buoys, only the spectra with valid corresponding photos, and only the cases with frazil and pancake ice).
- For  $T_{m,-1,0}$ , IC2 is actually outperforming IC4 step functions. The latter slightly underpredicts the highest period during WA3. Though, as with  $H_{m0}$  and  $m_4$ , the skill of IC2 and IC4 are similar.
- For  $T_{m,-1,0}$ , the IC1 models are again poor (low correlation and high scatter). The fixed  $k_i = 4e-5 \text{ m}^{-1}$  model is biased severely low, because the model is over-damping the dominant wave frequencies and under-damping the high frequencies.
- For  $m_4$ , the IC1 models are again very poor, clearly indicating an under-damping of the high frequencies.
- For  $m_4$ , all models have high scatter. Though the IC4 models have much lower bias and RMSE than IC1, they actually have higher scatter and worse correlation than the  $k_i = 4e-5 \text{ m}^{-1}$  IC1 model.
- Regarding  $m_4$  for IC2 and IC4: the  $m_4$  values are too high for WA6 and too low for WA7, which contributes significantly to the scatter. This may point to a difference in ice type that the models do not account for. This would be true if the ice in WA6 was more dissipative than pancake and frazil, while the ice in WA7 was less dissipative than pancake and frazil. However, the ASSIST observations (Sections 2.2.6 and 2.2.8) do not support this conclusion. Thus, we prefer another hypothesis: that since these two cases are very near the ice edge, their problems may be primarily associated with their ice concentration forcing, i.e. the ice edge is too far to the west in WA6 (see also Figure 68 and associated text) and may have been too far to the east in WA7. Also, the biases in WA6 and WA7 are not restricted to  $m_4$ : the same biases are seen in  $H_{m0}$  but are more pronounced in  $m_4$ .

- For  $H_{m0}$ , IC4M6H performs slightly better than IC4M6H2. However only the latter predicts the complete dissipation of wave energy at IS1. IC4M6H has +7% bias while IC4M6H2 has -6% bias, indicating that though the two functions are very close, they fall to either side of the mean observed wave height for the entire cruise.
- For  $m_4$ , the most noticeable difference between IC4M6H and IC4M6H2 is that the former has 21% bias and the latter only 5%. However, correlation and scatter are slightly worse with the latter, suggesting that IC4M6H2 effectively straddles the mean for the entire cruise, but still has significant biases—positive and negative—in individual experiments.

$k_i=0$



$k_i=40e-6 1/m$



IC4M6-H

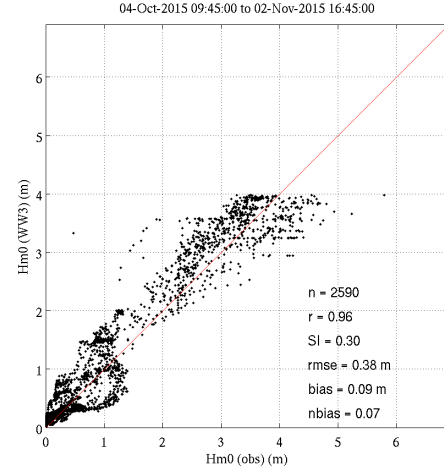
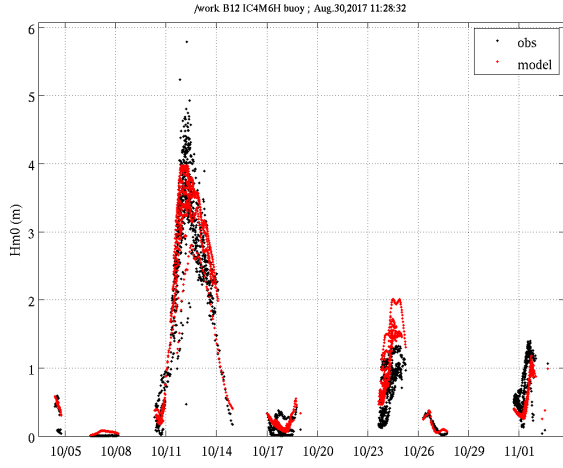


Figure 109. Time series, scatter plots, and statistics for  $H_{m0}$ : drifting buoys vs. hindcasts with three variants of  $S_{ice}$ . All use 10 km AMSR2 ice forcing. Model type is indicated on the left. The “ $k_i=[$ fixed value] $]$  models indicate that IC1 is used for  $S_{ice}$ .

# NRL Memorandum Report

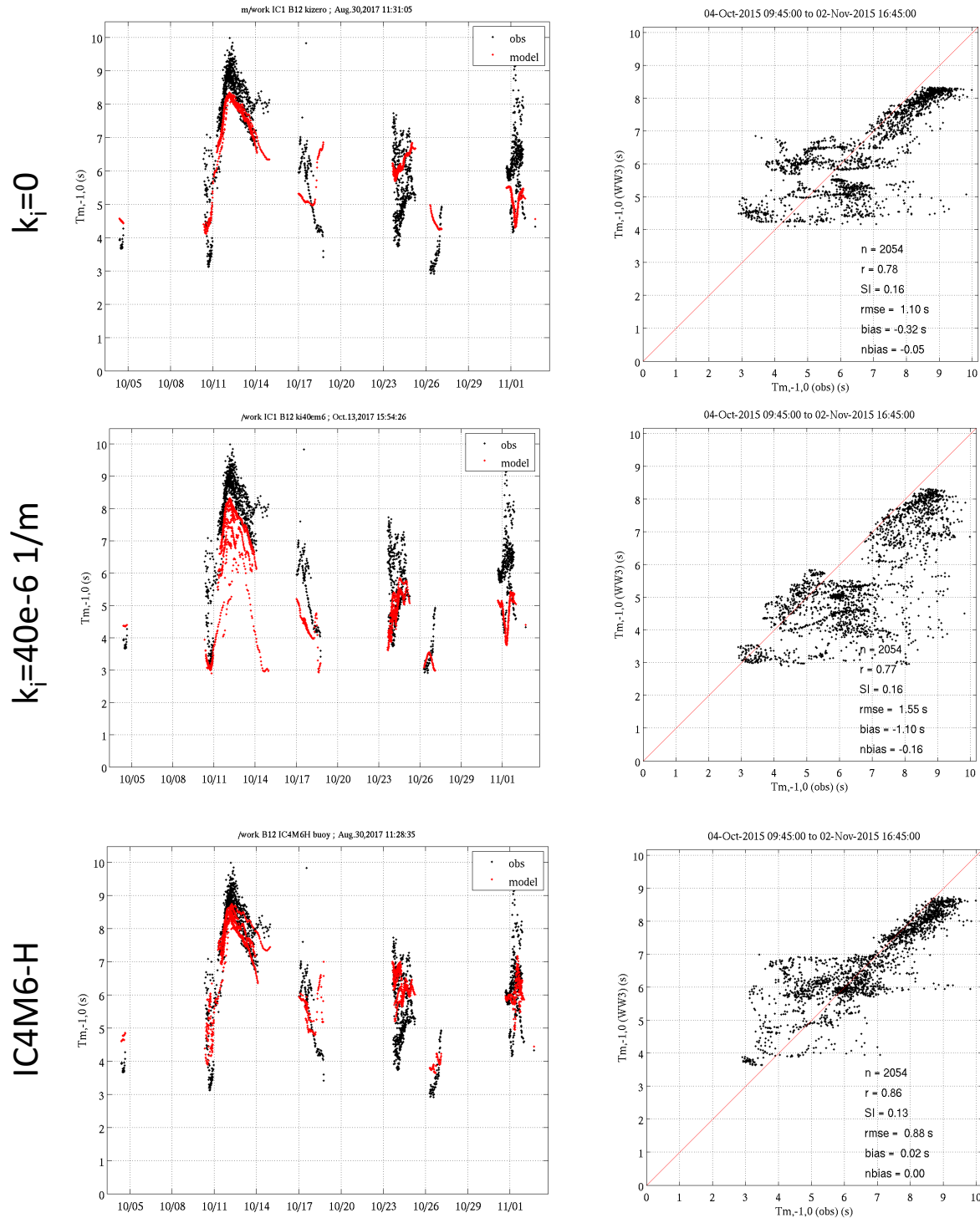


Figure 110. Like Figure 109, but comparing  $T_{m,-1,0}$ .

# NRL Memorandum Report

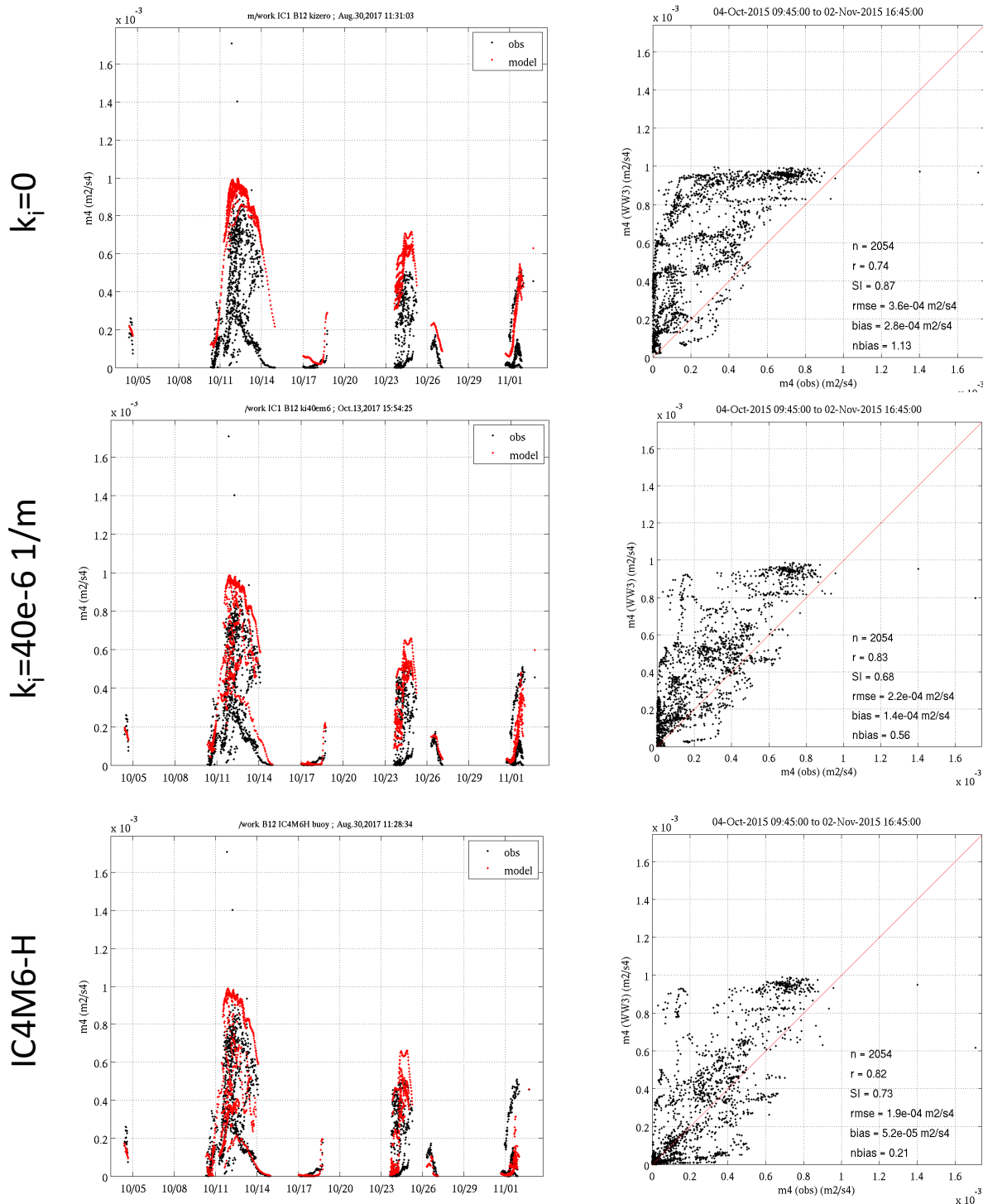
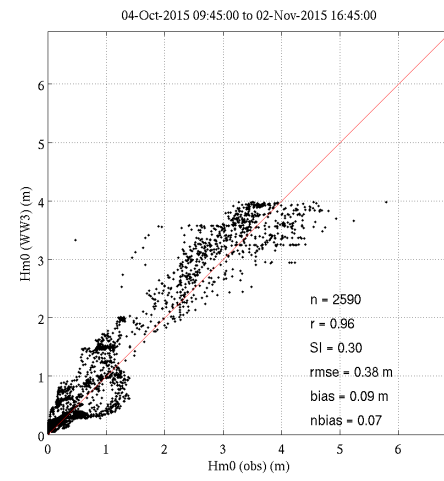
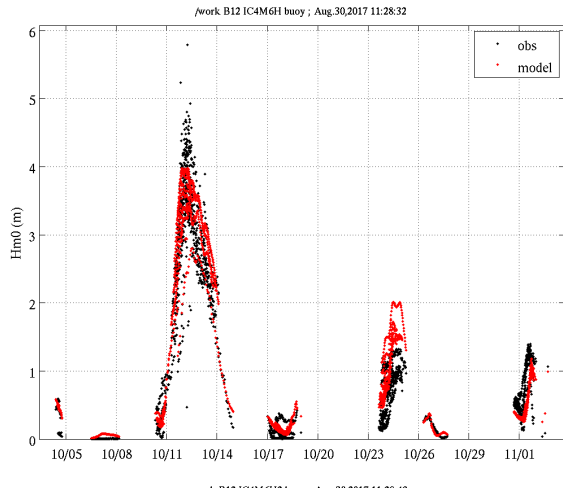
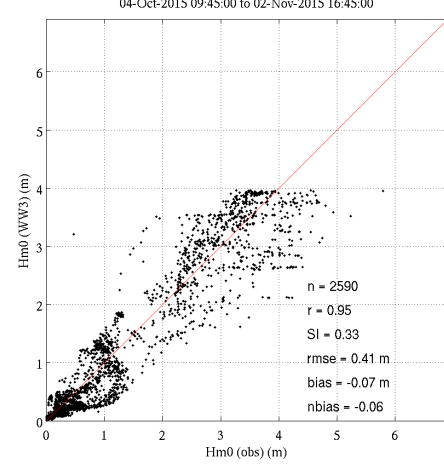
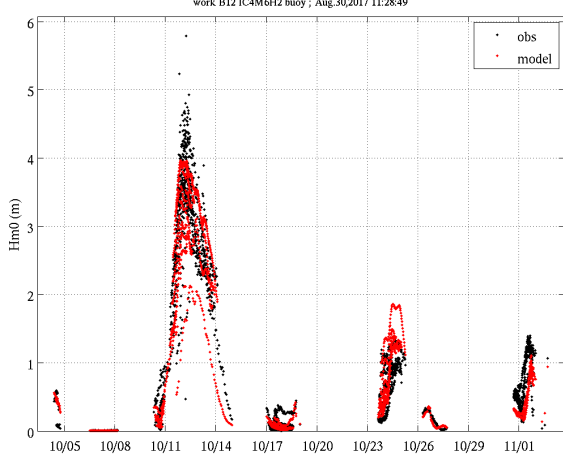


Figure 111. Like Figure 109, but comparing  $m4$ .

IC4M6-H



IC4M6-H2



IC2

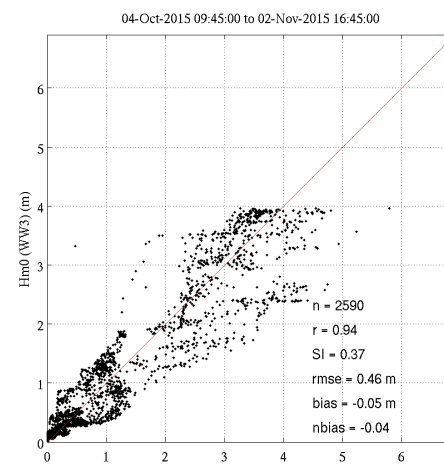
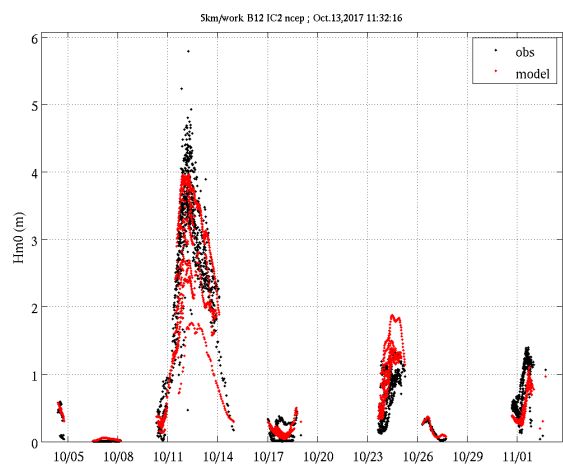
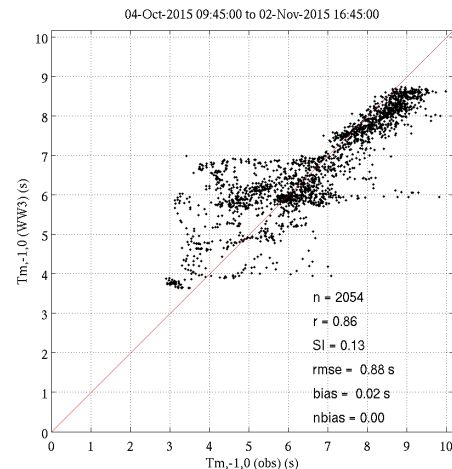
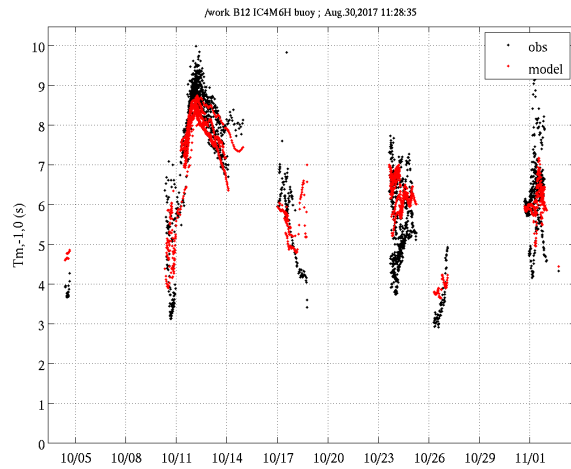


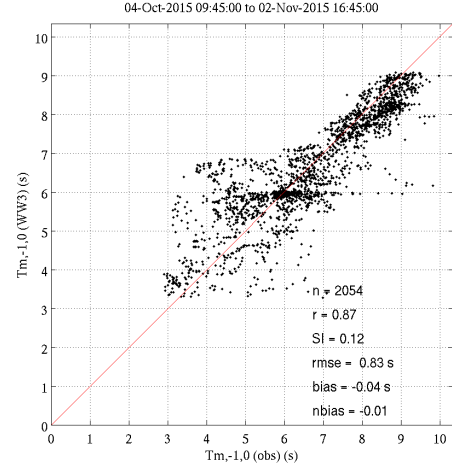
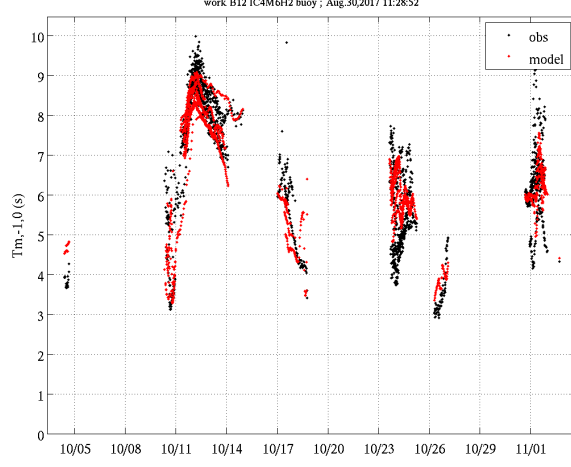
Figure 112. Like Figure 109, but comparing three other variants of Sice.

# NRL Memorandum Report

IC4M6-H



IC4M6-H2



IC2

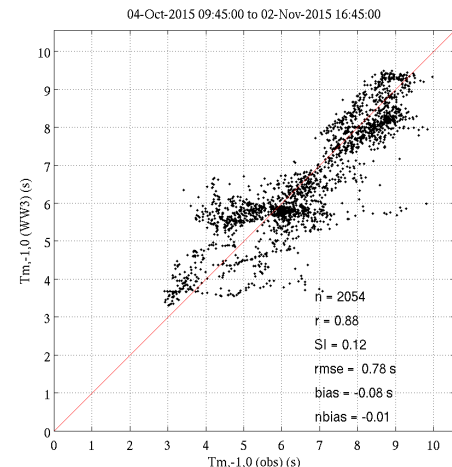
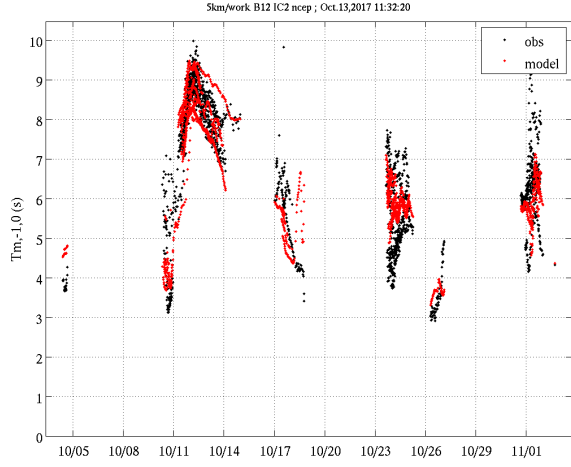
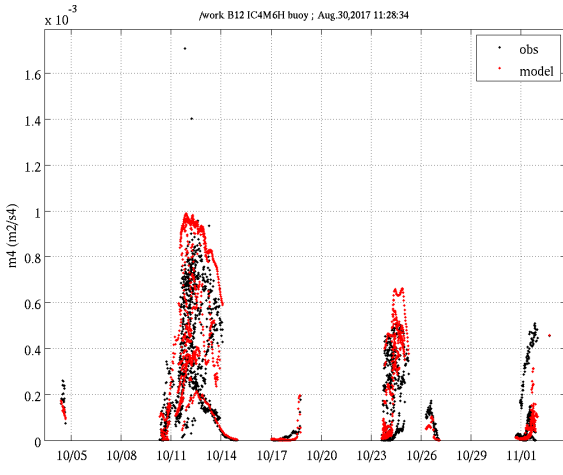
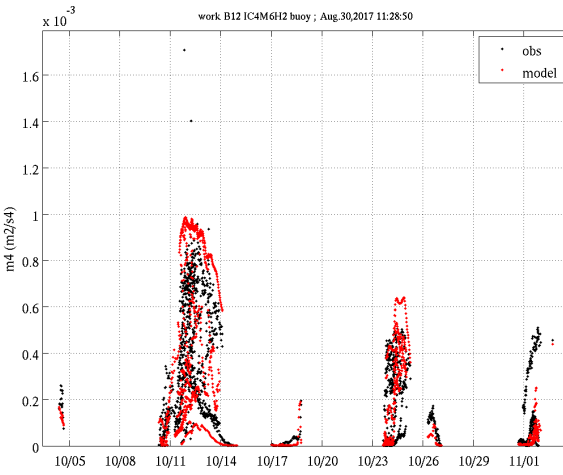


Figure 113. Like Figure 112, but comparing  $T_{m-1,0}$ .

IC4M6-H



IC4M6-H2



IC2

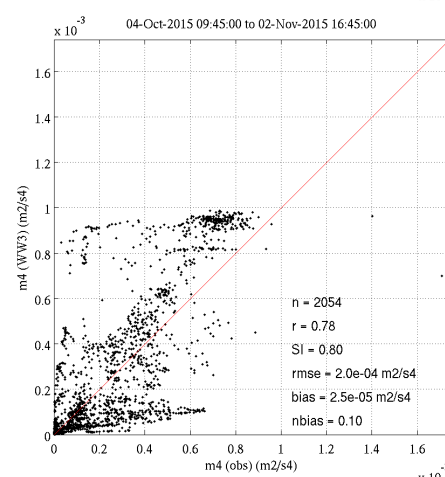
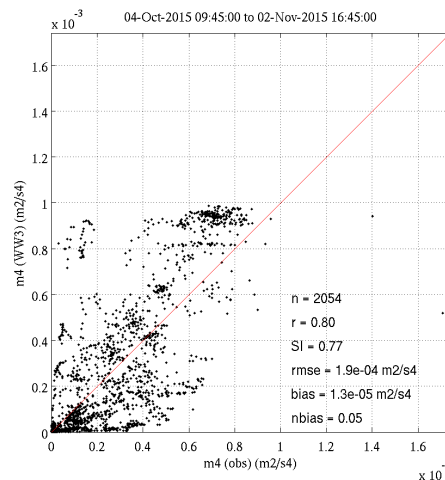
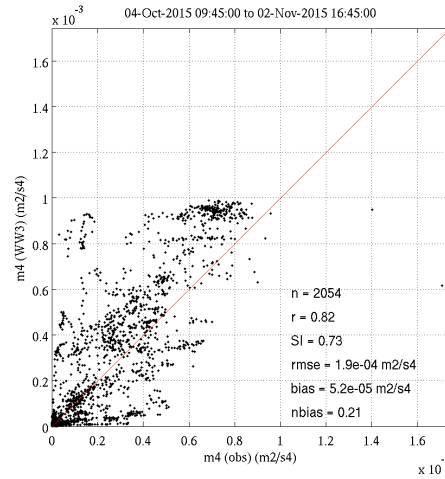
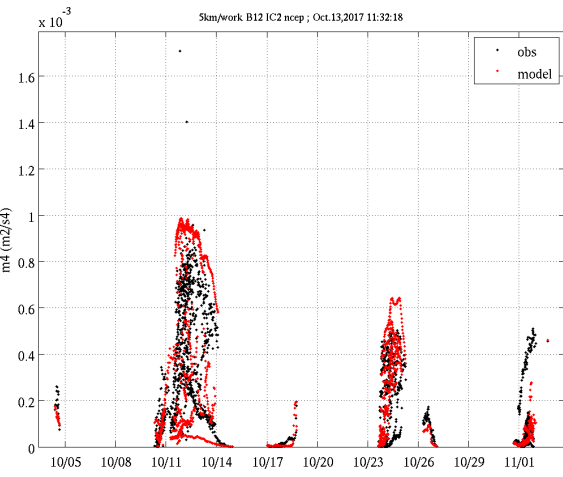


Figure 114. Like Figure 112, but comparing m4.

Figure 115 to Figure 117 study the same three wave parameters, but this time we look at different methods of providing ice concentration to WW3:

- For all three wave parameters and all four statistical measures (correlation, scatter, RMSE, and bias), the WW3 with the AMSR2 10 km shows the best skill. It is tied or superior in 12 of 12 categories, and there are ties in only 3 of the 12 categories.
- For all three wave parameters, the skill of WW3 with the GOFS 3.1 forcing is less accurate overall.
- For  $H_{m0}$  and  $m_4$ , the WW3 with GOFS 3.1 reanalysis is better than WW3 with GOFS 3.1 realtime forcing for most statistics. Surprisingly, the bias is worse with the reanalysis products -26% vs. -16% with  $H_{m0}$ . However, bias is especially susceptible to cancellation of errors, and we suspect that the WW3 with GOFS 3.1 realtime forcing is benefitting here from cancellation of errors.
- Surprisingly, for  $T_{m,-1,0}$ , the realtime GOFS 3.1 results in higher skill than the reanalysis GOFS 3.1.
- For  $H_{m0}$ , the WW3 with GOFS 3.1 reanalysis is clearly superior to the other three models during WA6 (October 23 to 26). This is consistent with Figure 68, which is a continuous time series from a moored buoy October 3 to 25 (emphasizing that it does not have the breaks that exist between drifting buoy wave experiments).
- For all three wave parameters, the skill of WW3 with the GOFS 3.1 reanalysis forcing is clearly inferior for the WA2 and RT buoy deployments, overpredicting  $T_{m,-1,0}$  and underpredicting  $H_{m0}$  and  $m_4$ . This implies that there was too much ice in the GOFS 3.1 reanalysis forcing for the WA2 and RT cases.
- For  $H_{m0}$ , correlation is 0.96 for all models except for WW3 with realtime GOFS 3.1 (0.90). For  $m_4$ , the correlation for WW3 with realtime GOFS 3.1 is especially low (0.40), compared with that of the other models (0.82, 0.81, and 0.65).

Though the 10 km AMSR2 is clearly superior as a forcing field for WW3, relative to the 3.125 km AMSR2, we do not know from these comparisons *why* it is superior. Most likely, it is associated with the much better temporal resolution, which better captures the changes—often rapid changes—occurring in and around the MIZ. It is possible that the more conservative handling of atmospheric effects in the 10 km NT2 product also plays a role in the accuracy of the WW3 hindcasts; in other words, the NT2 processing vs. the ASI processing. Comparisons such as Figure 53 and Figure 58 suggest that the latter does not play a large role.

## NRL Memorandum Report

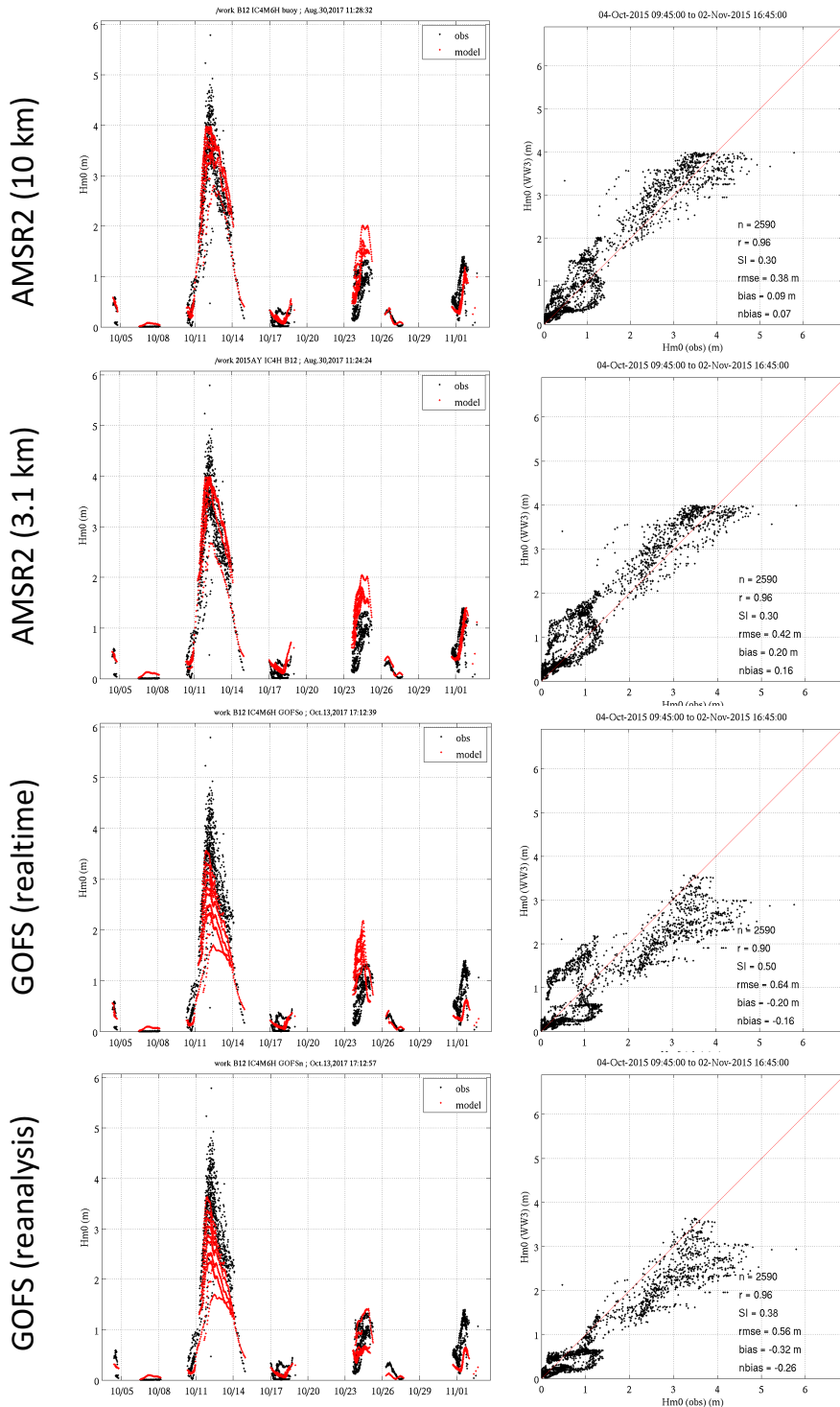


Figure 115. Time series, scatter plots, and statistics for  $H_{m0}$ : drifting buoys vs. hindcasts with four different methods of providing ice concentration. All use the IC4M6H method of  $S_{ice}$ . Ice forcing type is indicated on the left.

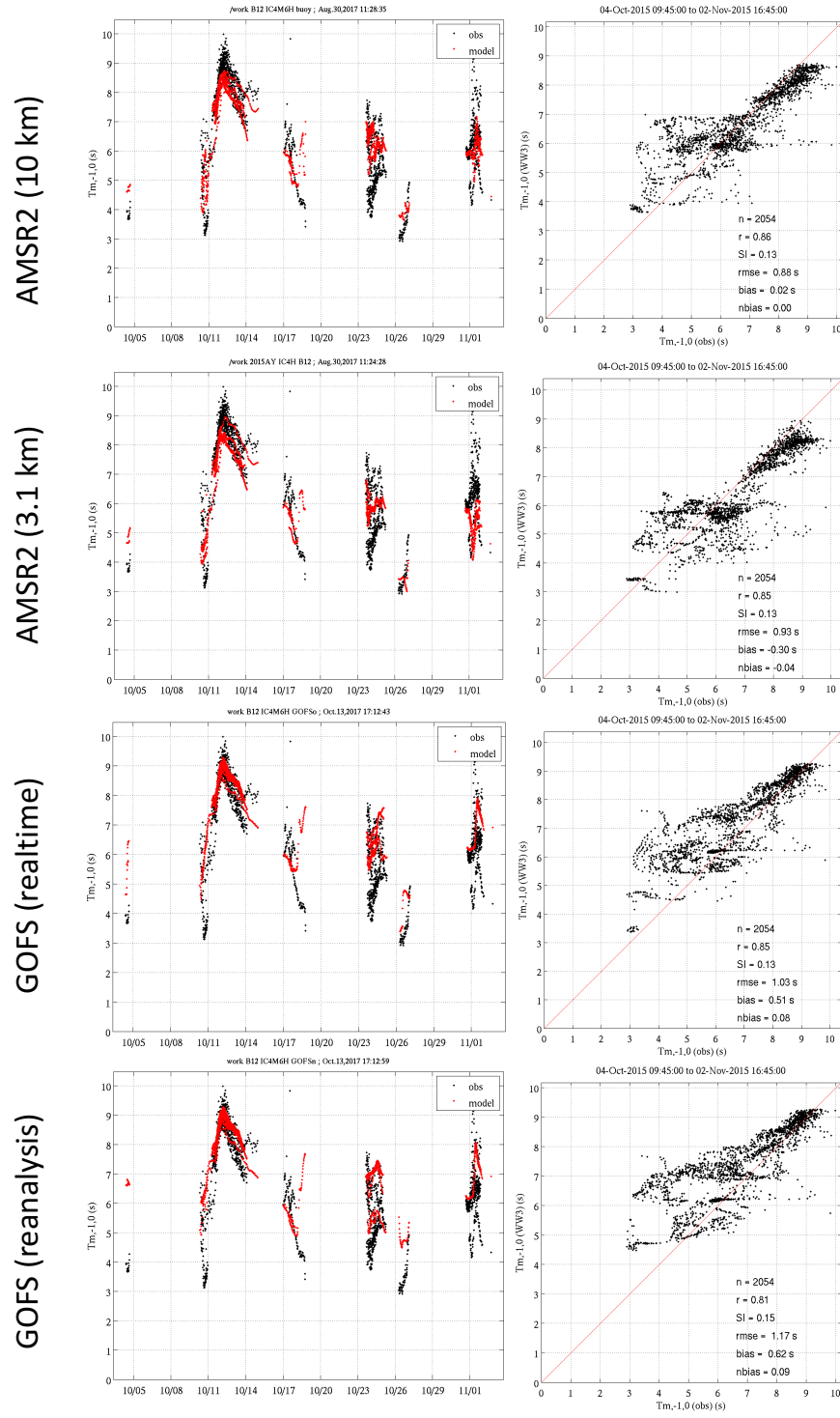


Figure 116. Like Figure 115, but comparing  $T_{m-1,0}$ .

# NRL Memorandum Report

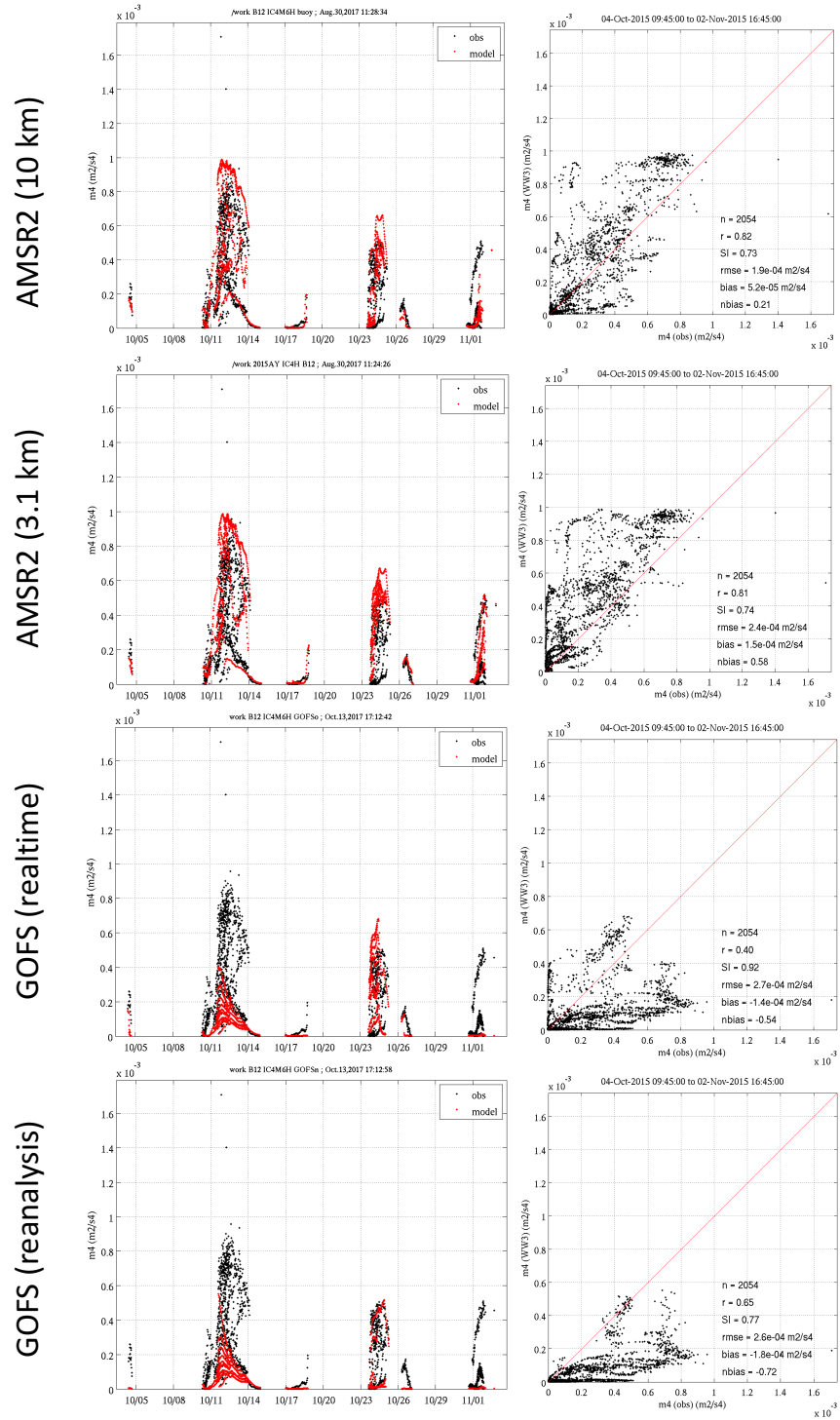


Figure 117. Like Figure 115, but comparing  $m4$ .

In Figure 118 and Figure 119, we look at time series from the models (1) to (5) numbered in Section 6.3.1, with ship-borne observations as ground truth. The values are co-located using WW3 “track output” and bilinear interpolation as described in Section 6.3.2 in context of the drifting buoys. We only use bulk parameters here, in contrast to our use of non-directional (1d) spectra from the buoy data. Along track wave observations come from two sources.

1. Ship lidar. This was operated by Ola Persson (NOAA) and Byron Blomquist (NOAA). Tripp Collins (while an NRL employee) and Chris Fairall (NOAA) participated in the processing of the lidar data. A paper about correction for Doppler shifting was recently published using this dataset: Collins et al. (2017). Original data includes the non-directional spectra, but we only use lidar waveheight here.
2. Ship radar. This was operated by Bjoern Lund (U. Miami) and data were processed by the same. We use the peak period and peak direction from this dataset. “Peak direction” refers here to the directional peak at the frequency of the peak period, the “peak of the peak”.

Unlike the drifting buoy deployments, these measurements are not tied to wave experiments, and the lidar measurements are continuous. In both cases, data were provided to us by Persson. In addition to waveheight, peak period, and peak direction, we present time series for  $m_4$ . However, we do not include observations in the  $m_4$  time series, because 1d spectra from the lidar are not readily available. Model  $m_4$  here is computed from the entire prognostic frequency range (Section 6.1.2)<sup>30</sup>.

Discussion of these two figures follows:

- The separation between the IC1  $k_i = 0$  model and the other models in the comparisons indicates the influence and relative importance of  $S_{ice}$ , according to the models.
- As expected, the  $S_{ice}$  term does have considerable influence on  $H_{m0}$  and  $m_4$ .
- The  $S_{ice}$  term has some modest influence on the peak period. The dissipation primarily affects wave energy above the peak (e.g.  $2f_p$ ), which would *not* affect the peak period. Preferential damping of frequencies at the peak ( $f_p$ ) over waves just below the peak (e.g.  $0.9f_p$ ) can result in a shift of peak frequency, and this is observed in some time periods, e.g. October 6-8 and October 20-23, but unfortunately, these differences (IC1  $k_i = 0$  model vs. IC2 and IC4 models) primarily exist when the radar data are not available, so observations are less useful than we might hope, for distinguishing model skill. Of course, we believe that the IC2 and IC4 models are more correct than the IC1 models.
- The peak period of the IC1  $k_i = 4e-5 \text{ m}^{-1}$  model is consistently lower than that from the IC2 and IC4 models. For some cases, radar observations do exist, and suggest that the IC1  $k_i = 4e-5 \text{ m}^{-1}$  is deficient, and more deficient than even IC1  $k_i = 0$ . In other words, having a non-zero and uniform-in-frequency  $S_{ice}$  term like IC1 or IC0 is actually worse for skill of peak period than having no  $S_{ice}$  at all! When radar observations do not exist, the IC1  $k_i = 4e-5 \text{ m}^{-1}$  model predicts extremely small peak periods, e.g. 1 to 2 seconds, and we believe that these are cases of extreme failure. Essentially, the IC1 model is damping the peak waves and then permitting regrowth of local (high frequency) windsea. This is obviously opposite to what actually occurs, which is better represented in the IC2 and IC4 models.

---

<sup>30</sup> Thus, these  $m_4$  values should not be directly compared with values in other figures in this report, since those use an  $f_2$  value corresponding to the maximum buoy frequency.

- The comparison of the peak direction is similar to the comparison of peak period. That is to be expected: if the IC1  $k_i = 4e-5 \text{ m}^{-1}$  model fails to predict peak frequency, it has small hope of predicting the peak direction at the peak frequency.
- For the peak period and peak direction comparisons, with the IC2 and IC4 models, there is actually little to say, except that these three models match the observations well.
- The waveheight time series during WA3 indicates the same issue that we remarked on during the drifting buoy comparison (Figure 109 to Figure 117): observations exist that are 4 to 4.5 meters, while all model results—even with  $k_i=0$ —are below 4 meters. As we discussed above, this is likely associated with the wind forcing.

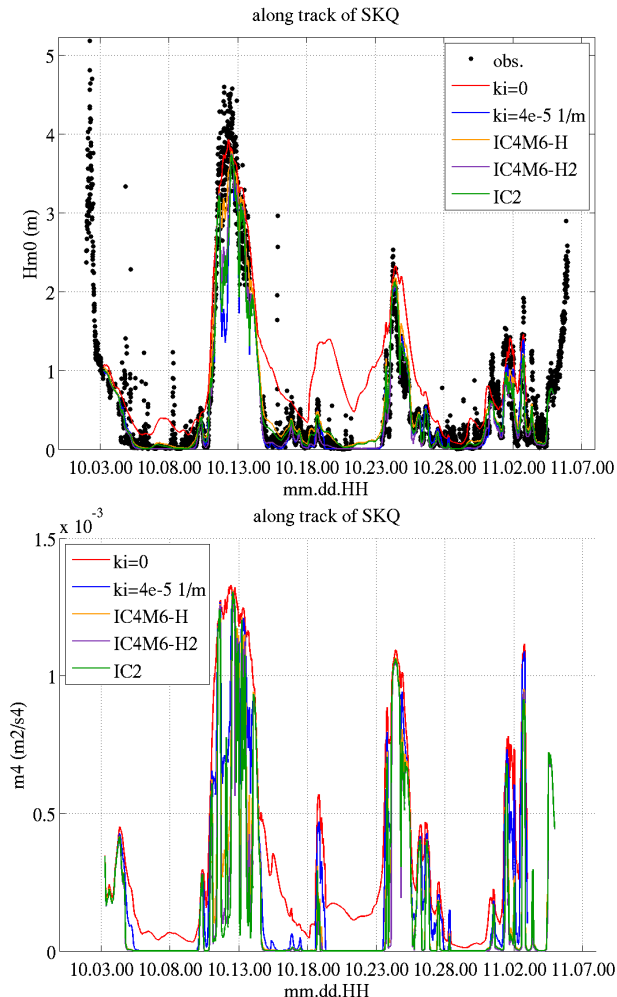


Figure 118. Time series comparisons along track of *Sikuliaq*, with five different model hindcasts. Top panel:  $H_{m0}$  comparison, with observations from ship lidar. Lower panel:  $m_4$  comparison (observations not available: see text).

Ship observations were provided by Ola Persson (NOAA) and the lidar was operated by Persson and Byron Blomquist (NOAA). The “ $k_i=[\text{fixed value}]$ ” models indicate that IC1 is used for  $S_{ice}$ .

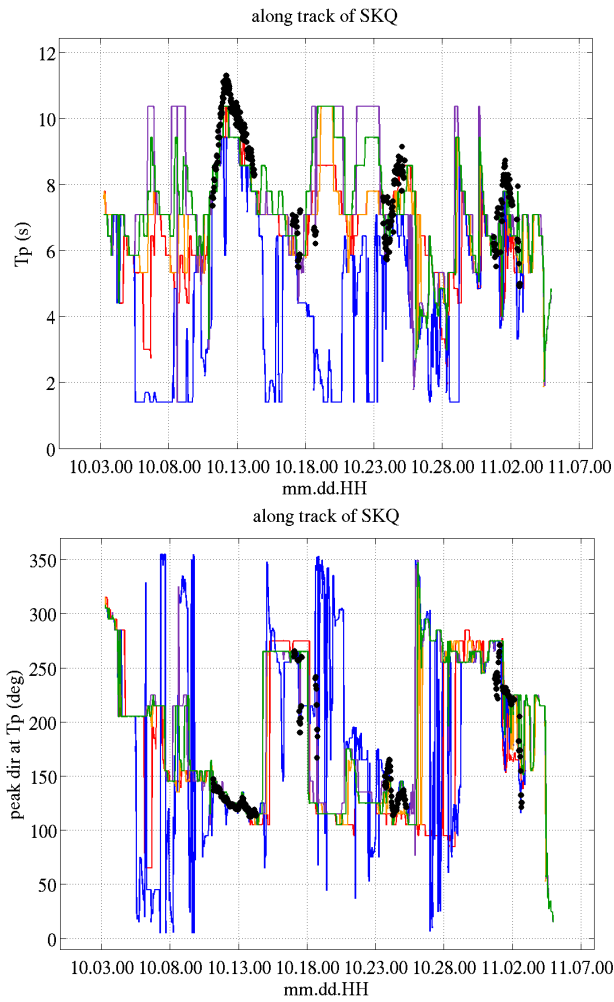


Figure 119. Time series comparisons along track of *Sikuliaq*, with the five model hindcasts shown in Figure 118. Observations (black points) are from ship radar. Top panel:  $T_p$  comparison. Lower panel: peak direction comparison. Ship observations were provided by Ola Persson (NOAA); the marine radar operation and data processing was performed by Bjoern Lund (U. Miami).

#### 6.3.4. Validation, by wave experiments individually

For each of the eight simulations numbered in Section 6.3.1, we produced time series plots and scatter plots, broken out by wave experiment, buoy type, and wave parameter. There are 35 wave experiment / buoy type / parameter combinations, and so 280 of each plot type. It is impractical to present so many plots, so instead we present examples in three figures (Figure 120 to Figure 122) and summarize the statistics in three tables, one for each wave parameter (Table 2 to Table 4). Only two of the eight models are presented: IC4M6H and IC4M6H2 with the 10 km AMSR2 forcing, since these were two of the three most skillful models in the overall comparisons for the wave experiments (Figure 109 to Figure 117). (The IC2 hindcast is the third that performed well, especially for wave period, but it is left out here.) Scatter plots presented in this section are for WA3 only, while tabulated statistics include all wave experiments.

#### Scatter plots

Figure 120 compares the IC4M6H model to the SWIFT and NIWA buoys in WA3. Figure 121 repeats the same SWIFT comparison, but contrasts with the UK buoys instead of the NIWA buoys. Figure 122 is like Figure 120, but evaluating the IC4M6H2 model. Discussion of the figures follows:

- With  $H_{m0}$ , the IC4M6H model tends to fall above the best fit line (+13% bias) when compared against the SWIFT buoys and below the line (-11% bias) when compared against the UK buoys, essentially splitting the difference between the two. Similarly, with respect to  $m_4$ , the bias is +51% and -5% for the two buoy types. There is larger difference between buoys types (SWIFT vs. UK) than between the two models (IC4M6H vs. IC4M6H2). Since these buoys were deployed along the same transect, this discrepancy is troubling. This is discussed further in Section 6.3.6.
- The +51% bias of the  $m_4$  comparison for the IC4M6H vs. SWIFT is disappointing. However, the biases for IC4M6H2/SWIFT, IC4M6H/UK, and IC4M6H2/UK are less bad: +37%, -5%, and -22%.
- Ice is more likely to be under-predicted by AMSR2 than over-predicted (wet ice may be undetected). This would imply under-prediction of high frequency damping and over-prediction of  $m_4$  (positive bias). However, we only see positive bias in comparison to the SWIFT buoys.
- Compared to the NIWA buoy, the IC4M6H model beautifully captures the damping of both the dominant wave energy and the high frequency energy. The only blemish is the underprediction of the highest waveheights, but we believe that this is associated with the wind forcing. Thus, the IC4M6H model seems well suited for the ice type encountered by the waves which arrived at the NIWA buoy. The good agreement is especially remarkable considering how much the spectra change before they arrive at the buoy, e.g.  $m_4$  is reduced from around  $0.9 \text{ m}^2\text{s}^4$  to around  $0.3 \text{ m}^2\text{s}^4$ : it is unusual for a model to accurately and consistently predict such large changes resulting from secondary source terms.
- The newer IC4M6H2 model is less skillful than the older IC4M6H at predicting the waves measured by the NIWA buoy, and is probably overpredicting dissipation across all frequencies. We believe that this means one of two things: either the model is not well suited to the ice type encountered by these waves, or the model needs to be nonlinear like IC2, in other words predict a reduced exponential decay rate when the energy and orbital velocities are smaller. The overprediction of dissipation by IC4M6H2 implies that an IC4M6 step function based on the dissipation profiles of Cheng et al. (2016) would also overpredict dissipation, since those dissipation rates are even higher than IC4M6H2: see Figure 95. To be clear: this does not necessarily imply that the Cheng et al. (2016)  $k_i(f)$  estimates are inaccurate, but rather that they would not produce accurate wave prediction (energy would be underpredicted) if applied as a parametric function  $k_i(f)$  to our WW3 hindcast of WA3.

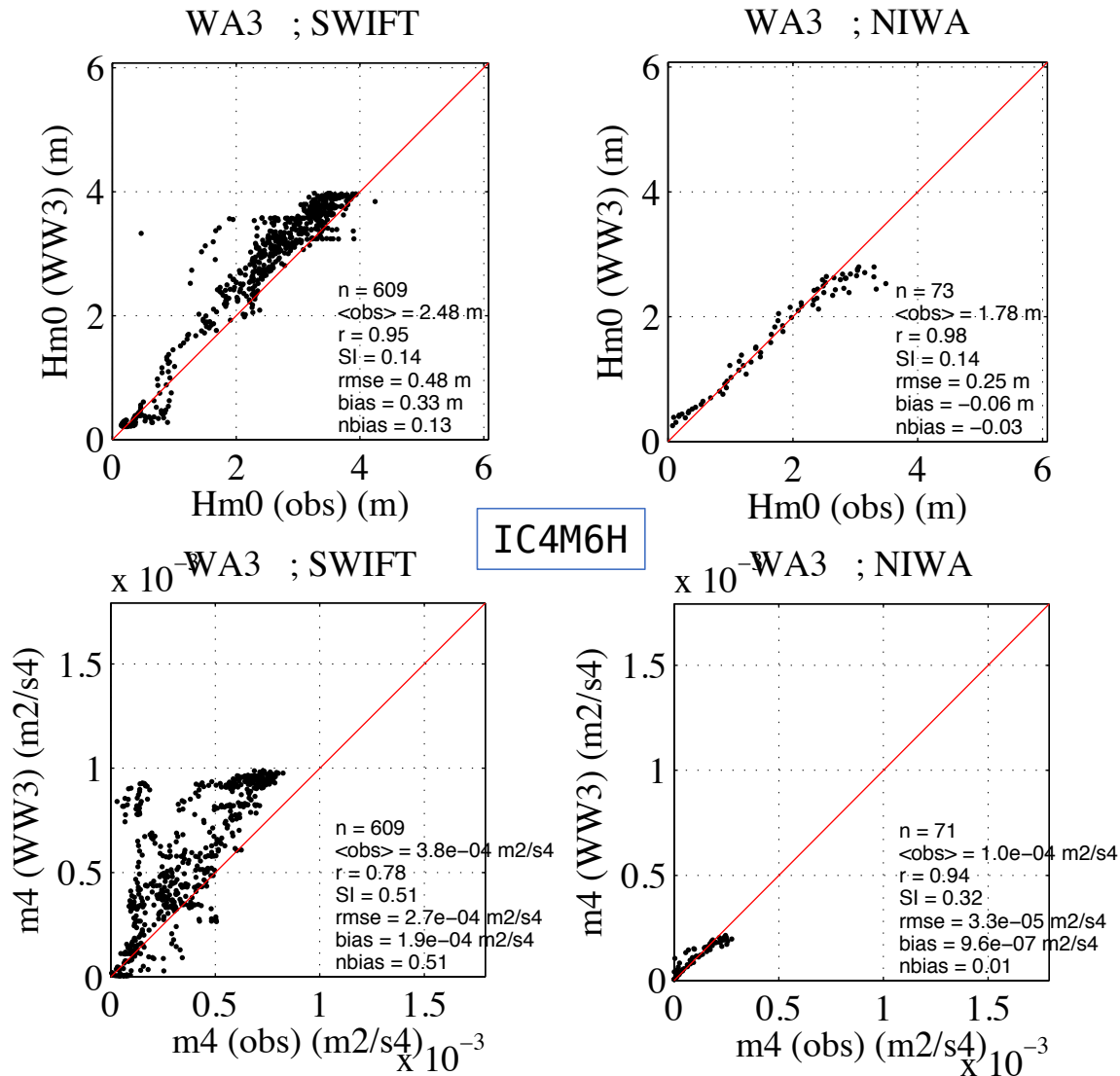


Figure 120. Example scatter plots and statistics for the IC4M6H hindcast. Top panels: H<sub>m0</sub>. Lower panels: m<sub>4</sub>. Left panels: WA3 SWIFT buoys. Right panels: WA3 NIWA buoy.

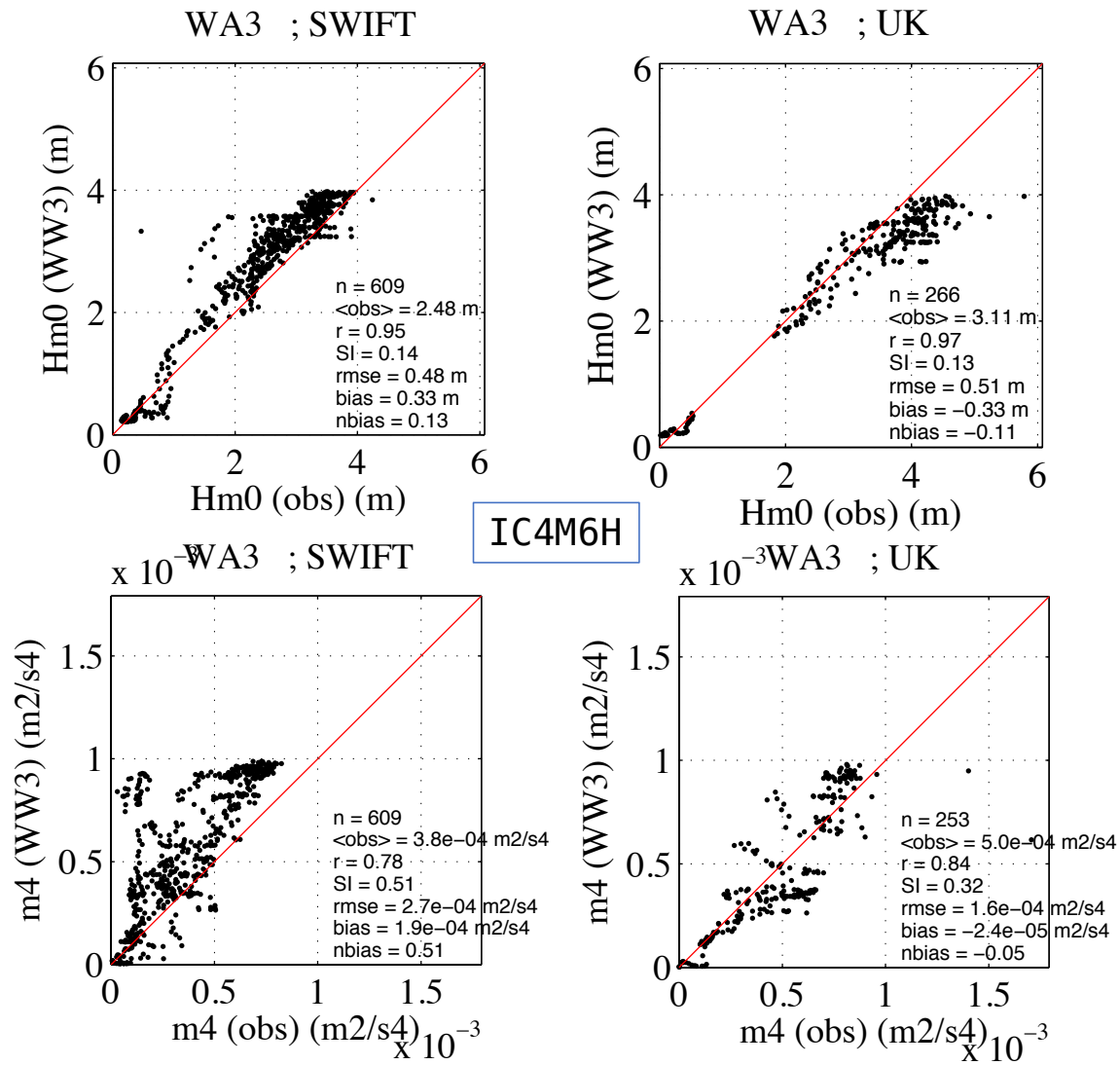


Figure 121. Same as Figure 120, except comparing SWIFTs against the UK buoys.

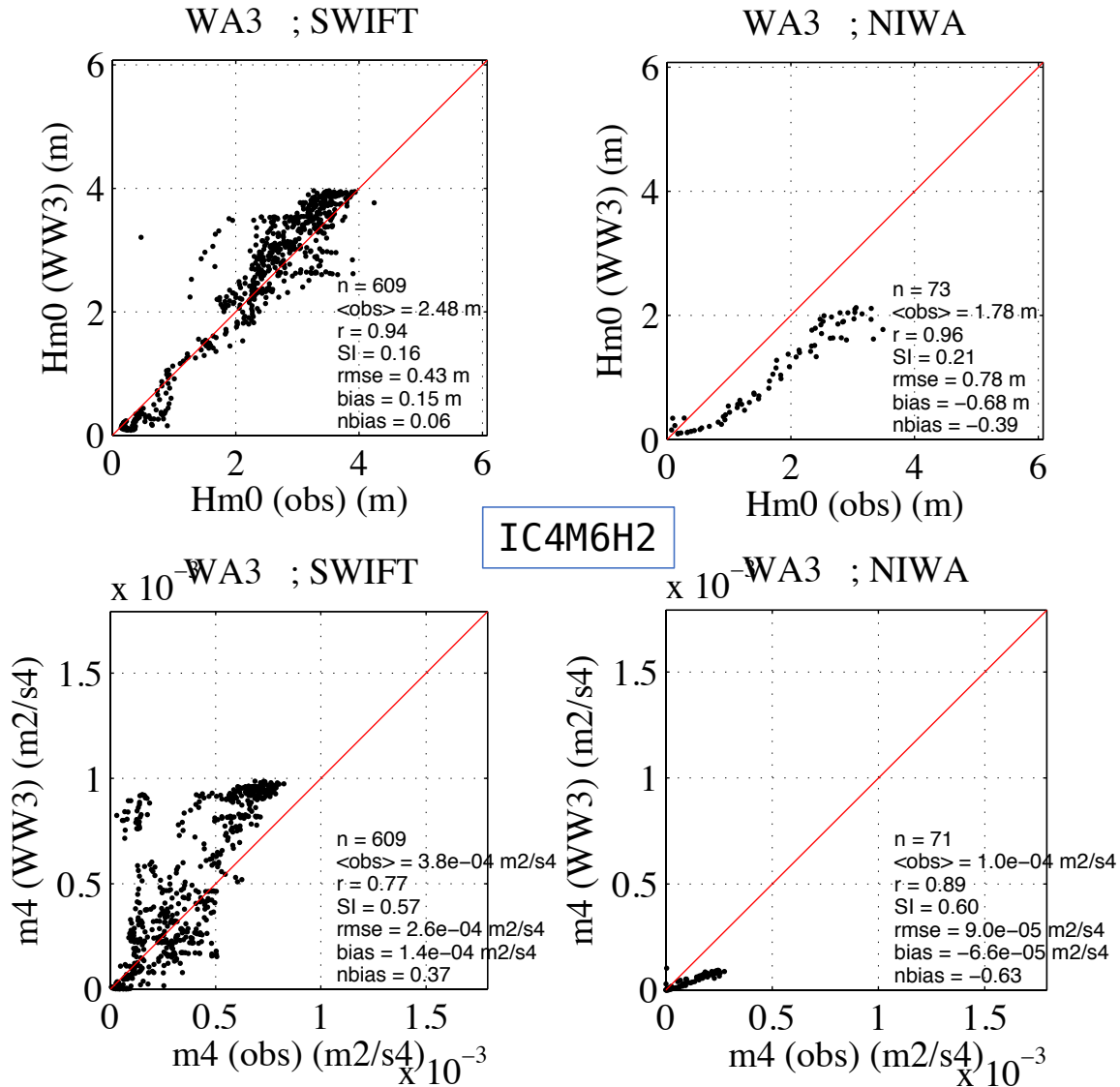


Figure 122. Same as Figure 120, except showing the IC4M6H2 hindcast.

#### Tabulated statistics

Statistics for  $H_{m0}$ ,  $T_{m,-1,0}$ , and  $m_4$  are shown in Table 2, Table 3, and Table 4, respectively. Discussion follows:

- Table 2: In WA2, the UK buoys were in ice (see Section 2.2.2) which the model was apparently unaware of. Thus, correlation with these buoys is poor. Most of the SWIFT data were collected in open water and thus correlation is better. This underscores the difficulty of making an accurate forecast or hindcast so near an ice edge.
- Table 2: In IS1, the correlation is poor for both models, which suggests that they are missing the dominant control on waveheight variation. Model IC4M6H2 correctly predicts the near-zero energy levels ( $H_{m0}=1$  cm), while dissipation is a bit too weak in IC4M6H ( $H_{m0}=6$  cm).
- Table 2: In WA3, correlation is 0.93 or better for all cases, indicating that the dominant control waveheight variation is captured by the models. Correlation is better for the

NIWA buoy (further in the ice) which again reinforces the conclusion that distance from ice edge tends to be a strong control on model skill, and the conclusion that the presence of ice does not necessarily have a negative impact on model skill.

- Table 2, WA3: Interestingly, correlation is better for all buoys with the less dissipative IC4M6H model, even though the IC4M6H2 model is based on inversion with the AMSR2 forcing used here. However, we should keep in mind that the IC4M6H2 step function is taken from a relatively small subset of the WA3 inversions: SWIFT buoys in relatively thick frazil and pancake ice.
- Table 2, WA3: Normalized bias tends to be small, and as already discussed, the sign of bias corresponds to the buoy type, rather than model type.
- Table 2, WA4-5: In comparison to SWIFT spectra, predictions from both models are adequately skilled, especially considering the low energy levels. In the case of the UK buoys, which were in more substantial ice, the IC4M6H model's dissipation is too weak, while the IC4M6H2 dissipation is appropriate.
- Table 2, WA6: The stronger dissipation of IC4M6H2 is more appropriate than the weaker dissipation of IC4M6H. Correlation is good, despite the small observed waveheight (weakly forced conditions).
- Table 2, RT: Correlation is again good, despite the small observed waveheight. Bias is excellent for both models (IC4M6H2 having negative bias and IC4M6H positive).
- Table 2, WA7:  $H_s$  bias is negative (-32% to -44%) for both models and both buoy types, and of course the more dissipative model has worse bias (-43% and -44%). As we discussed in Section 6.3.3, the negative bias is probably associated more with the accuracy of the ice forcing than with the  $S_{ice}$  physics.
- Table 3, wave period correlation is poor for all cases except WA3, implying that the dominant factors controlling mean period are not well represented in the models for those wave experiments. Of course, by looking at wave experiments individually, we are evaluating relatively flat time series of wave period, so it is challenging to achieve high correlation. Better correlation is found for the full cruise (e.g. Figure 113), since the time series is not flat.
- Table 3: In WA2, both models overpredict the mean period by 0.9 seconds. In all other cases, bias is quite low (e.g. 5% or 10%). The RMS error also tends to be small for mean period.
- Table 3, WA3: As was the case with waveheight, the IC4M6H model has higher  $T_{m,-1,0}$  skill than the IC4M6H2. But since  $T_{m,-1,0}$  is primarily controlled by open water physics, rather than by the  $S_{ice}$  physics, the differences between model skill in Table 3 are small.
- Table 4, WA4-5: correlation of  $m_4$  is poor, but mean values of observed  $m_4$  are very small and this is well-captured by the models.
- Table 4, WA2, RT, and WA7:  $m_4$  biases are all negative. In case of WA2, the  $H_{m0}$  bias has opposite sign, which implies that frequency variation of damping is not well represented, either because of forcing or  $S_{ice}$ . Given the irregular bands of ice, this is a challenging case for the model. In the case of RT, the observed  $m_4$  is small and correlation is good. In the case of WA7, as mentioned above, the negative bias is likely associated with the ice concentration forcing.
- Table 4, WA6: The prediction of  $m_4$  is poor in every respect for the UK buoys. Time series of the latter suggest that dissipation is too strong in the early part of the experiment

and too weak in the later part. This is indicative of the high difficulty of wave prediction near an ice edge, where buoys are drifting in and out of bands of ice (Section 2.2.6), and of course  $m_4$  is more sensitive to these ice bands than the other two wave parameters. In the case of the SWIFT buoys, which were on average in less substantial ice, the prediction is fair.

*Time series of individual buoys ( $H_{m0}$  only and WA3 only)*

Time series comparisons such as those shown in Section 6.3.3 allow us to include a lot of data in one plot, but unfortunately, they do not distinguish between different buoys deployed simultaneously. In Figure 123, Figure 124, and Figure 125 we include a few of the WA3 deployments, by individual buoys, but only for waveheight, and the UK buoys are not included. Figure 123 shows the six SWIFT buoys used along the southern (primary) transect of WA3; Figure 124 shows the two SWIFT buoys which were deployed on the northern transect and never recovered; and Figure 125 compares against the NIWA buoy.

Results from the IC0 model are also included here. Recall that the primary flaw of IC0 is that the “dissipation” is uniform in frequency space. The present comparison is not strongly sensitive to this flaw, since the comparison is for waveheight only. However, we have already demonstrated that flaw in the context of  $m_4$  prediction in Section 6.3.3, using the IC1  $k_i=40\text{e-6 m}^{-1}$  model which also is uniform in frequency space: in other words, the IC1 hindcast was used as a proxy for the IC0 model in Section 6.3.3<sup>31</sup>. However, in these three plots, one characteristic of IC0 is immediately obvious: an irregular rising and falling of waveheight which bears no resemblance to the measured values of S09, S14, and S15. This irregularity is caused by a combination of a) strong dissipation of the dominant waves (wave periods nears 10 seconds) and b) discontinuous update of the ice cover in WW3 forcing (recall that WW3 selects the “nearest neighbor in time” for the ice field). The IC4 model has the same discontinuous update, but does not have strong dissipation of the dominant frequencies, so it is much better correlated with the observed time series. The NIWA buoy is in ice throughout, so we do not see the irregular rising and falling in Figure 125, but we do see again that the IC0 model is too dissipative: it does not account for the fact that the wave energy of the dominant waves is only weakly dissipated by the sea ice, while IC4M6 readily accounts for this.

The differences between IC4M6H and IC4M6H2 are most noticeable at buoys S14 and S15 since these buoys were in more substantial ice. In the case of S15, the comparison favors IC4M6H (less dissipative) in the early part of the time series and IC4M6H2 (more dissipative) in the later part. As noted already, the NIWA buoy comparison strongly favors IC4M6H over IC4M6H2 throughout.

---

<sup>31</sup> This proxy was convenient for us, since there is an unresolved bug associated with “track output” for co-location with drifting buoys, used in conjunction with the IC0 switch. For the co-locations in these three figures, we interpolate from bulk field output rather than the “track output”.

Table 2. Statistics for significant wave height,  $H_{m0}$ . For dimensional quantities, units are in meters.

runid	experiment	Buoy type	n	<obs>	r	rmse	bias	SI	nrmse	nbias
B12_IC4M6H	WA2	SWIFT	33	0.31	0.76	0.22	0.15	0.55	0.72	0.46
B12_IC4M6H	WA2	UK	8	0.09	-0.30	0.32	0.32	0.30	3.56	3.55
B12_IC4M6H2	WA2	SWIFT	33	0.31	0.76	0.21	0.12	0.55	0.67	0.39
B12_IC4M6H2	WA2	UK	8	0.09	-0.38	0.29	0.29	0.30	3.29	3.28
B12_IC4M6H	IS1	SWIFT	129	0.01	-0.08	0.05	0.05	2.45	6.61	6.15
B12_IC4M6H2	IS1	SWIFT	129	0.01	-0.23	0.00	0.00	0.25	0.49	-0.43
B12_IC4M6H	WA3	SWIFT	609	2.48	0.95	0.48	0.33	0.14	0.19	0.13
B12_IC4M6H	WA3	UK	266	3.11	0.97	0.51	-0.33	0.13	0.16	-0.11
B12_IC4M6H	WA3	NIWA	73	1.78	0.98	0.25	-0.06	0.14	0.14	-0.03
B12_IC4M6H2	WA3	SWIFT	609	2.48	0.94	0.43	0.15	0.16	0.17	0.06
B12_IC4M6H2	WA3	UK	266	3.11	0.93	0.80	-0.60	0.17	0.26	-0.19
B12_IC4M6H2	WA3	NIWA	73	1.78	0.96	0.78	-0.68	0.21	0.44	-0.39
B12_IC4M6H	WA4-5	SWIFT	180	0.17	0.50	0.11	0.02	0.65	0.67	0.13
B12_IC4M6H	WA4-5	UK	266	0.03	0.39	0.12	0.11	1.70	3.71	3.29
B12_IC4M6H2	WA4-5	SWIFT	180	0.17	0.72	0.10	-0.07	0.48	0.63	-0.40
B12_IC4M6H2	WA4-5	UK	266	0.03	0.62	0.04	0.01	1.15	1.23	0.43
B12_IC4M6H	WA6	SWIFT	283	0.84	0.83	0.50	0.44	0.29	0.59	0.52
B12_IC4M6H	WA6	UK	179	0.52	0.91	0.39	0.37	0.28	0.76	0.70
B12_IC4M6H2	WA6	SWIFT	283	0.84	0.85	0.33	0.21	0.30	0.39	0.25
B12_IC4M6H2	WA6	UK	179	0.52	0.89	0.20	0.11	0.32	0.38	0.21
B12_IC4M6H	RT	SWIFT	121	0.15	0.91	0.05	0.01	0.33	0.33	0.06
B12_IC4M6H2	RT	SWIFT	121	0.15	0.90	0.05	-0.01	0.33	0.34	-0.07
B12_IC4M6H	WA7	SWIFT	188	0.8	0.78	0.34	-0.27	0.27	0.42	-0.33
B12_IC4M6H	WA7	UK	255	0.74	0.66	0.36	-0.24	0.36	0.48	-0.32
B12_IC4M6H2	WA7	SWIFT	188	0.8	0.79	0.40	-0.35	0.26	0.50	-0.43
B12_IC4M6H2	WA7	UK	255	0.74	0.70	0.41	-0.33	0.34	0.56	-0.44

Table 3. Statistics for mean period,  $T_{m,-1,0}$ . For dimensional quantities, units are in seconds.

runid	experiment	Buoy type	n	$\langle \text{obs} \rangle$	r	rmse	bias	SI	nrmse	nbias
B12_IC4M6H	WA2	SWIFT	20	3.81	0.32	0.9	0.9	0.04	0.24	0.23
B12_IC4M6H2	WA2	SWIFT	20	3.81	0.30	0.9	0.9	0.04	0.23	0.22
B12_IC4M6H	WA3	SWIFT	609	7.72	0.89	0.8	-0.3	0.09	0.10	-0.04
B12_IC4M6H	WA3	UK	253	8.03	0.95	0.6	-0.2	0.07	0.07	-0.03
B12_IC4M6H	WA3	NIWA	71	8.35	0.78	0.6	-0.4	0.05	0.07	-0.05
B12_IC4M6H2	WA3	SWIFT	609	7.72	0.88	0.8	-0.4	0.09	0.10	-0.05
B12_IC4M6H2	WA3	UK	253	8.03	0.93	0.5	-0.2	0.06	0.07	-0.02
B12_IC4M6H2	WA3	NIWA	71	8.35	0.75	0.5	0.0	0.06	0.06	0.00
B12_IC4M6H	WA4-5	SWIFT	105	5.4	-0.12	1.1	0.1	0.20	0.20	0.02
B12_IC4M6H	WA4-5	UK	26	6.55	0.51	1.1	-0.8	0.11	0.16	-0.12
B12_IC4M6H2	WA4-5	SWIFT	105	5.4	0.54	0.8	-0.3	0.14	0.15	-0.06
B12_IC4M6H2	WA4-5	UK	26	6.55	0.58	1.0	-0.7	0.10	0.15	-0.11
B12_IC4M6H	WA6	SWIFT	283	5.33	0.46	1.2	0.9	0.15	0.22	0.16
B12_IC4M6H	WA6	UK	179	5.89	-0.15	1.3	0.6	0.19	0.21	0.10
B12_IC4M6H2	WA6	SWIFT	283	5.33	0.35	1.0	0.6	0.16	0.19	0.11
B12_IC4M6H2	WA6	UK	179	5.89	-0.21	1.3	0.4	0.20	0.21	0.06
B12_IC4M6H	RT	SWIFT	67	3.55	0.56	0.6	0.3	0.14	0.17	0.09
B12_IC4M6H2	RT	SWIFT	67	3.55	0.59	0.6	0.3	0.14	0.16	0.08
B12_IC4M6H	WA7	SWIFT	186	5.64	0.42	0.7	0.3	0.11	0.12	0.05
B12_IC4M6H	WA7	UK	255	6.63	0.38	0.8	-0.5	0.10	0.13	-0.07
B12_IC4M6H2	WA7	SWIFT	186	5.64	0.42	0.7	0.4	0.11	0.13	0.07
B12_IC4M6H2	WA7	UK	255	6.63	0.43	0.8	-0.3	0.10	0.11	-0.05

Table 4. Statistics for fourth moment of spectrum,  $m_4$ . For dimensional quantities, units are in  $m^2 s^{-4}$ .

runid	experiment	Buoy type	n	<obs>	r	rmse	bias	SI	nrmse	nbias
B12_IC4M6H	WA2	SWIFT	20	1.90E-04	0.59	7.00E-05	-5.60E-05	0.23	0.37	-0.30
B12_IC4M6H2	WA2	SWIFT	20	1.90E-04	0.58	7.50E-05	-6.20E-05	0.23	0.40	-0.33
B12_IC4M6H	WA3	SWIFT	609	3.80E-04	0.78	2.70E-04	1.90E-04	0.51	0.71	0.51
B12_IC4M6H	WA3	UK	253	5.00E-04	0.84	1.60E-04	-2.40E-05	0.32	0.33	-0.05
B12_IC4M6H	WA3	NIWA	71	1.00E-04	0.94	3.30E-05	9.60E-07	0.32	0.31	0.01
B12_IC4M6H2	WA3	SWIFT	609	3.80E-04	0.77	2.60E-04	1.40E-04	0.57	0.67	0.37
B12_IC4M6H2	WA3	UK	253	5.00E-04	0.78	2.30E-04	-1.10E-04	0.41	0.46	-0.22
B12_IC4M6H2	WA3	NIWA	71	1.00E-04	0.89	9.00E-05	-6.60E-05	0.60	0.87	-0.63
B12_IC4M6H	WA4-5	SWIFT	105	1.80E-05	0.44	3.70E-05	-1.90E-06	2.14	2.14	-0.11
B12_IC4M6H	WA4-5	UK	26	1.50E-06	-0.47	2.20E-06	1.20E-06	1.27	1.50	0.84
B12_IC4M6H2	WA4-5	SWIFT	105	1.80E-05	0.36	3.80E-05	-5.30E-06	2.16	2.17	-0.31
B12_IC4M6H2	WA4-5	UK	26	1.50E-06	-0.35	1.60E-06	-8.80E-07	0.89	1.06	-0.59
B12_IC4M6H	WA6	SWIFT	283	2.70E-04	0.68	1.70E-04	5.00E-05	0.58	0.61	0.18
B12_IC4M6H	WA6	UK	179	8.90E-05	0.29	1.90E-04	5.10E-05	2.03	2.11	0.58
B12_IC4M6H2	WA6	SWIFT	283	2.70E-04	0.67	1.60E-04	1.50E-05	0.58	0.58	0.05
B12_IC4M6H2	WA6	UK	179	8.90E-05	0.27	1.80E-04	2.60E-05	1.96	1.97	0.29
B12_IC4M6H	RT	SWIFT	67	7.90E-05	0.87	4.60E-05	-3.70E-05	0.34	0.58	-0.47
B12_IC4M6H2	RT	SWIFT	67	7.90E-05	0.82	5.50E-05	-4.50E-05	0.39	0.69	-0.57
B12_IC4M6H	WA7	SWIFT	186	1.70E-04	0.61	1.80E-04	-1.20E-04	0.81	1.07	-0.70
B12_IC4M6H	WA7	UK	255	3.80E-05	0.59	3.30E-05	-1.20E-05	0.81	0.86	-0.30
B12_IC4M6H2	WA7	SWIFT	186	1.70E-04	0.57	2.00E-04	-1.40E-04	0.85	1.16	-0.79
B12_IC4M6H2	WA7	UK	255	3.80E-05	0.59	3.60E-05	-2.10E-05	0.77	0.95	-0.56

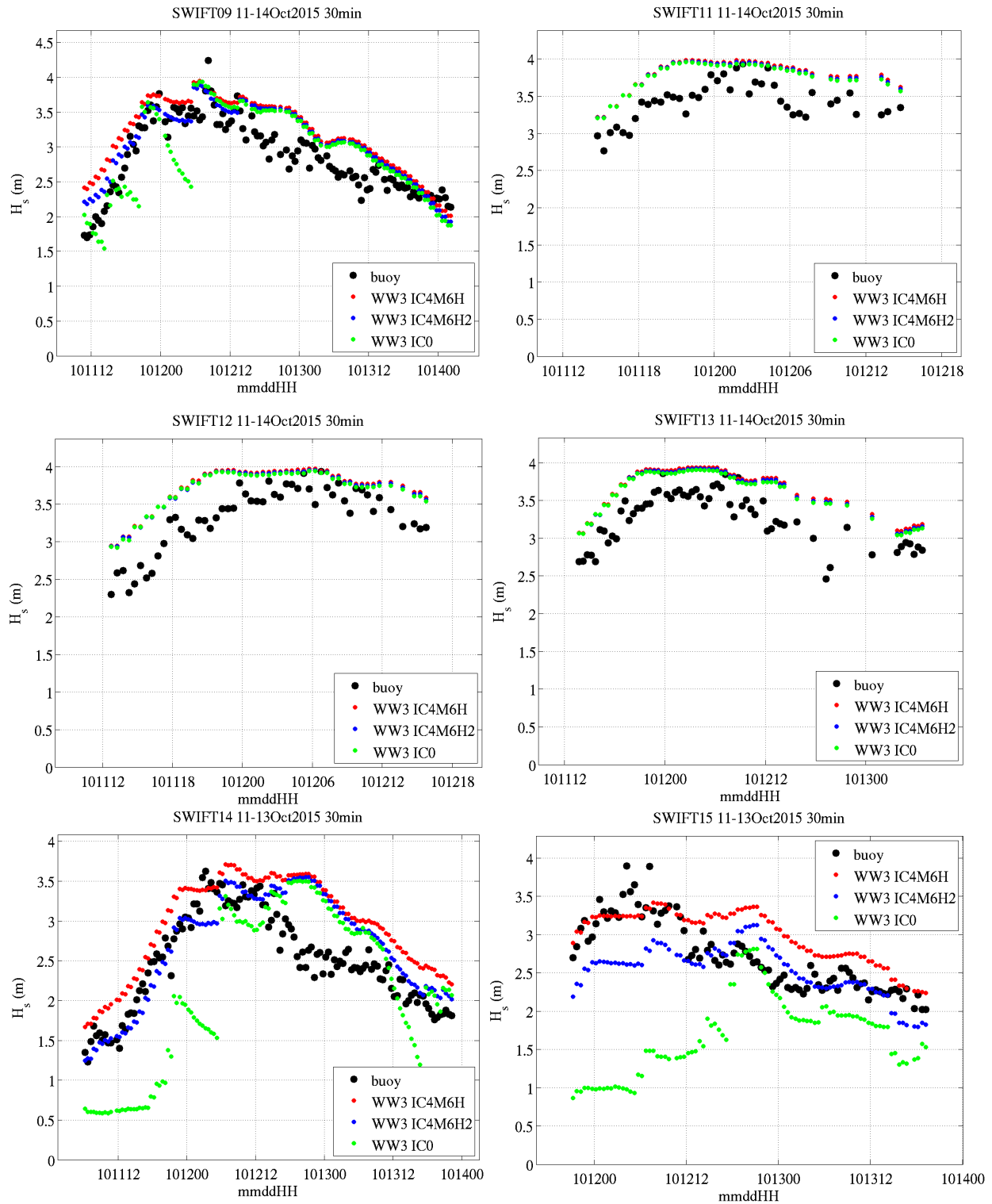


Figure 123. Wave height time-series comparison of models vs. SWIFT buoys along the southern transect of WA3. Models use IC4M6 source functions and IC0 of Tolman (2003).

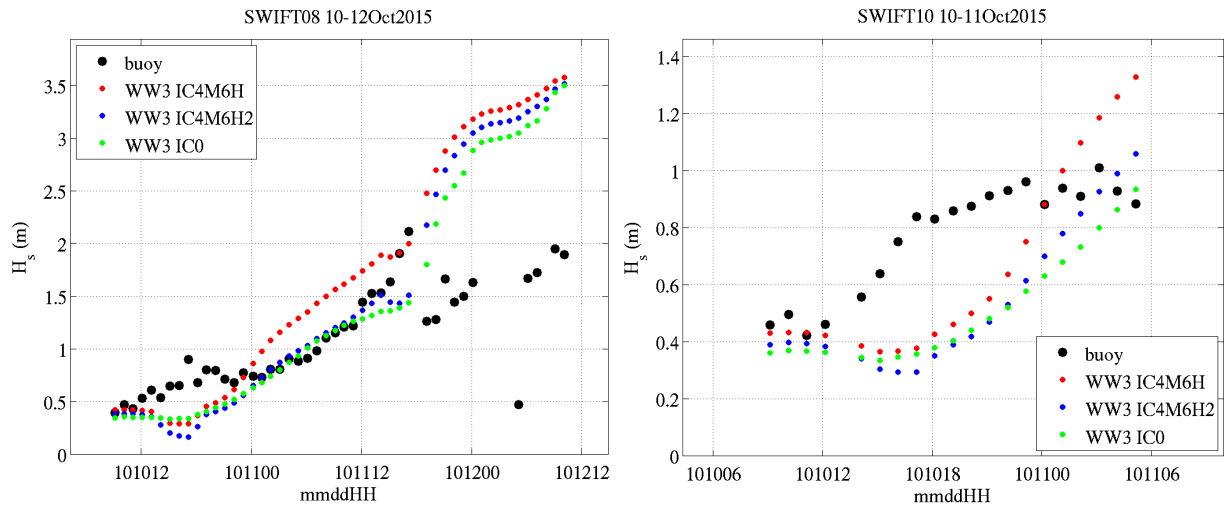


Figure 124. Like Figure 123, but comparing against data from the two SWIFT buoys deployed on the northern transect of WA3. These buoys were not recovered and data is from telemetry, so processing was different from data in Figure 123.

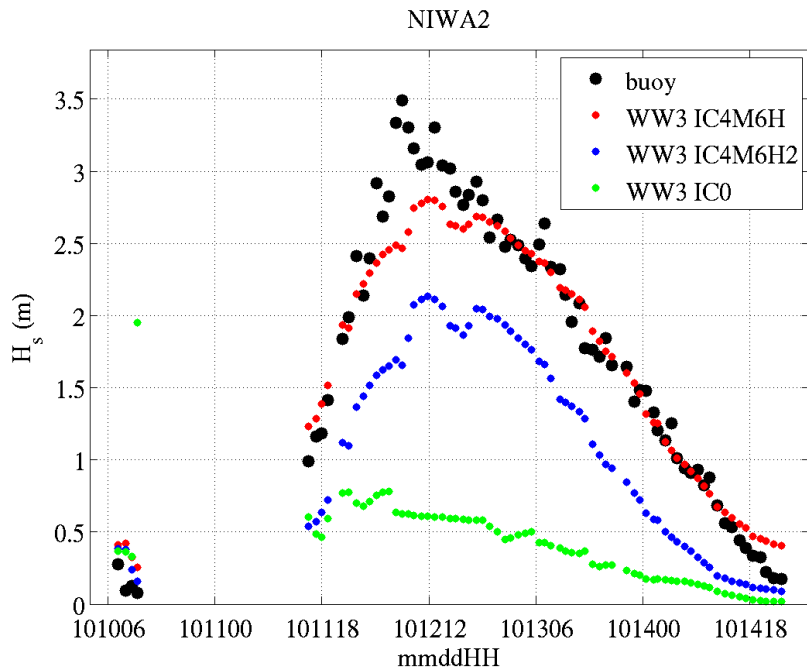


Figure 125. Like Figure 123, but comparing against data from the NIWA buoy deployed on the northern transect of WA3.

Figure 126 compares a different set of four models and four buoys. The models are:

- 1) IC1 with  $k_i=4e-5 \text{ m}^{-1}$ , as used in Figure 109;
- 2) IC2 (boundary layer dissipation), as used in Figure 112;
- 3) IC4M6H; and
- 4) IC4M6H2.

The buoys are listed in order from the location in open water to the location furthest into the ice:

- 1) SWIFT 11 in the southern transect of WA3, drifting in open water near 72.4N, 148.9W
- 2) SWIFT 14 in the southern transect of WA3, drifting pancake and frazil ice near 72.9N, 150.7W
- 3) The NIWA buoy, in the northern transect of WA3, drifting near 73.8N, 153.8W
- 4) The AWACBGA sub-surface buoy, moored at 75N, 150W

We should keep in mind, however, that the four locations are *not* arranged to be along a single line in the primary wave direction: that is true only for the first three. The AWACBGA buoy is offset to the right (north) of that axis. The latter two buoys were used to make a similar comparison in an earlier paper: Figure 8 of Cheng et al. (2017).

Since we have concerns about the high frequency energy from the AWAC buoys, only waveheight is plotted here, and so this is an evaluation of dissipation of the energy near the peak of the spectrum ( $T \approx 10$  s) by the sea ice. Some remarks follow:

- The IC1 model overpredicts damping of the spectral peak.
- The IC2 model overpredicts dissipation between S14 and NIWA2, but does well to predict the average dissipation upwave of AWACBGA. This may be caused by more dissipative ice upwave of AWACBGA, relative to the ice of WA3.
- The IC4M6H model adequately predicts the peak dissipation between the SWIFT buoys and NIWA2. However, the dissipation in this model is too weak to represent the dissipation upwave of AWACBGA, again implying that this ice is relatively more dissipative.
- Though the overprediction of the IC4M6H model at AWACBGA is likely associated with more dissipative ice, it is worthwhile to note that if this model was made nonlinear such that the exponential dissipation rate is smaller when waveheight is smaller (in other words, nonlinear dissipation, as with IC2), that would actually make the model worse. This highlights an important point: when interpreting these comparisons, it is very difficult to separate the effect of nonlinear dissipation from the effect of non-uniform ice type. Laboratory studies are better suited for studies of nonlinearity of dissipation.
- The IC4M6H2 model is too dissipative at both NIWA2 and AWACBGA, though only moderately so for the latter.

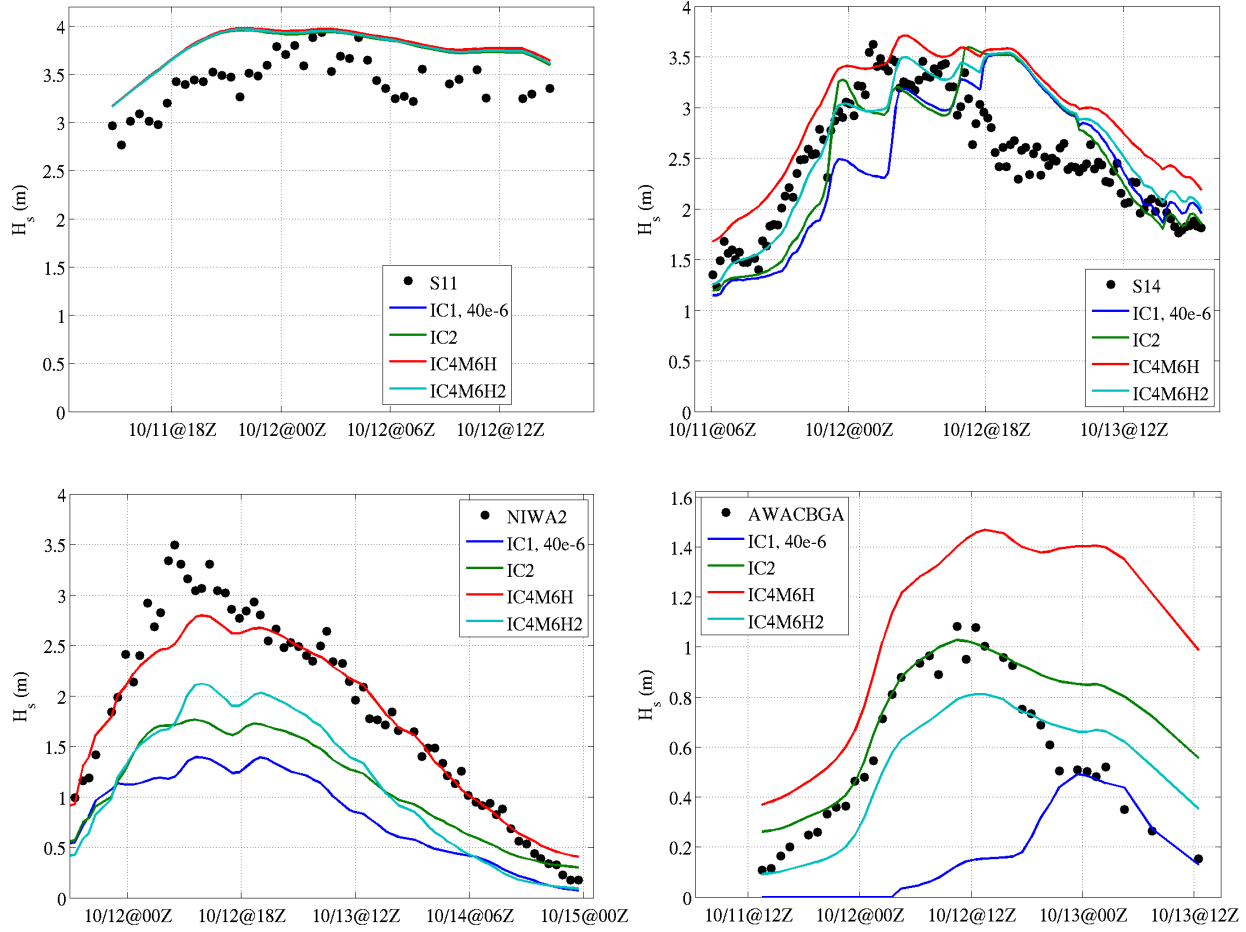


Figure 126. Comparison of four models, progressing from outside the ice to further into the ice: SWIFT 11, SWIFT 14, NIWA2, and AWACBGA.

### 6.3.5. Sensitivity analysis: thermal stability effects (WA3)

In the prior sections, we discussed how the WW3 results during WA3 seem to reach a hard limit near  $H_s=4$  meters, even with  $S_{ice}=0$ . The SWIFT buoys show  $H_s$  values of similar magnitude, or a bit less, but with much less grouping of values at 4 meters. The UK buoys, on the other hand, show several cases of  $H_s$  over 4.5 meters, and again with no apparent grouping. Some hypotheses about the model behavior are:

1. Forcing in the atmospheric model may be too smooth, relative to actual winds, especially within the primary generation area southeast of WA3. This smoothness is a common feature of global atmospheric models.
2. Forcing in the atmospheric model may be too weak. However, this would not explain the grouping near  $H_s=4$  meters. In principle, a systematic bias in  $U_{10}$  can be accommodated by using a larger  $\beta_{max}$  value in WW3, but in our case, this would presumably just shift the grouping upwards, e.g. to  $H_s=4.5$  meters.
3. The method of scaling wind input by open water fraction (such that wind input is zero under 100% ice cover) may be faulty. This assumption was discussed by Rogers et al. (2016), and in that paper, the inversion was recalculated using an alternative assumption (a sensitivity analysis). However, we should keep in mind that this model behavior also exists at the locations of the open water buoys: Figure 128.

4. The model may suffer from non-representation of thermal stability effects. In the real ocean, where the air is colder than the water, the atmosphere can become unstable, making winds gustier, which implies an enhanced flux of momentum (i.e. enhanced  $C_{drag}$ ). This effect is discussed in context of wave observations by Kahma and Calkoen (1992) and Cavaleri (2000).

Thorough testing of these hypotheses is beyond the scope of the present report. Instead, we ask two relatively simple questions:

1. Is the “problem” resolved by using another wind product?
2. Is the “problem” resolved by activating stability effects in WW3? WW3 ST4 physics includes the option to represent stability effects using the “STAB3” switch, which activates the method of Abdalla and Bidlot (2002). In all simulations presented above, the STAB3 switch was not used (thus no stability effects). To include STAB3, the user must provide air-sea temperature differences along with the usual 10-meter wind speeds.

To this end, we make comparisons to two new simulations:

1. A simulation which is identical to our baseline IC4M6H simulation (used in Section 6.3.4, for example) except that it is forced by ECMWF winds, and with a different  $\beta_{max}$  setting. These winds were discussed in Section 5, and were provided by Dr. Justin Stopa (Ifremer). The  $\beta_{max}$  parameter is set to 1.45 instead of 1.20 as used in the NAVGEM-forced simulations, consistent with settings used in the Ifremer global model. This change in  $\beta_{max}$  is necessary, since ECMWF winds tend to be weaker than NAVGEM winds.
2. A simulation with the “STAB3” switch activated. Whereas our baseline model uses NAVGEM winds prescribed at 0.5° resolution, here we use winds from a higher resolution NAVGEM (T425L60), archived at 0.28° resolution. Air temperatures are taken from the same NAVGEM product. Sea surface temperatures (SSTs) are also included with the NAVGEM fields, but rather than use these, we use SST from GOFS 3.1, under the assumption that the latter are more accurate. (This simulation was created to estimate the impact of thermal stability on wave growth under fetch-limited off-ice conditions during the month before the cruise, and to compare with the growth measured by satellite (TerraSAR-X). Those comparisons are part of a collaboration with Prof. Johannes Gemmrich (U. Victoria) and are not included in this report.)

The baseline simulation (IC4M6H with 10-km AMSR2 forcing) and IC1 with  $k_i=0$  are also included, for sake of comparison. Both new simulations use the 10-km AMSR2 ice forcing and IC4M6H  $S_{ice}$  routine, as with the baseline simulation. An example of air-sea temperature differences (ASTD= $T_{air}-T_{sea}$ ) is given in Figure 127. The ASTDs are quite small in this case, with values of around 1° C in the generation region southeast of WA3 and even smaller values over WA3. The latter are likely spurious, since the GOFS 3.1 ice cover is over-predicted in this region, which would imply under-prediction of SST. However, there is no reason to expect that the SSTs in the generation region southeast of WA3 are spurious.

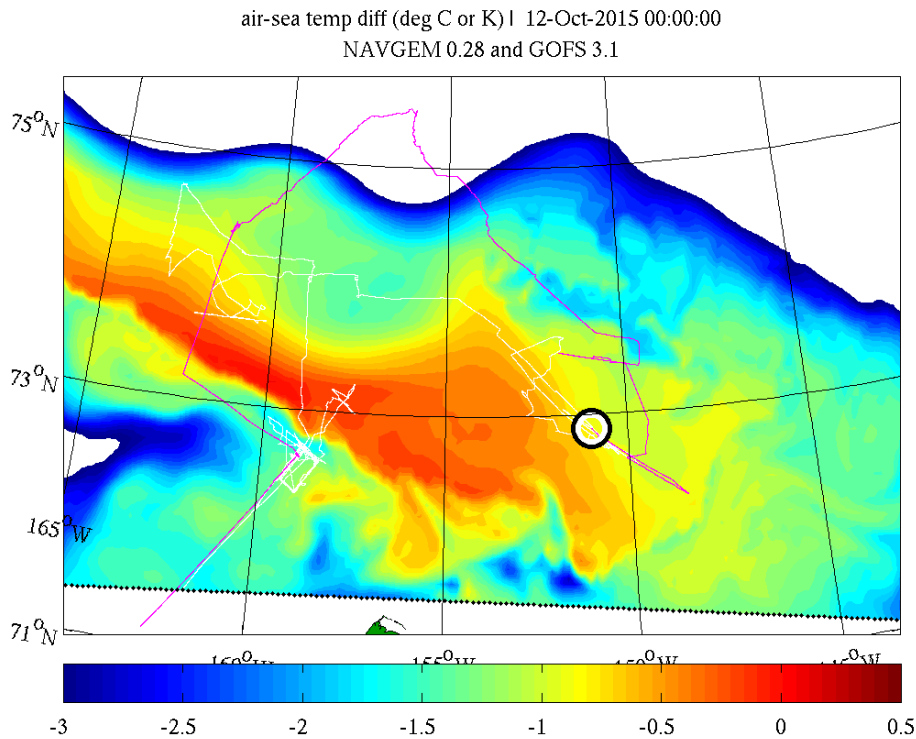


Figure 127. Air-sea temperature differences used in WW3 “STAB3” simulation, 0000 UTC 12 October 2015. Air-sea temperature differences less than  $-3^{\circ}\text{C}$  are shown as white.

Time series of significant waveheight are shown in Figure 128 and Figure 129. The former shows buoys that were predominately in open water, as evidenced by the similarity between the baseline model shown in green and the  $k_i=0$  model shown in blue. Figure 129 shows buoys that were predominately in ice, as evidenced by the dissimilarity between the baseline model and the  $k_i=0$  model.

Discussion points follow:

- The apparent  $H_s=4.0$  m “limit” in the baseline model and  $k_i=0$  model is strongly visible in Figure 128. Though this “limit” appears very artificial in the scatter plots (e.g. Figure 109), it does not appear unnatural in the time series. However, the models are of course much smoother than the observations.
- The existence of the limit for the  $k_i=0$  model implies that it is not associated with dissipation by sea ice. The existence of the limit for the open water buoys implies that it is probably also not associated with the model’s representation of wind input inside the sea ice.
- The highest waveheights measured by the UK buoys are around 4.8 meters. With the lidar (Figure 118), the maximum is around 4.5 meters. The SWIFT buoys and the models (including  $k_i=0$ ) have a maximum around 4.0 m. In the mean sense however, the models are have higher  $H_s$  than the SWIFTS (see bias in Table 2).
- Using the higher resolution NAVGEM and STAB3 has a noticeable impact on the model. One impact is a slightly increased variability. However, it does not result in better agreement with the drifting buoys.

- Waveheight is generally lower with the ECMWF wind forcing, implying that though the different  $\beta_{max}$  setting (NAVGEN vs. ECMWF) makes the WW3 energy level more similar than it would be otherwise, it does not fully close the gap. Because of the lower energy level, the WW3 with ECMWF forcing compares better with the SWIFT buoys than with the UK buoys.

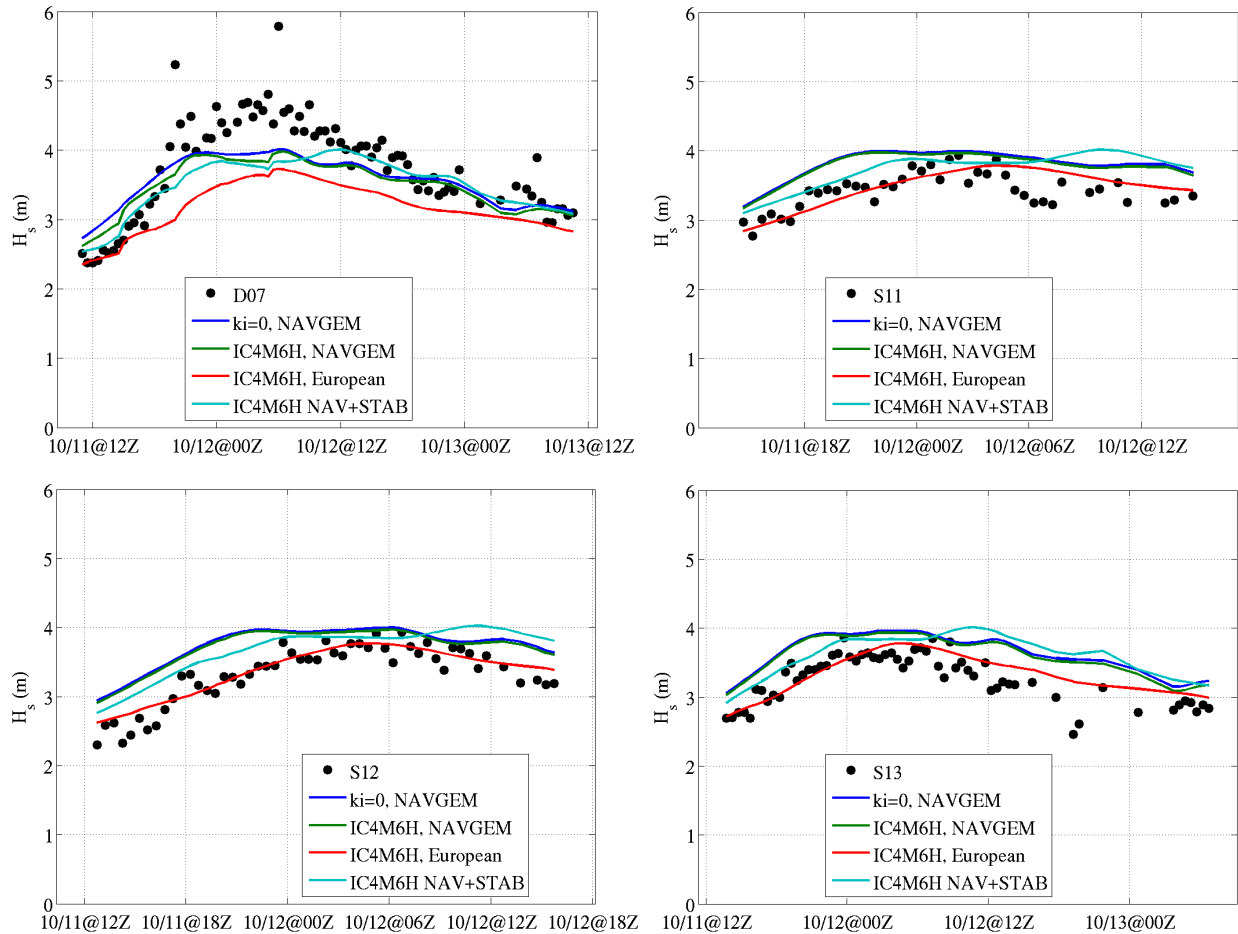


Figure 128. Time series of significant waveheight for four buoys that were predominately in open water. Green is the baseline model. Blue is the model without dissipation by sea ice. Red uses ECMWF winds instead of NAVGEM. Cyan includes air-sea stability effects.

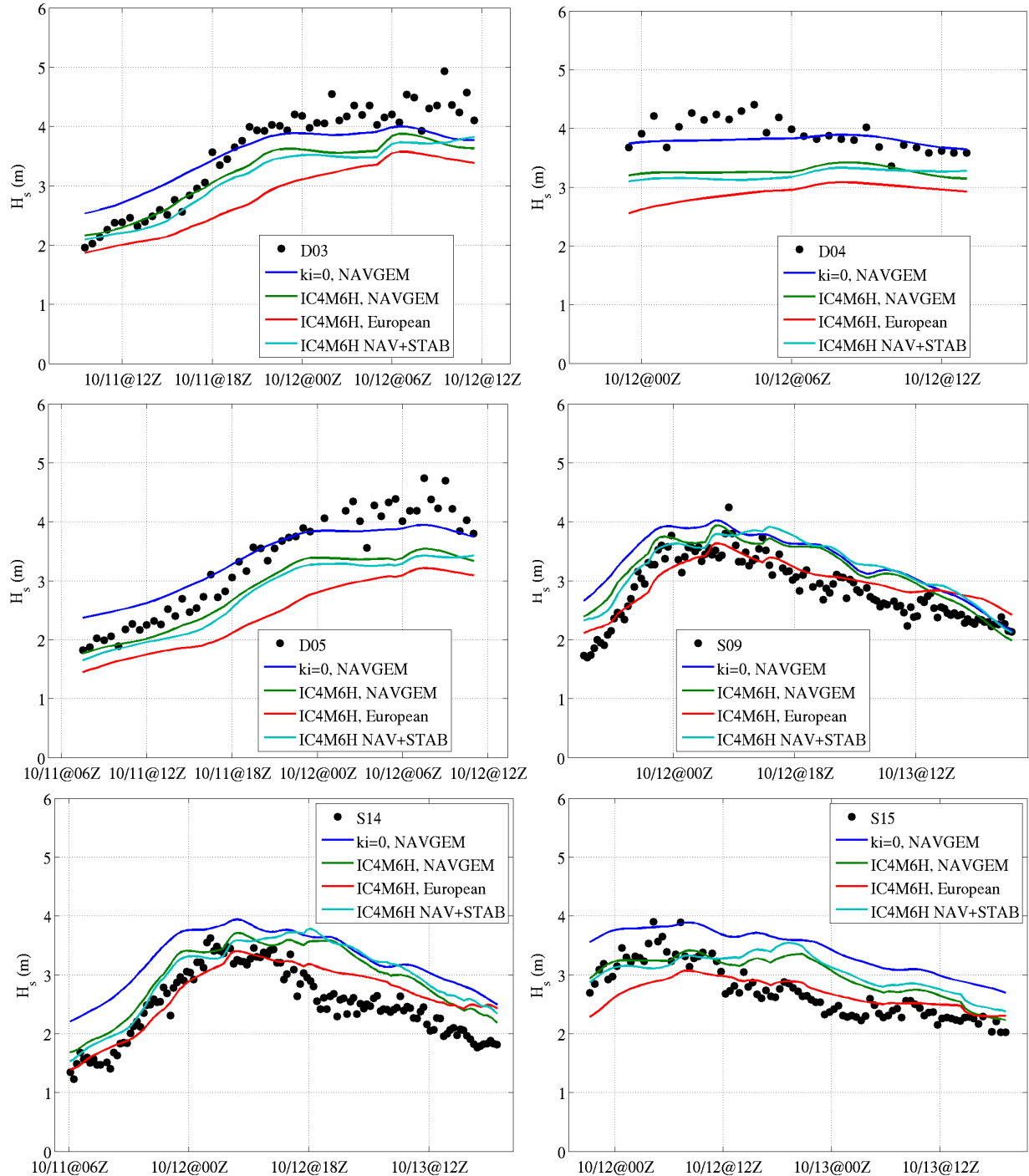


Figure 129. Like Figure 128, but for buoys that are predominately in sea ice, either for a portion of the time series (buoy S09) or most of the time series (the other five buoys).

### 6.3.6. Discussion: inconsistency between data from different buoy types in WA3

The conclusions above about model skill during WA3 unfortunately indicates a strong dependence on whether the SWIFT buoys or UK buoys are used for ground truth. This is true for both  $H_s$  and  $m_4$  but not  $T_{m,-1,0}$ . For example, in Table 2 ( $H_s$  statistics), the IC4M6H model has +13% bias relative to the SWIFTS, and -11% bias relative to the UK buoys, so there is

disagreement even on the *sign of the bias*. The  $H_s$  comparisons for individual buoys in Figure 128 and Figure 129 show this in graphical form: UK buoy  $H_s$  tends to be higher than the model and SWIFT  $H_s$  tends to be lower than the model. With respect to  $m_4$  statistics: in Table 4, the same model (IC4M6H) has +51% bias relative to the SWIFTS, and -5% bias relative to the UK buoys.

The observed mean  $H_s$  in Table 2 is 2.48 m for the SWIFTS and 3.11 m for the UK buoys. The observed mean  $m_4$  in Table 4 also indicates that the SWIFT values are significantly lower than the UK buoy values. This alone does not necessarily suggest a discrepancy, since the buoys are not co-located, but the model is co-located with both and allows us to conclude that there is a strong discrepancy. According to the model, the  $m_4$  is lower at the locations of the UK buoys ( $4.8\text{e-}4 \text{ m}^2\text{s}^{-4}$ ) than at the locations of the SWIFT buoys ( $5.7\text{e-}4 \text{ m}^2\text{s}^{-4}$ ), which is probably an outcome of greater ice concentrations (in model forcing) at the UK buoys and the low-pass filtering by the model's  $S_{ice}$  parameterization. However, if we compare the observations themselves, the  $m_4$  is higher at the locations of the UK buoys ( $5.0\text{e-}4 \text{ m}^2\text{s}^{-4}$ ) than at the locations of the SWIFT buoys ( $3.8\text{e-}4 \text{ m}^2\text{s}^{-4}$ )!

One possible explanation for the discrepancy is that the SWIFT buoys had a tendency to capsize (i.e. lay over horizontally) when the icing became severe, while the UK buoys, with their toroid shape, would maintain the same orientation even when encased in ice. However, we do not believe that this fully explains the discrepancy, because the discrepancy is consistent for all buoys and all times, and not all SWIFT buoys capsized, and even when they did, only the latter part of their measured time series would be affected (i.e. only after the icing became severe enough to cause the buoy to fall over).

A second possible explanation is in the noise filtering (Jim Thomson, personal communication). The processing of the SWIFT data may have had an overly aggressive noise filter, which would cause real energy to be incorrectly discarded. Alternatively, the processing of the UK buoy data may have had a noise filter that was not aggressive enough, which would cause noise to be incorrectly interpreted as real energy.

The discrepancy diminishes confidence in both buoys. This is ironic, since if data from one buoy type had been lost, this would have been a major loss to the experiment, but confidence in the remaining data would be higher. The lack of confidence is most severe for the  $m_4$  parameter, which is unfortunate, since this parameter is most responsive to the  $S_{ice}$  parameterization.

These concerns about data quality justify our approach of separating skill metrics (e.g. Table 4) and inversion results (e.g. Figure 80 and Figure 81) by buoy type. Other scientists in the Sea State program have adopted a similar approach.

## 7. Ice photos from SWIFT buoys (WA3)

In Rogers et al. (2016), photos from the SWIFT buoys during WA3 were used to characterize the ice cover. In this section, we revisit this topic. Section 7.1 introduces an updated scheme for categorizing the ice cover. Section 7.2 compares these numeric values to TKE dissipation and salinity measured by the same buoys. Section 7.3 presents these values in context with SAR imagery available during WA3.

This section is strictly about observations: the models are not used here. However, we do reference  $k_i(f)$  profiles which are calculated using model-data inversion.

### 7.1. New ice codes and application to $k_i$ profiles

The ice codes used by Rogers et al. (2016) were created during the cruise (October 2015). For a number of reasons, these were due for an update:

1. The old ice codes were created by inspecting directories of photos. These had 1-hour spacing. The new ice codes were created by inspecting mosaics of photos (e.g. Figure 140) with 30-minute spacing, to correspond with the interval of the reprocessed SWIFT data (reprocessing was performed by Ms. Madison Smith (APL/UW) after the cruise). They are centered at 15 and 45 minutes after the hour.
2. Old ice codes were numerically irregular, e.g. 000, 001, 102, 104, 206, etc. which made plotting of the ice codes awkward. The new ice codes are integers from 1 to 12, in order of increasing ice cover.
3. The old ice codes had only one value for “pancakes in frazil” (code 206). In the new codes, there are eight gradations of “pancakes in frazil”.

The ice codes consist of a numeric value (1 to 12) and an alpha-numeric shorthand notation:

1. OW1: open water
2. OW2: open water and trace pancakes
3. OW3: open water and grease ice (grease is thin frazil)
4. OW4: open water, grease, and trace pancakes
5. PF5: pancakes and grease with breaks of open water
6. PF6: dark frazil (almost as thin as grease), with few raised edges and lower concentration of pancakes
7. PF7: like PF6 but higher pancake concentration
8. PF8: like PF7 but dark areas are less than half of total frazil area
9. PF9: like PF8 but more raised edges on pancakes: around 20 or 30%
10. PF10: like PF9 but raised edges are 40% and higher, though there is still some darkish frazil in the photos
11. PF11: like PF10 but with a lighter frazil color
12. PF12: thickest frazil, with lightest color: dark gaps are less than 15%

Above, “trace pancakes” refers to either partially melted pancakes or debris and brash from pancakes which had become visibly battered by the wave motion.

Further coding accommodates non-usable or marginally usable photos:

- -99: night hours (dark photo)
- -88: daylight hours but blurry (ice or droplets on camera)

- negative number, e.g. -1, -2, ...-12: like the corresponding positive number but partially blurry. Thus, the estimate of ice type is unreliable.

The ice codes—old and new—are, of course, subjective. However, in the case of the new ice codes, the mosaics of photos are in a convenient format should a need arise to revisit the code assignments. The mosaics are available via the “Data” tab on the Sea State website: [http://www.apl.washington.edu/project/project.php?id=arctic\\_sea\\_state](http://www.apl.washington.edu/project/project.php?id=arctic_sea_state) (retrieved January 2018).

These new ice codes were used to make the plots of  $k_i(f)$  profiles in Figure 90 and Figure 91. The IC4M6H2 step function was determined using an average of  $k_i(f)$  profiles with ice codes 6 to 12.

It would not be impossible to make mosaics and then ice codes for other wave experiments. However, different numeric codes would need to be used, to account for the larger variety of ice types (small floes, thinner floes, thicker floes, nilas, grey ice, cemented pancakes, etc.).

## 7.2. Ice observations vs. TKE dissipation and salinity

The ice observations were compared against a number of quantities measured by the SWIFT buoys. The two most interesting of these are presented here. The first, turbulent kinetic energy dissipation rate (TKEDR), is following on the idea of Ms. Madison Smith and Dr. Jim Thomson (UW/APL), who presented two TKEDR profiles in a presentation at the AGU Fall Meeting of 2016. Our comparison is essentially the same, but including all cases for which there is a valid ice observation with a simultaneous TKEDR profile: Figure 130. The TKEDR is measured by an upward-looking ADCP, equipped on some of the SWIFT buoys. The plot indicates a remarkable correspondence between ice cover and the TKEDR, which suggests that the ice cover determines the mode of dissipation within the water column.

Whitecapping in open water contributes to near-surface production of turbulence. A warning is given here, however: one should be careful not to conflate TKEDR with wave dissipation. Much of the TKEDR in open water is associated with the vertical shear in the wind-driven currents. However, it is a reasonable hypothesis that much of the TKE dissipation in the ice-covered cases is associated with turbulent eddies created by interaction between the sea ice and the wave orbital motion. Further clarification of these processes is left for future study. In particular, it would be useful to replicate this behavior in the controlled conditions of a laboratory.

Figure 131 compares the integrated TKEDR against the dissipation rate from  $S_{ice}$  according to the parametric model IC4M6H, applied to the buoy spectra and integrated over frequencies. The WW3 model is not used here. The result shows that the  $S_{ice}$  dissipation is a similar order of magnitude to the measured dissipation rate, but the correlation is poor. This dissipation rate is from SWIFT 14, which was in significant frazil and pancake ice according to the ice coding. Of course, the ice codes are only available during daylight hours, so the day/night cycle is indicated in the figure.

Figure 132 compares the ice observations against salinity. For the open water cases, there is no apparent trend to lower or higher salinity. However, for the ice-covered cases, the salinity is

systematically higher than the mean salinity of the open water cases. This is consistent with the well-known process of brine rejection which occurs as seawater freezes.

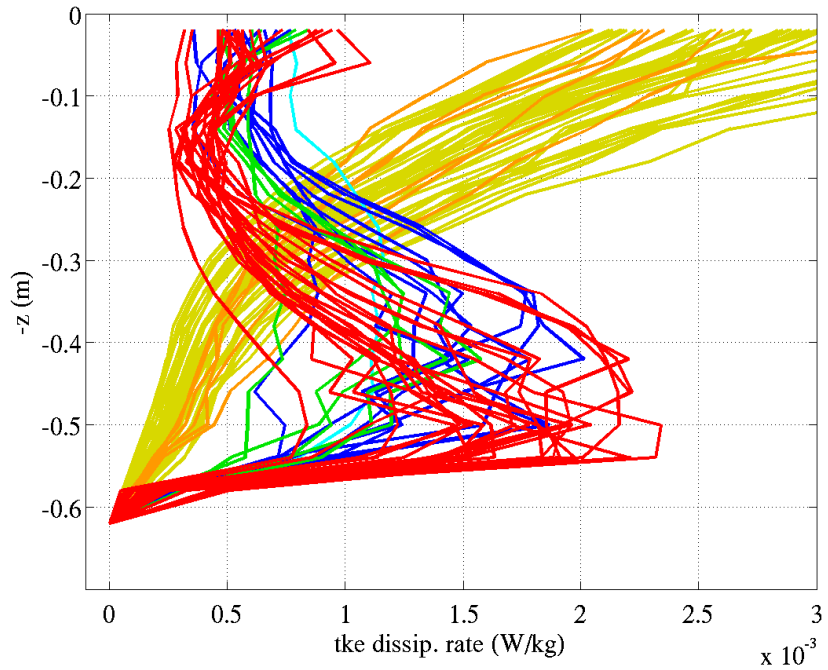


Figure 130. Vertical profiles of TKE dissipation rate measured by SWIFT buoys. Gold and orange corresponds to OW1 and OW3 respectively. Cyan corresponds to PF6. Blue corresponds to PF7 and PF8. Green and red correspond to PF9 and PF12 respectively.

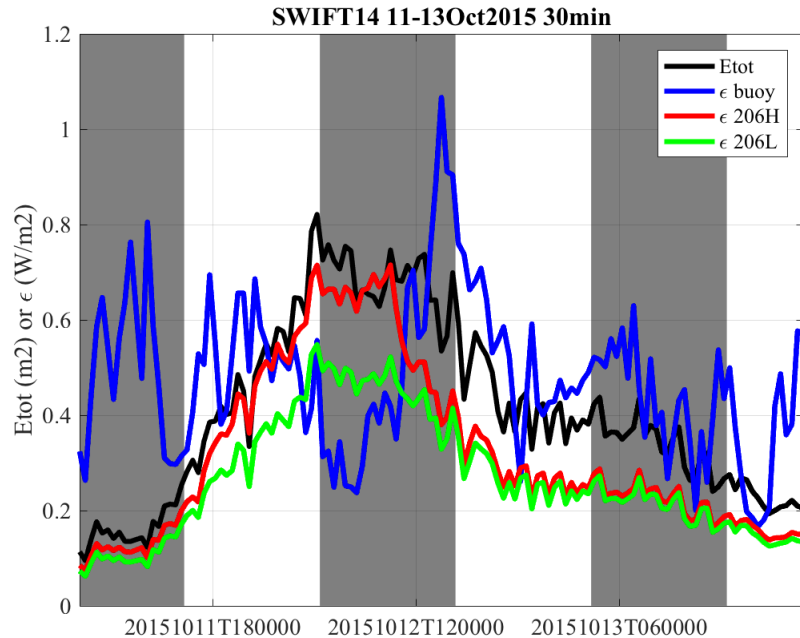


Figure 131. Time series of TKE dissipation: buoy (SWIFT 14) vs. parametric model. Black line is buoy total energy in  $\text{m}^2$ . Blue line is integrated buoy TKE dissipation in  $\text{W}/\text{m}^2$ . Red is the IC4M6H model applied to the buoy spectrum (WW3 is not used here). Green is like IC4M6H, but matching the dissipation of lighter pancake and frazil from Rogers et al. (2016). Grey regions of the plot indicate night-time, when ice observations from the buoy camera are unavailable.

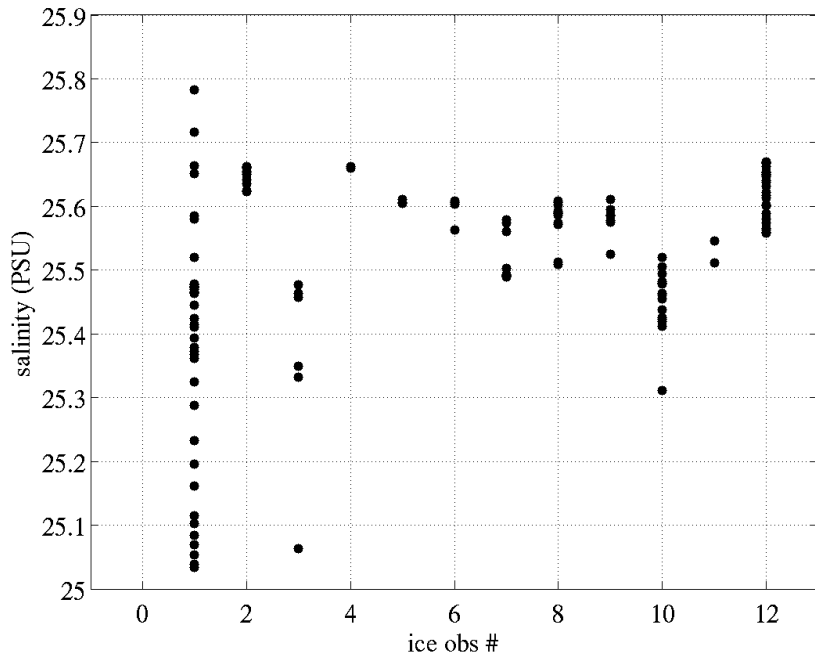


Figure 132. Salinity measured by SWIFT buoys, compared against corresponding ice observations.

### 7.3. Comparison to SAR

In this section, we compare the SWIFT ice observations against SAR imagery of ice during WA3. The ice cover changed rapidly during WA3, so we subdivide our figures by time. Each half-day (AM or PM, in UTC) is presented in a separate section. In all figures, a black line is used to mark the nominal location of the southern transect of WA3, to assist in comparison between SAR imagery and ice observation plots.

#### 7.3.1. October 11, PM

Figure 133 and Figure 134 show SAR images from the period of 1615 to 2345 UTC 11 October. Figure 135 shows the SWIFT ice observations from the same time.

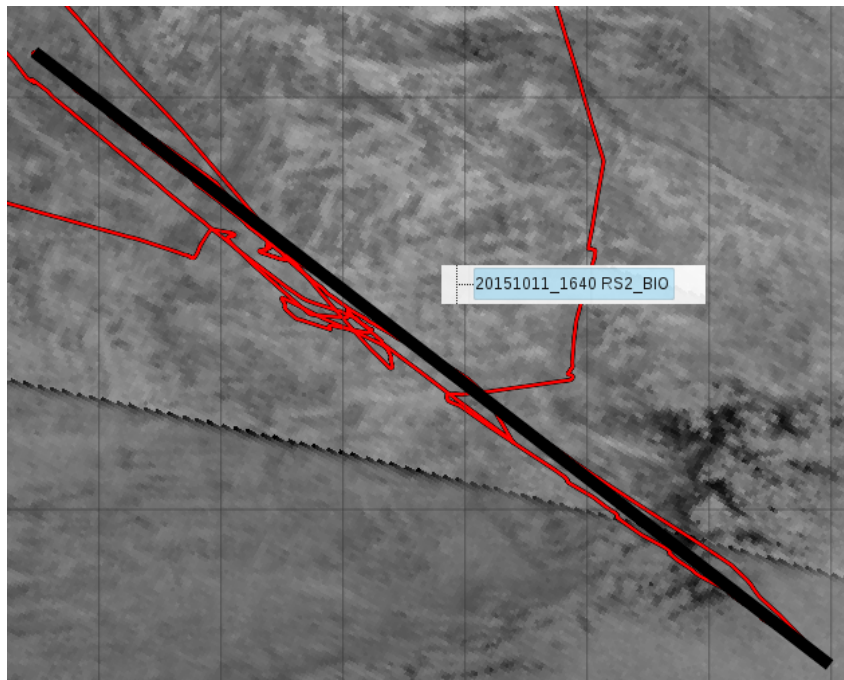


Figure 133. SAR image from screenshot of *Sikuliaq* Mapserver. BIO RadarSAT-2 for 1640 UTC 11 October 2015. The red line is the cruise track near WA3, and the thick black line indicates the southern transect during WA3. RADARSAT-2: © MDA 2015.

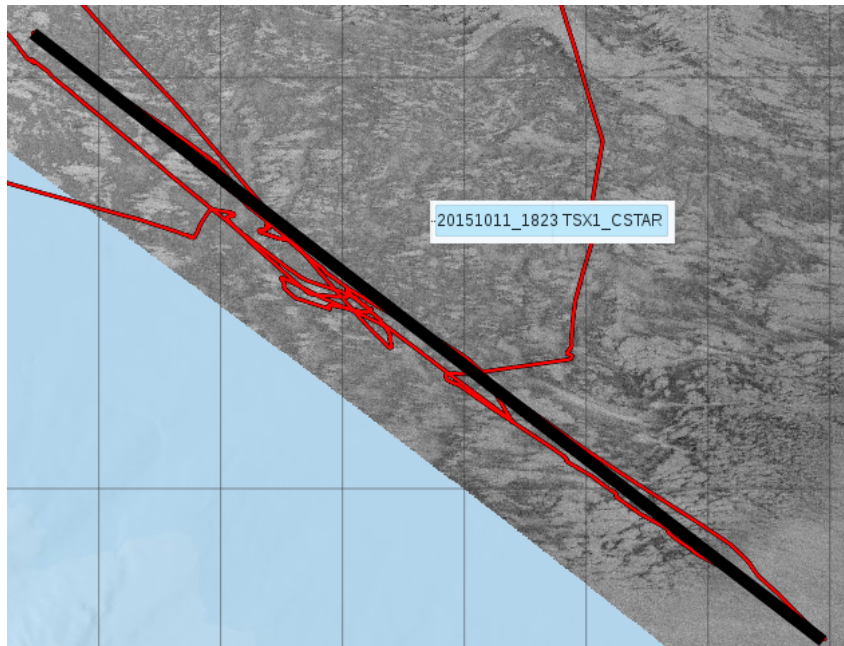


Figure 134. Like Figure 133, but showing the CSTARS TerraSAR-X image for 1823 UTC 11 October 2015.

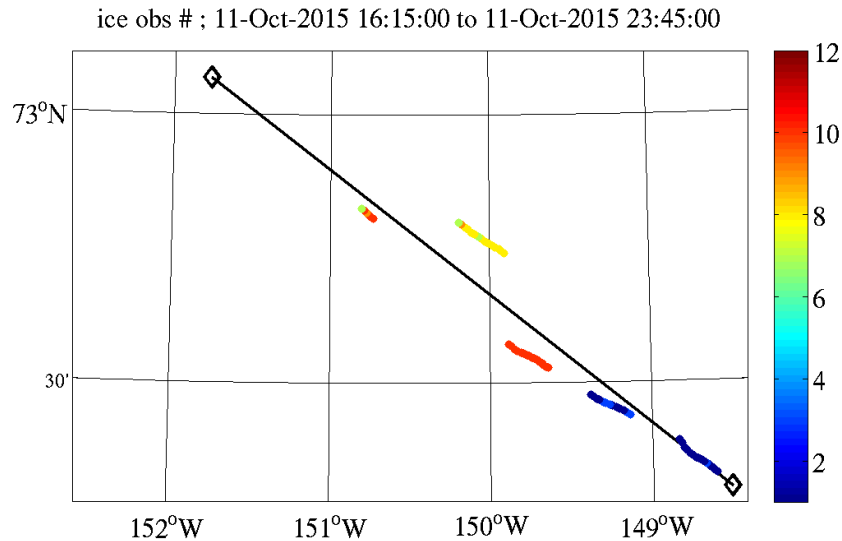


Figure 135. Ice observations from SWIFT cameras from 1615 to 2345 UTC 11 October 2015. Color scaling is according to the new 0-to-12 ice codes. The black line and diamonds indicate the southern transect of WA3 (same as black line in SAR images shown in this section).

### 7.3.2. October 12, AM

Figure 136 shows the ice observations from the period 0015 to 0315 UTC 12 October. Unfortunately, no SAR imagery is available from the 12-hour period, 0000 to 1200 UTC.

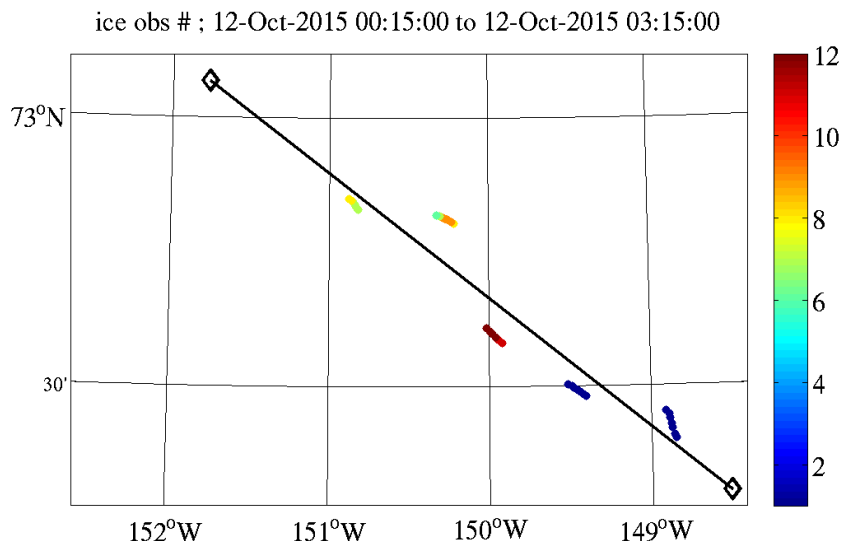


Figure 136. Like Figure 135, but for 0015 to 0315 UTC 12 October 2015.

### 7.3.3. October 12, PM

Figure 137 and Figure 138 show two SAR images during 1615 to 2345 UTC 12 October, and Figure 139 shows the ice observations during that period. The garnet color in Figure 139 corresponds to the irregular ice feature in which SWIFT14 was floating. Figure 140 shows the mosaic for SWIFT14 during the 30-minute period corresponding to the SAR image of Figure 138. This case is discussed in Section 4.3.2.

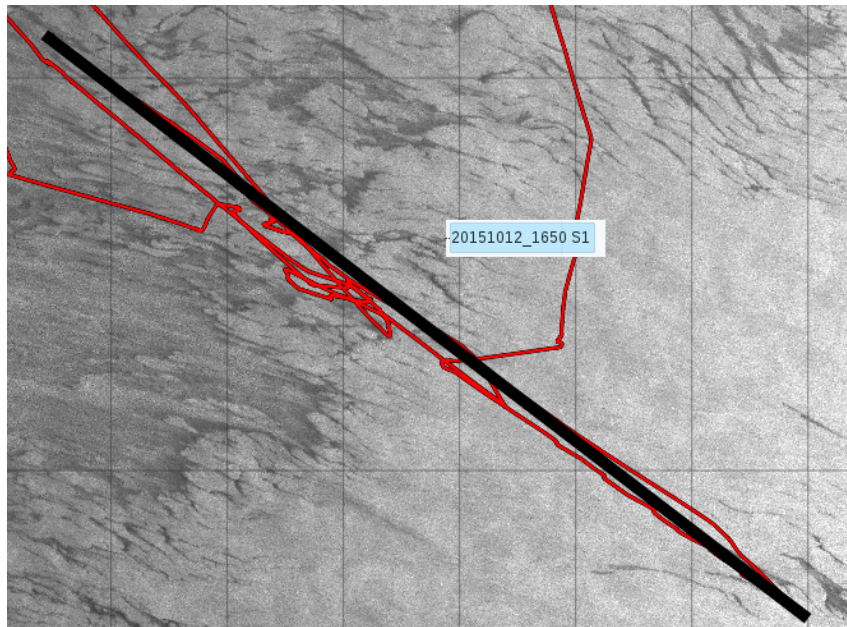


Figure 137. Like Figure 133, but showing the Sentinel-1 image for 1650 UTC 12 October 2015.

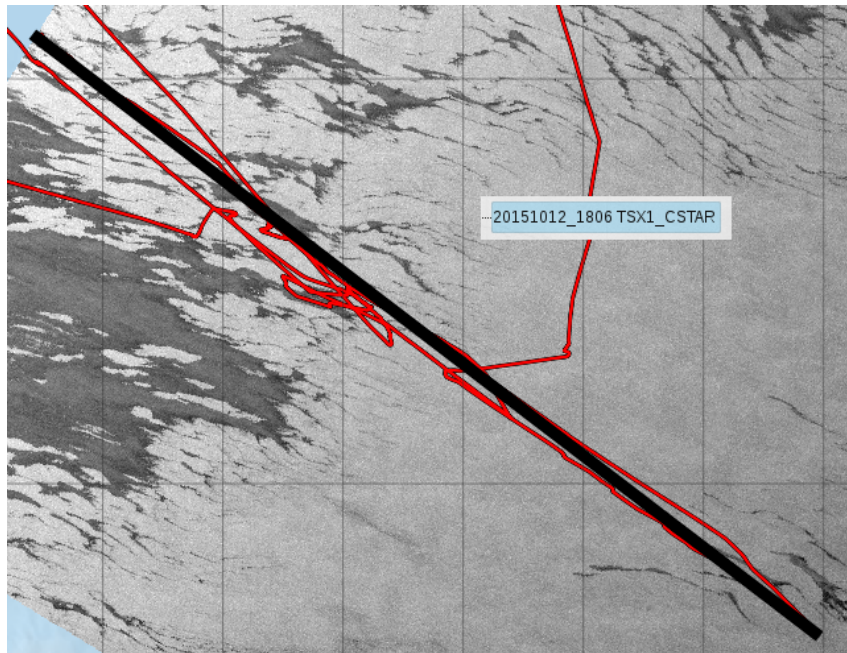


Figure 138. Like Figure 133, but showing the CSTARS TerraSAR-X image for 1806 UTC 12 October 2015.

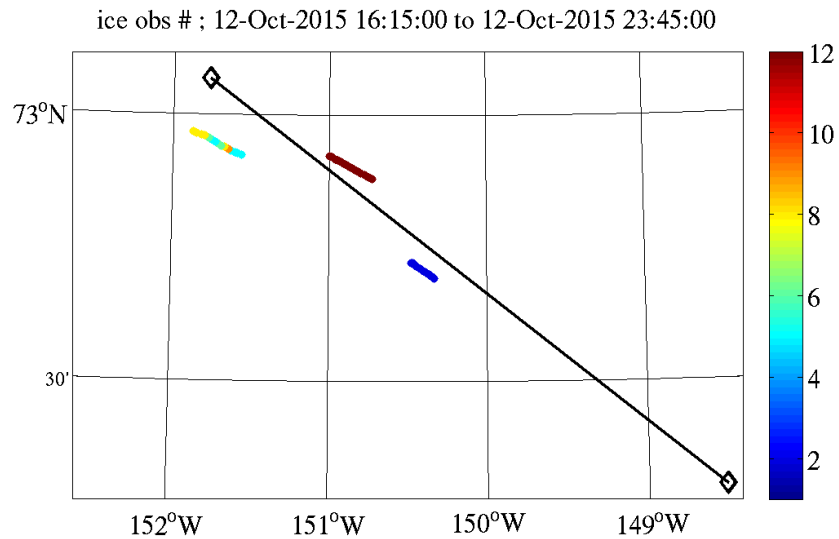


Figure 139. Like Figure 135, but for 1615 to 2345 UTC 12 October 2015.

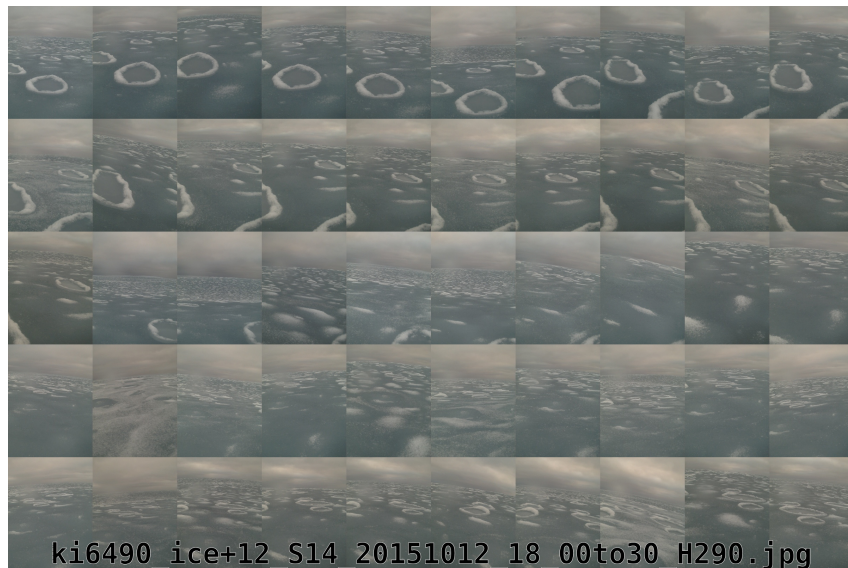


Figure 140. Mosaic of photos from SWIFT-14, 1800 to 1830 UTC 12 October 2015. Ice category on the new 0-to-12 scale is 12.  $H_s=2.90$  m.

### 7.3.4. October 13, AM

Figure 141 shows a SAR image taken during the period 0015 to 0315 UTC 13 October and Figure 142 shows the corresponding SWIFT ice observations. Ice observations are available only from two buoys during this period, since icing was taking a toll on the cameras. Figure 142 shows SWIFT14 is still in the band of ice that it was in 12 hours prior.

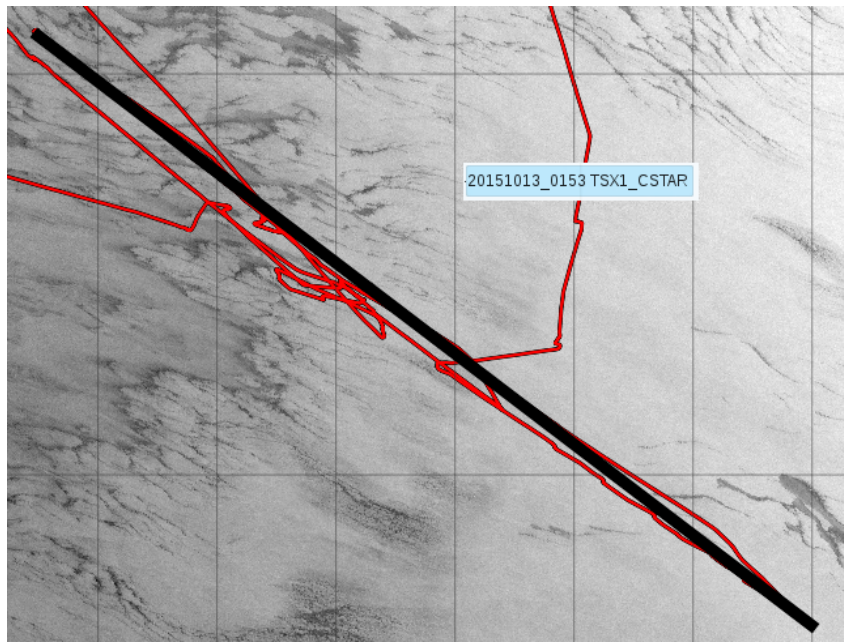


Figure 141. Like Figure 133, but showing the CSTARS TerraSAR-X image for 0153 UTC 13 October 2015.

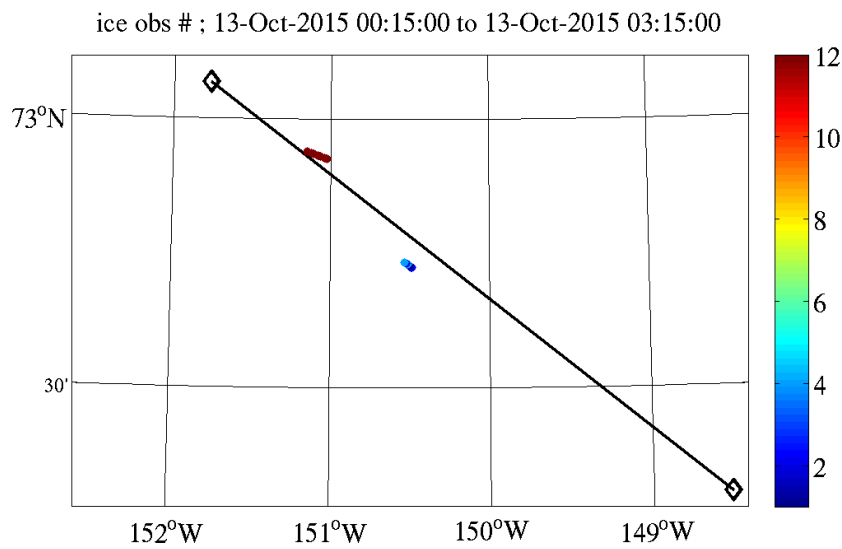


Figure 142. Like Figure 135, but for 0015 to 0315 UTC 13 October 2015.

## 8. Summary of conclusions

### *Hindcasting and forecasting (general)*

We find that the difficulty of the wave forecast is primarily determined by the proximity to ice edge. Though forecasting in ice is still much more challenging than forecasting in open water, the question of whether the point of interest is in ice or open water has lesser implications for the difficulty than the proximity to ice edge. This implies a paradox: a forecast for a position outside the ice for off-ice winds can be more difficult than a forecast for a position inside the ice for an on-ice wind/wave case, if the former is much nearer the ice edge than the latter.

### *Input fields: ice concentration*

- The obvious conclusion from the statement above regarding hindcasting and forecasting is: accuracy of the ice edge is crucial to the accuracy of the wave model, especially if near the edge.
- The temporal resolution of an ice product is often crucial near the ice edge. We find that ice concentration from AMSR2 with high temporal resolution provided overall best performance of WW3 for the time period of the cruise. It must be noted that we did not specifically isolate the impact of temporal resolution: it is possible that there are differences between skill of AMSR2 products based on the data processing method used (NT2 vs. ASI). However, it is our belief that temporal resolution is the crucial factor affecting wave model skill. In two cases that we looked at in detail, comparing NT2 processing vs. ASI processing, we did not see obvious major implications for the wave model.
- Based on the above result, in cases of smaller WW3 grids, such as our 5 km inner WW3 grid, we recommend that ice concentration fields from the high temporal resolution AMSR2 swath data be used operationally.
- The GOFS hindcast ice results in a more accurate wave forecast than the GOFS realtime product. This supports the view that timely updates to the ice fields (i.e. not a day or two late) is important to wave model skill.
- During the September period prior to the cruise (not included in our wave model skill estimates), the IMS/GOFS ice edge is clearly superior to AMSR2. This is consistent with conventional wisdom that passive microwave ice concentration is less accurate in the summertime. This implies a possible criterion: to use IMS/GOFS in the summer and AMSR2 in other seasons. However, our evaluation, being only for a limited region and only a 2-month period, is not sufficient to draw firm conclusions about how to force operational wave models: further supporting data is needed.
- Analyst-improved ice products such as IMS are a game-changer for improving forcing to our models, since they represent a method for an expert to make decisions regarding which satellite (or other observation type) to use in a particular situation. This is especially important if there is a strong seasonal (or otherwise situational) variation in reliability of different products. However, our experience indicates that it is crucial to take measures to limit impact of analyst error. One recommendation should be easy to implement: assign an “age” to data within IMS such that ice information that is too old can be excluded from assimilation into GOFS/CICE.

- We recommend that the following be provided to the Navy wave forecaster, in gridded form. The first two are already possible:

1. CICE analysis (not just nowcast/forecast)
2. L3 satellite products, e.g. AMSR2, SMOS

The third is not presently possible, but is recommended for research and development:

3. Information about ice type, for use in  $S_{ice}$  parameterizations. At minimum, this should come in two categories: rigid vs. loose (in other words: consolidated vs. unconsolidated) ice. The former would include unbroken sheet ice (such as existed southeast of the ship in our October 18 case) and floes that are large relative to typical wave lengths. The latter would include frazil ice, pancake ice, brash ice, and floes that are small relative to typical wave lengths. This information can come from satellite or model or both.

- It may be useful to run an ensemble of wave models with different ice forcing, and use this to characterize the uncertainty of the wave forecast in and near the MIZ.

- AMSR-2
- ice model analysis
- ice model forecast

Of these, only the last includes forecast ice fields. The first two imply “persistence forcing” for the wave model forecast.

- Given the uncertainty in the forcing, a possible consideration for operational wave forecasting is that it be provided in terms of “distance from ice edge” rather than in terms of absolute position. This would be useful for both off-ice wind cases and on-ice wind/wave cases. This would not require a change in model operation, but rather in interpretation and usage. It would be part of the process by which a forecaster produces an operational forecast from “model guidance”.
- As we note in our description in Section 4.1.2, our AMSR2 fields processed with the NT2 algorithm have relatively low spatial resolution: 10 km, compared to the 5 km resolution of the inner WW3 grid used for hindcasting. We find no evidence in our WW3 hindcasts that this has a negative impact of the modeling, even for the case of SWIFT 14 which was in a relatively small feature of pancake and frazil ice during WA3.

#### *Input fields: winds*

- For forecasting, the global atmospheric model NAVGEM proved to be much more skillful than the higher-resolution regional atmospheric model COAMPS for our case. (Here, we are referring to two Navy atmospheric products, run at the Fleet Numerical Meteorology and Oceanography Center.) Comparisons of nowcast winds indicate that NAVGEM and the European atmospheric model have comparable skill for forcing a wave model. The former showed better skill for predicting the highest winds within WA3, but the latter has slightly better overall correlation and scatter index scores. Though not analyzed here, it is our impression that the European model provided slightly more advanced notice (e.g. 1 or 2 days difference) of the WA3 wind/wave event.
- For the hindcasts of WA3, there is an apparent soft upper limit on waveheight near 4 meters. This exists even in open water and even for the model with  $S_{ice}=0$ . We believe the most credible hypothesis is that this is associated with failure in the wind forcing, e.g. an under-prediction of extremes in the primary generation region southeast of WA3. It is

not caused by thermal stability effects, since air-sea temperature differences are small during WA3.

#### *Numerical error*

It is difficult to make general conclusions about numerical error when representing  $S_{ice}$ , since it depends so strongly on the case being modeled. Our results indicate that this error should be kept in mind when modeling waves in the MIZ, and we have provided examples which provide guidance for the severity of error which can be expected. Numerical error can be reduced by using smaller spacing in geography and time. It will, of course, be most severe in cases of very strong dissipation: a model cannot accurately reproduce nearly 100% damping over just a few grid cells. Fortunately, this concern is balanced by another fact: once that energy is completely damped, the numerical error is moot; in other words, the error is localized. This again supports the view that model accuracy depends strongly on the distance from the ice edge.

#### *Validation methods*

We are satisfied with our choice of wave parameters for evaluation in and near the MIZ, and recommend it for others to use. Waveheight ( $H_s$ ) and dominant wave period (e.g.  $T_{m,0,-1}$  or  $T_{m,0,1,E4}$ ) are indisposable parameters. Fourth moment  $m_4$  is a good indicator for skill of dissipative  $S_{ice}$  formulations, and their "low-pass filter" effect. If a fourth parameter can be added (not used in the present study), we recommend one related to frequency spreading, since it has implications for wave groupiness in the ice, which could be crucial for estimation of the fracturing of ice by waves (Collins et al. 2015).

#### *Dissipation rate*

- In comparison of our dissipation vs. frequency profiles, we find the following:
  - There is excellent agreement with the recent study in Antarctica (Meylan et al. 2014). This agreement is actually counter-intuitive, given the dissimilar ice types.
  - There is a good match—via extrapolation—to the low-frequency observations by Arduin et al. (2016). This agreement is also counter-intuitive because of dissimilar ice types.
  - Dissipation from laboratory experiments (Zhao and Shen 2015) appears to be too high to provide a good extrapolation from our  $k_i$  profiles. This is a significant concern and requires further investigation to reconcile. We hypothesize that non-linearity (e.g. dependence on orbital velocity) may play a role.
  - Dissipation from the viscous model (i.e. Keller model or Wang and Shen with zero elasticity) does not agree with our profiles. The viscous model predicts  $k_i$  profiles which are much steeper than ours: weaker at low frequencies and stronger at high frequencies.
  - Dissipation from the non-linear boundary layer model (non-dispersive IC2) agree fairly well with our  $k_i$  profiles, especially in a qualitative sense, e.g. in the slope  $\partial k_i(f) / \partial f$ .

- Dissipation from Cheng et al. (2017), which is also from Sea State data, is higher than ours by a factor of around 3, but qualitatively they are very similar. We can only speculate as to the reasons for the differences.
- Dissipation in the aggregate study of Wadhams et al. (1988) is much higher than ours, but this discrepancy is not a major concern, given the dissimilar ice types and methods.
- Agreement with the slope of the Doble et al. (2015) curve— $k_i \propto f^{2.13}$ —is good only for lower frequencies. Both our estimates and the Doble et al. (2015) measurements suggest a stronger dependence on frequency at higher frequencies than is given by the  $f^{2.13}$  fit of Doble et al. (2015).
- Analysis of the slope of our  $k_i$  profiles suggest a  $f^2$  dependency at lower frequencies and  $f^{4.5}$  to  $f^5$  dependency at higher frequencies. This is in fact not unlike the parametric model of Meylan et al. (2014), which is  $f^2$  and  $f^4$ .
- A binomial form following Meylan et al. (2014),  $k_i = c_2 f^2 + c_4 f^4$ , provides good fits to our  $k_i$  profiles. The  $c_n$  coefficients are smaller in our case, consistent with the expectation that our ice is less dissipative than the ice encountered by Meylan et al. (2014).

#### *Hindcast skill scores*

- $H_s$  and  $m_4$  parameter bias results, compared against the ground truth of the drifting buoys, support the assertion that it is important to have an  $S_{ice}$  dissipation that depends on frequency, to reproduce the low-pass filter effect that sea ice has on wave energy (e.g. Collins et al. 2015). Comparisons of peak period and peak direction, with ship radar as ground truth, strongly supports the same assertion. For this comparison, we used the IC1 model (no frequency-dependence) and the IC2 and IC4 models (with frequency dependence). The model without frequency dependence strongly damps wave energy near the peak, but then permits regrowth of local, high frequency waves. Both behaviors are wrong, and this is strongly reflected in the skill of the prediction of dominant wave period. The IC2 and IC4 models have clearly superior skill in this regard.
- Even when we look at waveheight alone, the IC0 model (which, like IC1, has no frequency-dependence) is clearly inferior to the models with frequency dependence.
- For the  $m_4$  parameter, all models have high scatter. In the case of the models which have an  $S_{ice}$  dissipation that depends on frequency, we speculate that the scatter is primarily associated with forcing and the model's complete lack of knowledge of ice type (e.g. consolidated vs. unconsolidated). Thus, much work remains to be done for predicting spectral shape within the ice.
- The parametric model IC4M6H exhibits very high skill for predicting the damping—and its frequency dependence—in WA3, using UK buoys for ground truth near the ice edge and the NIWA buoy for ground truth further into the ice. However, the match to the SWIFT buoys is less favorable: these buoys report a smaller  $m_4$  than the model predicts.
- Variability of ice type makes it difficult to make general recommendations on the relative suitability of IC4M6H, IC4M6H2, and IC2 for future modeling. IC4M6H will tend to be better in cases where the ice is less dissipative. IC4M6H2 and IC2 will tend to be better in cases where the ice is more dissipative.

- When interpreting the hindcast results and field observations, it is very difficult to separate the effect of nonlinear dissipation from the effect of non-uniform ice type. Laboratory studies may be better suited for studies of nonlinearity of dissipation.

Conclusions regarding skill scores specific to individual wave experiments (WA2, WA3, etc.), individual hindcasts (e.g. run with particular  $S_{ice}$  parameterizations or ice concentration forcing), and individual wave parameters (waveheight, dominant period, and  $m_4$  parameter) are many and are not repeated here. The reader is referred to Section 6.3.

#### *Buoy discrepancy*

During the “large waves in ice” experiment (WA3), there is an apparent strong discrepancy between the spectra measured by SWIFT buoys and those measured by the UK buoys. This in turn creates a strong discrepancy in how we interpret model results. For example, in Table 4 ( $m_4$  statistics), the IC4M6H model has +51% bias relative to the SWIFTs, and -5% bias relative to the UK buoys. Concerns about data quality justify our approach of separating skill metrics (e.g. Table 4) and inversion results (e.g. Figure 80 and Figure 81) by buoy type.

#### *Use of SWIFT cameras for ice characterization*

The characterization of ice using buoy-mounted cameras has been valuable in our analysis of WA3. This is true for interpretation of wave spectra and  $k_i(f)$  profiles from associated inversions, e.g. Rogers et al. (2016) and Figure 91 here, where there is clear correspondence between ice type and dissipation rate. Herein, we also gave two other examples, this time not being derived from the measured spectra. First, there is a strong correlation between ice cover in WA3 (quantified in this report) and the TKE dissipation rate profiles measured by SWIFT buoys. Smith and Thomson (unpublished) reached a similar conclusion previously. This outcome is still lacking a full, conclusive physical interpretation, but the results show strikingly consistent correspondence. Second, there is a strong correlation between ice cover in WA3 and salinity measured by SWIFT buoys. This outcome can be explained by brine rejection during freezing.

## Acknowledgments

We thank Jim Thomson, Joe Talbert, Alex DeKlerk, Madison Smith (U. Washington/APL), Martin Doble (Polar Scientific Ltd.), and Peter Wadhams (Cambridge U.) for their substantial labors building, preparing, maintaining, deploying and recovering the wave buoys, and for the processing and management of the associated data. We thank Hayley Shen (Clarkson U.), especially for providing many of the photos used in this report. We gratefully acknowledge the support of the crew of the R/V *Sikuliaq* and the ship's marine technicians. In particular, we appreciate the Map Server which was made available to us during and after the cruise by Steve Roberts (U. Alaska). Fabrice Ardhuin and co-workers at Ifremer contributed important WW3 code that was used in the hindcasts, particularly the IC2 boundary layer parameterization. We thank Jean Bidlot (ECMWF) for the useful wind and wave forecasts provided during the cruise. We appreciate the 2 km CICE fields provided by David Hebert (NRL) during the cruise, used as forcing for WAVEWATCH III. NAVGEM and COAMPS forcing fields were available to use through to the excellent support of Michael Phelps (Jacobs Tech.). Johannes Gemmrich (U. Victoria) and his co-workers provided valuable support during the cruise via the U. Victoria ftp site. We appreciate the satellite data provided by several national space agencies and the crucial role of CSTARS, BIO, UW, U. Victoria, and the NIC in making this available for us to use in our research. Important ship meteorological and lidar data were provided by Ola Persson, Byron Blomquist, and Chris Fairall (NOAA). Ship-based radar was generously provided by Bjoern Lund and Hans Gruber (U. Miami). We appreciate the useful collaborations with Sukun Cheng (Clarkson U.), Alex Babanin and Qingxiang Liu (U. Melbourne), Tripp Collins (during his tenure at NRL), Mike Meylan (U. Newcastle), Hayley Shen, Jim Thomson, and Johannes Gemmrich. We acknowledge the useful comments from Prof. Shen on a draft of this report. Dr. David Wang (NRL) suggested some literature which turned out to be very useful. We thank the Sea State team for numerous discussions on varied topics, and the superb leadership of Dr. Jim Thomson throughout the DRI.

Model output presented here can be obtained from the first author by request. This work was supported by the Office of Naval Research Code 322, "Arctic and Global Prediction", directed by Drs. Martin Jeffries and Scott Harper, and by ONR through the NRL Core 6.2 Program. This is NRL contribution number NRL/MR/7320--18-9786 and is approved for public release.

## References

Abdalla, S. and J. R. Bidlot (2002). Wind gustiness and air density effects and other key changes to wave model in CY25R1. *Tech. Rep. Memorandum R60.9/SA/0273*, Research Department, ECMWF, Reading, U. K., 12 pp.

Ardhuin, F., W. E. Rogers, A. Babanin, J.-F. Filipot, R. Magne, A. Roland, A. van der Westhuysen, P. Queffeulou, J.-M. Lefevre, L. Aouf, and F. Collard (2010). Semi-empirical dissipation source functions for ocean waves: Part I, definitions, calibration and validations, *J. Phys. Oceanogr.* **40**, 1917–1941.

Ardhuin, F., P. Sutherland, M. Doble, and P. Wadhams (2016). Ocean waves across the Arctic: Attenuation due to dissipation dominates over scattering for periods longer than 19 s, *Geophys. Res. Lett.*, **43**, 5775–5783, doi:10.1002/2016GL068204.

Beitsch, A., L. Kaleschke, S. Kern, and X. Tian-Kunze (2013). AMSR2 ASI 3.125 km Sea Ice Concentration Data, V0.1, Institute of Oceanography, University of Hamburg, Germany, digital media. (<ftp://projects.zmaw.de/seacie/>).

Beitsch, A., L. Kaleschke, and S. Kern (2014). Investigating High-Resolution AMSR2 Sea Ice Concentrations during the February 2013 Fracture Event in the Beaufort Sea, *Remote Sens.*, **6**, 3841-3856

Cavaleri, L. (2000). The oceanographic tower Acqua Alta — activity and prediction of sea states at Venice, *Coastal Engineering* **39**, 29–70.

Cheng, S., W.E. Rogers, J. Thomson, M. Smith, M.J. Doble, P. Wadhams, A.L. Kohout, B. Lund, O.P.G. Persson, C.O. Collins III, S.F. Ackley, F. Montiel, and H.H. Shen (2017). Calibrating a Viscoelastic Sea Ice Model for Wave Propagation in the Arctic Fall Marginal Ice Zone. *J. Geophys. Res.*, **122** doi://10.1002/2017JC013275

Cole, D.M., R.A. Johnson, G.D. Durell (1998). Cyclic loading and creep response of aligned first-year sea ice. *J. Geophys. Res.*, **103** (C10), 21751-21758.

Comiso, J.C., D.J. Cavalieri, T. Markus (2003). Sea Ice Concentration, Ice Temperature, and Snow Depth Using AMSR-E Data. *IEEE Transactions on Geoscience and Remote Sensing*, **41**(2), 243-252.

Collins, C.O., and W.E. Rogers (2017). A Source Term for Wave Attenuation by Sea ice in WAVEWATCH III ®: IC4, NRL Report NRL/MR/7320--17-9726, 25 pp. [available from <https://www7320.nrlssc.navy.mil/pubs.php>].

Collins, C. O., W. E. Rogers, A. Marchenko and A. V. Babanin (2015). In situ measurements of an energetic wave event in the Arctic marginal ice zone, *Geophys. Res. Letters*, **42**, doi:10.1002/2015GL063063

Collins, C.O. , B. Blomquist, O. Persson, B. Lund, W.E. Rogers, J. Thomson, D. Wang, M. Smith, M. Doble, P. Wadhams, A. Kohout, C. Fairall, and H.C. Gruber (2017). Doppler Correction of Wave Frequency Spectra Measured by Underway Vessels, *J. of Atm. and Oceanic Techn.*, **34**, doi:10.1175/JTECH-D-16-0138.1

Dixon, T.W., V.A. Squire, O. Watzke (1998). Consequences of dissipation on the group velocity in a flexible ice cover. *Cold Regions Science and Techn.*, **27**, 75–81.

Doble, M.J. (2007). Growth and Motion at the Weddell Sea Ice Edge, PhD Dissertation for University of Southampton, 170 pp.

Doble, M.J. (2009). Simulating pancake and frazil ice growth in the Weddell Sea: A process model from freezing to consolidation, *J. Geophys. Res.* **114**, C09003, doi: 10.1029/2008JC004935.

Doble, M. J., and J.-R. Bidlot (2013). Wavebuoy measurements at the Antarctic sea ice edge compared with an enhanced ECMWF WAM: progress towards global waves-in-ice modeling, *Ocean Model.*, **70**, 166–173, doi:10.1016/j.ocemod.2013.05.012.

Doble, M. J., G. De Carolis, M. H. Meylan, J.-R. Bidlot, and P. Wadhams (2015). Relating wave attenuation to pancake ice thickness, using field measurements and model results, *Geophys. Res. Lett.*, **42**, 4473–4481, doi:10.1002/2015GL063628.

Elgar, S. (1987). Bias of effective degrees of freedom of a spectrum, *J. Waterway, Port, Coastal, and Ocean Eng.*, **113**(1), 77-82.

Hebert, D. A., R. A. Allard, E. J. Metzger, P. G. Posey, R. H. Preller, A. J. Wallcraft, M. W. Phelps, and O. M. Smedstad (2015). Short-term sea ice forecasting: An assessment of ice concentration and ice drift forecasts using the U.S. Navy's Arctic Cap Nowcast/Forecast System, *J. Geophys. Res.*, **120**, doi:10.1002/2015JC011283.

Helfrich, S. R., D. McNamara, B. H. Ramsay, T. Baldwin, and T. Kasheta (2007). Enhancements to, and forthcoming developments in the Interactive Multisensor Snow and Ice Mapping System (IMS), *Hydrol. Process.* **21**, 1576–1586.

Hodur, R. M. (1997). The Naval Research Laboratory's Coupled Ocean/Atmospheric Mesoscale Prediction System (COAMPS). *Mon. Wea. Rev.*, **125**, 1414-1430.

Hogan, T., and 16 Coauthors (2014), The Navy Global Environmental Model, *Oceanography*, **27**(3), 116-125.

Horvat, C. and E. Tziperman (2015). A prognostic model of sea-ice floe size and thickness distribution. *The Cryosphere*, **9**, 2119–2134.

Hunke, E. C. and W. H. Lipscomb (2008). *CICE: The Los Alamos Sea Ice Model. Documentation and Software User's Manual. Version 4.0.* T-3 Fluid Dynamics Group, Los Alamos National Laboratory, Tech. Rep. LA-CC-06-012.

Hwang, P.A., 2011. A note on the ocean surface roughness spectrum, *J. Atmos. Oceanic Technol.*, **28**, 436-443.

Kaleschke, L., C. Lupkes, T. Vihma, J. Haarpaintner, A. Bochert, J. Hartmann, and G. Heygster, (2001). "SSM/I Sea Ice Remote Sensing for Mesoscale Ocean-Atmosphere Interaction Analysis", *Can. J. Rem. Sens.*, **27**(5), 526-537.

Keller, J.B. (1998). Gravity waves on ice-covered water. *J. Geophy. Res.*, **103** (C4): 7663-7669.

Kahma, K. K., and C. J. Calkoen (1992). Reconciling discrepancies in the observed growth of wind-generated waves. *J. Phys. Oceanogr.*, **22**, 1389-1405.

Kohout, A. L., M. H. Meylan, D. R. Plew (2011). Wave attenuation in a marginal ice zone due to the bottom roughness of ice floes. *Annals of Glaciology*, **52**(57), 118-122.

Kohout, A. L., M. J. M. Williams, S. M. Dean, and M. H. Meylan (2014). Storm-induced sea-ice breakup and the implications for ice extent, *Nature*, **509**, 604–607.

Kohout, A. L., B. Penrose, S. Penrose, M.J.M. Williams (2015). A device for measuring wave-induced motion of ice floes in the Antarctic marginal ice zone. *Annals of Glaciology*, **56** (69), 415-424.

Komen, G. J., L. Cavalieri, M. Donelan, K. Hasselmann, S. Hasselmann, and P. A. E. M. Janssen (1994). *Dynamics and Modelling of Ocean Waves*. Cambridge Univ. Press, 532 pp.

Li, J., A. L. Kohout, and H. H. Shen (2015). Comparison of wave propagation through ice covers in calm and storm conditions, *Geophy. Res. Letts.* **42**(14), 5935–5941, doi: 10.1002/2015GL064715.

Li, J., Kohout, A. L., Doble, M. J., Wadhams, P., Guan, C., and Shen, H. H. (2017). Rollover of apparent wave attenuation in ice covered seas. *J. of Geophy. Res.*, **122**. <https://doi.org/10.1002/2017JC012978>.

Liu, A.K. and E. Mollo-Christensen (1988). Wave propagation in a solid ice pack. *J. Phys. Oceanogr.*, **18**, 1702-1712.

Liu, A. K., B. Holt, and P. W. Vachon (1991). Wave propagation in the Marginal Ice Zone: Model predictions and comparisons with buoy and Synthetic Aperture Radar data. *J. Geophys. Res.*, **96**, (C3), 4605-4621.

Markus, T., and D.J. Cavalieri (2000). An enhancement of the NASA Team sea ice algorithm. *IEEE Trans. Geosci. Rem. Sens.*, **38**(3), 1387-1398.

Markus, T., and D.J. Cavalieri (2009). The AMSR-E NT2 sea ice concentration algorithm: its basis and implementation. *J. Rem. Sens. Japan*, **29**(1), 216-225.

Masson, D. (1994). Interactions with ice. [This is Chapter II.7 of Komen et al. (1994).] 171-174.

Masson, D. and P.H. LeBlond (1989). Spectral evolution of wind-generated surface gravity waves in a dispersed ice field, *J. Fluid Mech.*, **202**, 43-81.

Metzger, E.J., J.D. Dykes, A.J. Wallcraft, L.F. Smedstad, B.C. Ruston, T.R. Whitcomb, S. Chen and J. Chen (2014). Operational Implementation Design for the Earth System Prediction Capability (ESPC): A First Look, *NRL Report*, NRL/MR/7320--14-9498, 27 pp.

Metzger, E.J., R.W. Helber, P.J. Hogan, P.G. Posey, P.G. Thoppil, T.L. Townsend, A.J. Wallcraft, O.M. Smedstad, and D.S. Franklin (2017). [Global Ocean Forecast System 3.1 Validation Testing](#), *NRL Report*, NRL/MR/7320--17-9722, 61 pp.

Meylan, M.H., D. Masson (2006). A linear Boltzmann equation to model wave scattering in the marginal ice zone. *Ocean Modelling*, **11**, 417-427.

Meylan, M., L. G. Bennetts, and A. L. Kohout (2014). In situ measurements and analysis of ocean waves in the Antarctic marginal ice zone, *Geophys. Res. Lett.*, **41**, 5046–5051, doi:10.1002/2014GL060809.

Mosig, J. E. M., F. Montiel, and V. A. Squire (2015). Comparison of viscoelastic-type models for ocean wave attenuation in ice-covered seas, *J. Geophys. Res.*, **120**, 6072–6090, doi:10.1002/2015JC010881.

Newyear, K. and S. Martin (1999). Comparison of laboratory data with a viscous two-layer model of wave propagation in grease ice, *J. of Geophys. Res.*, **104** (C4), 7837-7840.

Perrie, W. and Y. Hu (1996). Air-Ice-Ocean Momentum Exchange. Part I: Energy transfer between waves and ice floes, *J. Phys. Ocean.*, **26**, 1705-1720.

Posey, P. G., E. J. Metzger, A. J. Wallcraft, R. H. Preller, O. M. Smedstad, and M.W. Phelps (2010). "Validation of the 1/12° Arctic Cap Nowcast/Forecast System (ACNFS). *Naval Research Laboratory Memorandum Report* NRL/MR/7320-9287.

Posey, P.G., E.J. Metzger, A.J. Wallcraft, D.A. Hebert, R.A. Allard, O.M. Smedstad, M.W. Phelps, F. Fetter, J.S. Stewart, W.N. Meier, and S.R. Helfrich (2015). Improving Arctic sea ice edge forecasts by assimilating high horizontal resolution sea ice concentration data into the US Navy's ice forecast systems, *The Cryosphere*, **9**, 1735-1745.

Rabault, J., G. Sutherland, O. Gundersen, A. Jensen (2017). Measurements of wave damping by a grease ice slick in Svalbard using off-the-shelf sensors and open-source electronics. *J. of Glaciology*, **63**(238) 372–381, doi: 10.1017/jog.2017.1.

Rogers, W. E., and M. D. Orzech (2013). *Implementation and testing of ice and mud source functions in WAVEWATCH III®*, NRL Memorandum Report, NRL/MR/7320-13-9462, 31 pp.

Rogers, W. E. and S. Zieger (2014). New wave-ice interaction physics in WAVEWATCH III®, *22nd IAHR International Symposium on Ice*, Singapore, Aug 11-15, 2014, 8pp.

Rogers, W.E. and G.Ph. Van Vledder (2013). Frequency width in predictions of windsea spectra and the role of the nonlinear solver, *Ocean Modelling*, **70**, 52-61.

Rogers, W.E., J. Thomson, H.H. Shen, M.J. Doble, P. Wadhams and S. Cheng (2016). Dissipation of wind waves by pancake and frazil ice in the autumn Beaufort Sea, *J. Geophys. Res.*, **121** 7991-8007, doi:10.1002/2016JC012251.

Spreen, G., L. Kaleschke, G. Heygster (2008). "Sea Ice Remote Sensing Using AMSR-E 89 GHz Channels", *J. Geophys. Res.*, **113**, C02S03, doi:10.1029/2005JC003384.

Stammerjohn, S., R. Massom, D. Rind, and D. Martinson (2012). Regions of rapid sea ice change: An inter-hemispheric seasonal comparison, *Geophys. Res. Lett.*, **39**, L06501, doi:10.1029/2012GL050874.

Stopa, J.E., F. Arduin, F. Girard-Arduin (2016). Wave climate in the Arctic 1992-2014: seasonality and trends, *The Cryosphere*, **10**, 1605-1629.

Sutherland, G., T. Halsne, J. Rabault, A. Jensen (2017). The attenuation of monochromatic surface waves due to the presence of an inextensible cover. *Wave motion*, **68**, 88-96.

Thomson, J. (2012). Wave breaking dissipation observed with SWIFT drifters, *J. Atmos. Ocean. Tech.*, **29**, 1866–1882, doi:10.1175/JTECH-D-12-00018.1.

Thomson, J. (2015). ONR Sea State DRI Cruise Report: R/V Sikuliaq, Fall 2015 (SKQ201512S), 45 pp. retrieved from [http://www.apl.washington.edu/project/project.php?id=arctic\\_sea\\_state](http://www.apl.washington.edu/project/project.php?id=arctic_sea_state) on Aug. 9 2016. 45 pp.

Thomson, J., and W. E. Rogers (2014). Swell and sea in the emerging Arctic Ocean, *Geophys. Res. Lett.*, **41**, doi:10.1002/2014GL059983.

Thomson, J., V. Squire, S. Ackley, E. Rogers, A. Babanin, P. Guest, T. Maksym, P. Wadhams, S. Stammerjohn, C. Fairall, O. Persson, M. Doble, H. Gruber, H. Shen, J. Gemmrich, S. Lehner, B. Holt, T. Williams, M. Meylan, J. Bidlot, (2013). Science plan: Sea state and boundary layer physics of the emerging Arctic Ocean. *Technical Report 1306*, Applied Physics Laboratory, University of Washington. 59 pp.

Thomson, J., S. Ackley, H.H. Shen, and W.E. Rogers (2017). The Balance of Ice, Waves, and Winds in the Arctic Autumn. *Earth & Space Science News, Eos.org*, April 2017, 30-34.

Tolman, H. L. (1991). A Third-generation model for wind-waves on slowly varying, unsteady, and inhomogeneous depths and currents, *J. Phys. Oceanogr.* **21**(6), 782-797.

Tolman, H. L. (1997). *User manual and system documentation of WAVEWATCH-III version 1.15*, Tech. Note 151 NOAA/NWS/NCEP/MMAB, 104 pp.

Tolman, H. L. (2003). Treatment of unresolved islands and ice in wind wave models, *Ocean Modelling*, **5**, 219-231.

Tolman, H. L. (2002). *User manual and system documentation of WAVEWATCH-III version 2.22*, Tech. Note 222, NOAA/NWS/NCEP/MMAB, 133 pp.

Tolman, H. L. and the WAVEWATCH III® Development Group (2014). *User Manual and System Documentation of WAVEWATCH III® version 4.18*, Tech. Note 316, NOAA/NWS/NCEP/MMAB, 282 pp. + Appendices.

Wadhams, P. and J. Thomson (2015). The Arctic Ocean cruise of R/V Sikuliaq 2015, An investigation of waves and the advancing ice edge. *Il Polo*, **LXX-4**, 9-38.

Wadhams, P., V. A. Squire, D. J. Goodman, A. M. Cowan, and S. C. Moore (1988). The attenuation rates of ocean waves in the marginal ice zone, *J. of Geophys. Res.*, **93**, 6799–6818.

Wadhams, P., F. F. Parmiggiani, G. de Carolis, D. Desiderio, and M. J. Doble (2004). SAR imaging of wave dispersion in Antarctic pancake ice and its use in measuring ice thickness, *Geophys. Res. Lett.*, **31**, L15305, doi:10.1029/2004GL020340.

WAMDIG (1988). The WAM model – a third generation ocean wave prediction model. *J. Phys. Oceanogr.*, **18**, 1775-1810.

Wang, R., H. H. Shen (2010). Gravity waves propagating into an ice-covered ocean: A viscoelastic model, *J. Geophys. Res.*, **115**, doi:10.1029/2009JC005591.

Weber, J.E. (1987). Wave attenuation and wave drift in the marginal ice zone. *J. Phys. Oceanogr.*, **17**(12), 2351-2361.

The WAVEWATCH III® Development Group (WW3DG) (2016). *User manual and system documentation of WAVEWATCH III® version 5.16*. Tech. Note 329, NOAA/NWS/NCEP/MMAB, College Park, MD, USA, 326 pp. + Appendices.

Zhao, X., H.H. Shen (2015). Wave propagation in frazil/pancake, pancake, and fragmented ice covers, *Cold Regions Science and Tech.*, **113**, 71-80.